NAT'L INST. OF STAND & TECH
A11106 419493

NIST
PUBLICATIONS

NIST Special Publication 953

Technical Digest Symposium on Optical Fiber Measurements, 2000

Sponsored by the National Institute of Standards and Technology
in cooperation with the IEEE Lasers and Electro-Optics Society
and the Optical Society of America

1901-2001
NIST CENTENNIAL

NIST National Institute of Standards and Technology • Technology Administration • U.S. Department of Commerce

QC
100
.U57
NO.953
2000 c.2
AUTHENTICATED
U.S. GOVERNMENT
INFORMATION
GPO

The National Institute of Standards and Technology was established in 1988 by Congress to "assist industry in the development of technology . . . needed to improve product quality, to modernize manufacturing processes, to ensure product reliability . . . and to facilitate rapid commercialization . . . of products based on new scientific discoveries."

NIST, originally founded as the National Bureau of Standards in 1901, works to strengthen U.S. industry's competitiveness; advance science and engineering; and improve public health, safety, and the environment. One of the agency's basic functions is to develop, maintain, and retain custody of the national standards of measurement, and provide the means and methods for comparing standards used in science, engineering, manufacturing, commerce, industry, and education with the standards adopted or recognized by the Federal Government.

As an agency of the U.S. Commerce Department's Technology Administration, NIST conducts basic and applied research in the physical sciences and engineering, and develops measurement techniques, test methods, standards, and related services. The Institute does generic and precompetitive work on new and advanced technologies. NIST's research facilities are located at Gaithersburg, MD 20899, and at Boulder, CO 80303. Major technical operating units and their principal activities are listed below. For more information contact the Publications and Program Inquiries Desk, 301-975-3058.

Office of the Director
- National Quality Program
- International and Academic Affairs

Technology Services
- Standards Services
- Technology Partnerships
- Measurement Services
- Technology Innovation
- Information Services

Advanced Technology Program
- Economic Assessment
- Information Technology and Applications
- Chemical and Biomedical Technology
- Materials and Manufacturing Technology
- Electronics and Photonics Technology

Manufacturing Extension Partnership Program
- Regional Programs
- National Programs
- Program Development

Electronics and Electrical Engineering Laboratory
- Microelectronics
- Law Enforcement Standards
- Electricity
- Semiconductor Electronics
- Electromagnetic Fields[1]
- Electromagnetic Technology[1]
- Optoelectronics[1]

Chemical Science and Technology Laboratory
- Biotechnology
- Physical and Chemical Properties[2]
- Analytical Chemistry
- Process Measurements
- Surface and Microanalysis Science

Physics Laboratory
- Electron and Optical Physics
- Atomic Physics
- Optical Technology
- Ionizing Radiation
- Time and Frequency[1]
- Quantum Physics[1]

Materials Science and Engineering Laboratory
- Intelligent Processing of Materials
- Ceramics
- Materials Reliability[1]
- Polymers
- Metallurgy
- NIST Center for Neutron Research

Manufacturing Engineering Laboratory
- Precision Engineering
- Automated Production Technology
- Intelligent Systems
- Fabrication Technology
- Manufacturing Systems Integration

Building and Fire Research Laboratory
- Structures
- Building Materials
- Building Environment
- Fire Safety Engineering
- Fire Science

Information Technology Laboratory
- Mathematical and Computational Sciences[2]
- Advanced Network Technologies
- Computer Security
- Information Access and User Interfaces
- High Performance Systems and Services
- Distributed Computing and Information Services
- Software Diagnostics and Conformance Testing
- Statistical Engineering

---

[1] At Boulder, CO 80303.

[2] Some elements at Boulder, CO.

NIST Special Publication 953

Technical Digest Symposium on Optical Fiber Measurements, 2000

NIST

IEEE LASERS AND ELECTRO-OPTICS SOCIETY LEOS

OSA
Optical Society of America

Digest of a symposium sponsored by the
National Institute of Standards and Technology
in cooperation with the
IEEE Lasers and Electro-Optics Society
and the Optical Society of America

September 26-28, 2000
National Institute of Standards and Technology
Boulder, Colorado 80303

Edited by
P.A. Williams
G. W. Day

September 2000

U.S. Department of Commerce
Norman Y. Mineta, Secretary

Technology Administration
Dr. Cheryl L. Shavers, Under Secretary of Commerce for Technology

National Institute of Standards and Technology
Raymond G. Kammer, Director

Certain commercial entities, equipment, or materials may be identified in this document in order to describe an experimental procedure or concept adequately. Such identification is not intended to imply recommendation or endorsement by the National Institute of Standards and Technology, nor is it intended to imply that the entities, materials, or equipment are necessarily the best available for the purpose.

National Institute of Standards and Technology Special Publication 953
Natl. Inst. Stand. Technol. Spec. Publ. 953, 195 pages (September 2000)
CODEN: NSPUE2

U.S. GOVERNMENT PRINTING OFFICE
WASHINGTON: 2000

For sale by the Superintendent of Documents
U.S. Government Printing Office
Washington, DC 20402-9325

Preface

This year, SOFM is two decades old. After all these years, fiberoptic metrology is not only still important, but we are seeing a rise in metrology needs for the technologies resulting from fiber optics – components, integrated optics and fiber systems. Accordingly, we are pleased to see a significant number of component measurement papers in this year's Symposium.

The majority of this year's papers fall into one of three categories: dispersion, components and nonlinear optics. Dispersion is the largest category, containing two sessions of polarization-mode dispersion, a session of chromatic dispersion and a session for group-delay measurements on fiber Bragg gratings. Component papers include grating metrology as well as receiver and amplifier characterization. Nonlinear measurements fill two sessions with measurements of nonlinear coefficient and effective area. And, with all of this, it is nice to see original work still going on in fibers – we find a full session of papers relating to novel (engineered) fibers.

This year we have 44 papers (9 invited and 35 contributed), with strong international participation (slightly more than half originating outside the United States).

Happy reading.

Paul Williams
Gordon Day
Boulder, Colorado
September 2000

Except where attributed to NIST authors, the content of individual sections of this volume has not been reviewed or edited by the National Institute of Standards and Technology. NIST therefore accepts no responsibility for comments or recommendations therein. The mention of trade names in this volume is in no sense an endorsement or recommendation by the National Institute of Standards and Technology.

SYMPOSIUM COMMITTEE

G.W. Day, NIST, General Chair

P.A. Williams, NIST, Program Chair

M. Artiglia, CSELT

A.J. Barlow, PerkinElmer Optoelectronics

J. Benson, NPL

S.C. Fleming, University of Sydney

D.L. Franzen, NIST

N. Gisin, University of Geneva

M. Hackert, Corning, Inc.

T.A. Hanson, Corning, Inc.

J. Jackel, Telcordia Technologies

H. Nagai, Anritsu

W.A. Reed, Lucent Technologies

G.W. Schinn, EXFO

C. Shaar, GN Nettest

K.K. Wong, Codeon Corporation

CONTENTS

Characterisation of photonic crystal fibres

T. A. Birks, J. C. Knight, B. J. Mangan, A. Ortigosa-Blanch and P. St.J. Russell
Optoelectronics Group, Department of Physics, University of Bath, Claverton Down, Bath BA2 7AY, United Kingdom
pystab@bath.ac.uk

Abstract: Light is confined to the core of a photonic crystal fibre by an array of air holes in the cladding. Although the methods used to measure their characteristics are broadly similar to those applied to conventional fibres, the results of such measurements are often strikingly different.

Photonic crystal fibres

In 1996 we first reported an entirely new class of optical fibre, the photonic crystal fibre[1] (PCF, also known as holey fibre or microstructure fibre). Whereas conventional fibres confine light by total internal reflection between a high index core and a lower index cladding, a PCF has an array of air holes in the cladding that run along the length of the fibre. It is the presence of these holes that confines light to the fibre's core, so the solid part of the fibre (core and cladding) can be made from a single material, undoped fused silica.

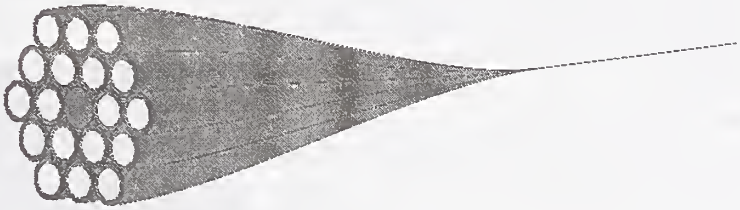

Fig. 1. The fabrication of a simple PCF from a stack of silica tubes with a central solid rod. In practice the stack would have around 10 tubes along one side.

Fabrication begins with a number of silica tubes and rods, with an outer diameter of 1 mm or a little less. These are painstakingly stacked into a close-packed array. The distribution of tubes and rods in the stack determines the type of PCF. For example, the simplest is made entirely from tubes, except for a single solid rod in the middle to form the core of the eventual fibre, Fig. 1. The stack is the fibre preform, to be drawn into fibre using a standard drawing tower[1,2]. A solid silica jacket can be added around the fibre to enlarge it and help strip cladding modes.

We have demonstrated a wide range of PCF designs, and developed the conceptual tools needed to understand their unique properties[1-12]. Other research groups, some in collaboration with us, have also reported theoretical and experimental advances[13-18]. In most of these studies, the core is a region of higher average index - usually the site of a "missing" hole. Such an "index guiding" fibre guides light by total internal reflection from a cladding that (because of the holes) has a lower effective refractive index. More recently, we demonstrated PCFs with a low-index core, such as an enlarged hole. Unlike previous hollow core fibres, which are leaky waveguides, these "band gap guiding" PCF can be true low-loss single-mode waveguides.

The characterisation of PCFs can be challenging at times, though the techniques themselves are essentially the same as those used to characterise conventional fibres. However, the *results* of such measurements are often strikingly different.

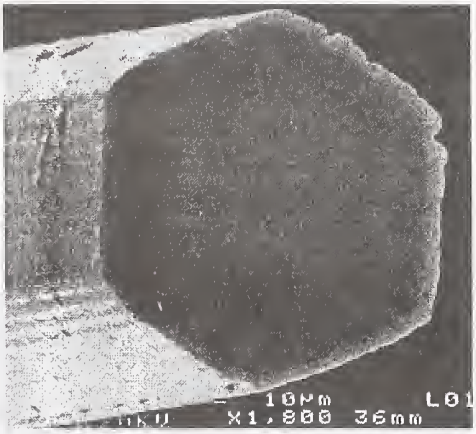

Fig. 2. SEM image of a PCF with $\Lambda = 2.3$ μm and $d/\Lambda = 0.15$. The central site with the "missing" air hole acts as the core.

Single-mode propagation in index-guiding PCFs

Our first PCF[1,2] had a solid core, and the diameter d of the holes was small compared to their pitch (centre-centre spacing) Λ, Fig. 2. This was the simplest structure to attempt. Our immediate question was: will the fibre guide light at all? Light from a He-Ne laser was coupled into one end of the fibre, and the output light was projected onto a screen to examine the far field pattern, Fig. 3. A coupling efficiency of 50 % was readily obtained. As well as confirming that the fibre was indeed a waveguide (and that physics is beautiful), this simplest of measurements indicated that the fibre was single-mode. Although clearly not gaussian, the far field pattern shared the full symmetry of the fibre, and did not change in distribution as the fibre was bent or the launch position and angle were varied.

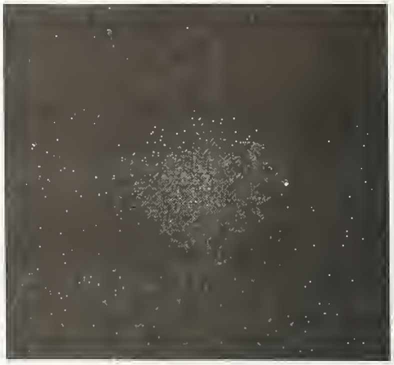

Fig. 3. Far field pattern at $\lambda = 633$ nm.

This experiment was repeated with every laser source we could lay our hands on. Surprisingly, we found that the fibre remained single-mode from 337 nm to 1550 nm. A measurement of the *near field* pattern at the fibre's endface, Fig. 4, turned out to be the key to developing our understanding of this behaviour. At short wavelengths, the light avoided the holes. In contrast, at longer wavelengths the light did not image the holes so well, and more of the light propagated in air. As a result, the light was "seeing" a lower effective cladding index at long wavelengths than at short wavelengths.

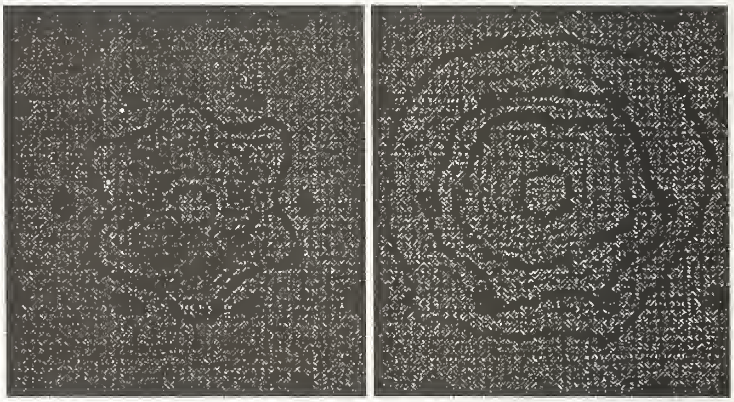

Fig. 4. Contour plots of near field at 633 nm and 1550 nm, superimposed to scale on an SEM image of the endface.

This insight led to our effective index model for the PCF[3], by which the effective V-value

$$V = \frac{2\pi\rho}{\lambda}\sqrt{n_{core}^2 - n_{cladding}^2}\,, \qquad (1)$$

can be found from a calculation of a rigorously-defined cladding effective index $n_{cladding}$. Unlike a conventional fibre, where V rises without limit as $\lambda \rightarrow 0$, V in a PCF has an upper bound. This is because, in the short wavelength limit, $n_{cladding}$ approaches n_{core} in such a way as to cancel the explicit λ dependence in eq. (1), Fig. 5. For sufficiently small relative hole sizes d/Λ, V will always be less than the second-mode cutoff value. Hence a PCF with small enough holes will be *endlessly single-mode*, at all wavelengths.

One remarkable consequence is that an endlessly single-mode PCF must also be single-mode for all *scales* Λ, for a given d/Λ. We confirmed this by making a PCF like that of Fig. 2 but with $\Lambda = 10$ μm and a core about 22 μm across. The fibre was single-mode even for a wavelength as short as 458 nm[4]. This directly shows that such a fibre with a core diameter of 75 μm would be single-mode at $\lambda = 1550$ nm!

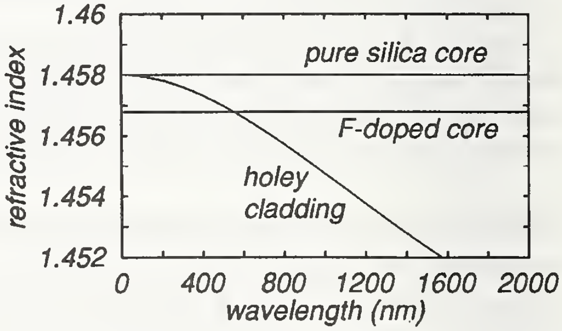

Fig. 5. The effective cladding index of a PCF, along with the index of pure silica and F-doped silica cores. Material dispersionn has been omitted for the sake of clarity.

Bend loss

The *useful* single-mode range of a conventional fibre is bounded at long wavelengths by a bend edge, beyond which the fibre suffers unacceptably high losses due to unavoidable bending. It turns out that the useful single-mode range of an endlessly single-mode PCF is bounded at short wavelengths by a *second bend edge*.

The fibre was subjected to a single turn bend of a given radius. The transmission spectrum of the bent fibre was measured using a white light source and optical spectrum analyser. The measurement was repeated for a number of radii of curvature[3]. A typical loss spectrum is shown in Fig. 6, along with the variation of the short-wavelength bend edge with radius. Firstly, note how tightly the fibre must be bent to induce significant loss. The existence of the new bend edge is a less restrictive limit on the useful range of a PCF than the second-mode cutoff of a conventional fibre.

Secondly, the effective index model predicts that the critical radius of curvature R_c, tighter than which unacceptable bend loss occurs, varies as

$$R_c \propto \frac{\Lambda^3}{\lambda^2} \ . \tag{2}$$

The close fit to this dependence confirms the validity of the model. The strong dependence on Λ indicates that large core PCFs are more susceptible to bend loss, and this is indeed a practical limit on the usefulness of large core PCFs.

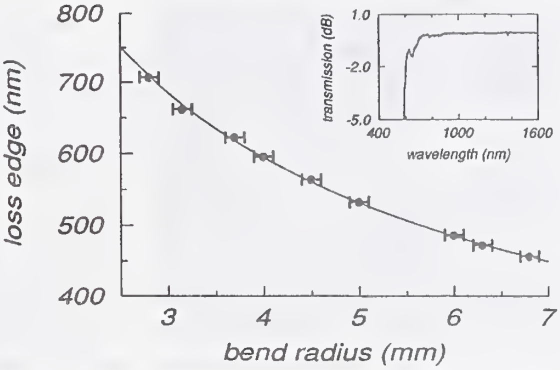

Fig. 6. The wavelength of 3 dB loss at the short-wavelength bend edge, versus bend radius, for the PCF of Fig. 2. The line is a fit to $\lambda \propto R^{-1/2}$ *Inset: a typical loss spectrum.*

Interestingly, a simple model for the stripping of cladding modes in a PCF predicts that the length of fibre required has the same dependence on Λ and λ as R_c in eq.(2). Hence large core PCFs are also harder to strip cladding modes from. This was a real experimental headache for us, because long lengths of our uncoated fibres needed to be immersed in index-matching fluid to observe the guided mode. Our present ability to surround the photonic crystal region of such fibres with a solid silica jacket (see, for example, Fig. 7) has greatly helped.

Depressed core PCFs

We made another PCF like that of Fig. 2, but the solid core rod was made of fluorine-doped silica[5], Fig. 7. This depressed the core index by 0.0012. Fig. 5 is a plot of n_{core} and $n_{cladding}$ for this fibre. The cladding index exceeds the core index at short wavelengths, where the fibre becomes an antiguide. It resembles the "dispersive fibres" reported by Morishita et al, and like them has a short wavelength cutoff[19]. Note that this is a wavelength below which *no* mode is guided, unlike the conventional "cutoff wavelength" below which *two* modes are guided.

Transmission and bend loss measurements confirm the existence of this cutoff, which is more graphically illustrated by the near-field images in Fig. 8. These show how the field spreads out from the core as the wavelength decreases, in contrast with the more familiar behaviour in conventional fibres. This property is expected to be valuable in evanscent field devices with stronger interactions at shorter wavelengths.

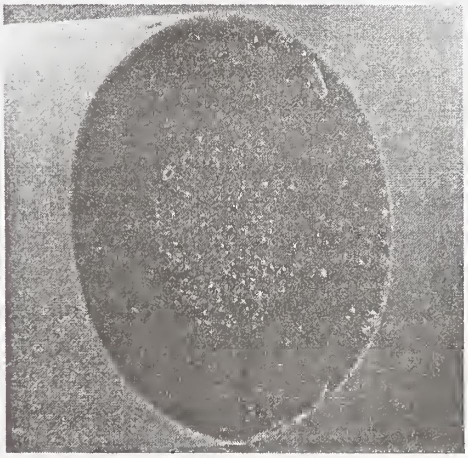

Fig. 7. SEM image of the depressed core PCF, showing the photonic crystal region surrounded by a solid jacket.

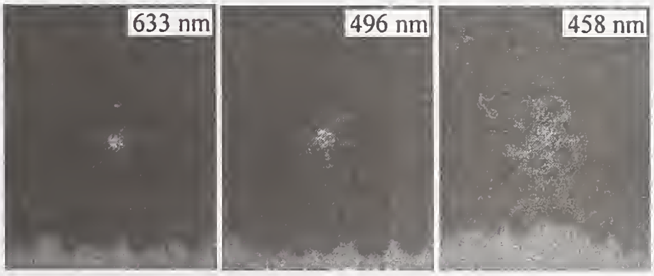

Fig. 8. Near field images at the output endface of the depressed core PCF, for three different laser wavelengths. At 458 nm, the light is not guided at all.

Multiple core PCFs

The original PCF was made from a stack of tubes and a single solid rod. A PCF with more than one core can be made just as easily, by including more than one solid rod in the array[6]. The strength of coupling between adjacent cores is represented by the coupling beat length L_b, the distance along which light couples from one core to the other and back again. Attempts to measure this directly were unsuccessful: scattering from the holes confounded our ability to transversely observe laser light in each core.

We contented ourselves with measurements of spectral beating, from which some idea of the coupling length can be deduced. Light from a tunable diode laser was focused into one core of a two-core PCF using a high power microscope objective, and the near field pattern at the other end was imaged. The division of power between the two cores was recorded as a function of wavelength, Fig. 9. The measurement was repeated for similar fibres with different pitches Λ. The spectral period λ_{fsr} is plotted against Λ in Fig. 10, where an exponential dependence is evident. (The normalised quantity plotted is L_b/λ if it is assumed that L_b is directly or inversely proportional to λ.)

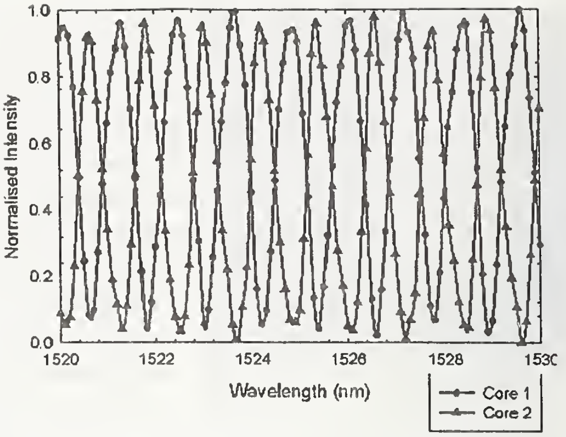

Fig. 9. The power transmitted in each core of a two-core PCF, versus wavelength.

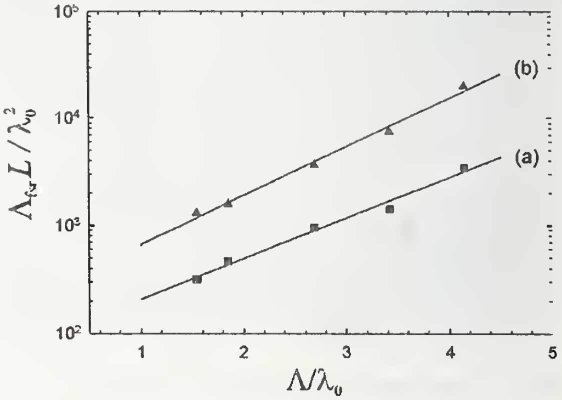

Fig. 10. The normalised spectral period of a two-core PCF versus pitch, for core separations of (a) $\sqrt{3}\Lambda$ and (b) $\sqrt{7}\Lambda$.

High birefringence PCFs

There are two sources of birefringence in optical fibres, stress birefringence (due to transverse stresses) and form birefringence (due to the shape of the core). In conventional fibres with only a small core-cladding index difference to play with, high birefringence (HiBi) fibres are made by inducing stresses across the core, giving birefringence beat lengths no shorter than a few mm at λ = 1550 nm. In contrast, the available index difference in a PCF is that between silica and air, and very large form birefringence becomes possible. We made a HiBi PCF by varying the sizes of the air holes near the core[7], Fig. 11.

The measurement challenge here is the determination of the birefringence beat length L_b. Again, it was not possible to measure this, and we had to resort to spectral measurements. Both eigenpolarisations were equally excited at the input of the straight PCF by the tunable laser. The light emerging from the other end of the fibre was passed through a polariser at 45° to the principal axes and then detected. The spectral beats measured are shown in Fig. 12.

An estimate of L_b can be found from this measurement with the help of some numerical modelling, which enabled us to fix the wavelength dependence of λ. The resulting estimated beat length of 0.43 mm is an order of magnitude smaller than the typical value for conventional HiBi fibres at this wavelength, and indicates the potentially superior polarisation holding properties of such PCFs.

Fig. 11. SEM image of a HiBi PCF.

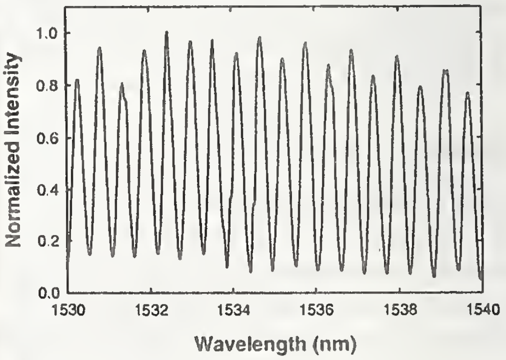

Fig. 12. Transmission spectrum through a HiBi PCF followed by a 45° polariser.

Group velocity dispersion measurements

With our improved control over the fabrication process, we were able to make PCFs with larger air holes relative to their separations. These were predicted to have unusual dispersion properties, including strong normal dispersion at 1550 nm[8] (for dispersion compensation) and anomalous net dispersion at wavelengths shorter than 1270 nm[9] (for nonlinear interactions[18], including soliton propagation at visible and near infrared wavelengths[10]).

Group velocity dispersion (GVD) in PCFs has been measured using white light interferometry[11]. The PCFs were large-hole structures, the most extreme of which is shown in Fig. 13. The measured GVD is shown in Fig. 14. The measurement compares well with the calculated GVD of a rod of silica in air, with the same diameter as the core of the PCF. This is not surprising; the thin webs of silica supporting the core do not contribute much to the properties of the fundamental mode.

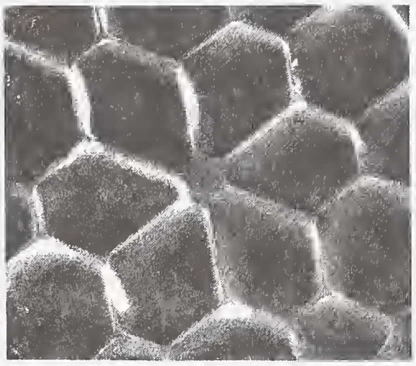

Fig. 13. SEM image of an extreme small core PCF with anomalous dispersion at visible wavelengths.

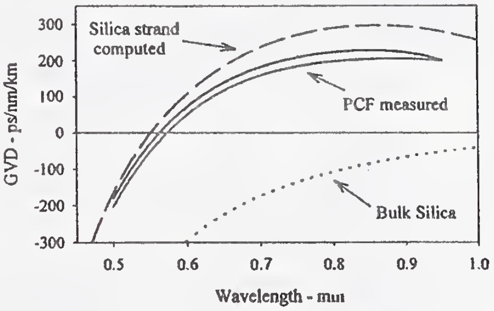

Fig. 14. GVD of the PCF of Fig. 14 (two polarisations), together with the GVD of the corresponding silica rod and of bulk silica.

Band gap guiding PCFs

All of the measurements described above were made on index-guiding PCFs. Despite their unusual structures these all guide light by total internal reflection, and so despite their distinctive properties they have many similarities with conventional fibres. In contrast, band gap guiding PCFs (Fig. 15) are radically different[12]. Because the core is hollow, light cannot be confined by total internal reflection - the cladding index (however defined) will always be greater. Instead, light is confined by a generalised Bragg scattering from the periodic array of large air holes[20].

Near field images of the fibre output, for white light input, clearly show a guided mode in the hollow core. However, the light is invariably strongly coloured. This is because of the wavelength dependence of the photonic band gap that confines the light. Transmission spectra of the fibre, Fig. 16, show passbands separated by wavelength ranges within which no light is guided. The transmission of this fibre is far in excess of that seen in previous "hollow core fibres", which are in reality antiguides and therefore leaky.

One remarkable property of the fibre is that there is very little Fresnel reflection at the ends. Whereas conventional fibres (and indeed index-guiding PCFs) have an index mismatch between the fibre and the air at the ends, the light in the hollow core PCF sees no such mismatch.

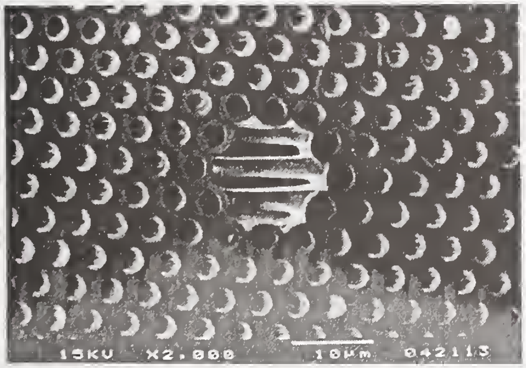

Fig. 15. SEM image of a band gap guiding PCF with a hollow core.

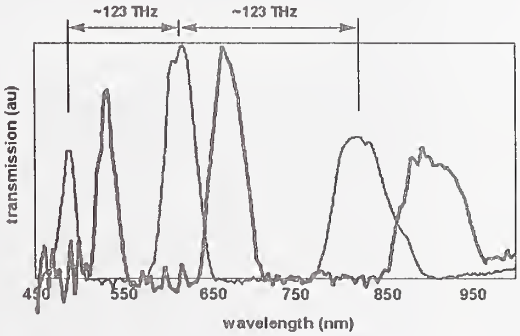

Fig. 16. Transmission spectrum of two similar hollow core PCFs with slightly different sizes.

Conclusions

We have reviewed some of the properties of photonic crystal fibres, and described how well-known measurement techniques can be applied to these remarkable structures. Although PCFs behave in many ways like ordinary fibres, some of their characteristics are strikingly different. These differences lead to a variety of applications for which PCFs out-perform conventional fibres. We are in the process of setting up a company to exploit these fibres[21].

Acknowledgements

Besides the authors, whole team of researchers has contributed to the many results described here, including R. F. Cregan, W. J. Wadsworth, J. Arriaga and D. Mogilevtsev. The work was supported by funding from EPSRC, DERA and Corning Inc, and our fibre drawing tower was donated by BT Labs. T. A. Birks is a Royal Society University Research Fellow.

References

[1] J. C. Knight, T. A. Birks, D. M. Atkin, P. St.J. Russell "Pure silica single-mode fibre with hexagonal photonic crystal cladding", Proc. OFC (1996) postdeadline paper PD3.

[2] J. C. Knight, T. A. Birks, P. St.J. Russell, D. M. Atkin "All-silica single-mode optical fiber with photonic crystal cladding" Opt. Lett. **21** (1996) 1547; errata *ibid* **22** (1997) 484.

[3] T. A. Birks, J. C. Knight, P. St.J. Russell "Endlessly single-mode photonic crystal fiber" Opt. Lett. **22** (1997) 961.

[4] J. C. Knight, T. A. Birks, R. F. Cregan, P. St.J. Russell, J. P. DeSandro "Large mode area photonic crystal fibre" Electron. Lett. **34** (1998) 1347.

[5] B. J. Mangan, J. Arriaga, T. A. Birks, J. C. Knight, P. St.J. Russell "Photonic crystal fibre with a short wavelength cutoff" Proc. CLEO (2000) 606.

[6] J. C. Knight, T. A. Birks, B. J. Mangan, P. St.J. Russell, G. G. Vienne, J.P. DeSandro "Multicore photonic crystal fibres" Proc. OFS (1997) postdeadline paper PD5.

[7] A. Ortigosa-Blanch, J. C. Knight, W. J. Wadsworth, J. Arriaga, B. J. Mangan, T. A. Birks, P. St.J. Russell "Highly birefringent photonic crystal fibers" to appear in Opt. Lett.

[8] T. A. Birks, D. Mogilevtsev, J. C. Knight, P. St.J. Russell "Dispersion compensation using single material fibers" IEEE Photon. Technol. Lett. **11** (1999) 674.

[9] D. Mogilevtsev, T. A. Birks, P. St.J. Russell "Group-velocity dispersion in photonic crystal fibers" Opt. Lett. **23** (1998) 1662.

[10] W. J. Wadsworth, J. C. Knight, A. Ortigosa-Blanch, J. Arriaga, E. Silvestre, P. St.J. Russell "Soliton effects in photonic crystal fibres at 850 nm" Electron. Lett. **36** (2000) 53.

[11] J. C. Knight, J. Arriaga, T. A. Birks, A. Ortigosa-Blanch, W. J. Wadsworth, P. St.J. Russell "Anomalous dispersion in photonic crystal fiber" to appear in IEEE Photon. Technol. Lett.

[12] R. F. Cregan, B. J. Mangan, J. C. Knight, T. A. Birks, P. St.J. Russell, P. J. Roberts, D. C. Allen "Single-mode photonic band gap guidance of light in air" Science **285** (1999) 1537.

[13] T. M. Monro, D. J. Richardson, N. G. R. Broderick, P. J. Bennett "Holey optical fibers: an efficient modal model" IEEE J. Lightwave Technol. **17** (1999) 1093.

[14] M. J. Gander, R. McBride, J. D. C. Jones, T. A. Birks, J. C. Knight, P. St.J. Russell, P. M. Blanchard, J. G.Burnett, A. H. Greenaway "Measurement of the wavelength dependence of beam divergence for photonic crystal fiber" Opt. Lett. **24** (1999) 1017.

[15] B. J. Eggleton, P. S. Westbrook, R. S. Windeler, S. Spalter, T. A. Strasser "Grating resonances in air-silica microstructured optical fibers" Opt. Lett. **24** (1999) 1460.

[16] S. E. Barkou, J. Broeng, A. Bjarklev "Silica-air photonic crystal fiber design that permits waveguiding by a true photonic bandgap effect" Opt. Lett. **24** (1999) 46.

[17] A. Ferrando, E. Silvestre, J. J. Miret, P. Andres, M. V. Andres "Full-vector analysis of a realistic photonic crystal fiber" Opt. Lett. **24** (1999) 276.

[18] J. K. Ranka, R. S. Windeler and A. J. Stentz "Visible continuum generation in air-silica microstructure optical fibers with anomalous dispersion at 800 nm" Opt. Lett. **25**, 25 (2000).

[19] J. Nishimura, K. Morishita "Changing multimode dispersive fibers into single-mode fibers by annealing and guided mode analysis opf annealed fibers" IEEE J. Lightwave Technol. **16** (1998) 990.

[20] T. A. Birks, P. J. Roberts, P. St.J. Russell, D. M. Atkin, T. J. Shepherd "Full 2-D photonic bandgaps in silica/air structures" Electron. Lett. **31** (1995) 1941.

[21] Blaze Photonics Ltd, http://www.blazephotonics.com

CARACTERIZATION OF THE GUIDING PROPERTIES OF A BRAGG TYPE PHOTONIC-BAND-GAP FIBER

P. ROY, F. BRECHET, P. LEPROUX, J. MARCOU and D. PAGNOUX

Institut de Recherche en Communications Optiques et Microondes
UMR CNRS n°6615
123 Avenue Albert THOMAS - 87060 LIMOGES cedex - FRANCE

Abstract: *A novel BRAGG type photonic band gap fiber, having a cladding made of alternate high and low index layers, is presented. Single mode propagation has been experimentally observed. The propagation of light into a BRAGG type photonic band gap fiber is strongly dependent on the wavelength. The transmission spectrum is experimentally measured.*

Introduction: In this paper, a BRAGG type photonic-band-gap (PBG) fiber is presented. It consists in a low-index cylindrical core surrounded by a cladding made of layers with alternating high and low indices (respectively n_2 and n_3), whose values are higher than that of the core. In the cladding, the radial quasi-periodical multilayer structure acts as a Bragg reflector and the light is kept confined into the antiguiding core. Theoretical studies have predicted single-mode propagation of light at an operating wavelength $\lambda_0 = 1060$nm and the ability to achieve zero-dispersion at short wavelengths [1],[2]. Thanks to these novel characteristics, the fiber is very attractive for applications in non linear optics : soliton propagation, parametric amplification and oscillators. In this communication, the very first propagation of a single-mode pattern into a BRAGG type PBG fiber is reported at $\lambda_0 = 1053$nm and its transfer function is measured.

Manufacture and test of a single-mode PBG fiber: A preform for drawing a PBG fiber has been manufactured by means of the classical MCVD technique. The fiber has been drawn to reach a 125µm diameter. Its index profile has been measured with a YORK FCm1000 device. This profile, superimposed with the theoretical electric field of the guided mode, is presented on

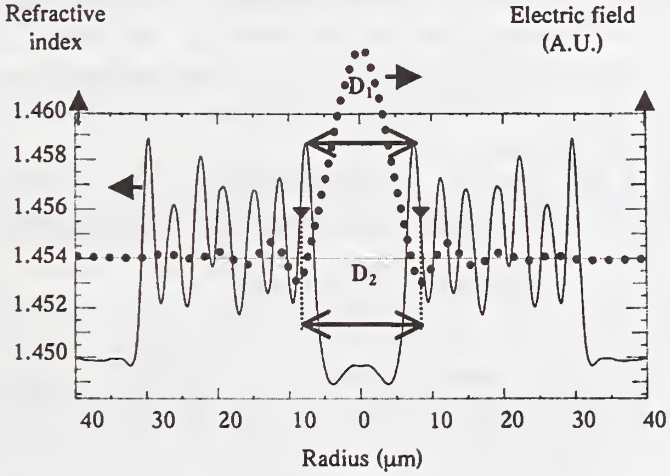

Figure 1 : Measured profile index and associated computed electric field of the manufactured PBG fiber.

figure 1. The fluctuations of the values of n_2 are due to unexpected variations of the concentration of Ge blended with silica to make high index layers during the MCVD process. The fluctuations of n_3 are attributed to the measurement device [3].

A 100mW pattern from a CW YLF solid state laser operating at $\lambda_0 = 1.053\mu m$ was launched into a 1m length of the fiber. Figure 2.a is the near field observed at the output when the input pattern is properly focused on to the central core. The guiding is made possible into the core thanks to the transverse photonic band gap effect. When the input pattern is focused on to the cladding, the light only propagates in the high index layers, as shown on figure 2.b.

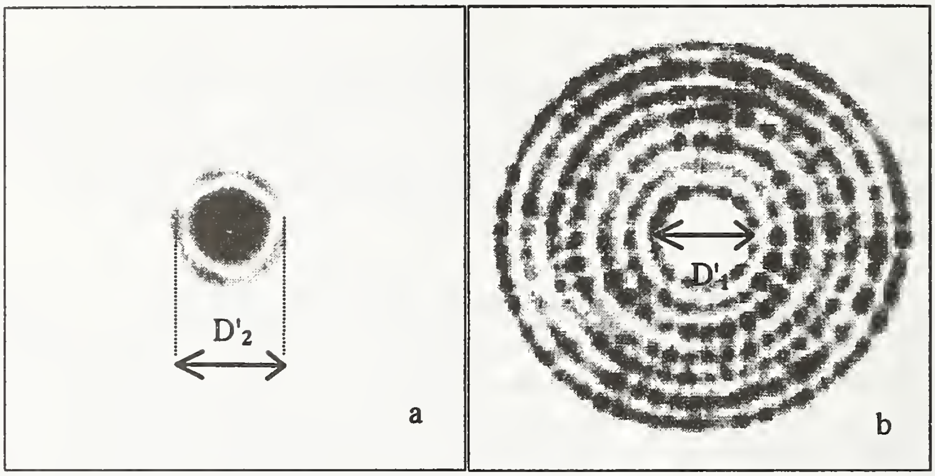

Figure 2 : Near field observed at the output of a PBG fiber, (a) when the input pattern is properly focused on to the central core and (b) when the input pattern is focused on to the cladding

On the index profile of figure 1, D_1 and D_2 are respectively the diameter of the middle of the first high index layer and the diameter of the first transition from n_2 to n_3. On figure 2, D'_1 and D'_2 are two dimensions measured on the output near field pattern : D'_1 is the diameter of the first ring of light when launched into the cladding (figure 2.b) and D'_2 is the diameter of the first ring of the single-mode pattern obtained with centered launching conditions (figure 2.a). According to the predicted conditions of propagation on the field [3], D_1 and D_2 must respectively correspond to D'_1 and D'_2. The ratios D_1/D_2 and D'_1/D'_2 are respectively equal to 1.12 and 1.13. These two ratios are very close to each other, showing that experimental results are in good agreement with theoretical predictions.

The measurement of the modulus of the transfer function of the fiber (called for convenience |TF|) as a function of wavelength is achieved with the experimental setup described

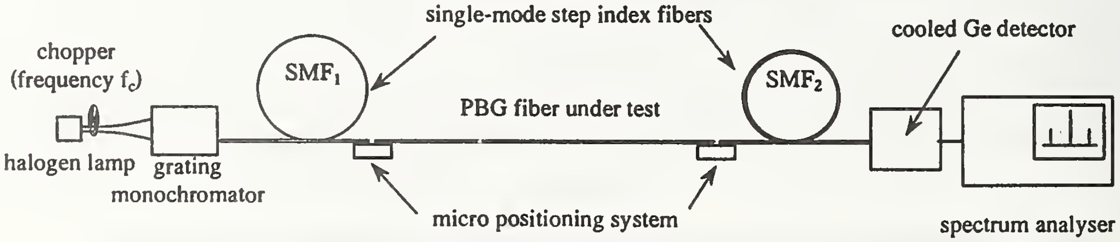

Figure 3 : Experimental measurement setup

on figure 3. The monochromatic beam from a grating monochromator chopped at the frequency $f_c = 80Hz$ is first launched into a short length of 850nm cutoff wavelength single-mode fiber (SMF1). The gaussian beam ($w_0 = 3.8\mu m$) from this fiber is then carefully launched into the core of a 40cm length of the PBG fiber. A second length of the same single-mode fiber (SMF2) is finely aligned at output end of the PBG fiber. Its role is to spatially filter the output beam from the upstream fiber and to collect the only power from its core. This power is detected at the output end of SMF2 by a cooled Ge-detector connected to an electrical spectrum analyser. The power P1(λ) in the f_c spectrum line of the detected optical signal is measured and registered, from 900nm to 1300nm. Then, SMF1 is directly connected to SMF2 and the reference power P2(λ) detected at the f_c frequency is measured versus wavelength and registered. Finally, the ratio $R(\lambda) = \frac{P2(\lambda)/P1(\lambda)}{(P2/P1)_{min}}$ provides the normalised |TF| of the tested PBG fiber. R(λ) is computed and plotted in dB on figure 4. The central wavelength is 1080nm. The measured 3dB and 10dB bandwidths are respectively 80nm and 140nm. Out of the transmission bandwidth, the |TF| dramatically decreases from –10dB to the minimum accurately measurable value (–50dB) within about 40nm (i.e. the slope reaches 1dB/nm). The measured values of the transmission bandwidth are approximately two times narrower than that we compute using a 3D BPM algorithm. In accordance with theoretical predictions, this narrowing is attributed to the unexpected irregularities of the actual index profile. However, the bandwidth of the manufactured fiber remains large enough for many non linear applications. In spite of the noted discrepancy, the spatial filtering behaviour of the fiber around 1060nm is clearly pointed out. Further measurements are planed with new fibers just manufactured.

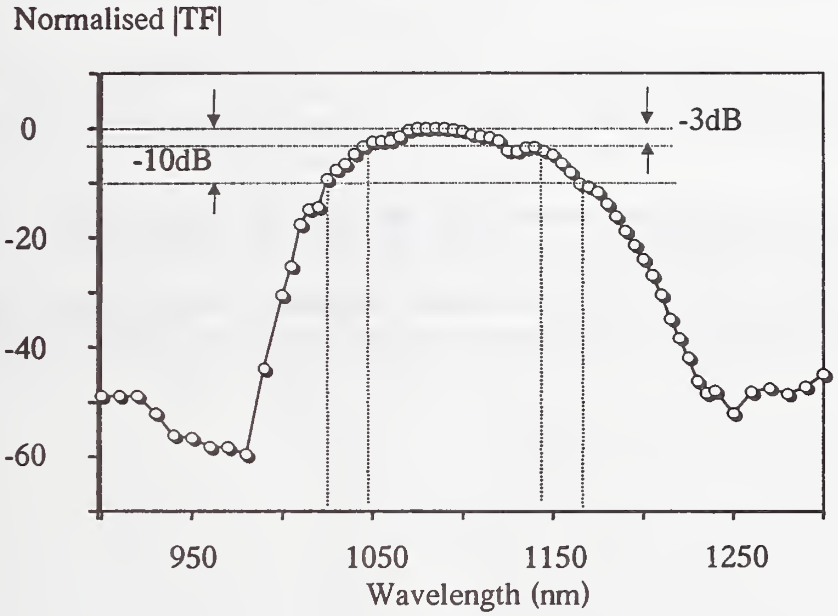

Figure 4 : Normalised modulus of the transfer function (|TF|) measured on the PBG fibre.

Conclusion: A depressed core index photonic band gap fiber has been manufactured and the propagation of light into the central core has been observed at $\lambda_0 = 1.053\mu m$, thanks to the transverse photonic band gap effect. The modulus of the transfer function (|TF|) of a PBG fiber has been measured. Experimental measurements with a 40cm piece of manufactured PBG fiber exhibit a 3dB bandwidth of 80nm around 1080nm. The slope of the |TF| reaches 1dB/nm out of the transmission bandwidth. The bandwidth is large enough for non linear applications such as parametric amplification into this fiber that is supposed to exhibit a zero dispersion at the central wavelength of the bandwidth.

Acknowledgements

The authors are grateful to B. Dussardier, G. Monnon and F. Ubaldi from LPMC Nice for manufacturing the preform and to J.M. Blondy and G. Boutinaud from IRCOM Limoges for drawing the fiber. This work is supported by the French CNRS under grant n° TL98006.

References

[1] P. YEH, A. YARIV, E. MAROM, "Theory of Bragg fiber", *Journal of Optical Society of America, Vol. 68, n°9, 1978.*

[2] J. MARCOU, P. ROY, "Monomode photonic band gap fibers for dispersion shifting towards short wavelengths", proceeding of *European Conference on Optical Communication, 1999 Nice, France.*

[3] F. BRECHET, P. ROY, J. MARCOU, D. PAGNOUX, " Single mode propagation into a depressed-core-index photonic-band-gap fiber designed for zero-dispersion propagation at short wavelengths ", *Electronics Letters, vol 36, n°6, pp.514-515, 2000.*

Ultra-broad supercontinuum generation in tapered telecommunications fibres

T. A. Birks, W. J. Wadsworth, P. St.J. Russell
Optoelectronics Group, Department of Physics, University of Bath, Claverton Down, Bath BA2 7AY, United Kingdom
pystab@bath.ac.uk

Abstract: Optical fibres tapered to about 2 microns diameter over a length of 90 mm were used to generate supercontinuum light from the 76 MHz femtosecond pulses emitted by an unamplified Ti:sapphire laser. Output spectra were broad enough to fill the wavelength range 370 - 1545 nm (over two octaves). This source of high-intensity single-mode "white" light should find widespread applications in optical fibre measurements, especially since it does not require any unconventional fibres for its operation.

Introduction

We report the generation of ultra-broad supercontinuum light in tapered telecommunications fibres. Powered by femtosecond pulses from a common unamplified Ti:sapphire laser, the generated light was guided in the fundamental mode of the fibre. Its spectrum could span over two octaves from the ultraviolet to the third telecommunications window (370 - 1545 nm at the 20 dB level). With an average spectral density of 0.25 mW nm^{-1}, this "white" light source has the brightness of a laser with the bandwidth of a light bulb.

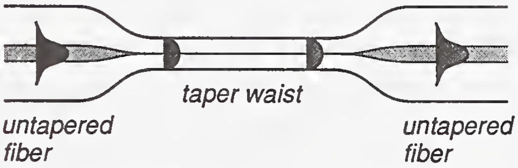

Fig. 1. A schematic diagram of a tapered fibre, showing how light in the core of the untapered fibre expands to fill the whole fibre in the taper waist.

Generation of supercontinuum light in a "microstructure" photonic crystal fibre (PCF) using low-energy fs pulses has already been demonstrated[1,2]. The fibre was an undoped silica-air structure, in which a small core (1-2 μm across) was surrounded by large air holes. The waveguide therefore resembled a thread of silica in air[3]. Unfortunately the need for the special fibre means that the technique is not widely available. The PCF work has however identified a number of applications for such sources. For example, the retention of the longitudinal mode structure of the modelocked laser has led to stunning recent advances in optical frequency metrology[4]. For optical fibre measurements, some obvious applications include transmission spectroscopy (of fibres and devices) and white light interferometry (for measuring fibre dispersion, for example[5]), which suffer from the low spectral density and spatial coherence of conventional broadband sources.

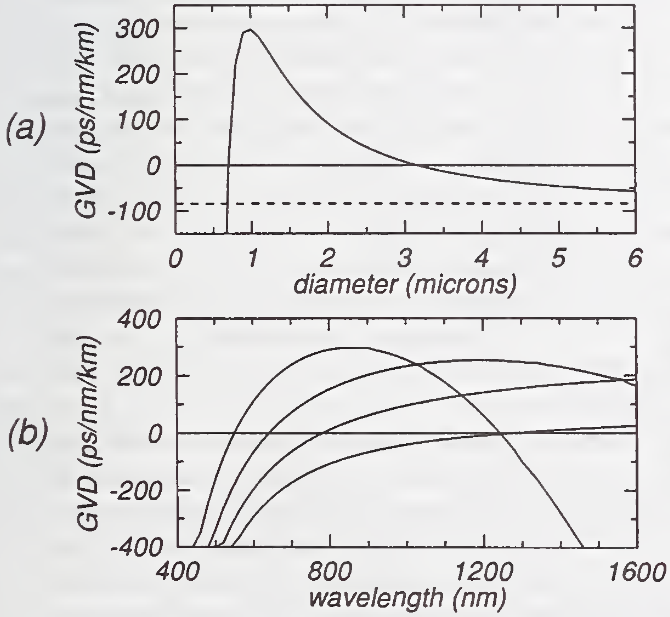

Fig. 2. Calculated GVD of a narrow tapered fibre waist in air: (a) versus waist diameter for λ = 850 nm (the broken line is an asymptote, the GVD of bulk silica); (b) versus wavelength for (left to right) waist diameters of 1.0, 1.5 and 2.5 μm, and for bulk silica. Positive values represent anomalous dispersion.

We tapered our conventional telecommunications fibre by heating and stretching it in a flame, to reduce its diameter to about 2 μm over a length of 90 mm. Fig. 1 depicts the resulting structure, with a narrow taper waist connected to untapered fibre at both ends by taper transitions. The residual fibre core is so small that the waist is effectively a simple thread of silica surrounded by air, light being guided at the outer boundary. In this respect it resembles the PCF described above.


Fig. 3. Typical visible output far-field pattern from one of the tapered fibres.

The large refractive index step between fibre and air allows light to be funnelled into a very small area, increasing its intensity and promoting nonlinear effects. Furthermore, the group velocity dispersion (GVD) can be reduced or even made anomalous at visible and near infrared wavelengths (Fig. 2). For a waist of diameter 1.8 μm, the calculated GVD and nonlinear effective area are +122 ps nm^{-1} km^{-1} and 1.21 μm^2, giving nonlinear and dispersion lengths of 0.6 mm and 150 mm respectively[6] (for laser pulses typical of our experiments). Significant self phase modulation is therefore expected despite the strong dispersion. Indeed, the anomalous dispersion helps to counteract the normal dispersion suffered by the pulses as they propagate through an isolator, a launch objective and some untapered fibre *en route* to the taper waist.

Results

The telecommunications fibre used was Corning SMF-28 (cutoff wavelength 1250 nm, NA = 0.1), which is widely available and costs a few cents per metre. The fibre was tapered using a travelling flame, which allowed us to form waists that were uniform in diameter and long but with relatively short transitions[7]. The tapered fibres reported here all had waists about 90 mm long, with 35 mm transitions. The optical insertion loss for light propagating through the structures was typically ~0.2 dB. Each tapered fibre was promptly glued at both ends in an enclosed housing after being made, in such a way that the waist and transitions remained surrounded by air.

The unamplified modelocked Ti:sapphire laser (Coherent MIRA) emitted 70-100 fs pulses with a repetition rate of 76 MHz and a wavelength of 850 nm. The light passed through an isolator and launch optics (spreading the pulses to 200-500 fs) and into the tapered fibre. The taper's input fibre was kept short to minimise further normal dispersion of the pulses; the output fibre was about 1 m long.

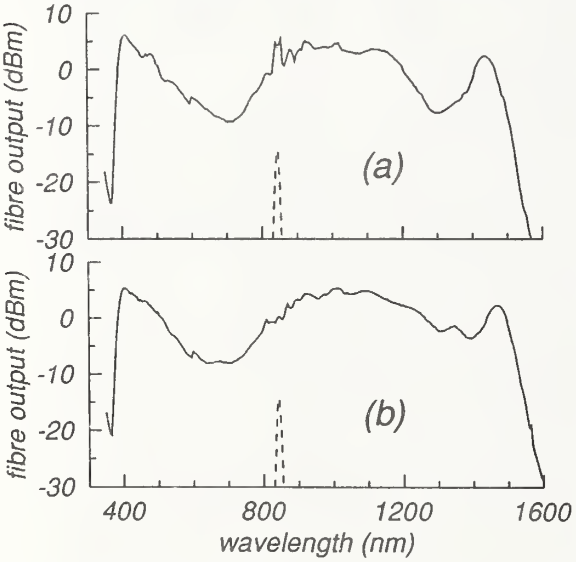

Fig. 4. Output spectra from tapered fibres with waists of 1.8 μm diameter, for an average laser power of 300 mW. The cutoff wavelengths of the fibres that were tapered were (a) 1250 nm (a standard telecoms fibre) and (b) 735 nm. The broken line is the spectrum of the input light, scaled vertically for comparison.

In most cases the output wave was visible as a very intense far-field spot, Fig. 3. Although both the untapered fibre (core-cladding waveguide) and the taper waist (cladding-air waveguide) were multimode at visible and Ti:sapphire wavelengths, the supercontinuum light was always generated in the fundamental mode.

The output spectra from two fibres identically tapered to 1.8 μm diameter are plotted in Fig. 4, for a time-averaged laser power of 300 mW (pulse energy 3.9 nJ). The spectra cover over two octaves in frequency, with Fig. 4(b) within 20 dB of the peak value throughout the range 370 - 1545 nm. Unlike all the other spectra reported here, Fig. 4(b) is for a fibre with a cutoff wavelength of 735 nm instead of 1250 nm, which was therefore single-mode at the laser wavelength. However, Figs. 4(a) and (b) are very similar because in the taper waist the two structures differ only in the size of the insignificant residual fibre core.

Output spectra from another tapered fibre are plotted in Fig. 5 for different laser powers (and hence pulse energies). Increasing the power broadens the spectrum without increasing the peak value.

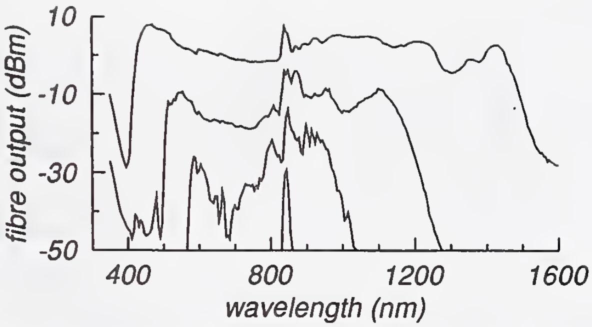

Fig. 5. Output spectra from a tapered fibre with a waist of 2 μm diameter, for (top to bottom) average powers of 380, 210 and 60 mW, together with the spectrum of the input light. The curves are scaled vertically for comparison; the three output spectra all had approximately the same peak value.

Spectra for four different waist diameters, two being simply copied from Figs. 4 and 5, are compared in Fig. 6. (Recall that waist diameter determines the GVD, Fig. 2, as well as the effective area.) The meaning of such a comparison for different laser powers is limited, but smaller diameters not only require less power, they also produce spectra that are less flat. A "bite" is progressively taken out at visible wavelengths, leaving an asymmetric spectrum. The resulting systematic decrease of the mean photon energy seems to indicate an increasing contribution from Raman scattering to the spectral broadening.

No spectral broadening was observed (or expected) in untapered fibre.

Discussion

Our results show that tapered fibres are as effective as PCFs for generating ultra-broad high-intensity single-mode spectra. Although our technique does have some disadvantages (including the limited interaction length and the need to protect the tapered fibre from dust and damage), definite advantages can be identified. Most significantly, no special fibre is required. A standard widely-available telecommunications fibre is all that is needed. That the fibre is multimode is no drawback because the supercontinuum is generated in the fundamental mode. The output is guided in a standard fibre and so is readily compatible with the familiar techniques and devices (fusion splices, connectors, directional couplers, polarisers, etc) of conventional fibre optics.

Furthermore, although the nonlinear interaction occurs in the narrow waist, the input laser pulses are coupled into a standard fibre core with a large diameter of about 9 μm. Hence the input light is not tightly focused, simplifying alignment and making the fibre's input endface relatively durable. The tapered fibre itself is surprisingly robust. None of our samples deteriorated over time (over the several days available), and indeed one tapered fibre in its housing was accidentally dropped onto a hard floor from a height of 1 m without being destroyed.

Tapering is a well-known technique, low in cost and quick to implement, which is widely used to make fibre directional couplers. (Indeed, the durability of such couplers gives confidence that tapers like ours would also be durable.) It takes only a few minutes to taper a fibre, and a few more to fix it in its housing. We could therefore generate samples very quickly and easily. It is also straightforward to form non-uniform taper waists with a given diameter profile. From Fig. 2, such a diameter profile entails a dispersion profile, a degree of freedom that is hard to implement in PCF but which should give greater control over the shape of the supercontinuum spectrum.

By providing a way to generate ultra-broadband light without special fibres, our results show that exciting nonlinear effects in silica do not require long lengths, high powers or complex structures. Tapered fibres should be effective hosts for a wealth of other nonlinear effects besides supercontinuum generation.

Conclusion

We have demonstrated the generation of an ultra-broad supercontinuum in standard telecommunications fibre that has been tapered to a diameter of ~2 µm. Femtosecond pulses from an unamplified Ti:sapphire laser are sufficient to give a spectrum over two octaves broad at the 20 dB level. The generated light was guided in the fundamental mode of the fibre, and its spectrum spanned the range 370 - 1545 nm. Such a light source will greatly simplify many optical fibre measurements.

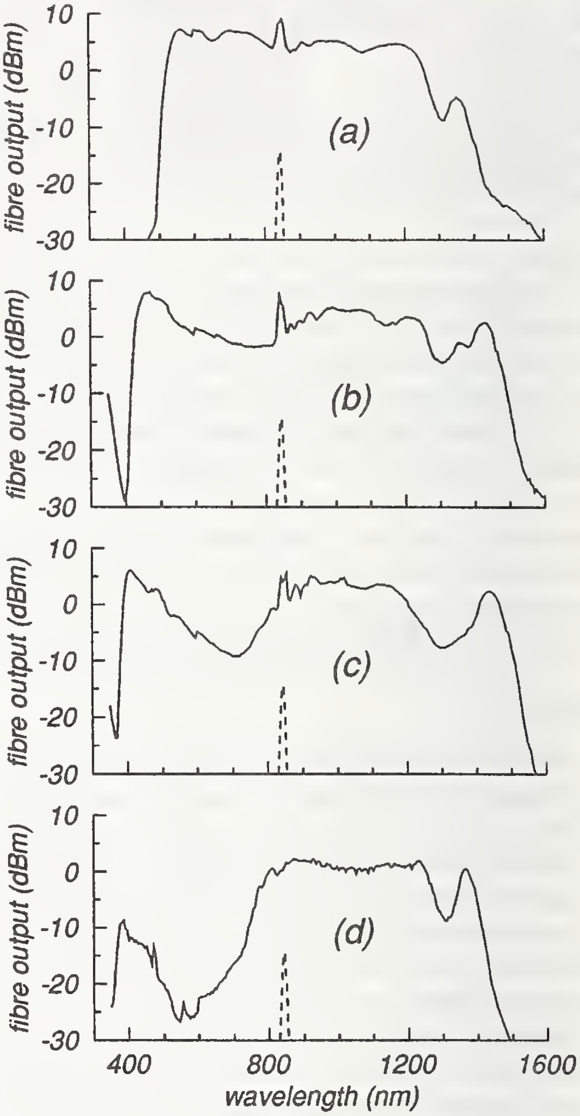

Fig. 6. Output spectra from tapered fibres with a waist diameter and average power respectively of (a) 2.5 µm and 430 mW, (b) 2.0 µm and 380 mW, (c) 1.8 µm and 300 mW, and (d) 1.5 µm and 70 mW. The broken line is the vertically scaled input spectrum.

References

[1] J. K. Ranka, R. S. Windeler and A. J. Stentz "Efficient visible continuum generation in air-silica microstructure optical fibers with anomalous dispersion at 800 nm" in *Conference on Lasers and Electro-Optics* (Optical Society of America, Washington DC, 1999), paper CPD8; J. K. Ranka, R. S. Windeler and A. J. Stentz "Visible continuum generation in air-silica microstructure optical fibers with anomalous dispersion at 800 nm" Opt. Lett. **25**, 25 (2000).

[2] W. J. Wadsworth, J. C. Knight, A. Ortigosa-Blanch, J. Arriaga, E. Silvestre, B. J. Mangan and P. St.J. Russell "Soliton effects and supercontinuum generation in photonic crystal fibres at 850 nm" in IEEE Lasers and Electro-Optics Society Annual Meeting (1999), paper PD1.5; W. J. Wadsworth, J. C. Knight, A. Ortigosa-Blanch, J. Arriaga, E. Silvestre and P. St.J. Russell "Soliton effects in photonic crystal fibres at 850 nm" Electron. Lett. **36**, 53 (2000).

[3] T. A. Birks, D. Mogilevtsev, J. C. Knight and P. St.J. Russell "Dispersion compensation using single-material fibers" IEEE Photon. Technol. Lett. **11**, 674 (1999).

[4] see, for example, T. W. Haensch, R. Holzwarth, J. Reichert and T. Udem "Precision spectroscopy with femtosecond light pulses" in *Quantum Electronics and Laser Science Conference* (Optical Society of America, Washington DC, 2000), 109.

[5] M. Tateda, N. Shibata and S. Seikai "Interferometric method for chromatic dispersion measurement in a single-mode optical fiber" IEEE J. Quantum Electron. **17**, 404 (1981).

[6] G. P. Agrawal, *Nonlinear Fiber Optics* (Academic Press, San Diego CA, 2nd Ed. 1995).

[7] T. A. Birks and Y. W. Li "The shape of fiber tapers" IEEE J. Lightwave Technol. **10**, 432 (1992).

A simple servo controlled scanning reflectance measurement method for determining the refractive index profile of a waveguide

Y. Park, N. H. Seong, Y. C. Youk, U. C. Peak, and D. Y. Kim
Department of Information and Communications, Kwangju Institute of Science and Technology, Oryong-dong 1 Puk-gu Kwangju, Korea.

A simple scanning method is described for determining the refractive index profile of an optical fiber by measuring reflectance of the end surface of an optical fiber. Instead of an objective lens, a lensed fiber is used for focusing probe light on a surface to be measured, and a dithering servo control is employed to maintain a constant distance between the lensed fiber and the surface. It is shown that this method is applicable to measure refractive index structures of fibers and planar waveguides.

INTRODUCTION

The most widely used technique for measuring the refractive index profile of an optical fiber is the refracted near field technique owing to its simplicity in principle. However, this technique has relatively low spatial resolution and needs complicated sample preparation such as immerging a fiber into an index matching fluid. It may not be used for determining the refractive index profile of a waveguide if its structure is not axially symmetric.

In this paper, a simple scanning reflectance measurement technique with an auto-focusing servo control is demonstrated for determining the refractive index profile of a cross section of a waveguide. Michelson interferometer type optical setup is used with a 3dB fiber directional coupler replacing a bulk beam splitter which splits the input and the output beams. In order to simplify the experimental setup, a lensed fiber is used for focusing probe light on a sample surface. A dithering servo control system is combined with the reflectance measurement setup by attaching the lensed fiber on a PZT stack. It is to apply small vibration to the lensed fiber along the vertical direction. The reflected light is coupled maximum into the lensed fiber when the sample surface is at the focusing point of the input beam. By detecting the power of the coupled light into the lensed fiber with a lock-in amplifier, the offset of the sample surface from the focusing point of the input beam is monitored. A feedback loop is constructed with a voltage adder to compensate this offset and the system makes the sample surface to be located at the focusing point of the input light all the time during scanning. As reflectivity is a function of the refractive index of the sample surface, the index profile can be obtained from the scanned reflectance profile measurement.

EXPERIMENTAL SETUP

A schematic diagram of refractive index profiling setup is shown in Figure 1. In this experiment, ASE(amplified spontaneous emission) noise from an EDF(Erbium doped fiber) is used as input optical light source to eliminate unwanted interference patterns. The half of the source power is measured by detector1 through a 3dB coupler to monitor fluctuations of input optical power and the rest is focused by a lensed fiber on the end surface of a sample surface. The reflected light from the sample surface is coupled back into the lensed fiber again and propagates backward direction. The power of this backward propagating light is measured by detector2 through the 3dB coupler. The transmitted light toward the detector1 and the reflected light toward the detector2 are stored while scanning the sample surface along the X and Y directions. The reflectance profile along the transverse direction of the sample is obtained by the ratio of power by the detector1 and the detector2. The Fresnel equation in Equation (1) is used to convert the obtained reflectance profile R(x,y) into the refractive index profile n(x,y) by assuming a normal incidence of the focused light onto the sample surface.

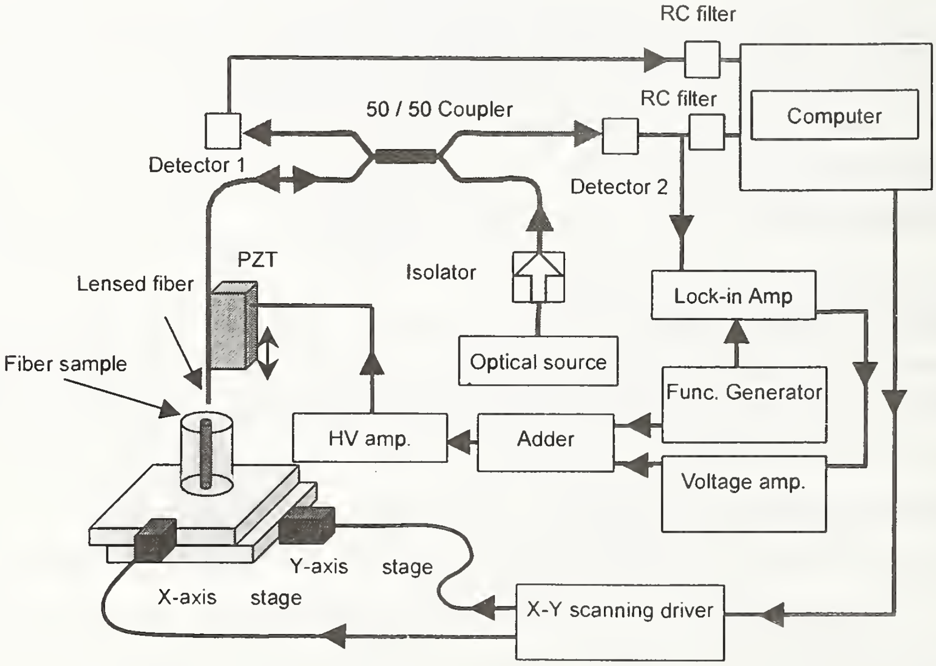

Figure 1 A schematic diagram of the refractive index profiler with auto-focusing apparatus.

$$n = \left(\frac{1+\sqrt{R}}{1-\sqrt{R}} \right) \tag{1}$$

At a fixed scan point, the power detected by the detector2 is the maximum when the sample surface is at the focusing point of the input beam. If the lensed fiber is dithered by a PZT along the vertical direction at a few kHz frequency, the optical power at the detector2 will oscillate with the same frequency. A lock-in amplifier is used to measure the phase as well as the power of the detected signal by the detector2. As the phase of the oscillating signal obtained by the detector2 changes by 180 degrees when the surface of the sample passes through the focal point of the input beam, the output signal of the lock-in amplifier changes its sign at the focal point of the input beam. Figure 1 show how the output voltage of the lock-in amplifier is applied to the PZT driver with a voltage adder as a feed back signal. This auto-focusing system makes the spot size of the input beam minimum at the sample surface and it brings out the maximum spatial resolution. It also keeps the distance between the sample surface and the lensed fiber constant while scanning the sample along the transverse direction.

RESULTS

Figure 2 shows the reflected optical power at the detector2 while the distance between the lensed fiber and the sample surface is changed by varying the voltage applied to the PZT when the sample surface is nearby the focal point of the input beam. Periodic oscillations are due to the interference between the reflected light from the surface of the lensed fiber and the reflected light from the sample surface.

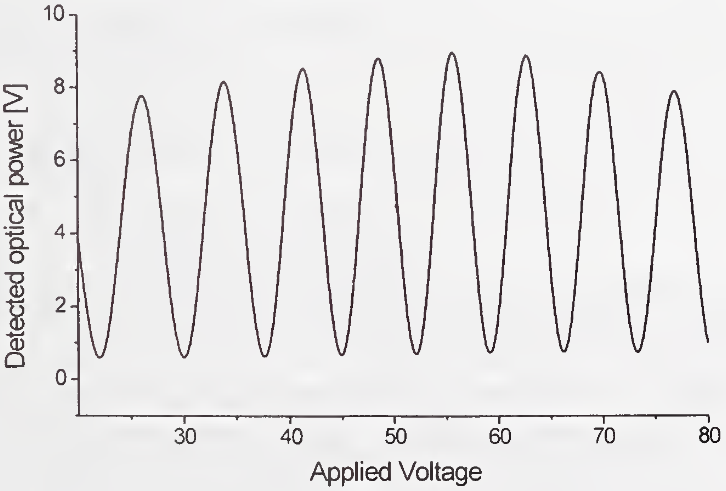

Figure 2. Detected optical power at detector2 as a function of the voltage applied to the PZT in Figure 1.

The period corresponds to the half of the center wavelength of the light source in space, which is about 1.54 μm in this case. The linewidth of the ASE noise source from an EDF is about 40 nm. The envelope of the fast oscillating signal is maximum when the voltage applied to the PZT is about 53 volt. The full width half maximum of the focused beam is estimated to be 2 ± 0.2 μm by using a knife-edge. Figure 3 shows the measured reflectance distribution and refractive index profile of a commercial graded index fiber around the core area. The refractive index profile is calculated from the reflectance profile by using the Fresnel equation. Total scanned length is 60 μm with 0.4 μm step size. 300 samples were acquired at 15k samples per second and averaged to each step. The maximum variation of the measured reflected light power is about 150mV.

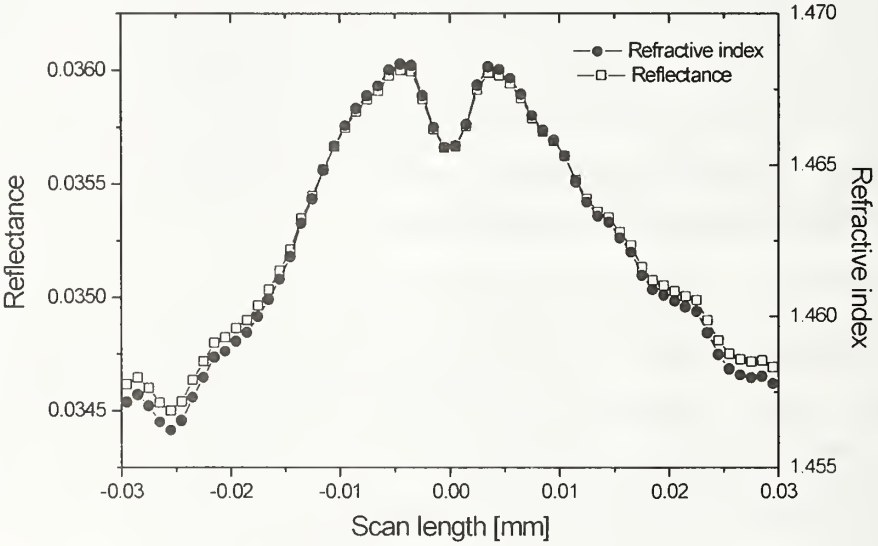

Figure 3. The measured reflectance and refractive index profile of a commercial graded index fiber

This work was supported in part by the KOSEF through the Ultra-Fast Fiber-Optic Networks Research Center and by the Korean Ministry of Education through the BK21 Program.

[1] W. J. Stewart, "Optical Fiber and Preform Profiling Technology," *J. of Quantum Electron.*, vol. QE-18, no. 10, pp. 1451-1466, 1982.

[2] W. Eickhoff and E. Wiedel, "Measuring method for the refractive index profile of optical glass fibres." *Opt. and Quantum Electron.*, vol. 7, no. 2, pp. 109-113, 1975.

[3] Timothy R. Corle, Gordon S. Kino, *Confocal scanning optical microscopy and related imaging systems*, San Diego: Academic Press, 1996.

Characterizing the filter response of Optical Routers

Chellappan Narayanan, Gail Bogert
Lucent Technologies,
Microelectronics Group,
9999 Hamilton Blvd.,
Breinigsville, PA 18031.

Introduction

Although silica based planar waveguide technology has been around for almost two decades, it is only in the last few years that we have seen a growth in the demand for planar waveguide components in the marketplace. The reasons for this change is the emergence of WDM technology, and the timely development of three key enabling technologies, the wavelength multiplexer/de-multiplexer, the Erbium-doped optical amplifier and wavelength tunable laser sources.

There are various ways of building an optical de-multiplexer. One promising device that can be realized using the silica-on-silicon planar waveguide technology is the waveguide router (WGR)[1]. It is also referred to by other name, such as phased array, arrayed waveguide grating, and Phasar. Silica planar waveguide technology provides a platform for low-cost mass fabrication of high quality DWDM components. The advantages of WGR include precise channel spacing, very good environmental stability, and negligible chromatic dispersion. The other attractive feature of this technology is that it offers the lowest cost approach to scaling to higher channel counts, because the manufacturing process steps are transparent to design type and number of channels.

Testing at various steps of the planar waveguide manufacturing process plays an important role in delivering a reliable and cost-effective product. First we will explain the terms used to describe the response of optical filters. Then we will focus on the characterization of optical routers. Specifically, we will cover testing at two different stages of the manufacturing process – Chip Level testing (front-end wafer testing) and final packaged device testing. Although most of what is discussed in this paper is applicable to any optical filter technology, there are certain aspects that are very specific to planar waveguide DWDM.

Waveguide Router: Principle of Operation

An arrayed waveguide router (Figure 1) consists of two star couplers connected by an array of waveguides of constant linear path length difference. This device structure forms a 1:1 optical imaging system. For each wavelength at the input waveguide an image is formed at a different point in the image (output) plane. In other words, as the wavelength is swept at the input the image sweeps across the output plane. By placing waveguides appropriately in the output plane a wavelength de-multiplexer is formed.

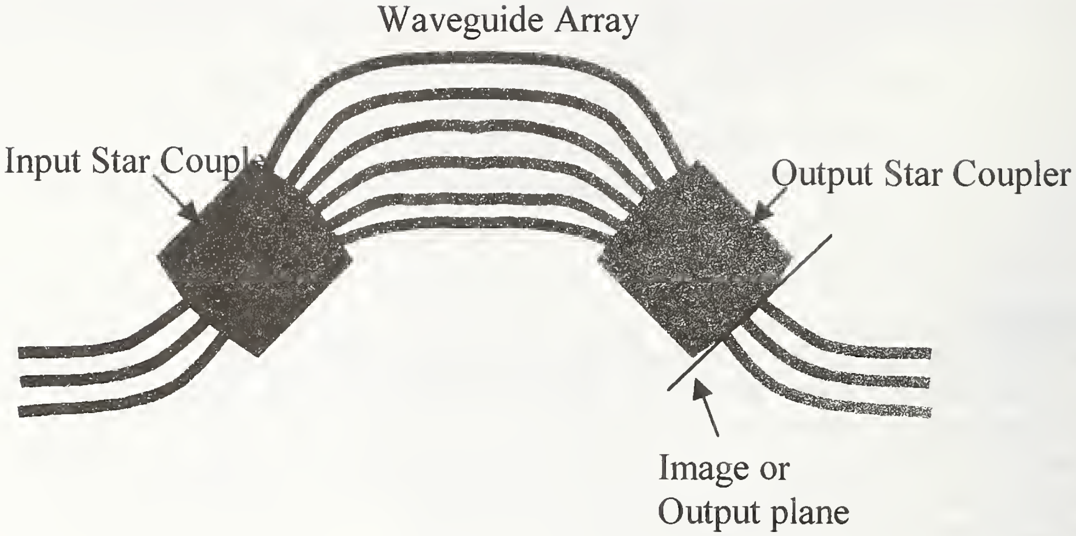

Figure 1: Layout of a waveguide grating Router

DWDM Optical Performance Parameters

Parameters specifying the optical performance of a DWDM are summarized in Table 1.

Parameter	Symbol	Comments
Number of Input Ports	N_I	Usually 1
Number of Output Ports	N_O	8,16,32, etc
Wavelength Grid	λ_1, λ_2 …..	Nominal Wavelength for all outputs
Passband Center Wavelength	$\lambda_{C1},\lambda_{C2}$….	Actual wavelengths for all outputs
Passband Wavelength Offset	$\Delta\lambda_{C1},\Delta\lambda_{C2}$ ….	$\Delta\lambda_{Ci}= \lambda_{Ci}- \lambda_i$
Channel Spacing	CS	$\| \lambda_{i+1}- \lambda_I\|$ or $\| \nu_{i+1}- \nu_I\|$; 100GHZ~0.8nm
Free Spectral Range	FSR	Spectrum periodicity
Insertion Loss	L	Peak or within a band
Insertion Loss Uniformity	ΔL	Difference between maximum and minimum across all output ports
Passband width	B	At a given insertion loss value
Passband Ripple (Flatness)	R or F	In a given wavelength window
Adjacent Channel crosstalk	AX	Window width? Relative to λ_{Ci} or λ_i? Relative to peak loss or passband loss
Non-adjacent channel crosstalk	NX	Same as AX
Total Crosstalk	TX	Same as AX
Polarization Dependent Loss	PDL	Max variation of L over all polarization states
Polarization Dependent Wavelength	PDW,PDλ	Max variation of λ_{Ci} for all

		polarization states
Return Loss	RL	-55 to –35 dB
Chromatic Dispersion	CD	Negligible for silica WGR
Polarization mode dispersion	PMD	Negligible for silica WGR

Table1: DWDM Optical Performance Parameters

The definition of insertion loss (L) and crosstalk is shown in Figure 3. The vertical dotted lines represent the wavelength grid (λ_1,λ_2, λ_3….) which specifies the desired nominal center wavelength of the passband of each port. There is an industrial standard for the wavelength grid set by the ITU and is generally followed by the system vendors. The grid points are usually equally spaced in frequency. The distance between the grid points is the channel spacing (CS, e.g., 100GHZ ~ 0.8nm). A wavelength window of width (WB), which is 40 to 50% of the channel spacing (usually less) and centered at each wavelength grid (shown as a shadowed area in Figure 3), is used to measure the crosstalk, insertion loss and other parameters.

The crosstalk parameter specifies how much power is received from adjacent channels. It is generally described by a matrix [$X_{i,j}$] where - $X_{i,j}$ (in dB) is the maximum power transmission of port I within the wavelength window around the wavelength grid j relative to the peak transmission (L_{peak}) or the passband transmission (L_{band}).

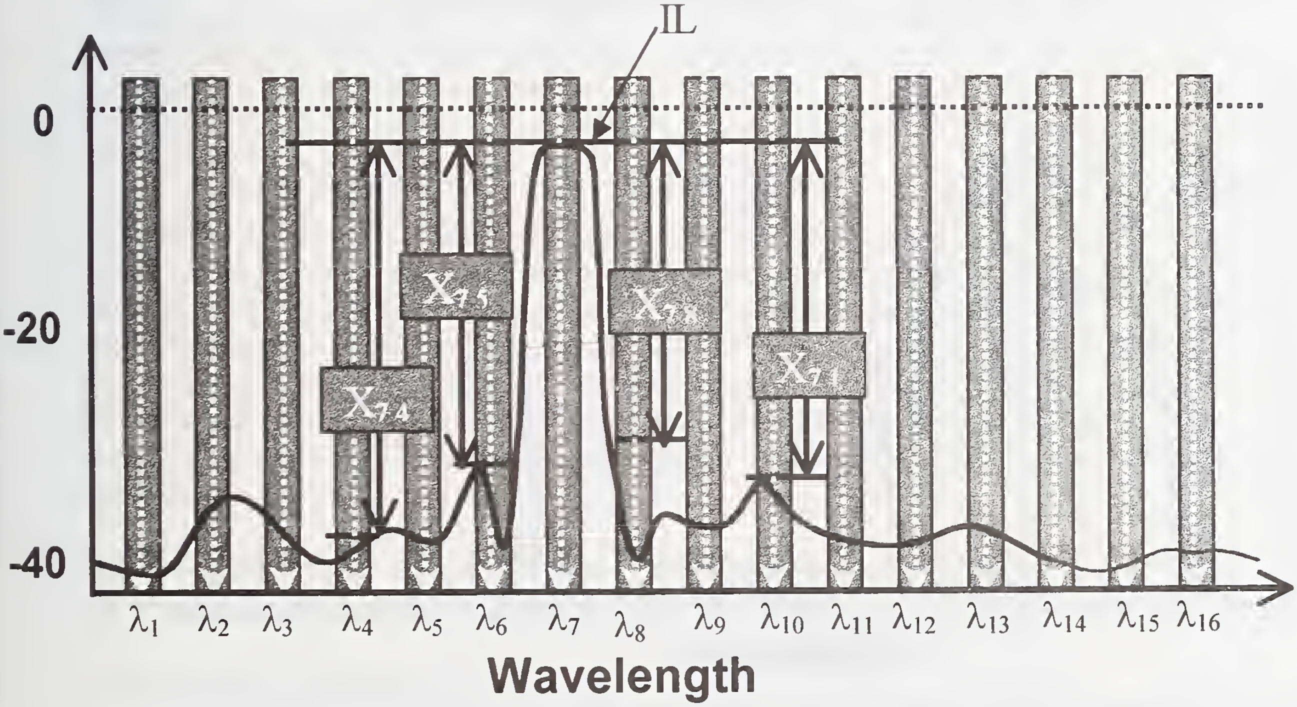

Figure 2: Insertion Loss (L) and Crosstalk (X)

The crosstalk is defined as a positive number in dB. The adjacent channel crosstalk of port i is the minimum of $X_{i,j-1}$ and $X_{i,j+1}$. The non-adjacent channel crosstalk is the minimum of $X_{i,j}$ with $|i-j|>1$. The absolute value of the sum of the power values of - $X_{i,j}$

with j not equal to i, is the total accumulated crosstalk (TX). From a system perspective, it is meaningful to measure the crosstalk relative the ITU grid wavelengths since the lasers are set to be operating at the ITU wavelengths. However, the measured results are dependent on the channel offset (difference between the passband center and the nominal center wavelength, $\Delta\lambda_{Ci} = \lambda_{Ci} - \lambda_i$). For a channel-offset-independent characterization of the wavelength isolation, which is more meaningful to component designers, the crosstalk can be measured relative to the passband center, λ_{Ci}.

The passband width (B) is the width of the filter at a specified level below the peak (as shown in Figure 4). Passband widths at several insertion loss values (e.g., 1dB, 2dB, 3dB, 30dB) are specified to quantify the passband shape. The 30dB width is a measure of the steepness of the filter slopes and an indication for the crosstalk. Another parameter that specifies the passband shape is the passband ripple (R) or the flatness (F), which is the maximum insertion loss variation in the wavelength window.

The center wavelength of a given port (λ_{Ci}) is usually measured at the center of the passband at –3dB transmission. The channel offset ($\Delta\lambda_{Ci}$) of the port is the difference between the center wavelength and the nominal wavelength (ITU grid wavelength).

The parameters described above can be measured using an unpolarized light source. The polarization dependent loss (PDL) and wavelength (PDW, PDλ) are the maximum variation in insertion loss and center wavelength over all polarization states.

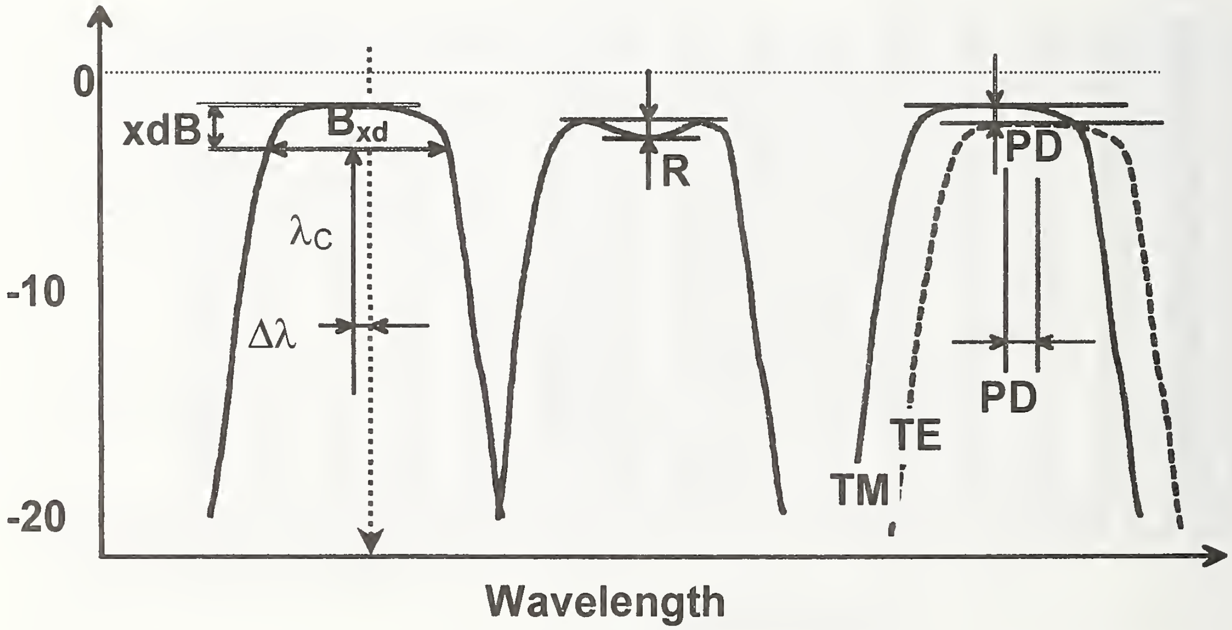

Figure 3: Spectral Plots showing the Passband Width (B), Ripple (R), Center Wavelength (λ_c), and Offset ($\Delta\lambda_c$), Polarization dependent Loss (PDL), and Polarization dependent wavelength (PDW)

Chip-Level Testing

The inadequacy of the wafer level inspection to predict the optical conformance of a device to customer specifications necessitates the introduction of a screening step before the device is packaged and Final Tested. At this step, only critical parameters that contribute to low yield and other parameters that will assist in the packaging of the device need to be measured.

WGR devices are extremely sensitive to processing variations and the current technologies cannot achieve with high yield the channel accuracy (<0.05nm) that is required by system vendors. Therefore, WGR devices generally have extra inputs and outputs so that the channel wavelength can be tuned after wafer processing. The input waveguide spacing at the interface of the input star coupler is different from the output waveguide spacing at the interface of the output star coupler. By moving to a different input and correspondingly a different set of outputs the channel wavelength can be coarsely tuned so as to match the wavelength-comb of the device to that of the ITU wavelength grid. The proper input and output combinations are determined at this stage of testing, and this information is later used for fiber attach.

Final Testing

The last area of testing before the product is shipped to the customer is called the "Final Testing." The product is tested according to a customer specification to determine if it is in conformance. The conforming device yield performance from this area is used to drive a change in the device design and to establish control limits for the optical parameters at Chip-level testing.

The channel wavelength of WGR devices are temperature sensitive (0.012nm/deg C), and therefore have to be temperature stabilized. The devices are generally operated using a heater/sensor combination, which requires that the operating temperature of the device be above maximum ambient temperature that the device is going to see in operation. The maximum operating temperature is generally dictated by reliability concerns. So, there is a temperature range of operation, which can be used to fine-tune the wavelength. The operating temperature of the device is determined by minimizing the wavelength offsets for all the channels.

The next section discusses the two types of measurement schemes that are available to characterize the wavelength performance of DWDM filters.

Measurement Schemes

There are basically two ways to configure a test system for the characterization of a DWDM demultiplexer. The first configuration uses a broadband light source and an optical spectrum analyzer, which acts as the wavelength selective receiver. The polarization controller serves to characterize the polarization dependencies of the device under test, such as center wavelength shift or the PDL. The channels are tested one at a time and the optical switches allow the automation of the testing. The required wavelength accuracy by system vendors (10 pm) has pushed the capability of the spectrum analyzers to its limit. Any variation in pressure, temperature, or index of the medium in which the spectrum analyzers operate can cause deviations in the measurement of the wavelength that are unacceptable. Therefore, the spectrum analyzers need to be calibrated around the wavelength window of operation before measurement of each device, using a more accurate instrument consisting of a wavelength meter and a tunable laser source. The wavelength of the tunable laser source is precisely measured by the wavelength meter and then again by the OSA. The delta between both the values is recorded as a correction factor in a look-up table. This method of calibrating the OSA requires expensive equipment and adds to the cost. Furthermore, to accurately characterize the wavelength dependence of a DWDM device using the above test system requires time- consuming measurements. For example, to characterize a device over a 30nm range with 0.1nm resolution requires 300 measurements, which takes few hours of testing time. To increase throughput, more testing stations are required - which is an expensive proposition

An alternative setup that speeds up the measurement time uses a swept wavelength selective tunable laser and a broadband power meter as the receiver. Each channel has its own dedicated power meter. With this approach in one sweep of the laser the spectral data of all the channels is available at once. For this system to be useful for DWDM measurements the tunable laser has to have a wavelength accuracy of 5pm and a dynamic range (or isolation) of better than 60 dB. The fine wavelength accuracy is achieved by using a built-in wavelength meter that is able to read the wavelength of the laser source accurately in a matter of milliseconds. Unlike the previous method which tests each channel one at a time, this configuration allows all channels to be tested simultaneously. Using this configuration the measurement time is cut down from a few hours to less than an hour per device.

Conclusion

DWDM components are described by a new and complex set of parameters. By carefully selecting and combining the right set of instruments, both measurement accuracy and throughput can be optimized. Because of its high throughput and reasonable accuracy, the swept laser system configuration is replacing old test systems that use the OSA.

References

[1] Y.P.Li and C.H.Henry, “Silicon Optical Bench Waveguide Technology,” Chapter 8 in *Optical Fiber Telecommunications IIIB*, edited by I.P.Kaminow and T.L.Koch, 1997, Academic Press.

[2] C. Dragone, “A NxN optical multiplexer using a planar arrangement of two star couplers,” *IEEE Photonics Technology Letters*, vol. 3, pp 812-814 (1991)

[3] C. Dragone, “Frequency Routing Device having a wide and substantially flat passband,” patent number 5412744.

Saturated Optogalvanic transition in Krypton at 1564 nm

David A Humphreys: National Physical Laboratory, Queens Road, Teddington, Middlesex, TW11 0LW.

Introduction

The rapid increase in demand for bandwidth in WDM systems brings a need for higher accuracy wavelength reference standards. These can be realised through saturated transitions where the natural linewidth can be measured by selecting atoms or molecules that have no velocity component along the axis of the optical beam. However, to obtain saturation in a gas such as acetylene requires significant levels of optical power. Previous workers have identified a number of optogalvanic excited-state transitions in noble gasses at wavelengths used for optical fibre communications[i]. Saturation of these transitions has been demonstrated at wavelengths up to 1547.8 nm[ii,iii]. In this paper we present the first measurements of a Krypton saturated optogalvanic transition in the L-band. As these are excited-state transitions they have a broader linewidth than the saturated molecular transitions but are more readily achievable at modest optical powers.

Saturated optogalvanic system

The saturated optogalvanic system is shown in Figure 1. A chopper in the return beam discriminates between the saturated and unsaturated signals. A lock-in amplifier (1) operating at the chopper frequency recovers the saturated signal and this is passed to a second lock-in amplifier (2) to recover the error signal. Lock-in amplifier (3) operates at twice the dither frequency and monitors the quality of lock that can be achieved. The cascaded lock-in amplifiers (1 & 2) give excellent discrimination of the saturated signal, compared with previous results.

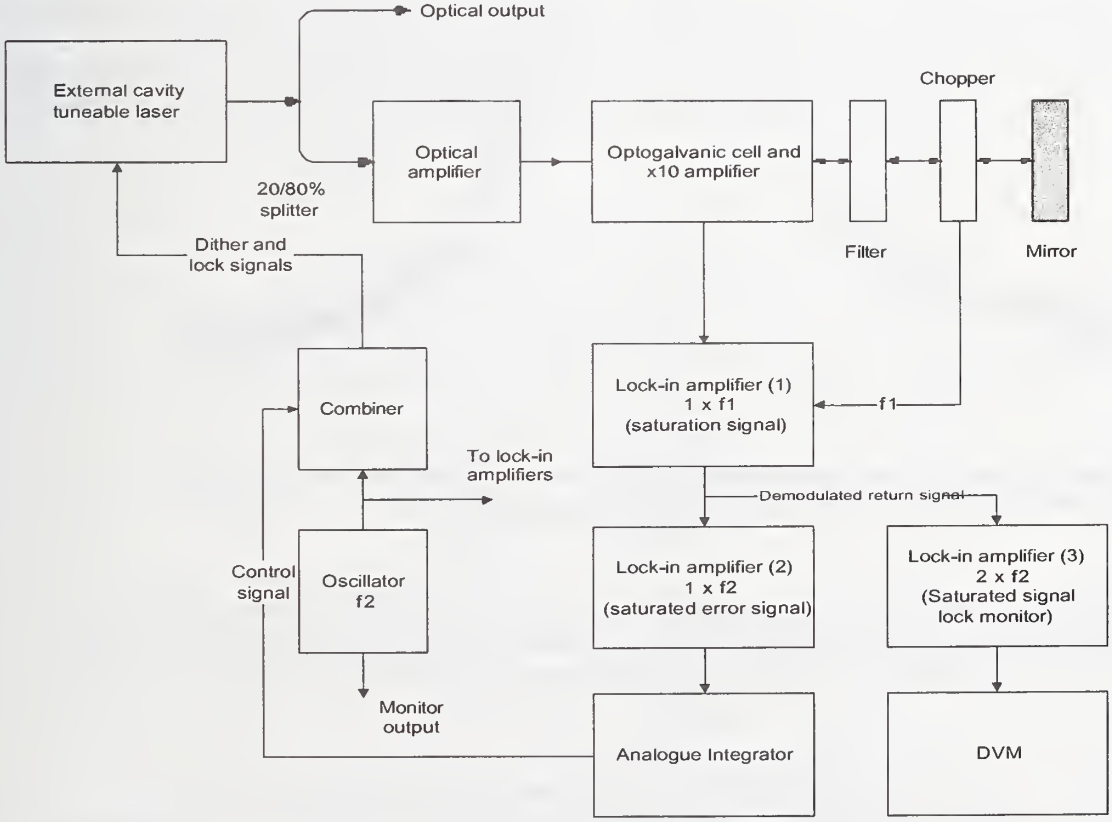

Figure 1 Instrument layout for Saturated optogalvanic system

A commercial hollow cathode cell, filled with Krypton to a pressure of 130 Pa and operating at a discharge current of about 100 μA was used for the measurements. Saturation has also been successfully obtained in Cells with a higher pressure (600 Pa). A lens was used to collimate the beam, giving a diameter of approximately 2.4 mm, estimated from the fibre NA and the lens focal length. The filter transmission is 64%, reducing the intensity of the returned signal to 40% of the unchopped pump power. The chopper was operated over the frequency range (1200 – 1650) Hz and the external cavity laser was modulated at 123 Hz to give a peak to peak modulation of 127 MHz.

Results

Measurements of the power dependence of the saturation have been made for a range of pump powers (1 - 7.8) mW in the collimated beam. The results obtained at an optical power level of 7.8 mW and with no dither signal are shown in Figure 2. The full width of the saturated dip is (67 - 81) MHz measured at (6.9 - 7.8) mW. This compares with the Doppler broadened linewidth, (410-427) MHz measured at (1 - 2) mW.

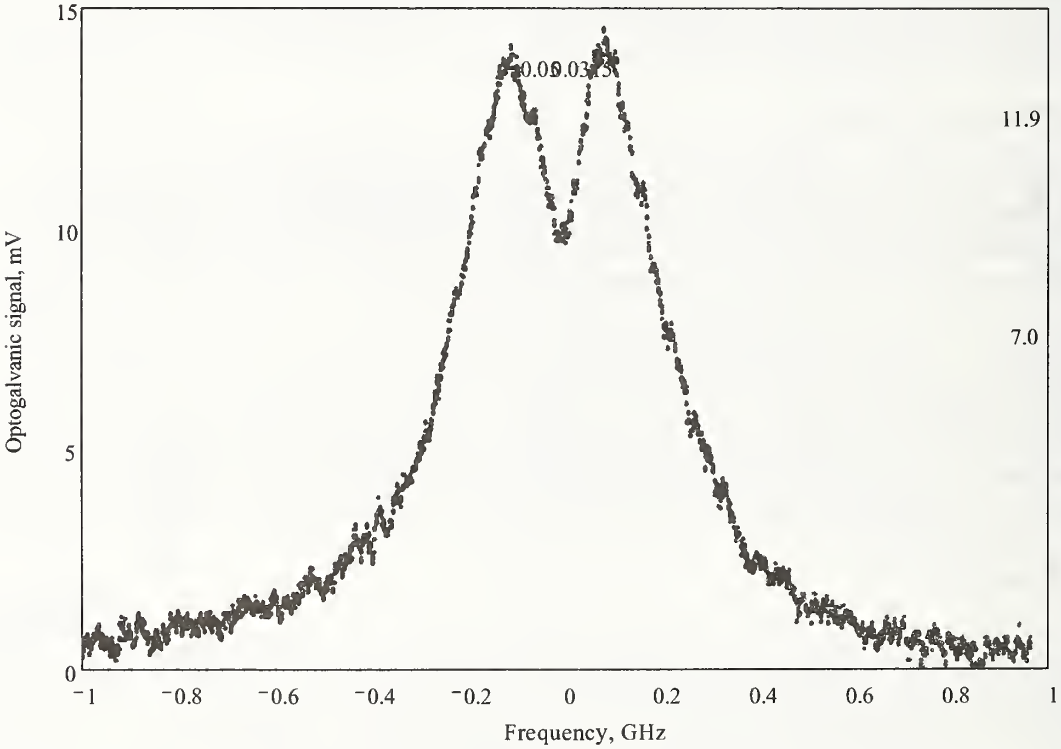

Figure 2 Saturated response at 7.8 mW showing markers at the 50% points of the saturated and Doppler-broadened transition to indicate the accuracy improvement that can be realised

The integral of the optogalvanic trace was used to estimate the saturation. The saturation threshold has been defined as the point where the integral of the measured optogalvanic signal, normalised to the optical power, has been reduced by a factor of $1/\sqrt{2}$. This occurs at 680 W/m^2, corresponding to an optical power of 5.7 mW, as shown in Figure 3.

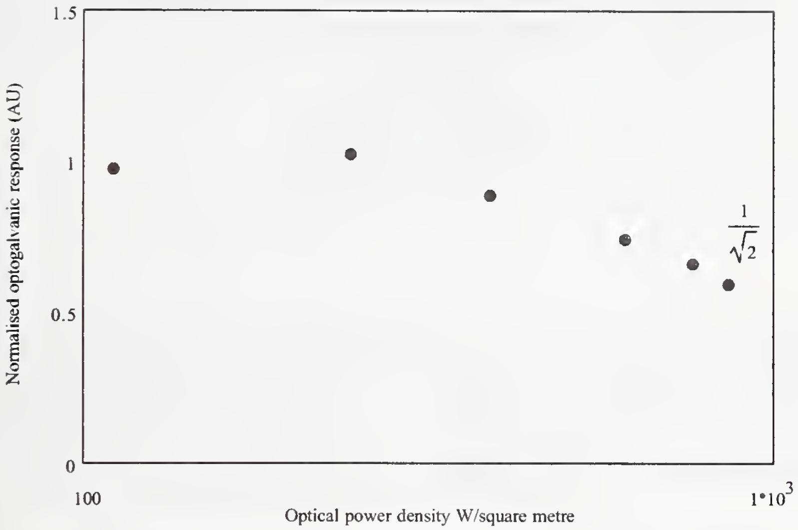

Figure 3 Power density dependence of optogalvanic signal

Measurements against a $^{13}C_2H_2$ unsaturated reference

The wavelength of the saturated lock signal was measured against acetylene reference lines using a wavemeter. The absorption cell contained $^{13}C_2H_2$ at 1.07 kPa with an optical path length of 300 mm. An integrating lock loop was used to stabilise the external-cavity laser to the maximum absorption. The measurement system is shown in Figure 4. Three lines (R25, R26 and R27) were measured to quantify the contribution due to offsets in the laser lock.

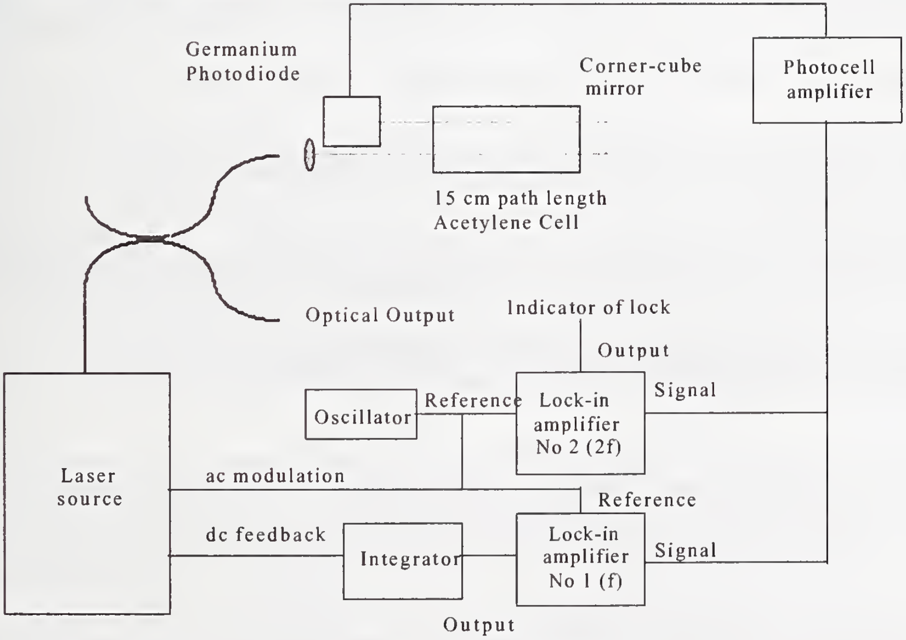

Figure 4 Acetylene unsaturated lock system used as a local reference

Each of the reference lines was measured for a 60 minute period and the saturated Krypton reference was measured for a 120 minute period. The results for the Krypton reference measured over the period are shown Figure 5. The mean value for the Krypton saturated transition is estimated as 1563.97644 (14) nm at 95% confidence.

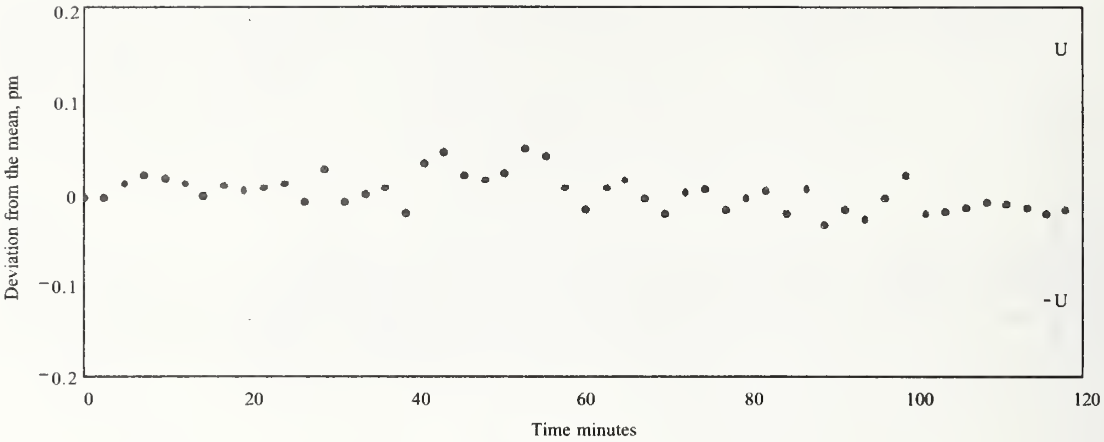

Figure 5 Stability of the saturated lock over a 120 minute period.

Summary

Saturated optogalvanic standards offer the potential for higher accuracy, compared to unsaturated transitions, and the benefit of modest optical power requirements (<10 mW). Measured results for the saturated transition in Krypton at have been reported for the first time at 1563.97644 (14) nm, using $^{13}C_2H_2$ reference wavelengths. Stable locking in excess of two hours was achieved.

Acknowledgements

I wish to thank The UK department of Trade and Industry for providing financial support for this work and Mr F Wonnacott of Anritsu UK for providing the wavemeter.

References

---

[i] *Y. C.* Chung: 'Frequency locked 1.3 and 1.5 μm semiconductor lasers for lightwave systems applications', *J. Lightvawe Tech.,* vol. *8,* p. *869, 1990.*

[ii] A. J. Lucero, Y. C. Chung, S. Reilly, and R. W. Tkach: 'Saturation measurements of excited-state transitions in noble gases using the optogalvanic effect', *Optics Lett.,* vol. 16, no. 11, pp. 849-852, 1991.

[iii] U. H. P. Fischer and C. v. Helmolt: 'Saturation and Isotopic Shift of the Kr84 Excited-State Transition at 1547.825 nm', IEEE Photonics Technology Letters, vol. 7, No. 1, January 1995, pp.65-67.

Characterization of Multimode Fiber for 10 Gbps Operation

(Invited)

John S. Abbott
Corning Inc. HP-ME
Corning, NY 14831

Introduction

The demand for ever-increasing data transmission rates is driving continuous development in the data communication marketplace. Sources, fiber, receivers, and connectors are all being re-engineered to provide low cost solutions to fill the growing need. At the 1998 Optical Fiber Measurement Symposium, the technical developments for 1Gigabit per sec (Gbps) Multimode Mode (MM) applications were described [1]. This paper summarizes recent work extending the capability to 10 Gbps systems and the fiber characteristics (and their measurement) which make this practical.

The Telecommunication Industry Association (TIA) supports industry's need to develop standard approaches for meeting the requirements of high-speed applications. Technical considerations requiring resolution to develop the MM 10 Gbps systems are being addressed at this time through the TIA FO-2.2.1 Task Group on Modal Dependence of Bandwidth [2], which earlier dealt with characterization of fibers and lasers for 1 Gbps applications. The results reported herein draw extensively from the work of this group. Currently, 10 Gbps 850nm vertical cavity surface emitting lasers (VCSELs) are just reaching commercialization and they have not been extensively characterized. However, there is a demand for optical fiber that can be installed today for 1 Gps applications and upgraded in the near future to use at 10 Gbps when such lasers are available. Although this paper focuses on the characterization of the fiber, the characterization of the lasers will be of equal importance.

Light Propagation in MM Optical Fibers; Bandwidth and DMD Fundamentals

Multimode fiber information carrying capacity is characterized using a bandwidth length product (MHz-km), which is a key factor determining how far a system can operate at a given bit rate [3]. In simple terms the bandwidth is measured by taking the fast Fourier transform (FFT) of an output pulse and comparing the amplitude versus frequency to the FFT of the input pulse. The ratio of the two FFTs represents the broadening occurring as the pulse propagates down the fiber, and the –3dB bandwidth used in system models is defined as the frequency where the ratio has dropped to 0.5 of the zero frequency value. Methods exist for measuring the bandwidth in the frequency domain without using an actual pulse [4], but this paper will emphasize pulse-based methods which give a better intuitive understanding of the multimode light propagation.

The pulse spreading as the pulse propagates down the multimode fiber depends primarily on intermodal dispersion – the relative delays of the individual modes – and the chromatic dispersion of the glass, which broadens each mode depending on the wavelength of the laser and its spectral width. At 850nm the chromatic dispersion can be the limiting factor in how narrow a pulse can be propagated, if a broad spectral source like an LED is used.

In modern high bandwidth multimode fibers, the index profile is approximately parabolic, and there is strong coupling between individual modes that have the same propagation parameter β. The light propagation can be understood as the propagation of a relatively small number of degenerate mode groups travelling at different speeds. The absolute delay τ_m of each individual mode is related to the propagation parameter by $\tau_m = (1/c)\ d/dk\ \beta_m$, and the relative delay $\delta\tau_m$ of each mode compared to that in a 'perfect' profile is given by $\delta\tau_m = (1/c) \int \delta n(r)\ d/dk(k\ \psi_m^2(r))\ r\ dr$, where $\delta n(r)$ is the index perturbation [5],[6] and $\psi_m^2(r)$ is the solution to the scalar wave equation [7], [8]. The output pulse depends on the relative mode delays $\delta\tau_m$ and the modal power P_m. An example making this clear is given in Figure 1 below. The relative mode group delays in Fig 1(a) are calculated using an index profile measured with the refractive near field (RNF) [4]. The modal power distribution (MPD) is given in Fig 1(b) for an "overfilled launch" (OFL) somewhat typical of an LED and the standard bandwidth measurement before the Gigabit Ethernet (GbE) work. In an OFL bandwidth measurement an equal amount of power is launched into each individual mode; the shape of the MPD in Fig 1b is determined by the increasing number of individual modes in the higher order mode groups and the increasing attenuation of the highest order mode groups. Finally in Fig 1(c) the weighted mode group delays are plotted, along with the resulting output pulse if a small amount of chromatic dispersion is assumed (if no chromatic dispersion is assumed, the impulse response would be a sum of delta functions $\Sigma\ P_m\ \delta(t - \delta\tau_m)$). Agreement between the measured and predicted pulse shape for a variety of index profiles is used to verify the profile data, the calculation of the mode delays, and the assumed MPD.

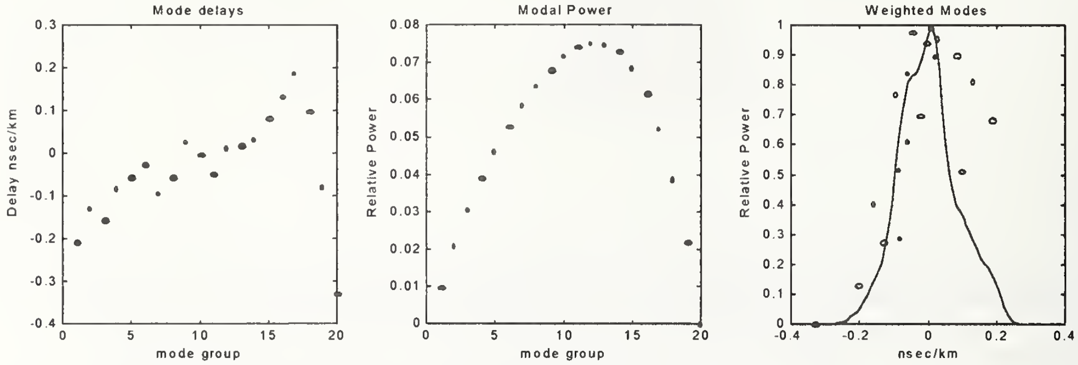

Figure 1. Example showing how the output pulse depends on both mode delays and modal power distribution.

This example shows that the output pulse, and hence the bandwidth, depends on both the properties of the fiber, which determines the mode delays, and the laser, which determines the MPD. Generally the 1 Gbps and the expected 10 Gbps lasers put dramatically less power into the outer modes than the curve in Fig 1(b), so that even with the same mode delays as in Fig 1(a), the output pulse in Fig 1(c) can change significantly.

The relative mode delays can be analyzed if the MPD is tightly controlled and only a small subset of the mode groups carry significant power. This is the basis for the differential mode delay (DMD) measurement [4] used as a tool for process tuning. By scanning a diffraction-limited Gaussian spot across the core diameter and recording the centroid of the output pulse as a function of launch position, it is possible to estimate the mode delays. Accurate frequency-based methods for the DMD measurement have been developed at NIST [9], and an example from one of the round robin cables from 1GbE development is given in figure 2. In this example, the profile is approximately optimized for a wavelength between 850nm and 1300nm, so that at 1300nm the outer modes arrive later than the center modes while at 850nm the inner modes arrive later. If the profile were optimized for 1300nm, the DMD curve at that wavelength would be flat and all mode groups would arrive at the same time.

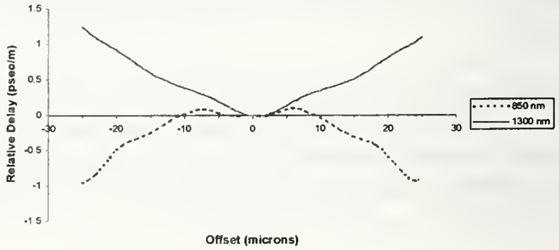

Figure 2 - Differential Mode Delay for TIA TG 2.2 Round Robin Cable (Fiber 7)

When a pulse-based method is used for the DMD measurement, it is possible to obtain additional information about the mode delays and MPD and more completely characterize the fiber. Figure 3 is a contour plot of the DMD measurement pulses for a fiber manufactured in the late 1980's, with a mean

DMD shape somewhat similar to that in Figure 2. This example (which is not typical) shows a complex pulse structure which is different at 850nm than 1300nm because the detailed modal structure is different.

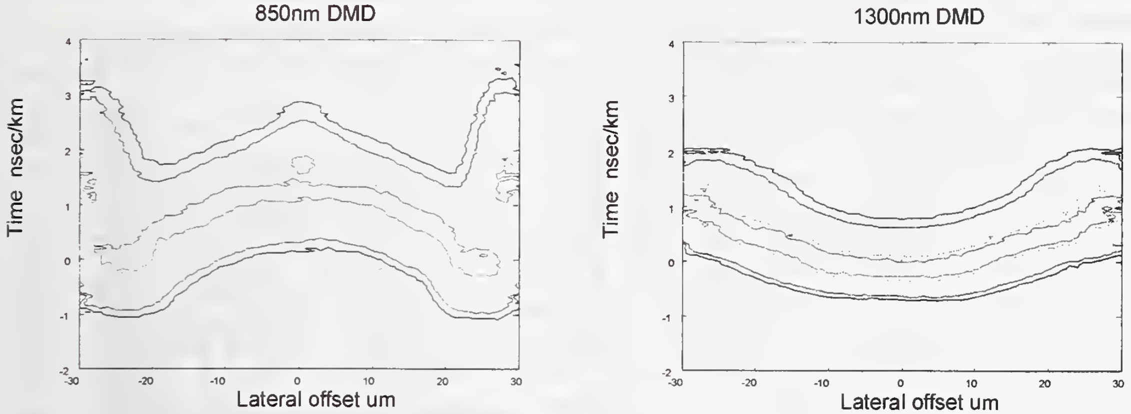

Figure 3. Example of DMD pulses of fiber with index perturbation

Figure 4 gives an example of a 1300nm-optimized fiber with a DMD which is flat and with little change in the pulses as the launch position is shifted.

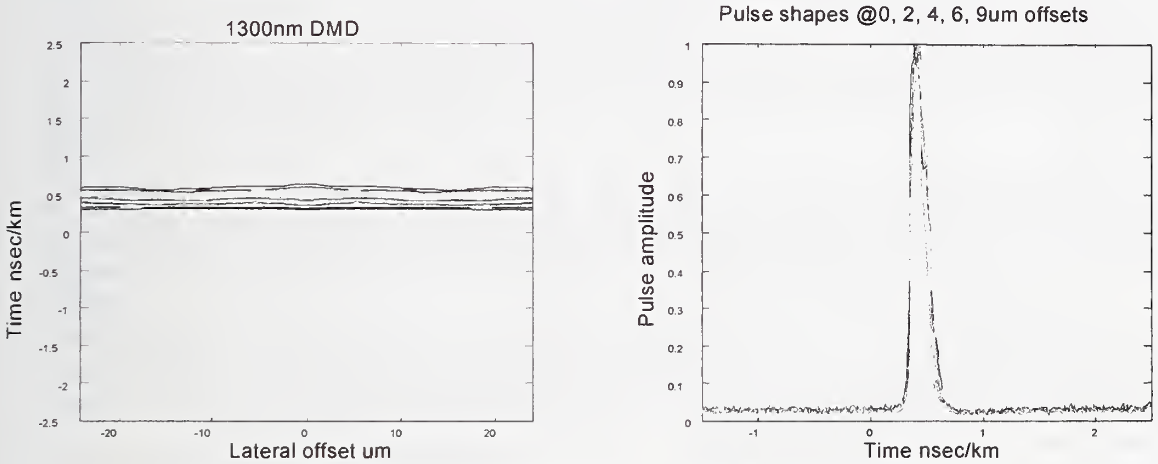

Figure 4. DMD of fiber optimized for a particular wavelength

Bandwidth Requirements for 1- and 10 Gbps Systems; Encircled Flux & MPD

As mentioned above, the multimode bandwidth is a key factor in determining the bit rate a given length of fiber can support. A detailed “link model” was developed and documented by engineers at Agilent and used in 1 GbE development [10]. The model, though necessarily approximate, is extremely useful and provides a systematic tool for evaluating the effect of different system parameters on the length which can be supported. For 1 Gbps transmission at 850nm over 62.5 μm fiber, a bandwidth of 385MHz-km will support a 500m length [11]. For 10 Gbps transmission at 850nm over 50 μm fiber, the estimated bandwidth for 300m is 1800-2200 MHz-km[12]. The exact value depends on assumptions in the link model. Lab tests have demonstrated transmission on longer lengths[13]. In these examples, the fiber, transmitters, and/or other system components presumably do better than one or more of the worst case assumptions used in the model. When measured with an actual laser, the bandwidth is customarily referred to as “effective modal bandwidth” (EMB), to make it clear that the measurement depends on the particular laser and modal power distribution.

The next step in characterizing the fiber for 1 Gbps or 10 Gbps operation is to determine when the fiber will meet the required EMB with available lasers. In the course of the work of the TIA FO 2.2.1 Task Group on Modal Bandwidth, there have thus far been two experiments of extensive round-robin testing of Gigabit Ethernet fiber at various laboratories to establish the level of repeatability and the sensitivity of bandwidth to launch conditions. NIST has been central to all the work. The first Round Robin is reviewed in reference [1]. The second round robin, the so-called "Validation Cable", was completed in late 1999 and the results summarized at the June 2000 TIA meeting in Quebec [2]. This round robin involved some 95 different fibers each measured with 60+ different lasers at various labs. At 850nm, the standard link model [9] indicates that a bandwidth of 385MHz-km is needed to go 500m at 1 Gbps over 62.5 µm fiber. The fibers included 1/3 expected to fail with some lasers, 1/3 expected to pass with most lasers, and 1/3 to be intermediate. The results established the use of an "encircled flux" criterion to characterize the launch power distribution of Gigabit lasers. Figure 5 indicates by shading how the "effective modal bandwidth" (EMB) for many fibers shifts above or below 385MHz-km depending on the particular laser used and the resulting modal power distribution. In this diagram the <u>columns</u> correspond to different fibers and the <u>rows</u> to different lasers. This diagram has all lasers but only the 62.5µm fibers from one cable. The lasers are ranked by the encircled flux (rows at the top have smaller spots) The larger spot lasers tend to have more cases where a fiber measured below 385MHz-km.

Figure 5. Validation Cable results.
White cells have EMB BW>385MHz-km

The encircled flux EF(r) is defined as the fraction of the total intensity within a radius r. It was found necessary to characterize the lasers by the fraction inside a small radius like 4.5µm and the fraction inside a larger radius like 15µm. A transition in the bandwidth was seen between lasers with an encircled flux of 0.65 at 15µm and those with an encircled flux of 0.85.

Figure 6 plots the encircled flux at 4.5µm versus the flux at 15µm radius for the lasers in the Validation Experiment. The recommendation by FO-2.2.1 for enhanced 1GbE defines spots with less than 75% of the encircled flux inside of a 15µm radius as 'too large' for 1GbE, and spots with more than 25% of the encircled flux inside of a 4.5µm radius as 'too small'. Some initial results presented by Picolight [14] for a 10Gbit laser are included with this data. For that particular laser the spot is much smaller than the typical 1Gbit lasers. Therefore, the fiber profile needs to be better controlled near the center

In general the requirements for both fiber and laser must be considerably tighter for 10GbE applications. In order to achieve anything near a 2000MHz-km effective modal bandwidth with a variety of 10 Gbps lasers, the fiber index profile needs to be optimized for 850nm. The fiber DMD must look something like figure 4a and there can be little change in the output pulse as the DMD input is varied, similar to figure 4b.

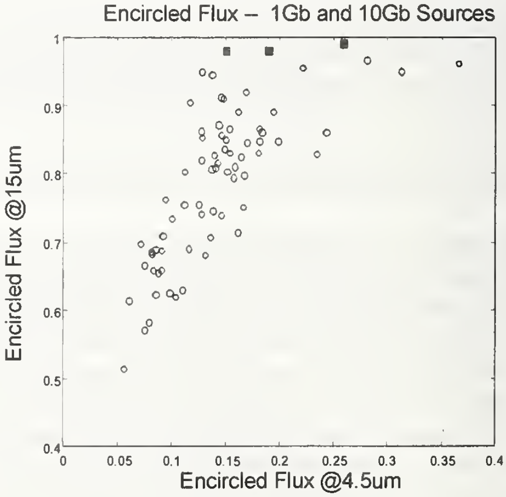

Figure 6. Encircled Flux from Validation Expt. Lasers (0um offset) and a 10 Gb/sec laser (0, 6, 10um offset).

In the enhanced 1GbE recommendation made by TIA FO 2.2.1, the fiber is characterized for 500m 1GbE (385 MHz-km EMB) applications by measuring the bandwidth with a special 23.5μm core MM fiber. The resulting MPD is similar enough to the 1GbE sources whose EF is near the 75% 15um threshold that the validation experiment showed this to successfully screen the fiber. The 'restricted mode launch' (RML) has a repeatable MPD analogous to the repeatable MPD generated by an overfilled launch used successfully for systems with LEDs.

The purpose of an RML bandwidth is to generate a relevant MPD. Until 10 Gbps lasers are better characterized, it is difficult to prescribe an RML launch, and there is not a consensus on even whether the same idea can be successfully applied, because the significant change in the MPD with slight offsets of a small spot laser launch. What can be done initially is to test the fiber with MPDs that appear plausible, and verify that the bandwidth meets the 300m 10 Gbps requirement. One way to do this is to use the pulses generated by the DMD offset launches, with the input pulse deconvolved, to construct output pulses corresponding to different but plausible MPDs. Assuming that some 10 Gbps lasers have a spot analogous to the DMD spot, for example, the DMD pulses themselves serve as one 'surrogate'. The 'bandwidth' at each offset position (out to a radius determined by the connector tolerance) needs to be above 2000MHz-km or whatever is dictated by the system requirements. The effect of other MPDs can be generated by taking a weighted average of the DMD pulses. A. J. Ritger has shown [15] the OFL pulse and bandwidth can be estimated by using a weighting of r^2, as long as the outer pulses are deweighted because of modal attenuation (this is analogous to the curve in figure 1b, if one substitutes $(r/25\mu m)^2$ for m/m_{max}). Weightings consistent with a physically realizable laser would have a maximum weighting for the DMD pulse at some offset position 'r' and taper down for offsets less than and greater than this position.

In the limit that every weighting must be considered, one arrives at the idea of a template [15] [16] , where the earliest mode for any offset position x, $0 < x < x_{max}$, and the latest mode for any offset position are specified to lie within the 'bit rate window'. The maximum offset considered (15μm in reference [15] and [16]) is determined based on connector tolerances and the laser spots being considered. Figure 7 [16] gives an example of the template. This is a sufficient condition for the fiber meeting the 10 Gbps requirement, but is more stringent than necessary. It overestimates how much power the modes excited with 0 offset can have simultaneously with those excited with 15μm offset. It would be better to have a smaller template (like 5 to 10μm) and have it shift over the whole region. Then the 'latest – earliest' modes are calculated from 0 to 5μm, 1 to 6μm, 2 to 7μm, etc. (if the template is 5μm long, for example) out to 10 to 15μm.

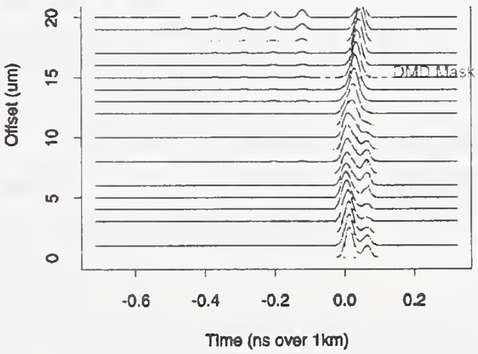

Figure 7. Example DMD mask from 0um to 15um from reference [16]

Current Opportunities and Limits

If we are be able to bracket the MPDs generated by actual 10 Gbps lasers, we may be able to devise an RML launch which can efficiently screen most of the fiber, so that the DMD can be used for sampling rather than the direct measurement of each fiber. In the case of 1GbE VCSEL sources, it was found that the nearfield and farfield distributions tended to stay in proportion, so that a specification on the encircled flux (measured in the near field) also restricted the far field. In the case of 10GbE sources, this needs to be checked once again. The output pulses from 10Gbps lasers need to be compared to the RML pulses or pseudo-pulses generated from DMD data, and this is complicated by the VCSEL lasers being modulated rather than pulsed sources. The temporal aspects of the VCSEL modulation may cause the effective spot shape to shift during the modulation cycle, which could also complicate development of a surrogate RML measurement.

However, the fundamental issues are relatively simple. To achieve 10 Gbps over 300m, a certain effective modal bandwidth is required. This bandwidth depends on the relative mode delays inherent in the fiber and the modal power distribution due to the laser and its deployment. The mode delays must be controlled (by controlling the index profile) so that the required EMB is reached for the variety of MPDs which occur in practice.

Acknowledgments

The author expresses his appreciation to all of the individuals and organizations contributing to the work of the TIA FO 2.2.1 task group and its work on 1Gbit and 10Gbit systems. The work of NIST, and John Schlager in particular, should be noted. The contributions and insights of John Ritger, Paul Kolesar, and their colleagues at Lucent are also especially appreciated. The ideas, results, comments, and enthusiastic support of colleagues at Corning are gratefully acknowledged.

References

[1] Hackert, M.J., 'Characterizing Multimode Fiber Bandwidth for Gigabit Ethernet Applications', Symposium on Optical Fiber Measurements, Boulder, Sept. 1998, pp.113-118
[2] Hackert, M.J., 'TIA FO-2.2.1 June 12, 2000 Update', presentation at TIA plenary, Quebec, June 2000.
[3]Bandwidth model developed for IEEE P802.3z Specification for 802.3 Full Duplex Operation Supplement to Carrier Sense Multiple Access with Collision Detection (CSMA/CD) Access Method and Physical Layer Specification for 1000 Mb/s Operation.
[4] Marcuse, D., Optical Fiber Measurements. New York: Academic Press, 1981. p.287
[5] Olshansky, R., 'Pulse broadening caused by deviation from the optimal index profile', Applied Optics **15** (1976) 2, p.782
[6] Abbott, J.S., 'Light Propagation in Gbit LANs', presentation at IMA workshop on Analysis and Modeling of Optical Devices, Minneapolis,September 9-10, 1999.
[7] Snyder, A.W., and Love, J.D., Optical Waveguide Theory. New York: Chapman and Hall, 1983.
[8] Mammel, W.L., & Cohen, L.G., 'Numerical Prediction of fiber transmission characteristics from arbitrary refractive-index profiles', Appl. Optics 21 (1982) 4 pp 699-703.
[9] Mechels, S.E., Schlager, J.B., and Franzen, D.L., 'High-Resolution Differential Mode Delay Measurement in Optical Fibers using a Frequency-Domain Phase-Shift Technique,' Photonics Technology Letters, **9** (1997) 6, pp. 794-796.
[10] Cunningham, D.C., and Lane, W.G., Gigabit Ethernet Networking. Indianapolis: Macmillan Technical Publishing, 1999.
[11] Pondillo, P.L., 'TIA FO-2.2.1 Validation Analysis Results for Recommendation of Enhanced Performance over 62.5um Fiber' presentation at TIA FO-2.2.1 meeting, Boulder, December 1999.
[12] Kolesar, P., and Swanson, S. 'Next Generation Multimode Fiber Objectives', presentation for TIA TR42.8 at TIA interim meeting Greensboro March 24, 1999.
[13] 'Multimode optical fiber transmits 10Gbit/s over 2.8 km', Laser Focus World, 36 (June 2000) 6, p.11.
[14] Jewell, J, et al., '850nm Serial PMD Experimental Update', presentation at TIA meeting, Ottawa June 2000.
[15] Ritger, A.J., 'Modal Dispersion Measurements', presentation to TIA FO-2.2.1 meeting, Savannah, January 2000.
[16] Golowich, S.E., et al.,'50um Multimode Serial 10Gb Simulations', presentation at TIA Plenary, Quebec, June 2000.

Short Pulse, Small Spot Size, Central Launch in Multimode Fibres: Comparison between Measurement and Computation

M.J.N. van Stralen[1], B.P. de Hon[2], M. Bingle[2], F.J. Achten[1]

[1]Plasma Optical Fibre B.V., P.O. Box 1136, 5602 BC Eindhoven,
The Netherlands
[2]Eindhoven University of Technology, Faculty of Electrical Engineering,
P.O. Box 513, 5600 MB Eindhoven, The Netherlands

Introduction

Until recently, most optical networks based upon transmission through multimode fibres operate at bit rates of 100 Mb/s or less. Light emitting diodes (LED's) are often used because of their low cost and the ease of connection. The spot size of LED's exceeds the core size of the fibre, and hence the fibre is fully illuminated. For systems that require higher data rates, such as the Gigabit Ethernet networks, commercially available LED's are too slow. Diode lasers such as 850 nm vertical cavity surface emitting lasers (VCSEL's), can be used in these systems and have smaller spot sizes. The resulting partial illumination of a multimode fibre changes the performance as far as the bandwidth or pulse broadening [1] are concerned.

We have conducted experiments at 1300 nm to investigate the propagation of short-pulse power signals, and their excitation by a source with a small spot size. In this paper, we present our first results concerning the comparison between the measured and computed results.

Experimental Set-up

The experimental set-up is depicted in Figure 1. A semiconductor laser is connected to a single-mode patch cord, while the detector is connected to a multimode patch cord with a 62.5 μm core diameter. The fibre under test is mounted between the two patch cords using fibre coupling devices. A symmetric launch is obtained at the interface when the fibre axes are aligned.

Figure 1: Experimental set-up.

The laser is internally triggered at a fixed repetition rate. The centre wavelength, the wavelength spacing and full width of the distribution of impulses at half amplitude were measured to be 1297.5 nm, 0.7345 nm and 8.84 nm, respectively, as shown in Figure 2a. The temporal response of the laser was measured by using a short sample of the test fibre (1 m) in the set-up. This pulse is depicted in Figure 2b. Its full width at half amplitude is about 70 ps.

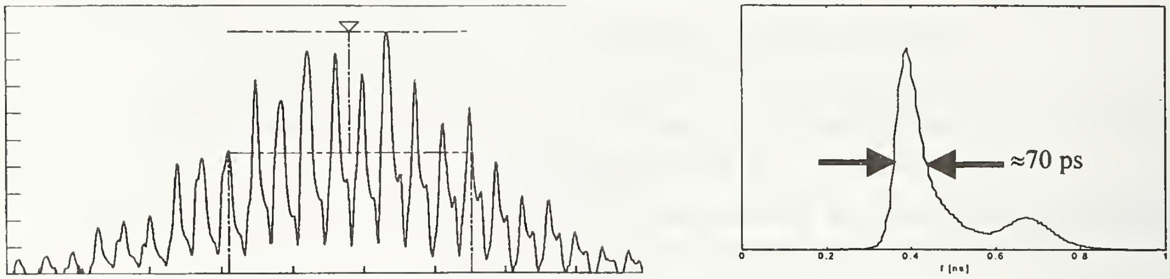

λ_{centre} =1297.6 nm; $\Delta\lambda$=8.84 nm; resolution=0.1nm

(a)

(b)

Figure 2: Measured spectral characteristics (a) and temporal response (b) of the laser.

The detector is mounted inside an optical-to-electrical converter. The conversion from mW light power to mV electric voltage is linear. The electrical pulse is sampled with a sampling head. The trigger signal of the laser is used to display the pulse.

Numerical Multimode Fibre Model

As part of the collaboration between Plasma Optical Fibre and the Eindhoven University of Technology, a full-wave multimode fibre model has been developed. In its present form, the HE_{1n} and EH_{1n} modes are calculated. The propagation coefficients and modal field distributions are calculated at multiple frequencies. To a good approximation the illumination by the single-mode fibre has a Gaussian field distribution. In the model it is decomposed into the modal constituents of the multimode fibre to obtain the modal amplitudes. The observed pulse at the receiving end of the fibre is the time-averaged instantaneous power, calculated with the aid of analytic signals.

The Sellmeier model is employed to determine the refractive index profile in the frequency range of interest from the preform measurements at 632.8 nm. The Sellmeier coefficients used are those for bulk glass [2]. Profile changes due to the drawing process have not been taken into account. The modal attenuation coefficients due to material losses are assumed constant over the pertaining frequency band about 1300 nm. These attenuation factors were not known *a priori* for the fibres under test.

Experimental and numerical results

Two multimode fibres have been investigated. Each fibre has a core diameter of 50 µm and a length of 8.9 km. One fibre is optimised for an overfilled launch in the 850 nm window, while the other fibre is optimised in the 1300 nm window.
From preliminary computations using a single carrier frequency, the resulting pulses showed virtually no pulse broadening. After inclusion of the ensemble of carrier frequencies according

to the measured distribution and spacing, pulse broadening increased significantly. These results still showed insufficient pulse broadening. However, the calculated the zero-dispersion wavelengths of most modes lie between 1300 nm and 1310 nm, while the measured zero-dispersion wavelength is about 1320 nm. This discrepancy of about 15 nm is probably due to the deviation from the assumed refractive index model. To compensate for this discrepancy the centre wavelength of the laser was shifted downward by 15 nm in the computation. The attenuation of the pulse has been accounted for through power normalisation. Figure 3 shows the measured and computed output pulses in both fibres.

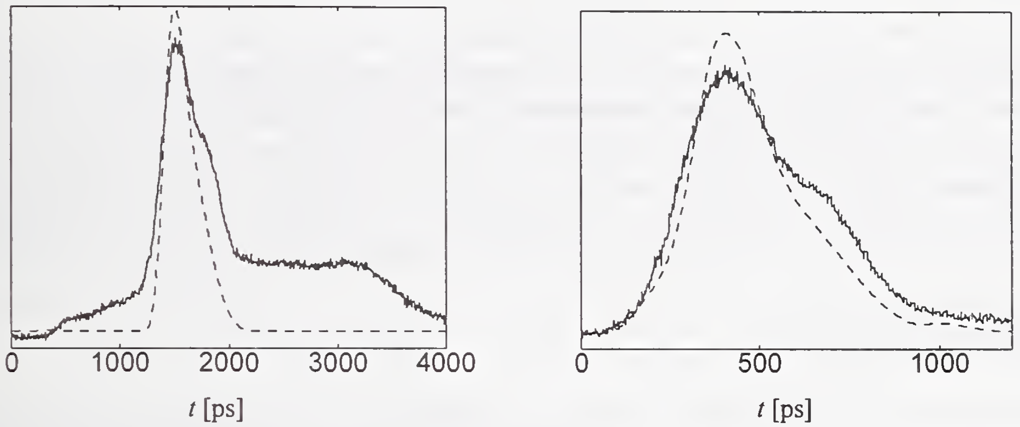

(a) (b)

Figure 3: Measured (solid) and computed (dashed) output pulses for the 850 nm optimised fibre (a) and the 1300 nm optimised fibre (b).

From a comparison between the measurements and the computed results, it appears that the fundamental mode dominates the pulse propagation. The measured output pulse of the 850 nm optimised fibre appear to also contain power of other mode groups on both sides of the pulse. This is confirmed by moving the single-mode patch cord away from the central axis.

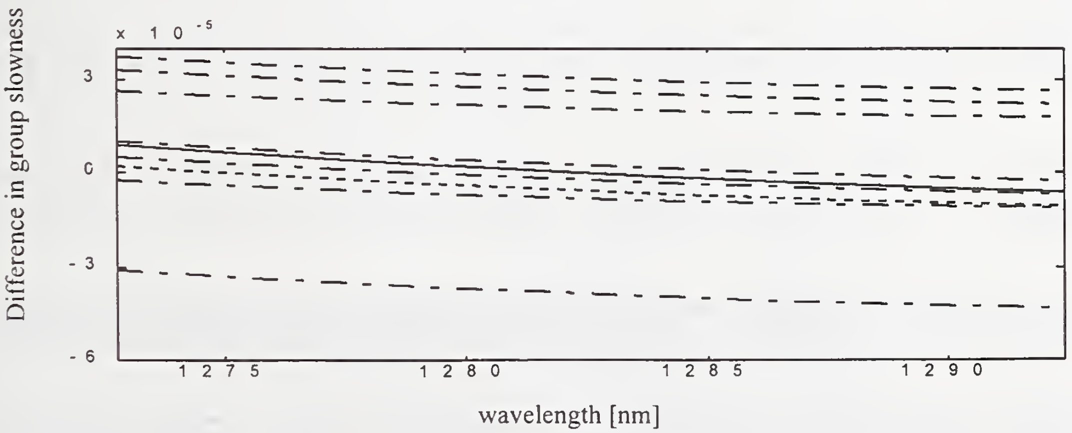

Figure 4: Difference in group slowness for modes *n*=1 (HE_{11} solid; EH_{11} dashed) and *n*>1 (dash-dot) with respect to HE_{11} mode at the central wavelength. The modes near the cladding are not included in the figure. (1300 nm optimised fibre)

From the numerical model, extra information about the pulse transmission can be extracted. For example, the group slownesses (group delay per metre) of the HE_{1n} and EH_{1n} modes have been plotted in Figure 4. Non-dispersive pulse propagation would indicate that all the group slownesses are equal and constant. Similarly, the changes with frequency of the group slownesses form a measure for intramodal dispersion, while differences between mode group slownesses are a measure for intermodal dispersion.

Conclusions

In Gigabit Ethernet systems and other high data-rate networks, multimode fibres are under-filled launched since the fast lasers used have smaller spot sizes than ordinary LED's. The overall bandwidth differs from the standardised, overfilled, launch bandwidth. In order to analyse the pulse broadening effects using under-filled launch conditions, a numerical method for pulse transmission through multimode glass fibres has been developed and compared with experimental results. In the rotationally symmetric experimental set-up, the pulse propagation was shown to be dominated by the fundamental mode. Although the intramodal dispersion is small, its effect is considerably enhanced due to the spectral width of the laser, leading to significant pulse broadening.

The advantage of comparing experimental results with numerical simulation is that underlying physics of wave propagation become clear. As an example, the group slowness (group delay per metre) is discussed.

In conclusion, comparison between calculations and measurements pertaining to a rotationally symmetric experimental set-up shows good agreement.

Future work

In the near future, off-set launch conditions will be experimentally studied. The numerical model will be extended to include the other mode groups. The refractive index model will be refined.

References

[1] L. Raddatz, I.H. White, D.G. Cunningham and M.C. Nowel, "Influence of Restricted Mode Excitation on Bandwidth of Multimode Fiber Links", IEEE Photonics Technology Letters, Vol. 10, No. 4, 1998, p. 534.

[2] W. Hermann and D.U. Wiechert, "Refractive Index of Doped and Undoped PCVD Bulk Silica", Mat. Res. Bull., Vol. 24, 1989, p. 1083.

Measurement of the Non-Linear Index of Refraction, N_2

Dan L. Philen
Lucent Technologies, Bell Laboratories, 2000 Northeast Expressway, Norcross, Ga. USA 30071
770-798-3910, fax 770-798-4655, philen@lucent.com

Introduction: Concern about non-linear effects in optical fibers has become more important because of the advent of optical amplifiers, long system spans, and high power divided among many closely spaced channels. This is also more apparent in trans-oceanic systems where distances range from 6,000 to 10,000 km and there is no regeneration of the signal, only optical amplification, for the entire distance. Knowledge of the non-linear refractive index is necessary for the initial system design of these advanced systems.

The refractive index of a material is a function of the frequency and strength of the incident electric field. For silica, it can be accurately represented by the first two terms in a power series: a linear term, which is function of frequency (wavelength) only, and a non-linear term, which is a function of the electric field strength (intensity).

$$N(\omega, |E|^2) = N_1(\omega) + N_2 \, |E|^2$$

The intensity dependence of the refractive index leads to the non-linear effects of Self-Phase Modulation (SPM) and Cross-Phase Modulation (XPM). SPM leads to a broadening in frequency of an optical pulse causing the frequency components of one signal channel to overlap those of another. The magnitude of SPM is obtained by noting that the phase of the optical field changes by:

$$\Phi = \frac{N(2\pi L)}{\lambda} = (N_1 + N_2 \, |E|^2)\, \frac{2\pi L}{\lambda}$$

One can use the self-phase modulation phenomenon for measuring N_2. Here, the phase shift at the peak of an optical pulse is measured as a function of peak power and fiber length. The relationship between the SPM phase shift, the fiber properties and the incident light is:

$$\delta\Phi = \frac{2\pi L}{\lambda} \, \frac{N_2 \, Pm}{A_{eff}} \qquad (1)$$

Here, the dependence of N_2 on the field strength has been replaced by the power density, Pm/A_{eff}, which is the peak power divided by the effective area of the fiber.

Experimental Methods: There are basically two techniques involving the use of self-phase modulation. One uses relatively low average power, but very short pulses, while the other uses relatively high power continuous wave (CW) sources.

Short pulse SPM method:
This technique uses a Gaussian pulse of approximately 35-70 ps width at a very high repetition rate. (See for instance, Ref. 1,2) Various researchers have used pulse rates varying from 100 MHz to 2 Ghz. The pulse width seems to be critical in this measurement so as to avoid electrostrictive effects. Electrostrictive effects come into play when an initial pulse width is equal to or greater than about 1 ns. Generally, a pulse of less than 100 ps is deemed acceptable. In addition, while the average power may be in the ten to hundreds of milliwatts range, the pulse width needs to be very small in order to get reasonably high peak power to see the effect. Long fiber lengths – on the order of several kilometers – are also needed to observe the effect clearly.

A typical experimental set-up can be described in the following figure.

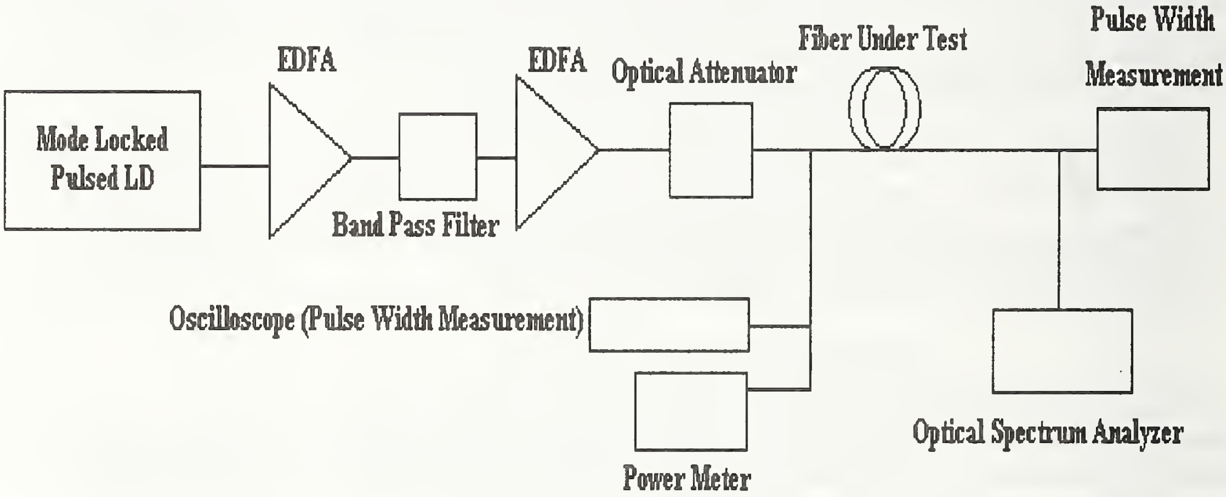

A pulse of approximately 50 ps in duration is launched through the first EDFA and then a 2 nm band pass filter. It is then again amplified through the final EDFA to the desired launch power. The optical attenuator is used to vary the power launched into the test fiber. Initial and exit pulse widths are measured in order to estimate the average pulse width within the fiber. The phase shift is determined using the number of peaks viewed on the optical spectrum analyzer, i.e., phase shift, Φ_{spm}, is [Number of peaks - ½]π.

A typical phase shift spectrum of 8.5 pi is shown in the following figure.

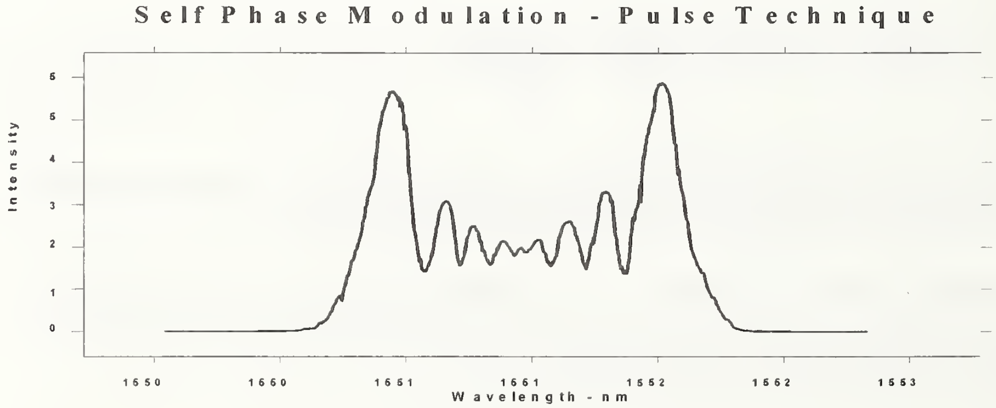

5

Once the desired phase shift is achieved, the power at the input of the test fiber is measured using a power meter. The end of the input is cut and cleaved and measured using a large area detector. The peak power is then calculated using the average power measured, the pulse width, and the repetition rate. The N_2 is then calculated using the SPM equation shown in eq. (1) above, where L is the effective length, Pm is the peak power, A_{eff} is the effective area, and λ is the operating wavelength.

The ease of this measurement is the fact that SPM is measured directly. The phase shift is easily determined from the display on an optical spectrum analyser (OSA) and then power measured. One disadvantage of this technique is the extremely high power required to acquire an appropriate phase shift observable on the OSA and the overall sensitivity of the method to the dispersion characteristics of the test fiber.

The Continuous Wave (CW) Method:

The measurement of the phase shift due to SPM is done using the technique described in Reference 3. The technique uses two tunable, external cavity lasers (ECL), that are tuned closely together, to generate a beat signal from the two optical frequencies. At high power levels, SPM side lobes are generated and the side lobe phase relative to the original signal phase is measured as a function of power.

The method is very simple, in that the lasers are operated CW, thus no intricate timing or short pulse generation is needed. The two ECLs are combined through fiber couplers, and their polarization aligned using fiber polarization rotators. The combined signals are then amplified by a high power erbium amplifier and injected into the test fiber. The output from the fiber under test is monitored using an Optical Spectrum Analyzer (OSA). The experimental arrangement is shown the following figure.

N_2/A_{eff} Measurement

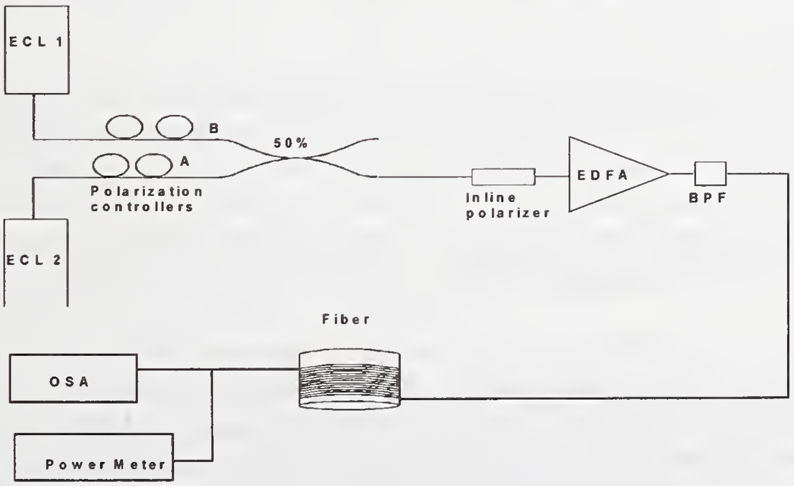

The method is also very versatile in that very long lengths of fiber are not required to observe the SPM effect. Thus, short fiber lengths are used, allowing measurement of fibers with very high dispersion, e.g., dispersion compensating fiber (DCF). The phase shift is calculated for various input powers, and a plot of phase shift vs. optical power gives the value of N_2/A_{eff}.

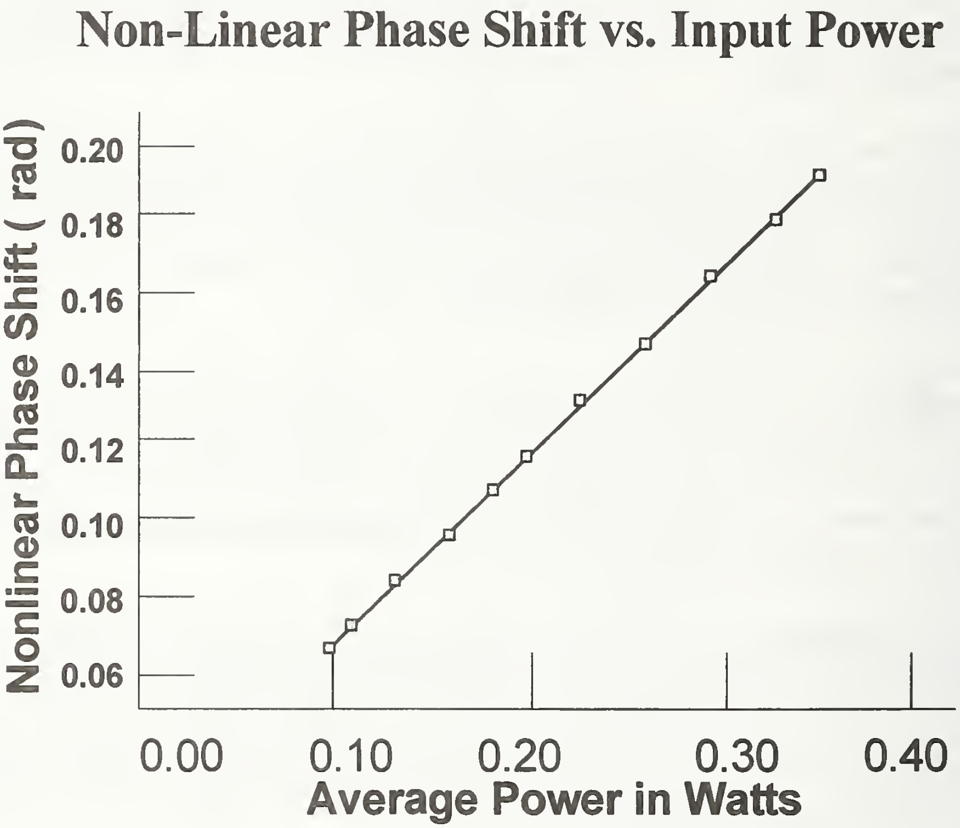
Non-Linear Phase Shift vs. Input Power

Discussion of the Methods:

The entire problem of measuring N_2 with either method can be reduced to the problem of managing the dispersion of the test fiber. Historically, the short pulse method was first used because one could easily generate short pulses of a few 10s of ps, even if high powers were not readily available. Thus, very long lengths of fiber were used, sometimes on the order of 10 to 20 km. In order to keep the total dispersion low in the test fiber, one had to operate near lambda zero or the pulse would broaden sufficiently in the fiber and reduce the observed effect.

In the short pulse method, as long as there are no appreciable dispersive effects, the phase shift is easily seen on the OSA and a plot of phase shift vs. power gives the desired slope of N_2/A_{eff}. However, if there are any dispersive effects, then sophisticated computer modeling needs to be done to recreate the observed spectrum to determine the non-linear conditions. The recent availability of high power erbium amplifiers has eased this problem considerably, and allowed researchers to measure fibers far away from lambda zero (such as in dispersion compensating fibers), and use shorter lengths in order to manage the total dispersion.

In the CW method, reasonably high power tunable CW sources are readily available. Coupling these with a high power erbium amplifier makes the set-up very straightforward. The difference in the CW technique compared to the short pulse technique is that one does not determine the phase shift directly, but measures the phase of the side lobes generated from the beat signal.

The ratio of the side lobe intensity to the fundamental (I_0/I_1) is related to the non-linear phase shift, Φ_{spm} through Bessel functions of the nth order J_n:

$$\frac{I_0}{I_1} = \frac{J_0^2(\Phi_{spm}/2) + J_1^2(\Phi_{spm}/2)}{J_1^2(\Phi_{spm}/2) + J_2^2(\Phi_{spm}/2)}$$

Several efficient algorithms exist for performing the inversion of this function that enables the phase shift to be calculated from the measured values of I_0/I_1.

To manage the dispersion in the CW method, the following condition should be satisfied:

$$2\,\pi\, C\, (\Delta\lambda_0/\lambda)^2\, \Phi_{spm}\, L\, D << 1$$

where L is the fiber length in km, and D is the fiber chromatic dispersion in ps/nm-km and $\Delta\lambda_0 = (\lambda_b - \lambda_a)$, or the separation between the two CW lasers. In practice one may check this condition by measuring the ratio of the side lobe to the fundamental while varying the separation between the two lasers. When that intensity ratio is constant, one is inside the dispersion envelope, i.e. when the separation between the two CW lasers becomes too large, the ratio of the side lope to the fundamental will “fall off” as the separation is increased.

One of the most important parameters to determine in either method is the measurement of the optical power. While the CW method does not directly measure the phase shift, the short pulse method does not directly measure the peak power. Both techniques measure the average power, and an accurate and calibrated power meter is essential for both techniques. In the short pulse method, the peak power is determined from the measured average power, the pulse repetition rate, and the measured pulse width. Even with fast detectors available today, the short (10s of ps) pulses require that the detector response (rise and fall times) be de-convolved from the measured pulse width to get an accurate determination of the true pulse width in order to calculate the peak power.

Another consideration in the CW method is the need to avoid stimulated Brillouin scattering at high power levels. This limits the about of power that can be injected into the fiber and can easily be monitored using a 1% coupler at the input.

Finally, one sees that it is the value of N_2/A_{eff} that is directly measured, and that if one wants knowledge of N_2 itself, one needs an independent measurement of the effective area, A_{eff}. The effective area is usually determined from the far field scanning method or the variable aperture method.

For completeness, it should be noted that the non-linear index has also been measured using four wave mixing (4) and Cross Phase Modulation (5) but are not covered in detail in this paper.

References:

1) "Measurement of the nonlinear index of silica-core and dispersion shifted fibers," K.S. Kim, R. H. Stolen, W. A. Reed, K.W. Quoi, Optics Letters, Vol. 19 pp-257-259, Feb. 1994.

2) "Non Linear Index Measurement by SPM at 1.55 µm," R. H. Stolen, K.S. Kim, S. E. Evangelides, G.T. Harvey, W. A. Reed, OFC '95, San Diego, CA, Feb 1995, paper FD1.

3) "Direct continuous-wave measurement of n_2 in various types of telecommunication fiber at 1.55 um", A. Boskovic, S. V. Chernikov, J.R. Taylor, L. Gruner-Nielsen, and O.A. Levring, Optics Letters, Vol 21, No. 24, Dec. 15, 1996 pp. 1966-1968.

4) "Measurement of fiber nonlinear Kerr coefficient by four-wave mixing", L. Prigent and J.P. Hamide, IEEE Phot. Tech Lett, Vol. 5 pp 1092-1095, 1995

5) "Measurement of nonlinear refractive index in optical fibers by cross phase modulation method using depolarized pump light," Optics Letters, Vol 20, pp 988-990, May 1995

Acknowledgements:

I would like to acknowledge helpful discussions and guidance from Alexander Robayo, of Tyco Submarine Systems Labs, Jerry Cline of Corning Inc., Igal Brener of Tellium Co., and Roger Stolen, of Virginia Tech.

Measurement Conditions of Nonlinear Refractive Index n_2 for Various Single-Mode Fibers by CW Dual-Frequency Method

Kazuhide Nakajima, Takuya Omae and Masaharu Ohashi
NTT Access Network Service Systems Laboratories
Tokai, Ibaraki, 319-1193 Japan

Abstract

The measurement conditions of the cw dual-frequency method based on self-phase modulation (SPM) is investigated theoretically for single-mode fibers, dispersion-shifted fibers, and dispersion compensating fibers by solving the nonlinear Schrödinger equation. The effect of the chromatic dispersion on the estimation of nonlinear refractive index n_2 is clarified. It is also shown that suitable fiber length depends on the dynamic range in the measurement system.

1. Introduction

Optical fiber nonlinearities can represent a serious drawback in dense WDM systems with optical amplifiers. The nonlinear refractive index of the fiber is one of the very important parameters in designing such transmission systems. Until now, there have been many reports on test methods of nonlinear refractive index n_2 using nonlinear effects such as self-phase modulation (SPM)[1]-[2], cross-phase modulation (XPM) [3] and modulation instability (MI)[4]. SPM method is based on the phase shift due to SPM by using continuous wave (cw) [1] or short pulse [2]. In particular, cw dual-frequency method based on self-phase modulation is simple in estimating n_2. However, measurement conditions such as fiber length and input power have not been clarified.

In this paper, we investigate the measurement conditions of the cw dual-frequency method for various single-mode fibers by solving the nonlinear Schrödinger equation. Moreover, we clarify the effect of chromatic dispersion on the estimation of the nonlinear refractive index n_2.

2. Theoretical Background

When two intense optical signals at frequencies ω_a and ω_b propagate in a single-mode fiber, self phase modulation (SPM) in the fiber acts on the beat envelope to create sidebands in the frequency domain. The ratio of intensities (I_0/I_1) of the fundamental frequencies and the sidebands is related to the nonlinear phase shift, which allows the nonlinear coefficients (n_2/A_{eff}) to be calculated. The ratio I_0/I_1 is related to the nonlinear phase shift ϕ_{SPM} through Bessel functions as [1]

$$\frac{I_0}{I_1} = \frac{J_0^2(\phi_{SPM}/2) + J_1^2(\phi_{SPM}/2)}{J_1^2(\phi_{SPM}/2) + J_2^2(\phi_{SPM}/2)}. \tag{1}$$

The nonlinear phase shift is expressed as

$$\frac{\phi_{SPM}}{2} = \frac{2\pi}{\lambda}\frac{n_2}{A_{eff}} L_{eff}\overline{P}, \tag{2}$$

where $\lambda=(\lambda_a+\lambda_b)/2$, P is the average input power, and L_{eff} is the effective length given by

$$L_{eff} = \frac{1-e^{-\alpha L}}{\alpha}, \qquad (3)$$

where L is the fiber length and α is the optical loss at wavelength λ.

In this measurement principle, the effect of chromatic dispersion is neglected and the following condition must be satisfied [1]:

$$2\pi c(\Delta\omega_0/\omega)^2\phi_{\mathrm{SPM}}LD << 1, \qquad (4)$$

where $\Delta\omega_0=(\omega_a-\omega_b)$.

It is difficult to estimate the suitable measurement conditions from Eq. (4), in particular, suitable fiber length, for various single-mode fibers.

3. Simulation Results

In order to clarify the measurement conditions for various kinds of single-mode fibers, we solved the generalized nonlinear Schrödinger (NLS) equation describing a propagation of signals in the optical fiber using split-step Fourier method. [5]

In simulations, measurement conditions for the conventional single-mode fibers (SMF), dispersion-shifted fibers (DSF) and dispersion-compensating fibers were investigated. Their fiber parameters used in the calculations are listed in Table 1. The channel spacing of two signals was chosen to be 0.3 nm.

Table 1 Fiber parameters

Parameter	SMF	DSF	DCF
A_{eff} (μm^2)	80	45	20
$n_2 \times 10^{20}$ (m/W)	2.28	2.4	2.7
Chromatic dispersion (ps/km/nm)*Note1	16	*Note 2	-80.0
Dispersion slope (ps/km/nm^2)	0.057	0.071	-1.0
Optical loss (dB/km)	0.21	0.21	0.4

Note1: Wavelength is 1550 nm. Note 2: Chromatic dispersion ranges from 0 to 10ps/km/nm.

Figure 1 shows the relationship between input power P and power ratio I_0/I_1 for the DSF with a dispersion of 5 ps/km/nm. It is found that the power ratio I_0/I_1 decreases as the input power increases. The phase shift due to SPM was calculated by solving the equation (1), in which we substitute the power ratio I_0/I_1 as shown in Fig. 1.

The relationship between the input power and the phase shift is shown in Fig. 2. It is found that the phase shift due to a small power change increases as the input power P increases for longer fibers. On the other hand, for shorters fiber, the phase shift is in proportion to the input power P.

Figure 3 shows the relationship between the input power P and relative error of the nonlinear refractive index n_2. It is seen that for the higher input power or lower input power, the relative error increases. This is because the modulation instability occurs at higher power. It is also found that the relative error increases with increasing fiber length L.

Next, we calculated the suitable fiber length to estimate the nonlinear refractive index with a relative error of less than 5 % as shown by the solid curve in Fig.4. Here, we define the dynamic range as the power range, which means the power difference between signals and sidebands. We can not estimate the nonlinear refractive index accurately if the dynamic range of the measurement system is smaller than the power ratio. The dynamic range is critical for the estimation of n_2. The relationship between input power and fiber length is also shown in Fig. 4. It is seen that the required fiber length depends on the dynamic range in the measurement system.

Figure 5 shows the relationship between input power P and fiber length for the DSFs with various dispersion values. It is found that the required fiber length depends on the dispersion value. As the dispersion increases, the required fiber length decreases. It is also seen that the appropriate fiber length with a dispersion of less than 10 ps/km/nm is from 1 to 2 km for the dynamic range of 40 dB.

Figure 6 shows the fiber length plotted as a function of input power P for the SMF and DCF. Both fibers have large dispersion values compared with the DSF. It is seen from Fig. 6 that the measurable area of DCF is amaller that that of SMF.

As a result, the appropriate conditions for n_2 estimation are summarized in Table 2.

Table 2 Measurement conditions of n_2 estimation for SMF, DSF and DCF

Fiber	$\Delta\lambda$ (nm)	Fiber length (km)	Average input power P (mW)	Dynamic range (dB)
SMF	0.3	0.5 - 1	20	40
DSF	0.3	1-2	20	40
DCF	0.3	0.1-0.15	20	40

4. Conclusions

The measurement conditions of the cw dual-frequency method based on SPM have been investigated theoretically by solving the nonlinear Schrödinger equation using split-step Fourier method. It has been clarified that the measurement conditions can be determined from the fiber length, average power and dynamic range.

Acknowledgments The authors thank K. Tajima and K. Kurokawa for fruitful discussion and T. Horiguchi for continuous encouragement.

References

[1] A. Boskovic, S. V. Chernikov, J. R. taylor, L. Gruner-Nielsen and O. A. Levring, Opt. Lett., vol. 21, pp. 1966-1968, 1996.
[2] R. H. Stolen and Chinlon Lin,Phy. Rev., vol. 17, pp.1448-1453, 1978.
[3] A. Wada, T. O. Tsun, and R. Yamauchi, Proc. ECOC'93, paper MoB1.2, Berlin 1993.
[4] M. Artiglia, B. Ciaramella, and B. Sordo, Electron. Lett., vol. 31, pp. 1012-1013, 1995.
[5] G. P. Agrawal, Nonlinear Fiber Optics, 2nd Edition. New York: Academic Press, 1995.

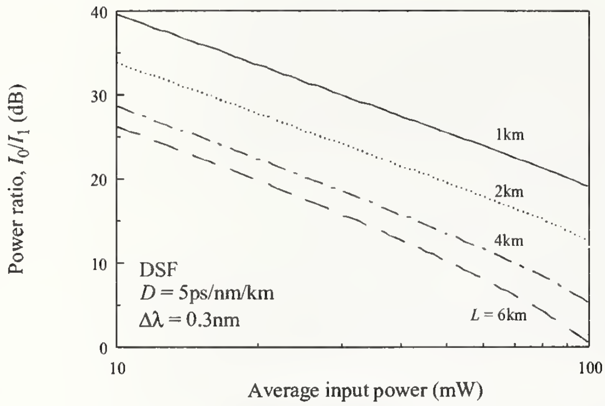

Fig. 1 Relationship between input power and power ratio (I_0/I_1)

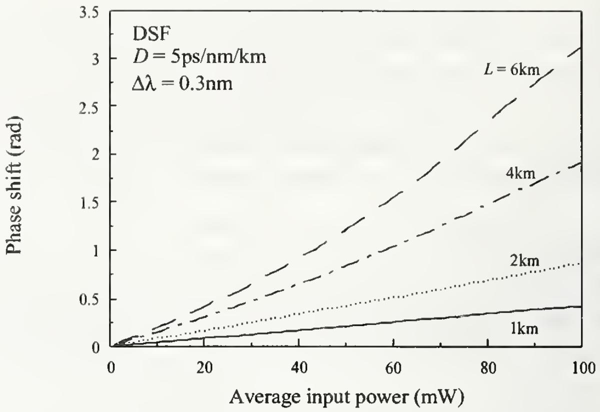

Fig. 2 Relationship between input power and phase shift

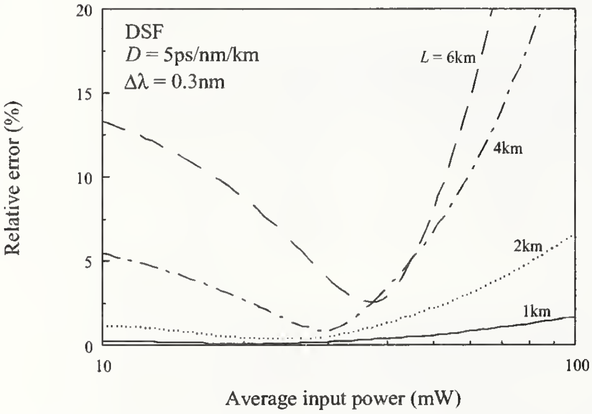

Fig. 3 Relationship between input power and relative error

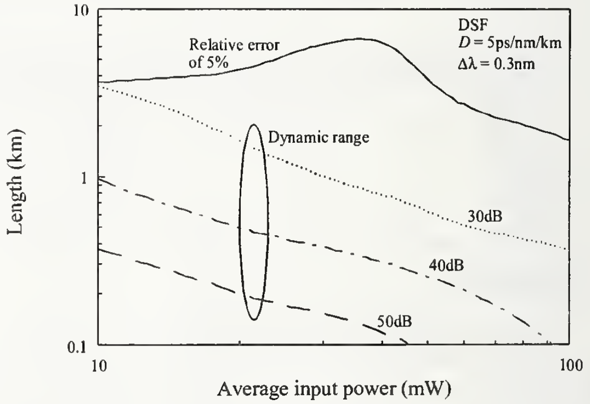

Fig. 4 Relationship between input power and fiber length

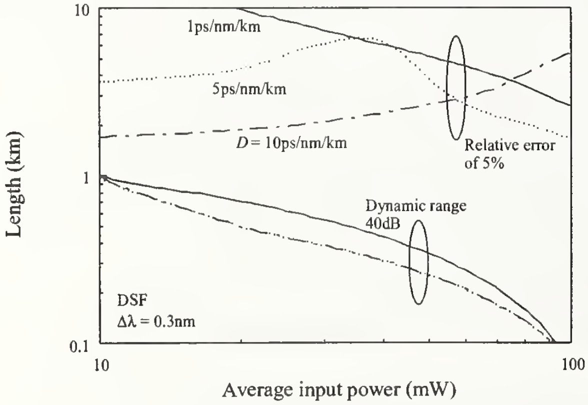

Fig. 5 Meaurement conditions for DSF with various dispersion values

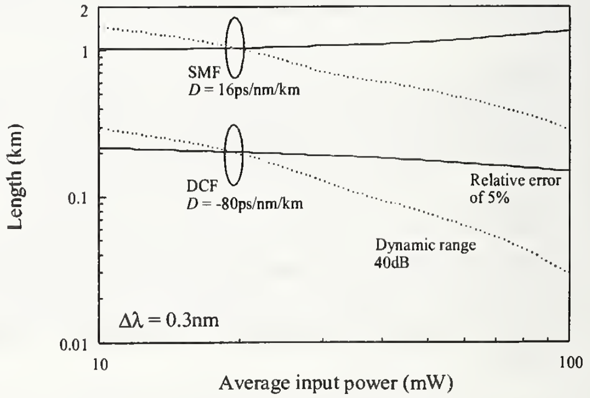

Fig. 6 Meaurement conditions for SMF and DCF

KDD Nonlinear Coefficient Round Robin Measurements for various Dispersion Shifted Fibers in Japan and UK

Yoshinori Namihira

KDD R&D Laboratories Inc.
2-1-15 Ohara, Kamifukuoka, Saitama 356-8502, Japan

Introduction: Optical nonlinearites limit the maximum transmitted power through optical fibers and they have become a serious problem in ultra-long distance transmission systems using Er-doped fiber amplifiers (EDFAs) such as trans-oceanic optical fiber undersea cable systems. Therefore, accurate determination of the nonlinear coefficient {(n_2/A_{eff}); n_2 is the nonlinear refractive index, A_{eff} is the effective area [1,2]} of optical fibers is required for the amplified optical transmission systems. To date, the nonlinear coefficient of the optical fibers have been measured by using the self-phase modulation (SPM) method with a pulsed laser diode (LD) [3-8], and the SPM method with dual continuous wave (CW)-LDs [9-11], the cross-phase modulation (XPM) method [12,13] and the four-wave mixing (FWM) method [14] at 1550nm.

Heretofore, intercomparison of (n_2/A_{eff}) measurements in various dispersion shifted fibers (DSFs) at 1550nm have been reported by COST-241[15], and KDD and Imperial college [16].

Recently, KDD round robin (n_2/A_{eff}) measurements in Japan and UK for various DSFs coordinated by KDD R&D Labs. (Y. Namihira) have been successfully performed [17,18].

This paper presents KDD (n_2/A_{eff}) round robin measurements in Japan and UK for DSFs, non-zero DSF (NZDSF) and large effective area DSF (LEDSF) using two kinds of SPM methods with pulsed-LD [3-8] and dual CW-LDs [9-11], and XPM method [12,13] at 1550nm regions.

Experiments: The experimental set-ups of the (n_2/A_{eff}) measurements for the various DSFs are shown in Fig.1. In Fig.1, (a), (b) and (c) are SPM method with a pulsed-LD, SPM method with dual CW-LDs, and XPM method, respectively. Here, n_2 can be estimated by (n_2/A_{eff}) multiplying the A_{eff}. The A_{eff} was measured by the far-field scan (FFS) technique [19].

The five test samples prepared by KDD as shown in Table 1 were circulated to the five Laboratories ; KDD R&D Labs., Imperial College (UK), Fujikura, Furukawa, and Sumitomo. The DSF1, DSF2 and LEDSF were fabricated by the VAD technique in Japan, and the DSF3 was fabricated by the MCVD technique in USA, and the NZDSF was fabricated by the OVD technique in USA.

SPM method with a Pulsed-LD: In Fig.1(a), as a pulsed-LD, mode locked-LD[3,4], gain switched DFB-LD[5-6], and transform limited (TL) Gaussian pulse-LD[7,8] were used.

The output optical pulse due to SPM was measured by the optical spectrum analyzer (OSA). As the input optical power increases, the maximum phase shift increases in proportion to the input peak power. The (n_2/A_{eff}) can be obtained from the numbers of peaks in the SPM broadened spectra [1].

SPM method with dual CW-LDs : In Fig.1(b), the optical beat signal was derived from dual CW-LDs operating at around 1550nm [9-11]. The beat signal was then amplified in a preamplifier (EDFA1) and transmitted through a optical band pass filter (OBPF) to suppress the amplified stimulated emission and a polarizer to a following high power erbium amplifier (EDFA2). The polarization controllers (PC) was used to ensure identical polarization and equal intensities of the two frequencies. The amplified beat signal was then directed into fiber under test (FUT) via a variable optical attenuator (OATT), which was used to control the input power. Both the launched power and the spectra were monitored with an accurately calibrated optical power meter (OPM) and an OSA.

XPM method: In Fig.1(c), the probe signal power is set relatively weak so that (n_2/A_{eff}) in FUT is dominantly caused by amplified strong pump CW-LD through XPM and that the effect of SPM is negligible [12,13]. When pump CW-LD or CW-SLD [13] is modulated in its intensity, probe CW-LD is modulated in this phase through XPM [12,13]. Therefore, (n_2/A_{eff}) can be determined by measuring frequency components induced by phase modulation with the self-delayed heterodyne detection technique while changing pump power [12,13].

Results and Discussions: The KDD nonlinear coefficient round robin measurements in Japan and UK measurements at random polarization states (RP) using SPM method with a pulsed-LD, SPM method with dual CW-LDs, and XPM method for DSFs, NZDSF and LEDSF at 1550nm are summarized in Table 1. Here, DL [ps/nm] is the product of chromaric dispersion D [ps/nm-km] and fiber length L [km] [8] Also, $n_2(RP) = \eta n_2(LP)$, $\eta=8/9$ for SPM[20,21], and the correction factor $\eta=2/3$ for XPM[13] were used. LP represents linear polarization states.

Fig.2 shows the one standard deviation (σ) spread among the optical fiber types used in the KDD round robin measurements. The offsets from average value (%) and nominal average values of (n_2/A_{eff}) and n_2 are shown in Tables 2 and 3, respectively. From Fig.2, Tables 1 and 2, it was found that measurement spreads of (n_2/A_{eff}) values of conventional DSFs were less than +/- 8 %. On the other hand, the values of NZDSF and LEDSF were larger than that of the DSFs. It can be considered that DL of DSF is less than 4.0 [ps/km], but that of NZDSF and LEDSF are greater than 7.0 [ps/km] and 11.0 [ps/km].

Fig.3 indicates the one standard deviation (σ) spread among the measurement methods (participants). From Fig.3 it was found that measurement spreads of (n_2/A_{eff}) values of XPM method were less than +/- 7 %. Meanwhile, the values of SPM methods with a pulse-LD (P-SPM) and dual CW-LDs (CW-SPM) were larger than that of the XPM method. It can be considered that there is no effect of chromatic dispersion in fiber length (DL) in the XPM, but two SPM methods were found to be strongly affected by the DL [8]. From Table 1, it is confirmed that DL of DSF is less than 3.6 [ps/km], but that of NZDSF and LEDSF are greater than 6.5 [ps/km] and 10.5 [ps/km], respectively.

From Tables 2 and 3, it was found that the averaged values of (n_2/A_{eff}) and n_2 at RP of DSFs were ~4.71 x 10^{-10} [1/W] and ~2.27 x 10^{-20} [m^2/W], respectively. Also, the averaged values of (n_2/A_{eff}) and n_2 at RP of NZDSF and LEDSF were ~3.95 x 10^{-10} [1/W], ~2.18 x 10^{-20} [m^2/W], and ~2.75 x 10^{-10} [1/W], ~2.05 x 10^{-20} [m^2/W], respectively. The averaged n_2 values of ~2.27 x 10^{-20} [m^2/W] of DSFs at RP is in good agreement with that of 2.1 - 2.3 x 10^{-20} [m^2/W] range of published results of the SPM method with a pulsed-LD [5-8,16-18], and SPM method with dual CW-LDs [9-11,16-18] and FWM [14] method, respectively.

Conclusions: From the KDD nonlinear coefficient round robin measurements in Japan and UK for various dispersion shifted fibers (DSFs), the measured values of (n_2/A_{eff}) and n_2 using two SPM methods and one XPM method were found to be in good interlaboratory agreement within the limits of chromatic dispersion in fiber length DL is less than ~ 4 [ps/nm]. It was confirmed that the averaged values of (n_2/A_{eff}) for DSFs, NZDSF, and LEDSF at random polarization state were ~ 4.7, ~ 4.0 and ~ 2.8 x 10^{-10} [1/W], respectively.

***Acknowledgement*:** The author express special thanks to the following organizations; KDD R&D Labs., Imperial College (UK), Fujikura, Furukawa and Sumitomo for testing in support of the KDD Round Robin (n_2/A_{eff}) measurements in Japan and UK.

***References*:**

[1] R. H. Stolen et al., Phys. Rev. A14, pp.1448-1453, 1948.
[2] Y. Namihira, Electron. Lett., vol.30, no.3, pp.262- 263, 1994.
[3] K. S. Kim et al., Optics Lett., vol.19, no.14, pp.257-259, 1994.
[4] R. H. Stolen et al., JLT, vol.16, no.6, pp.1006-1012, 1998.
[5] Y. Namihira, Electron. Lett., vol.30, no.14, p.1171, 1994.
[6] H. Nakamura et al., IEICE, Tech. Rep. OCS95-81, p.29, 1995.
[7] Y. Namihira, OFMC'97, NPL, Teddington, UK, pp.50- 53, 1997.
[8] Y. Namihira, SOFM'98, NIST, Boulder, Co. USA, pp.83-86, 1998.
[9] A. Boskovic et al., Optics Lett., vol.21, no.24, pp.988-990, 1996.
[10]A. Nihonyanagi et al., IEICE, Nat.Conv.Rec.B-10-164,p.525, 1999.
[11] T. Ajchareeyasoontorn et al.,IEICE, N.C. R , B-13-19,p.623, 2000.
[12] A. Wada et al., ECOC'92, Berlin, Germany, pp.45-48, 1992.
[13] T. Kato et al., Optics Lett., vol. 20, no. 9, pp.988-990, 1995.
[14] L. Prigent et al., PTL, vol.5, no.9, pp.1092-1095, 1993.

[15] A. Fellegara et al, Electron. Lett., vol.33, no.13, p.1168, 1997.
[16] Y. Namihira et al., OFMC'99, Nantes, France, p.66, 1999.
[17] Y. Namihira et al., OECC2000, 14C4-5, Makuhari Messe, Chiba, Japan, July, 2000.
[17] Y. Namihira, ECOC2000, Session 8.2.5, Munich, Germany, September, 2000.
[19] Y. Namihira et al., IEICE, Tech. Rep. OFT 99-4, 1999.
[20] S. G. Evangelides et al., JLT, vol., 10, no. 28, pp. 28-35, 1992.
[21] S. V. Chernikov et al., Optics Lett., vol., 21, no. 19, p.1559, 1996.

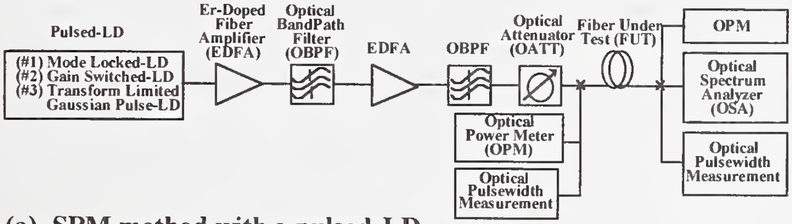

(a) SPM method with a pulsed-LD

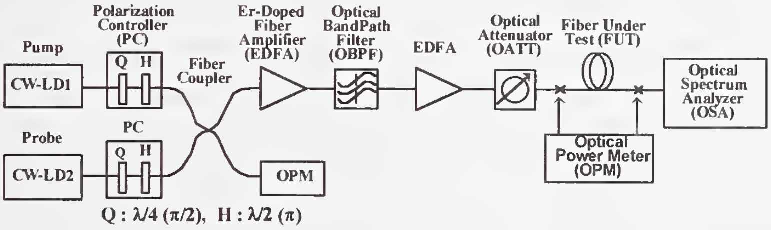

(b) SPM method with dual CW-LDs

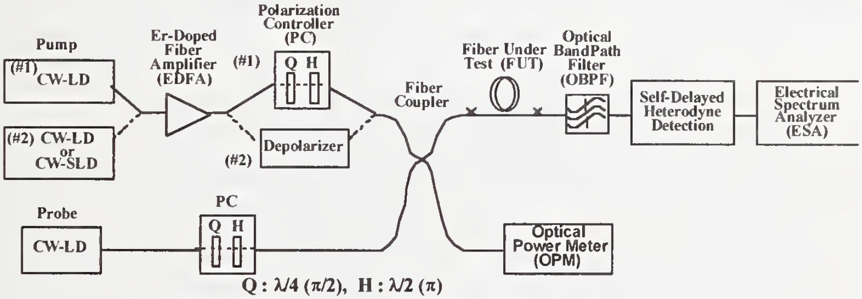

(c) XPM method

Fig.1 Experimental set-ups for nonlinear coefficient (n2/A*eff*) measurements.

Table 1 Fiber parameters of KDD nonlinear coefficient round robin measurements

Fiber	L [km]	A*eff* [μm²] @1550 nm	D [ps/km-nm] @1550 nm	λo [nm]	So [ps/km-nm²]	DL [ps/nm] @1550 nm	Measuremt Methods
DSF1	2.46	47.10	-0.59	1558.2	0.072	-1.45	P-SPM CW-SPM
	6.99					-4.47	XPM
DSF2	2.93	45.00	-1.24	1566.4	0.075	-3.63	P-SPM CW-SPM
	6.98					-9.28	XPM
DSF3	3.27	52.10	-0.79	1560.6	0.075	-2.58	P-SPM CW-SPM
	6.99					-5.52	XPM
NZDSF	2.92	54.60	-2.23	1578.1	0.079	-6.51	P-SPM CW-SPM
	15.0					-33.9	XPM
LEDSF	2.95	73.67	-3.58	1576.1	0.133	-10.56	P-SPM CW-SPM
	5.97					-24.84	XPM

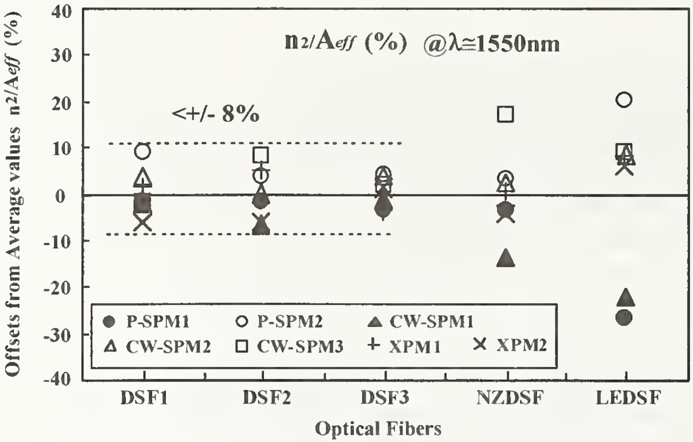

Fig.2 Measurement spread among the various optical fiber types of offsets from the average values of (n2/A*eff*)

Table 2 Offsets from average values (%) and nominal values of (n2/A*eff*)

Fiber	Offsets from Average n2/A*eff* (%)							n2/A*eff* □~10^{-10} [1/W]	
	P-SPM1 η=1.0	P-SPM2 η=1.0	CW-SPM1 η=8/9	CW-SPM2 η=8/9	CW-SPM3 η=8/9	XPM1 η=2/3	XPM2 η=2/3	Average	σ (%)
DSF1	-2.40	8.79	-2.40	3.20	-1.98	-6.34	1.12	4.83	0.24 (4.9)
DSF2	-1.83	3.61	-6.89	-0.47	7.69	-6.69	4.58	5.14	0.29 (5.6)
DSF3	-3.70	3.74	-1.78	3.26	1.82	0.86	-4.19	4.16	0.14 (3.2)
NZDSF	-4.09	3.00	-13.96	2.24	16.67	-4.34	0.47	3.95	0.37 (9.3)
LEDSF	-27.31	19.94	-22.59	7.94	8.67	5.76	7.58	2.75	0.49 (17.7)

$n_{RP} = \eta \cdot n_{LP}$, RP : Random Polarization State, LP : Linear Polarization State

Table 3 Offsets from average values (%) and nominal values of n2

Fiber	Offsets from Average n2 (%)							n$_2$ □~10^{-20} [m^2/W]	
	P-SPM1 η=1.0	P-SPM2 η=1.0	CW-SPM1 η=8/9	CW-SPM 2 η=8/9	CW-SPM 3 η=8/9	XPM1 η=2/3	XPM2 η=2/3	Average	σ (%)
DSF1	-2.50	8.87	-2.94	3.19	-0.75	-6.87	1.00	2.29	0.12 (5.0)
DSF2	-0.61	3.24	-7.47	-0.61	8.81	-7.47	4.10	2.33	0.14 (6.0)
DSF3	-3.80	3.53	-2.42	3.08	3.08	0.33	-3.80	2.18	0.07 (3.3)
NZDSF	-3.08	2.89	-14.57	1.97	18.04	-5.38	0.13	2.18	0.22 (9.9)
LEDSF	-26.24	19.68	-23.31	7.47	10.40	4.54	7.47	2.05	0.36 (17.6)

$n_{RP} = \eta \cdot n_{LP}$, RP : Random Polarization State, LP : Linear Polarization State

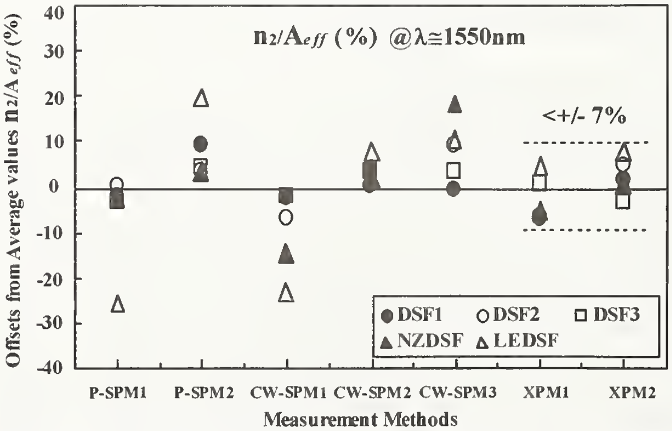

Fig.3 Measurement spread among the participants (Measurement methods) of offsets from the average values of (n2/A*eff*)

Kerr coefficient for chaotic light in optical fiber

S. M. Pietralunga, P. Martelli, M. Ferrario, and M. Martinelli*

CoreCom, Via Ampère 30, 20131 Milano, Italy

**Politecnico di Milano,Dipartimento di Elettronica e Informazione,*
P.zza L. da Vinci, 32, 20133 Milano, Italy

Nonlinear effects are becoming a central issue in optical communications, relying on the transmission of wideband amplified optical signals. In particular, the Kerr optical coefficient n_2 is the key parameter in a variety of fiber-optic nonlinear phenomena like soliton transmission, self-phase modulation (SPM) and cross-phase modulation (XPM) in WDM systems. In recent years, several detailed studies have been published, aimed at improving the knowledge of the physics governing the Kerr effect in optical fibers [1-5]. The role of different mechanisms, contributing to the effective n_2, in dependence of the wavelength and modulation bandwidth of the optical signal has been investigated. Namely, an ultra-fast electronic and a fast Raman contributions have been isolated [5], and the effect of the electrostriction has been evaluated [2,4]. The above quoted characterizations have always been performed using laser beams, which can be satisfactorily described as coherent light. No quantitative evaluation of the Kerr coefficient for light of chaotic statistics has ever been reported.

The aim of this work is to communicate the results of the direct measurement of n_2 in optical fiber for chaotic light at $\lambda = 1.55\ \mu m$ and to detail the dependence of the Kerr response on light statistics. It results a value of $n_{2p}^{Kerr} = 4.7 \cdot 10^{-16} cm^2 / W$ for polarized chaotic light, almost two times as large as the value commonly measured in the case of coherent beams.

It is well known that the dispersive and absorptive properties of the materials are related respectively to real and imaginary parts of the complex optical susceptibility function. In particular, the Kerr effect is connected to nonlinear photon absorption processes by nonlinear $\chi^{(3)}(\omega,-\omega,\omega)$ susceptibility [6-8]. Since $\chi^{(3)}$-related nonlinear absorption processes are ruled by the second-order degree of coherence $g^{(2)}(0)$ of light [9], one can expect that the photon statistics, which affects the $g^{(2)}(0)$ value, also determine the Kerr coefficient n_2. When considering transformations between real and imaginary parts of $\chi^{(3)}$ nonlinear susceptibility, it is seen that nonlinear absorption contributions are linearly transformed into their dispersive counterparts. In particular, if Two-Photon-Absorption (TPA) is made to vary, the same scaling factor must be found in the corresponding electronic contribution to the optical Kerr effect. In fact, since the TPA rates for coherent and chaotic light are different as a consequence of differences in $g^{(2)}(0)$, corresponding variations on the amount of Kerr effect should be measured.

The intensity dependent optical nonlinearity, which affects the propagation of an intense single light beam in optical fiber through SPM, is generally expressed as the superposition of three different contributions:

$$n_2 = n_2^e + n_2^R + n_2^{es}, \qquad (1)$$

representing respectively the ultrafast Kerr effect of electronic origin, the Raman contribution and the electrostrictive effect [3,4]. The electronic contribution n_2^e is the dispersive counterpart of the TPA. In dependence on the nature of light, the single beam degree of second-order coherence $g_{11}^{(2)}(0)$ assumes different expressions. Since $g_{11}^{(2)}(0)$ linearly affects the TPA rate[9], different values of second-order coherence imply different TPA absorption probabilities. In the limit of negligible TPA, the values $g_{11coh}^{(2)}(0)=1$ and $g_{11cha}^{(2)}(0)=2$ can be assumed to be valid along all the path of propagation. In turn, the electronic component of n_2 is expected to be enhanced by the photon statistics contribution to TPA. When focusing on chaotic light, it can be demonstrated that the properties of second-order coherence are also affected by the Degree Of Polarization (DOP) of the beam. In particular the value of $g_{11cha}^{(2)}(0)$ decreases from 2 to 3/2, as the DOP degenerates in passing from completely polarized to unpolarized light[9]. As what concerns the other two parts of the Kerr coefficient, the Raman-related effect can be considered to be independent on $g_{11}^{(2)}(0)$[9] and no electrostrictive contribution to the nonlinear dephasing is expected for chaotic beams, no matter how intense, because of ultrafast amplitude fluctuations characteristic of thermal light.

Therefore, the following relation between the nonlinear Kerr effect for respectively chaotic and coherent light beams is expected to hold:

$$n_2 = n_2^{Kerr}\Big|_{cha} = n_2^e\Big|_{cha} + n_2^R > n_2^e\Big|_{coh} + n_2^R = n_2^{Kerr}\Big|_{coh}. \qquad (2)$$

Moreover, independently on the nature of the light beam, the DOP of light directly affects the overall SPM mechanism. In particular, if unpolarized light is used, the Kerr effect is weighted by a numerical coefficient 5/6, while a factor 8/9 must be accounted for in case of polarized light, the state of polarization of which becomes randomized with propagation[3].

In order to measure the Kerr effect in chaotic light, SPM on a CW ASE (Amplified Spontaneous Emission) chaotic beam has been evaluated. The ASE from the cascade of two Erbium Doped Fiber Amplifiers (EDFA) has been used. The input spectrum is filtered by a bandpass filter of gaussian spectral shape and 1/e-bandwidth of 1.4 nm, centered at 1550 nm. The ASE emission is depolarized in itself and readily suitable for characterization of Kerr effect in unpolarized light. A linear optical polarizer can be inserted in order to proceed with characterizations using polarized light. The chaotic light, is then amplified by a third EDFA, sent through a variable attenuator and launched into a 8.8 Km-long Dispersion Shifted fiber coil of effective area $A_{eff}=54\ \mu m^2$, with zero-dispersion at 1550 nm. Since measurements are performed at zero dispersion wavelength, no dispersion-related phenomena are expected to seriously affect the results. The effective broadening of the ASE spectrum is evaluated using an optical spectrum analyzer which resolves $\Delta\lambda = 0.05$ nm.

An example of directly measured spectral broadening is reported in Fig. 1, where the original gaussian-filtered spectrum is compared to nonlinearly broadened ones, respectively for polarized and unpolarized light.

The experimental broadening of the ASE spectrum has been recorded at different input powers and corresponding values of the 1/e bandwidth are reported in Fig. 2. In particular, Figure 2(a) and Figure 2(b) refer respectively to unpolarized and polarized light.

Experimental results have been analyzed within the theoretical frame elaborated by Manassah [10], which gives the formal mathematical description of nonlinear SPM occurring for low-coherence optical pulses propagating in optical dispersionless fibers, characterized by a nonlinear refraction index n_2, without actually making any reference to the physical nature of this parameter, or to the dependence of n_2 in itself on light statistics. Nor any quantitative evaluation has ever been given up to now.

Nonlinear spectral broadening data are fitted by the Fourier transform of the following correlation function:

$$K(T,L) = A_o^2 \exp(-i\omega_o T)\frac{f}{\left[1+\alpha^2(1-f^2)\right]^2}, \qquad (3)$$

where A_o^2 is the intensity of the propagating field, ω_o is the spectral central wavelength, $f = \exp(-T^2/T_c^2)$ is the input gaussian correlation function for a light of initial coherence time Tc and the phase shift parameter α is related to fiber optic Kerr coefficient by $\alpha = (\omega_o n_2 A_o^2 / c)L$, where c is the speed of light.

The parameter n_2 to be considered is the effective nonlinear coefficient, taking into account the normalization factors 8/9 and 5/6 respectively for polarized and unpolarized light.

From fitting procedure, the values $n_{2u}^{Kerr} = 3.65 \cdot 10^{-16} cm^2/W$ and $n_{2p}^{Kerr} = 4.7 \cdot 10^{-16} cm^2/W$ are deduced, respectively for unpolarized and polarized chaotic light. In Fig. 2 the corresponding results are drawn as solid curves. This must be compared to the calculated dependence of expected SPM-induced broadening on beam power, as obtained by substituting the value $n_2^{Kerr} = 2.58 \cdot 10^{-16} cm^2/W$ for the Kerr coefficient in DS fibers, derived from coherent light measurements [11]. This corresponds to the dashed curves in Fig. 2, which evidently do not match experimental data.

The role played by second-order degree of coherence in defining the results can be clarified when the different contributions to the Kerr coefficient are isolated and discussed. By making reference to Eq. (2), the expression for n_2 can be detailed as:

$$n_2^{Kerr} = n_2^e + n_2^R = \tilde{n}_2(g_{11}^{(2)}(0) + \mu). \qquad (4)$$

In Eq. (4), $n_2^e = \tilde{n}_2 \cdot g_{11}^{(2)}(0)$ is the electronic contribution, scaled by the dependence of two-photon absorption on second-order photon statistics, and $n_2^R = \tilde{n}_2 \cdot \mu$ is the Raman contribution, where $\mu = 0.22$ [3]. Eq. (4) matches experimental results by assuming $g_{11}^{(2)}(0) = 3/2$ and $g_{11}^{(2)}(0) = 2$ respectively for chaotic unpolarized and polarized light, and $\tilde{n}_2(1+\mu) = 2.59 \cdot 10^{-16} cm^2/W$ which corresponds to the commonly estimated value of Kerr coefficient in Dispersion-Shifted optical fibers [11].

In conclusion, the fiber optic nonlinear Kerr effect for chaotic light has been experimentally evaluated, using a CW ASE beam at $\lambda = 1.5$ μm and its dependence on second-order photon statistics has been demonstrated. In particular, only the electronic contribution to the Kerr coefficient is enhanced by the increased second-order degree of coherence characteristic of chaotic light. This however results in an enhancement of the overall Kerr coefficient of almost a factor of two, when comparing measurements performed on coherent and polarized chaotic light. Such an enhancement is certainly significant and we think that it might contribute to refine the modeling of transmission in long-haul amplified optical fiber links.

REFERENCES

1. R. W. Boyd and E. L. Buckland, J. Nonl. Opt. Phys. Mat. **7**, 105 (1998).
2. E. L. Buckland and R. W. Boyd, Opt. Lett. **21**, 1117 (1996).

3. E.L. Buckland, *Origin of the Third-order Nonlinear Optical Response in Silica Fibers* - PhD Thesis, (UMI Co. MI Ann Arbor, 1997)
4. Melloni, M. Frasca, A. Garavaglia, A. Tonini and M. Martinelli, Opt. Lett. **23** 691 (1998).
5. S. Smolorz, F. Wise and N. F. Borrelli, Opt. Lett., **24** 1103-5 (1999)
6. D.C. Hutchings, M. Sheik-Bahae, D. J. Hagan, E. W. Van Stryland, Opt. and Quant. Electron., **24**, 1(1992)
7. P.N. Butcher and D. Cotter, *The elements of Nonlinear Optics*, (Cambridge University Press 1993), pp.174-175.
8. M. Weissbluth, *Photon-Atom Interactions*, (Academic Press, London, 1989) p. 392.
9. R. Loudon, *The Quantum Theory of Light, 2nd Ed.* (Oxford Univ. Press, Oxford, 1983).
10. J. T. Manassah, "Self-phase modulation of incoherent light revisited", Opt. Lett., **16**, 1638 (1991).
11. K. S. Kim, R. H. Stolen, W. A. Reed and K.W. Quoi, Opt. Lett., **19**, 257 (1994); A. Boskovic S.V. Chernikov, J.R. Taylor, L. Gruner-Nielsen and O.A. Levring, Opt. Lett., **21**, 1966(1996).

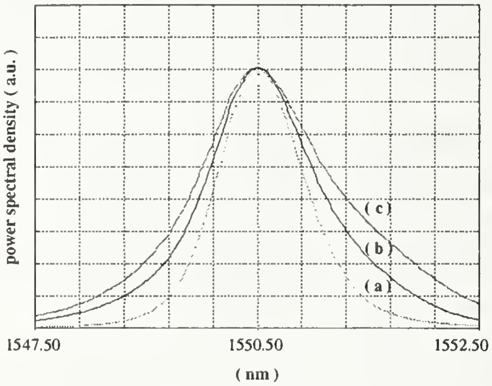

Fig. 1. Measured SPM spectral broadening of chaotic light. (a): input spectrum; (b): output spectrum in case of unpolarized ASE; (c): output spectrum in case of polarized ASE.

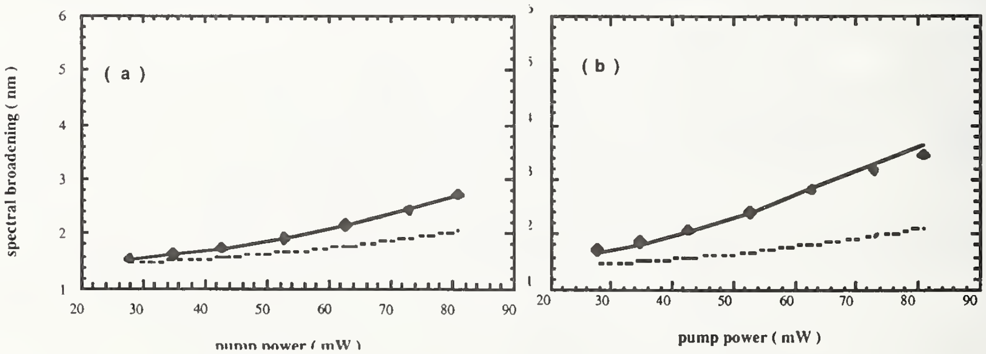

Fig. 2. Dependence of 1/e bandwidth for SPM-broadened spectra on input beam power. Experimental results are represented by isolated dots. Solid line represent theoretical previsions from Eq.(3), where the Kerr coefficient is scaled with second-order degree of coherence; dashed line represent the theoretical result in the absence of scaling. (a): unpolarized ASE light; (b): polarized ASE light.

Estimation of the Polarization Coupling Length in Standard Telecom Fibers from Measurements of Nonlinear Polarization Rotation

C. Vinegoni, M. Wegmuller, N. Gisin

Group of Applied Physics, University of Geneva,
20 Ecole-de-Medecine, CH-1211 Geneve 4, Switzerland

Abstract:

An analytical solution for the influence and strength of nonlinear polarization rotation (NPR) in an optical fiber is presented. It agrees well with our measurements of NPR in a polarization maintaining fiber, made possible by removing the much larger, fluctuating linear birefringence with a Faraday mirror. The same technique is then employed to measure NPR in standard fibers, where its dependence on the polarization mode coupling length can be exploited to get a direct estimate for this important fiber parameter.

INTRODUCTION

The potential of NPR to build ultrafast devices has been recognized a long time ago and received considerable attention since then. It has been proposed to exploit it for optical switches, logic gates, multiplexers, intensity discriminators, nonlinear filters, or pulse shapers. An inherent problem to all this applications is the stability of the output state of polarization (SOP), generally subjected to fluctuations of the linear birefringence caused by temperature changes and drafts in the fiber environment. We recently proposed a method [1] for removing the overall linear birefringence, and therefore also its fluctuations, in a passive way by employing a Faraday mirror (FM) [2] and a double pass of the fiber under test. It was also demonstrated that the nonlinear birefringence, leading to NPR, remains unaffected, i.e. the NPR of the forward and backward path add up. This allows to measure NPR both in polarization maintaining (PM) fibers and in standard fibers. However, the random variations of the intrinsic local birefringence axes in a standard fiber reduce the NPR. This reduction depends on the polarization mode coupling length h, and can be intuitively understood by examining the extreme case of a fiber with a coupling length close to zero. All orientations of the SOP with respect to the local birefringence axes will be encountered with equal probability, and as the sense of rotation of the NPR depends on exactly this parameter [1], it averages out to zero. Consequently, it should be possible to derive information about the coupling length from the amount of NPR reduction.

The paper is organized as follows: First, the analytical model developed in [1], valid for PM fibers, is reviewed and generalized for standard fibers. We then present results for NPR measurements in a PM and 2 different standard fibers, and compare them with the simulations to obtain information about the coupling length h.

THEORY

In a dielectric medium, an intense elliptical input pulse induces birefringence – via the optical Kerr effect - due to the different amounts of intensity along the major and minor axis of the polarization ellipse. It is well known that in isotropic media, this self-induced birefringence leads to a rotation of the polarization ellipse while propagating in the medium. In an optical fiber however, the situation becomes more complicated as there is also the local intrinsic birefringence to be considered. Generally, the polarization ellipse changes are hard to predict in that case as the linear and nonlinear birefringence interact in a complicated manner. Starting from the nonlinear Schroedinger equation written in the form as given by Menyuk and assuming that the linear birefringence is much larger than the nonlinear one, it is possible to show that the evolution of the polarization vector ψ is given by [1]:

$$(1) \qquad \partial_z \psi \approx i\omega B_{\text{eff}} \sigma_\theta \psi$$

where σ_θ accounts for the linear birefringence with axis θ. The amount of linear birefringence B is replaced by an effective birefringence B_{eff}, which includes the action of the nonlinear birefringence. The solution for Eq.1 is straightforward, $\psi_z = \exp(i\omega B_{\text{eff}} \sigma_\theta z)\psi_0$, and corresponds to a rotation of the input polarization vector around the linear birefringence axis σ_θ with a rotation angle β given by

$$(2) \qquad \beta = \omega B_{eff} z = \omega(B - \frac{\alpha}{2} m_\theta(0))z$$

where $\alpha = n_2 P/(3cA_{\text{eff}})$, n_2 is the nonlinear Kerr coefficient, P the power, and A_{eff} the effective area. $m_\theta(0)$ is the projection of the input SOP on the birefringent axis.

In principle the NPR can now be measured by varying the input power P and observing the corresponding change in the output SOP. However, the contribution of the nonlinear term is negligibly small compared to the linear one, and the slightest change in B will completely cover the NPR. A way out of this problem is to make a double pass of the fiber under test by means of a Faraday mirror. The linear birefringence accumulated during the forward path is thereby automatically removed on the return path. The nonlinear birefringence on the other hand does not cancel out but adds up [1]. This is because after reflection at the FM, which transforms the SOP to its orthogonal counterpart, the sense of rotation of the NPR remains the same as during the forward path.

As mentioned before, the situation is more complex in a standard fiber, and the NPR depends on the polarization mode coupling length h. To calculate the NPR for this case, we therefore resort to numerical simulations. The fiber is modeled as a concatenation of linearly birefringent trunks with length h and random birefringence axis orientation. For each of these trunks, Eq.1 still holds as for typical standard fibers (beatlength of less than 100 m), the linear birefringence is still much larger than the nonlinear one. The SOP can therefore be calculated piece by piece, with the projection m_θ being different for each new trunk. The final SOP will obviously depend on the choice of the (random) birefringence axis orientations, with variations being larger for large coupling lengths h. We therefore made 100 runs for each specific coupling length to get a mean value of the NPR.

EXPERIMENT

The experimental setup is shown in Fig.1. The light source consists of a distributed feedback laser (DFB), operated in pulsed mode at a wavelength of 1559 nm. Typically, pulses with a duration of 30 ns, a repetition rate of 1 kHz, and a peak power of up to 6 W (after amplification by an EDFA) are used. The light is then launched into the fiber under test (FUT) via a 90/10 coupler and a polarization controller (PC1). The coupler is inserted for the detection of the backward traveling light after the double pass of the FUT, with its 90% output port connected to the source in order to maintain high launch powers. The polarization controller, PC1, allows to adjust the polarization of the light launched into the FUT, which is important for the strength of the NPR as demonstrated by Eq.2. Note that for low launch powers (negligible NPR), the action of PC1 is removed by the Faraday mirror, and its setting is therefore of no importance in that case. The output SOP is examined by an analyzer consisting of a polarization controller PC2 and a polarizing beam splitter (PBS). To achieve a good sensitivity of the analyzer, it is calibrated for equal power in the two PBS output arms for low power launch signals where no NPR occurs. The two PBS output channels were monitored by a fast photodiode (200 ps response time) and a sampling scope. The measurements were then performed in the following way: for a given launch power, the polarization launched into the FUT was adjusted (PC1) to give the smallest possible output power at the monitored PBS channel. Consequently, the difference between the two PBS output channels is maximized, corresponding to a maximum value of the NPR.

RESULTS

First, a PM fiber with a length of 200 m was measured. The results are shown in Fig.2. One can see that for this fiber NPR starts to be important for launch powers above 1 W, and that in spite of the linear increase that would be experienced in the absence of NPR (straight line), the output power actually starts to decrease for input powers above 2.5 W. The measured data (squares) are then compared to the calculated values (solid curve) using Eq.1, where $m_\theta(0)$ was varied in order to give a minimum output power from the PBS channel like in the experiment. As Fig.2 shows, the agreement between measurement and model is good.

The same type of measurement was then performed for different standard fibers and compared to the corresponding simulations. The fiber lengths were typically 1 to 1.5 km, so that a large number of couplings is obtained, allowing for comparison with the mean simulation values. An example of the numerical results for a fiber length of 1.5 km is shown in Fig.3. One can see that the mean output power becomes indeed larger for smaller coupling lengths, indicating a reduced NPR.

Fig.4 shows the results for 2 standard fibers with large and small PMD. Note that for ease of comparison, the figure gives the strength of NPR, i.e. the reduction of the output power from the value without NPR. As expected, the two standard fibers exhibit an NPR that is much lower than for a PM fiber (note that the results for the PM fiber had to be rescaled to account for its different length and n_2/A_{eff} parameters). However, the amount of NPR for the two standard fibers is also distinctively different. From comparison of the experimental results with the numerically obtained data (lines), the coupling lengths can be estimated to about 75 m for the small PMD and 625 m for the large PMD fiber. A value of $h<100$ m is quite reasonable for a good (i.e. low PMD) standard fiber. The coupling length of $h \sim 600$ m for the high PMD 'standard' fiber is large, but its high PMD value of 1.9 ps/$\sqrt{\text{km}}$ could indeed indicate that there might be well defined birefringent axes in that fiber. Moreover, a different estimation for the coupling length of these fibers from PMD and beat length measurements using Optical Frequency Domain Reflectometry [3] is in good qualitative agreement with the results presented here.

CONCLUSIONS

A model and measurements of NPR in optical fibers were presented. As the amount of NPR depends on the polarization mode coupling length, we were able to retrieve this important fiber parameter by comparing the measured and numerical data.

Acknowledgements: Financial support from the Swiss OFES in the frame of the COST 265 project is acknowledged

REFERENCES

[1] C. Vinegoni, M. Wegmuller, B. Huttner, and N. Gisin "Measurement of nonlinear polarization rotation in a highly birefringent optical fiber using a Faraday mirror", *J. Optics A*, accepted for publication in 2000

[2] M. Martinelli, "A universal compensator for polarization changes induced by birefringence on a retracing beam", *Opt. Comm.* 72, 341-344 (1989).

[3] B.Huttner, J.Reecht, N.Gisin, R.Passy, and J.P. von der Weid, "Local birefringence measurements in single-mode fibers with coherent optical frequency-domain reflectometry", *IEEE Photon. Technol. Lett.*, **10** 10, 1458-1460, 1998

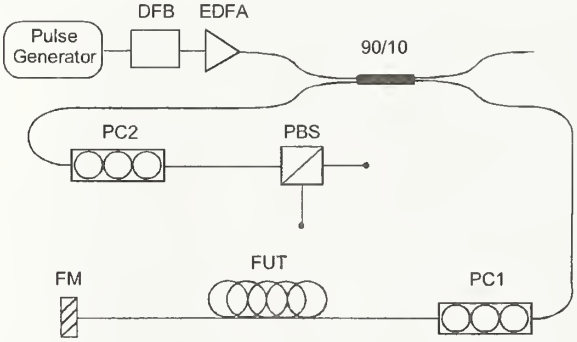

Figure 1: Experimental setup

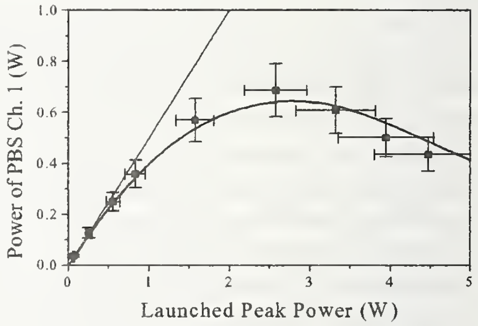

Figure 2: Minimum output power of PBS channel 1 for a 200 m long PM fiber

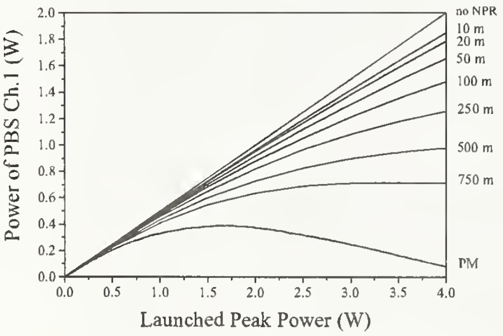

Figure 3: Numerical results for a fiber length of 1.5 km with different polarization mode coupling lengths h

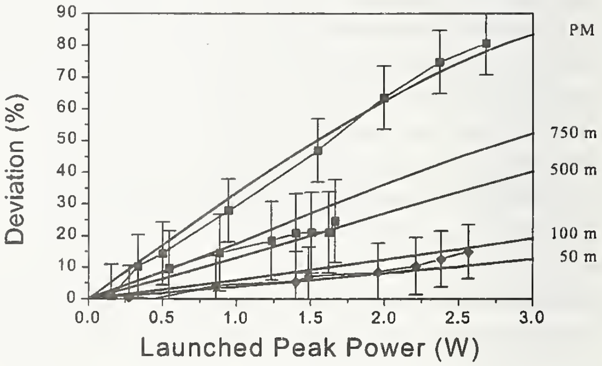

Figure 4: Experimental and numerical results of NPR strength in different fibers

A comparison of three techniques for effective area measurement of single-mode optical fibres

David A Humphreys, Robert S Billington , Andrew Parker[1]**, Brian Walker, Dominic S Wells.** *National Physical Laboratory, Teddington, Middlesex, UK, TW11 0LW, UK.*
Andrew G Hallam[2] *GN Nettest Ltd., York House, School Lane, Chandlers Ford, Hampshire S0534DG, UK*
Isabelle Bongrand Laboratoire de Physique de la Matiere Condensée (L.P.M.C), Université de Nice, Faculté des sciences, Parc Valrose, 06108 NICE CEDEX 2, FRANCE

Introduction

Non-linear effects such as four-wave mixing (FWM), self-phase modulation (SPM) and stimulated Brillouin scattering (SBS) are important considerations where intense electric fields are present in optical fibre. The effective area (Aeff) is a crucial parameter in predicting the degree of non-linear behaviour as it can be used to convert between aggregate optical power in the fibre and the intensity of the optical field.

Unlike mode-field diameter (MFD), effective area is defined only in terms of the near-field distribution of the fibre. Any technique must therefore be capable of measuring this distribution, either directly or through the use of transforms from other measurements. We compared three different techniques for measuring Aeff that have previously been used to measure MFD. These were: the direct far-field (DFF) scan, variable aperture in the far-field (VAFF) and near-field (NF) scan. We also investigated the transverse offset method (TO) but no results are presented owing to technical limitations of the measurement system.

Definition *of Effective Area, Aeff*

The effective area of an optical fibre with mode-field amplitude distribution is defined[i] as:

$$A_{eff} = \frac{2\pi\left(\int_0^\infty |E_a(r)|^2 rdr\right)^2}{\int_0^\infty |E_a(r)|^4 rdr} = \frac{2\pi\left(\int_0^\infty I(r)rdr\right)^2}{\int_0^\infty I^2(r)rdr}$$

where $I(r)$ is the intensity of the electric field of the fundamental mode at radius r from the axis of the fibre.

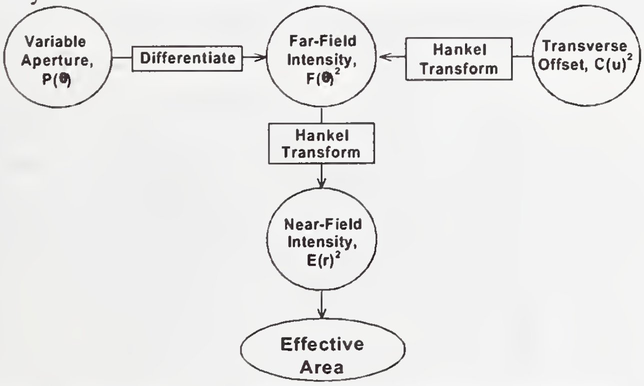

Figure 1 Relationship between the techniques used to measure the effective area

---

[1] A Parker is now with Nortel Networks, Brixham Road, Paignton, Devon, UK TQ4 7BE (parkera@nortelnetworks.com).

[2] A Hallam is now with Halcyon Optical Services, Sandridge', Winchester Road, Waltham Chase, Hants UK SO32 2LG (ahallam@halcyonos.fsnet.co.uk).

Techniques for Measuring the Mode-Field Distribution

The inter-relationship between the methods used to measure Aeff is shown in Figure 1. Clearly the near-field scan method is the most direct since the effective area can be calculated directly from the measured data. The other techniques all require some degree of numerical processing, which can introduce errors. However, once the practicalities of the measurements are taken into account, the most direct method, i.e. the near-field scan is not necessarily the best option.

Results

The effective areas of six fibres[3] were measured near 1550 nm and 1310 nm. The results are shown in Tables 1, 2 and 3 for the far-field, near-field and variable aperture methods respectively.

Table 1 - Far-Field Scan Method

	1549-nm		1309-nm	
	Aeff	Std. Deviation.	Aeff	Std. Deviation.
	(µm^2)	(µm^2)	(µm^2)	(µm^2)
AllWave®	80.94	0.23	66.39	0.13
TrueWave RS®	53.84	0.20	38.47	0.14
Matched Cladding	83.39	0.31	67.79	0.27
Dispersion Shifted	46.05	0.09	29.75	0.16
LEAF™ -'ve Dispersion	67.25	0.30	34.11	0.54
LEAF™ +'ve Dispersion	68.40	0.58	38.84	0.26

Table 2 - Near-Field Scan Method (NF)

	1549-nm		1309-nm	
	Aeff	Std. Deviation.	Aeff	Std. Deviation.
	(µm^2)	(µm^2)	(µm^2)	(µm^2)
AllWave®	80.63	0.23	66.18	0.13
TrueWave RS®	-	-	38.26	0.15
Matched Cladding	83.04	0.31	67.57	0.27
Dispersion Shifted	45.72	0.09	29.56	0.16
LEAF™ -'ve Dispersion	66.73	0.31	33.88	0.53
LEAF™ +'ve Dispersion	67.89	0.57	38.57	0.26

Table 3 -Variable Aperture in the Far-Field Method (VAFF)

	1550-nm		1310-nm	
	Aeff	Std. Deviation.	Aeff	Std. Deviation.
	(µm^2)	(µm^2)	(µm^2)	(µm^2)
AllWave®	79.44	0.70	63.68	0.53
TrueWave RS®	54.3	2.0	37.72	0.23
Matched Cladding	81.94	0.80	65.41	0.34
Dispersion Shifted	45.8	1.0	29.52	0.57
LEAF™ -'ve Dispersion	67.38	0.72	34.16	0.31
LEAF™ +'ve Dispersion	68.1	1.3	39.00	0.60

The results from these three methods can be seen to be generally in good agreement. The notable exceptions to this are the VAFF results for the AllWave® and matched cladding fibres, which are

---

[3] AllWave® and TrueWave RS® are registered marks of Lucent Technology and LEAF™ is a trademark of Corning Inc.

consistently lower than the values from the other two methods. The reason for this is the inversion of side-lobes in the far-field intensity distribution.

Not all fibre types exhibit side-lobes. However, where they appear, the amplitude of the far-field must be given the correct sign before using the Hankel transform to calculate the near-field. Failure to do so can lead to an underestimate of the effective area of typically (2 - 3) %. This is the origin of the discrepancies between the VAFF results and the DFF and NF results for the attenuation flattened and matched cladding fibres. It can be seen from Figure 3 that for VAFF measurements, the scarcity of points and the small differences in the signal level at high angles values make side-lobe identification difficult.

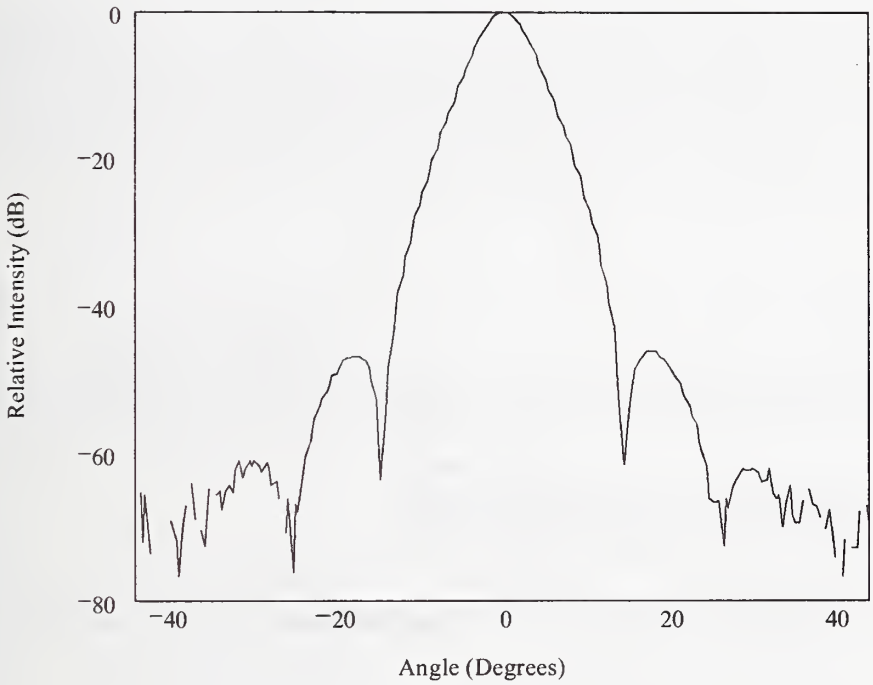

Figure 2 Example of a measured far-field intensity distribution including side-lobes. Matched cladding fibre at 1551 nm.

Summary

Three techniques have been used to measure the effective area of single-mode optical fibre. The near-field scan method is the most direct but requires an imaging system, which can introduce uncertainty through aberrations. The variable aperture method is quick and convenient but may not permit side-lobe inversion. The far-field scan method has significant advantages due to its ease of operation, repeatability and facility to invert side-lobes.

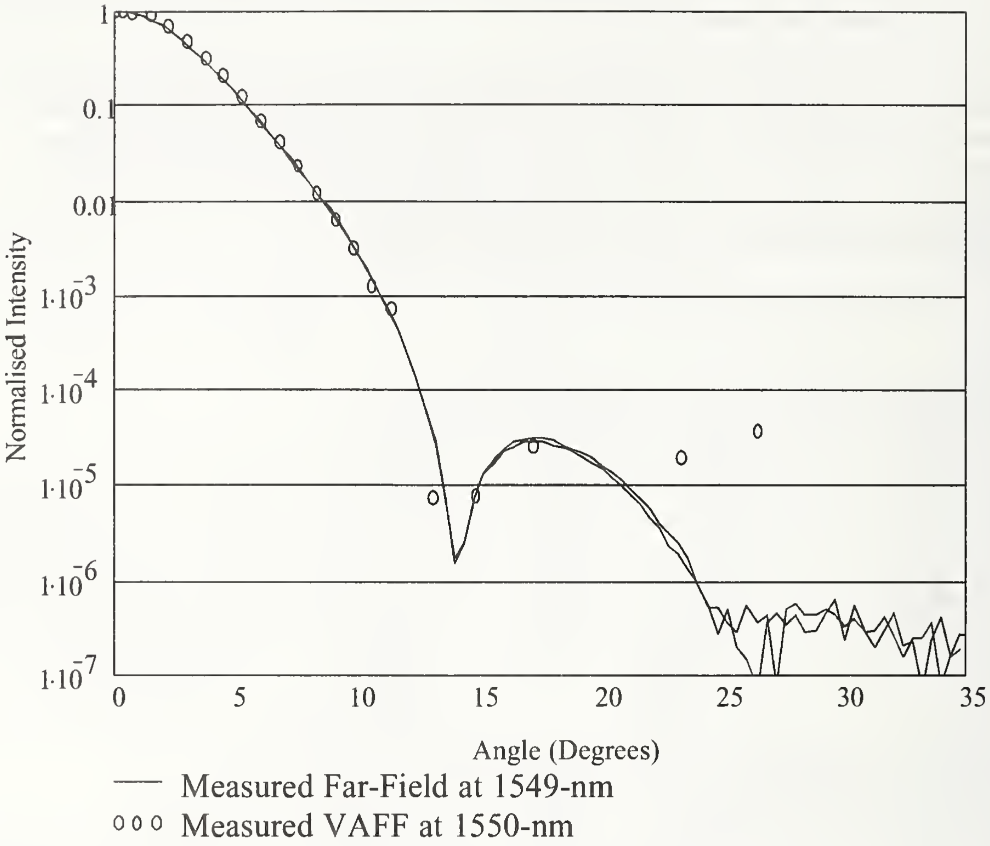

Figure 3 DFF and VAFF measurements of the far-field distribution from an AllWave® fibre.

Acknowledgements

I wish to thank The UK department of Trade and Industry for providing financial support for this work.

References

---

[1] ITU COM 15-273-E "Definition and Test Methods for the Relevant Parameters of Single-Mode Fibres - Appendix on Nonlinearities for G.650", (1996).

Model for calculation of Mode Field Diameter along the fibre using bi-directional OTDR measurements

J. Mezger, G. v. Broekhoven, P. Pleunis, R. v. Laere

Plasma Optical Fibre BV
PO Box 1136, 5602 BC Eindhoven, The Netherlands
Tel.: (+31) 40 292 38 33
E-mail: h.mezger@plasma.nl

Abstract:
A new model for the calculation of the Mode Field Diameter of Single-Mode fibres from OTDR measurements is presented. The model gives a high accuracy (s = 0.002 μm) and good information about MFD uniformity along the fibre. The model is insensitive for MFD variations of the reference fibre near the coupling to the fibre under test.

Introduction

The OTDR is becoming one of the most important measurement devices for qualifying Single-Mode fibres. Especially when the OTDR is used in combination with an optical switch, two reference fibres and two coupling devices as indicated in figure 1.

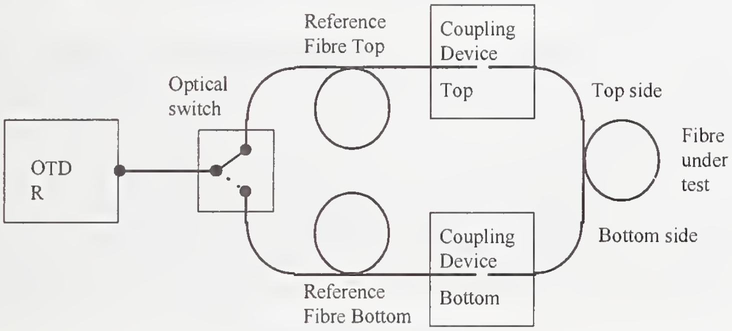

figure 1, OTDR set-up

From the OTDR trace several important parameters can be derived, not only length, attenuation and homogeneity but also parameters like Mode Field Diameter (MFD), Cut-off wavelength and even Chromatic Dispersion can be determined.

In the literature a number of contributions are presented, showing models for the calculation of the MFD using bi-directional OTDR measurements [1, 2, 3, 4, 5, 6, 7, 8, 9]. Here the MFD at the end of the reference fibres, sometimes indicated as dead-zone fibres, is used as reference.

In this contribution the model for calculation of the MFD along the fibre under test is adjusted in such a way that the reference, needed for the calculation, is placed inside one of the reference fibres at a position several hundred meters from the coupling position. As a result the used reference value is no longer dependent on re-cleaving of the reference fibre and the relatively inaccurate determination of the splice loss at the coupling is no longer necessary, which determinations are used in the methods described by ITU [8] and IEC [9].

The model calculations are directly based on differences in the OTDR signals.

The MFD of the reference fibre at the reference position is determined using the MFD model and a large number of comparative measurements between the MFD determined by the Variable Aperture

Far Field method (VAFF) and the OTDR set-up for adjustment of the parameters used in the model. These comparative measurements also guarantee a good agreement between both methods.
Using the model it appears that the repeatability of the calculated MFD at the ends of the fibres is about a factor of ten better then using commercially available VAFF measurement equipment, respectively s = 0.002 µm and s = 0.02 µm.
The result of the described technique is a useful and accurate measurement method for the MFD of Single-Mode fibres.

Theory

The MFD can be determined from the difference in bi-directional backscatter signal across a splice with a reference fibre and the fibre under test [1, 2, 3, 4, 5, 6, 7, 8, 9].
The relation can be easily adjusted to make it applicable for any position in the fibre under test and for using a reference position at a different position than the end of the reference fibre top:

$$MFD_i = MFD_r \bullet 10^{\frac{g(\Delta_T - \Delta_B) + f}{20}}$$

where:

MFD_r : MFD at reference point (inside reference fibre top) [µm]

MFD_i : MFD at point i [µm]

Δ_T : difference in backscatter signal [dB] between the reference position and the position at which the MFD is to be determined when measured from T(op) to B(ottom)

Δ_B : difference in backscatter signal [dB] between the reference position and the position at which the MFD is to be determined when measured from B(ottom) to T(op)

g : adjustment factor (wavelength and fibre design dependent)

f : adjustment factor (wavelength and fibre design dependent)

To reduce the influence of noise on the OTDR trace the OTDR signal at the reference position is obtained by averaging the OTDR signal over a distance of several hundred meter around the reference position.

Set-up

The results are obtained using commercially available OTDR's which show a good linearity. (According to manufacturer: < .04dB/dB.) The linearity can be checked by performing a bi-directional OTDR measurement on a fibre with good uniformity. There should not be any deviations from straight line visible larger than 0.01 dB which change with the measurement direction.
To avoid cross-talk between the two branches, blocking switches are added in the set-up. In this way the isolation is increased to above 120 dB. The coupling devices used are selected for their stability.

Results

The figures 2 and 3 show the comparison of the MFD obtained by a VAFF set-up and MFD calculated from OTDR measurements. Regular production measurements have been used for the comparison.
To avoid the influence of erroneous measurements, the difference between both methods should be within the limits of repeatability of the VAFF method, ± 0.1 µm. These measurements are indicated in the graph with a solid dot.

ITU and IEC propose a validation check [8, 9]. In the graphs the following information is indicated:

- the Bias (averaged difference between both methods),
- the Std. Dev. Bias (standard deviation of the differences: σ_d),
- the equivalence level or empirical accuracy (B = $|Bias| + 2\sigma_d/\sqrt{n}$, with n being the sample size),
- regression coefficient, r^2.

For both wavelengths a value of 0.005 μm is obtained for B, which is much smaller than the upper limit given by ITU and IEC, B < 0.1 μm.
The correlation between both methods is good, as is indicated by the regression coefficients, $r^2 > 0.9$.
The scatter in the graphs is mostly caused by the measurement error of the VAFF method

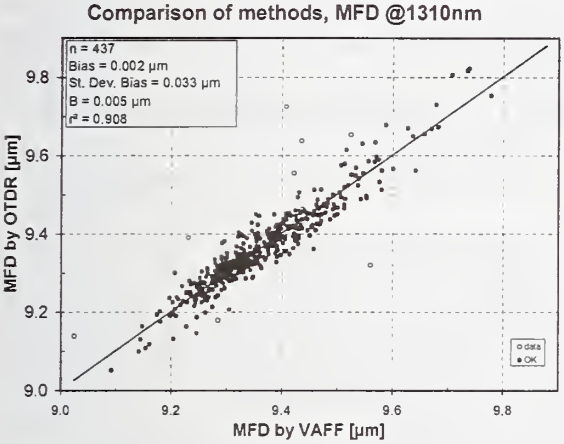

figure 2

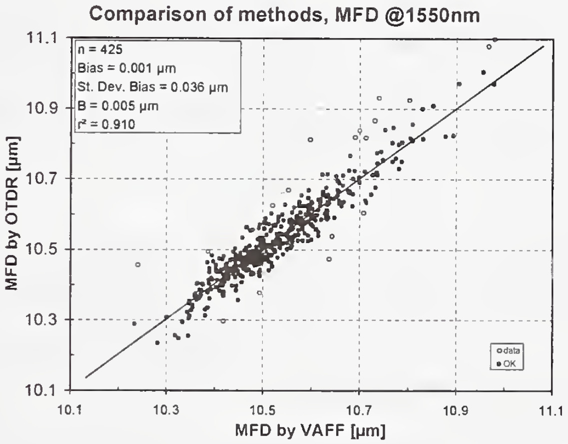

figure 3

Figure 4 shows an example of the MFD determination along the fibre for a SM fibre using an OTDR and the MFD model. The calculated MFD along the reference fibres is also indicated. It should be noted that the MFD cannot be calculated close to the splice positions (indicated by the dotted lines) as a result of the dead-zone of the OTDR.
The noise on the MFD traces is a result of the noise on the OTDR traces.
The undulation in the MFD trace is caused by small variations in fibre parameters which are well within fibre specifications.

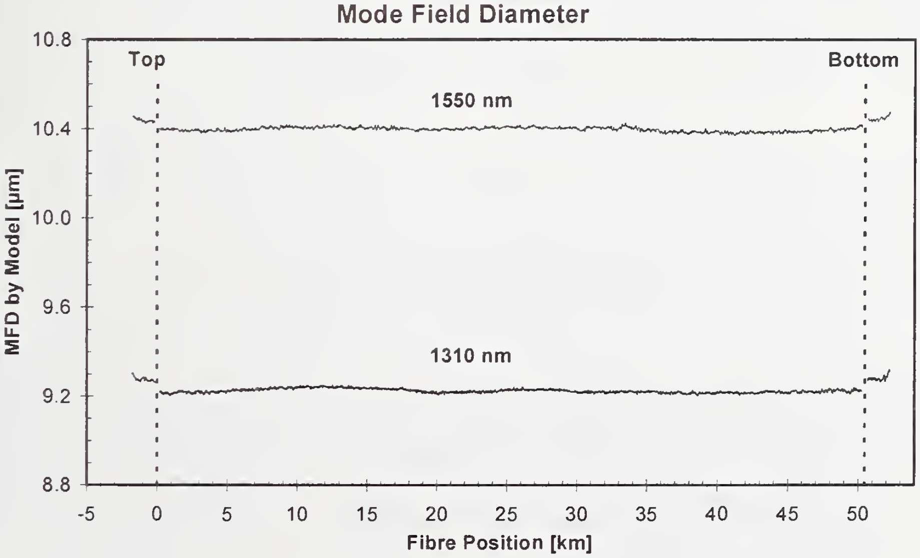

Figure 4

Conclusions

The presented model for the calculation of the MFD from a bi-directional OTDR measurement gives an accurate prediction of the local MFD.
An excellent relationship between the model and the VAFF measurement for both wavelengths is obtained.
The repeatability of the MFD at the ends of a fibre determined with the model is about a factor of ten better then using commercially available VAFM measurement equipment.

References

1. D. Marcuse; Loss Analysis of Single-Mode Fiber Splices, Bell System Technical Journal, May-June (1977).
2. P. Divita, V. Rossi; Backscattering Measurements in Optical Fibers; Separation of Power Decay From Imperfections Contributions, Electronic Letters 15. P.467, (1979).
3. M.S. O'Sullivan, R.S. Lowe; Interpretation of SM Fiber OTDR Signatures, Proceedings SPIE'86 Optical Testing and Metrology (1986).
4. K.W. Kowaliuk, J. Ferner; A Technique to Estimate the Cutoff Wavelength Profile in SingleMode Fibers Using a Switchable Dual Wavelength OTDR, Proceedings NIST '88 Symposium on Optical Fiber Measurements (1988).
5. J. Warder, C. Saravanos; Mode Field Diameter and Cutoff Wavelength Profile Measurement using Dual Wavelength OTDR, Proceedings NIST '92 Symposium on Optical Fiber Measurements (1992).
6. W.T. Anderson, Consistency of Measurement Methods for the Mode Field Radius in a Single-Mode Fiber, Journal of Lightwave Technology, Vol. LT-2 No. 2, April 1984.
7. M.J. Hackert, G.W. Loughran, Development of mode field diameter and cut-off Wavelength measurements by optical Reflectometry, Proceedings Optical Fibre Measurements Conference (1995).
8. ITU G650 - Definition and test methods for the relevant parameters of Single-Mode fibers. Clause 2.1.4. Third alternative test method for MFD. (Draft revised version, agreed April 2000)
9. IEC test method 60793-1-45, method D. (Committee draft under vote: 86A/533/CDV).

A Novel Far-Field Scanning Technique for Rapid Measurement of Optical Fiber Parameters

Jeffrey L. Guttman, Razvan Chirita, and Carmen D. Palsan
PHOTON, inc., 6860 Santa Teresa Blvd., San Jose, CA 95119
phone:408-226-1000, fax: 408-226-1025, e-mail: jguttman@photon-inc.com

Abstract: A new far-field scanning technique allows for accurate measurement of Mode-Field Diameter and Effective Area of single-mode fibers in less than 20 seconds with greater than 64 dB dynamic range. The Numerical Aperture is measured in real-time. An instrument based on this technique is described, and measurement results are presented.

1. Introduction

A new technique for rapidly scanning the far-field of optical fibers is described. The far-field data is used for computing parameters of single-mode and multi-mode fibers in accordance with the Telecommunication Industry Association/Electronic Industries Association (TIA/EIA) Standard Direct Far-Field (DFF) Methods. The Mode-Field Diameter and Effective Area of single-mode fibers is obtained in less than 20 seconds with greater than 70 dB dynamic range. The Numerical Aperture of multi-mode fibers can be obtained in real-time with up to 24 dB dynamic range.

The speed of the measurement makes it possible to test greater numbers of fibers economically. It also provides the ability to acquire statistical data, and potentially eliminate variations in measured parameters due to source fluctuations. Finally, the technique lends itself to the design of compact instruments suitable for portable field use.

2. Measurement Technique

An instrumentation system was constructed based on the measurement technique. The principle of operation of the system [1] is as follows: The end of the optical fiber under test is positioned at the axis of rotation of an optical fiber collector. The plane of rotation of the optical fiber collector is the far-field measurement plane. The collected light then propagates to a stationary InGaAs detector. The detector signal is amplified by a transimpedance amplifier followed by a voltage amplifier with a total programmable gain range of 140 dB. The amplified signal is input to an automated PC based data acquisition system. An optical encoder on the rotating collector and a phase-lock circuit provide motion control and precise angular sampling.

The distance between the end of the fiber under test and the optical collector is 6.62cm. A 500 μm diameter pinhole at the entrance to the optical collector yields a 0.43° detector field-of-view at the source. The data is acquired with an angular sampling resolution of 0.055°. The scan rate is 10 Hz, so single far-field scans are obtained in 50 ms, with updates obtained every 100ms. The system operates under control of MS Windows-based software. The scan unit dimensions are 16.5 cm x 16.5 cm x 20.3 cm (6.5 in. x 6.5 in. x 8 in.).

The far-field data is obtained by acquiring multiple high speed scans at different incremental gain settings. The data from these multiple scans are then reassembled to provide the far-field pattern in less than 20 seconds. This method makes it possible to obtain far-field profiles with dynamic range comparable to that obtained using conventional lock-in amplifier techniques, but at much higher speed. In the present system the gain ranging method allows far-field profiles to be obtained with dynamic range of 64 dB for a single-mode fiber source operating at a power level of 1mW. For a 1 Watt fiber source, the obtainable dynamic range is 94 dB.

During data acquisition, to obtain adequate signal-to-noise ratio (SNR) at each gain setting, an appropriate number of averages are used. When the individual scan data is reassembled to obtain the final profile, an algorithm is used for detection of amplifier saturation and rejection of invalid data.

3. Measurement Results

Measurements were made using a Fabry-Perot laser diode source operating at a nominal wavelength of 1300 nm and output power of 2 mW. A typical far field profile obtained for a sample single-mode fiber is shown in Figure 1. The data shows the complete scan range from -90° to +90° with signal amplitude ranging over 9 decades. Two sets of cusps are clearly defined, and two more cusps can be seen where the signal approaches the background noise level at the 0.1 amplitude level.

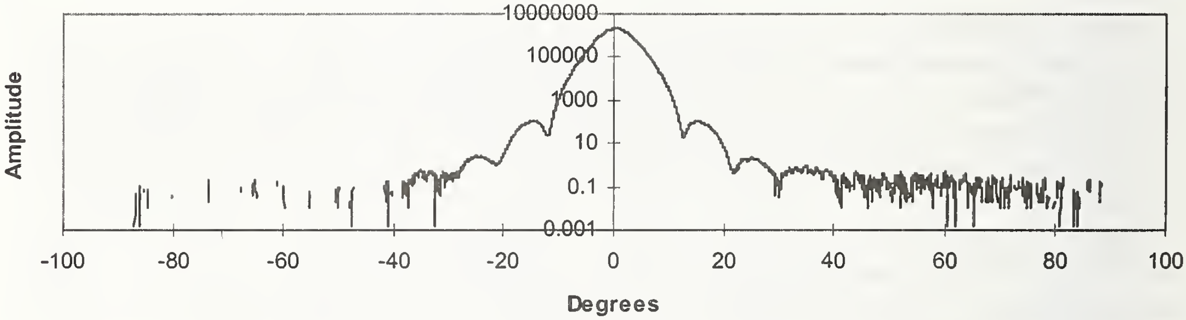

Fig. 1. Far-field profile of a single-mode optical fiber obtained with the new instrument.

The Mode-Field Diameter (MFD) is calculated using the Petermann II Integral in accordance with the TIA/EIA Standard DFF Method given in FOTP-191[2], with slight modification. In particular, the data is translated in angle by the centroid of the measured distribution. Also, the data is not folded. Instead, the integral is calculated for both negative and positive theta angles. The Effective Area, (A_{eff}) is calculated according to the TIA/EIA Standard DFF Method of FOTP-132 [3], using a threshold algorithm to eliminate noise from the computation and to more accurately determine the locations of the cusps, necessary for sign reversal of the data.

Comparative measurements of 2 different fibers were obtained to assess the accuracy of the technique. These fibers were measured independently by different laboratories using their far-field goniometric measurement systems, and then using the Photon inc. system. The far-field profiles obtained from these measurements are shown in Figure 2 and Figure 3. The numerical values for MFD are given in Table 1. The agreement is excellent.

Table 1. MFD values for the Comparative Measurements with Lab #1 and Lab #2

	Lab #1	Lab#2	Photon Inc.	Δ
Fiber #1	9.099 μm		9.092μm	0.007μm
Fiber #2		9.515μm	9.490	0.015μm

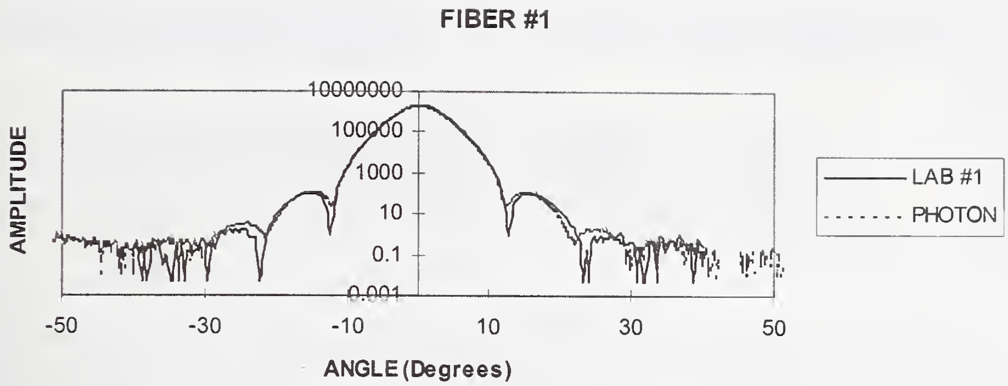

Figure 2. Comparative far-field measurements: ST single-mode fiber measured at Lab #1 and at Photon, inc.

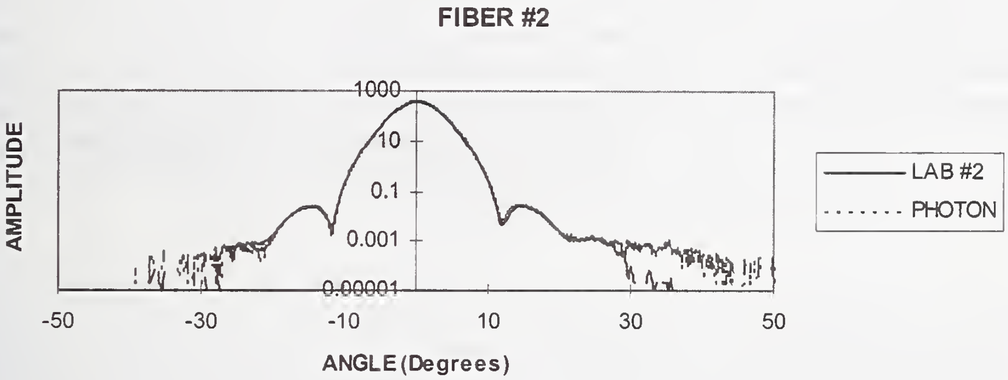

Figure 3. Comparative far-field measurements: bare single-mode fiber measured at Lab #2 and at Photon, inc.

Measurements were performed to assess the "push-button" repeatability of the instrument. Table 2 summarizes the results for 3 different series of measurements of MFD, and Table 3 summarizes the corresponding results for A_{eff}. The results for series "A", with 250, measurements, had a 3σ repeatability of 0.004 μm for MFD and 0.463 μm^2 for A_{eff}. Similarly, the series "B" measurement had a 3σ repeatability of 0.0054 μm for MFD and 0.485 μm^2 for A_{eff}, and for series 'C' the values are 0.0095 μm for MFD and 0.512 μm^2 for A_{eff}.

Table 2. Mode-Field Diameter "Push-Button" Repeatability for 3 Series of Measurements

Series (# of Measurements)	MODE-FIELD DIAMETER (μm)			
	MIN	MAX	MEAN	3 x STANDARD DEVIATION
A (250)	9.3886	9.3954	9.3920	0.0040
B (250)	9.3860	9.3953	9.3901	0.0054
C (1000)	9.4367	9.4588	9.4463	0.0095

Table3. Effective Area "Push-Button" Repeatability for the 3 Series of Measurements of Table 2

Series (# of Measurements)	EFFECTIVE AREA (μm^2)			
	MIN	MAX	MEAN	3 x STANDARD DEVIATION
A (250)	69.603	70.099	69.770	0.463
B (250)	69.444	70.035	69.727	0.4846
C (1000)	69.736	71.384	71.013	0.512

The results show the 3σ push-button repeatability of the instrument is better than 0.01 μm for MFD and approximately 0.5 μm^2 for A_{eff}. These values are of the same order of uncertainty due alone to problems associated with the computation algorithms for MFD and A_{eff}. Some of the variation in parameter values is also attributed to fluctuations in the source amplitude and wavelength during the measurement, as evidenced by the broader range of MFD and A_{eff} values for the longer series "C" measurements. Finally based on numerous series of measurements, the overall accuracy of the instrument is conservatively specified at ±0.5% for MFD and approximately ±1% for A_{eff}.

The measurement of Numerical Aperture (NA) is measured in accord with the TIA/EIA Standard using the Far-Field Method described in FOTP-177 [4]. Specifically, the NA is obtained from the inverse sine of the 5% intensity half angle. Angular width measurements are obtained with a standard deviation of approximately 0.05°, which gives a 3σ variation of approximately ±0.001 in the NA value for typical single-mode optical fibers, which is better than ±1%.

4. Summary

A new technique has been developed for rapid measurement of the far-field profile of optical fibers. It provides far-field profile data with dynamic range comparable to that obtained using conventional lock-in amplifier techniques, but at a fraction of the time. The far-field data is used for computing parameters of single-mode and multi-mode fibers in accordance with the TIA/EIA Standard DFF Methods. The DFF method for MFD is referred to as "the reference method" [2]. The Mode-Field Diameter and Effective Area of single-mode fibers is obtained in less than 20 seconds with greater than 64 dB dynamic range for a 0dBm source. The NA of multi-mode fibers can be obtained in real-time with up to 24 dB dynamic range.

An instrument based on the new technique has measurement accuracy specified at ±0.5% for MFD and approximately ±1% for A_{eff}. The accuracy for NA measurement is better than ±1%. The speed of the measurement makes it possible to test greater numbers of fibers economically. It also provides the ability to acquire statistical data, and potentially eliminate variations in measured parameters due to source fluctuations. Finally, the compact size of the scan unit makes it suitable for portable field use.

5. References

1. Patent # 5,949,534
2. "Measurement of Mode-Field Diameter of Single-Mode Optical Fiber", Fiberoptic Test Procedure FOTP-191, Telecommunications Industry Association, Standards and Technology Department, 2500 Wilson Blvd., Suite 300, Arlington, VA, 22201 (1998).
3. . "Measurement of the Effective Area of Single-Mode Optical Fiber", Fiberoptic Test Procedure FOTP-132, Telecommunications Industry Association, Standards and Technology Department 2500 Wilson Blvd., Suite 300, Arlington, VA, 22201 (1998).
4. "Numerical Aperture Measurement of Graded-Index Optical Fibers", Fiberoptic Test Procedure FOTP-177, Telecommunications Industry Association, 2001 Pennsylvania Ave. N.W., Washington, D.C. 20006 (1992).

The Status of International Fiber Measurement Standards

W. B. Gardner
Rapporteur for Q. 15/15, ITU-T
2000 NE Expressway
Norcross, GA, 30071, USA

A. H. Cherin
Convener, Working Group 1, IEC SC86A
2000 NE Expressway
Norcross, GA 30071, USA

Abstract Fiber test methods which have been approved by the international standards bodies ITU-T and IEC are summarized. Current directions of the standardization efforts in these two organizations are described, including the recent restructuring of the fiber standards documents.

Work in the International Telecommunication Union (ITU-T) Working Party 4 of Study Group 15, and the International Electrotechnical Commission (IEC) Working Group 1 of SC86A over the past two years has culminated in significant milestones being reached at the April 2000 meetings of these organizations:

- The ITU-T "determined" key fiber Recommendations, including G.650, which contains the single-mode fiber test methods. G.650 has been submitted to the World Telecommunication Standardization Assembly for decision in October 2000.

- The IEC measurement standards have been restructured and modernized to reflect current industry capabilities and system requirements.

Multiple test methods have been adopted over the past decade for most of the conventional transmission, geometrical, and mechanical parameters of single-mode fibers. Recent standards-writing efforts in both organizations have been directed mostly toward polarization mode dispersion (PMD) and such nonlinear attributes as effective area (A_{eff}) and the nonlinear coefficient (n_2/A_{eff}) of single-mode fibers.

Table I lists all of the test methods contained in ITU-T's Recommendation G.650, with the Reference Test Method indicated in each case. The latter is the test method selected for resolving any disagreements that may arise in testing.

Table I Single-mode fiber test methods in ITU-T Recommendation G.650

- 5.1 Test methods for the mode field diameter
  - 5.1.1 Reference test method: The far-field scan
  - 5.1.2 First alternative test method: The variable aperture technique
  - 5.1.3 Second alternative test method: The near-field scan
  - 5.1.4 Third alternative test method: Bidirectional backscatter difference
- 5.2 Test methods for the cladding diameter, core concentricity error and cladding non-circularity
  - 5.2.1 Reference test method: The near-field image technique
  - 5.2.2 First alternative test method: The refracted near-field technique
  - 5.2.3 Second alternative test method: The side-view technique
  - 5.2.4 Third alternative test method: The transmitted near field technique
- 5.3 Test methods for the cut-off wavelength
  - 5.3.1 Reference test method for the cut-off wavelength (λ_c) of the primary coated fibre and reference test method for the cut-off wavelength (λ_{cj}) of jumper cables: The transmitted power technique
  - 5.3.2 Alternative test method for λ_c: The split-mandrel technique
  - 5.3.3 Reference test method for the cut-off wavelength (λ_{cc}) of the cabled fibre: The transmitted power technique
  - 5.3.4 Alternative test method for the cut-off wavelength (λ_{cc}) of the cabled fibre
- 5.4 Test methods for the attenuation
  - 5.4.1 Reference test method: The cut-back technique
  - 5.4.2 First alternative test method: The backscattering technique
  - 5.4.3 Second alternative test method: The insertion loss technique
- 5.5 Test methods for the chromatic dispersion
  - 5.5.1 Reference test method: The phase-shift technique
  - 5.5.2 First alternative test method: The interferometric technique
  - 5.5.3 Second alternative test method: The pulse delay technique
- 5.6 Test methods for prooftesting
  - 5.6.1 Reference test method: Longitudinal tension
- 5.7 Test methods for polarization mode dispersion
  - 5.7.1 Reference test method: The Stokes parameter evaluation technique
  - 5.7.2 First alternative test method: State of polarization method
  - 5.7.3 Second alternative test method: Interferometric technique
  - 5.7.4 Third alternative test method: The fixed analyzer technique

The Reference Test Method for PMD in Table I is a consolidation of the Jones Matrix Eigenanalysis and Poincare Sphere methods; the combination of the two has been given the name "Stokes parameter evaluation technique". The fixed analyzer technique is sometimes referred to as the wavelength scanning technique.

Recommendation G.650 also contains two test methods in (non-normative) Appendices:

Appendix IV Test method for measuring chromatic dispersion uniformity based on the backscattering technique
Appendix V Test methods for effective area (A_{eff})

The attributes which these techniques measure are not yet specified in any of the ITU-T Recommendations. In the absence of any requirement to measure these attributes, their test methods appear in Appendices for information only.

The ITU-T has drafted both pulsed and cw test methods for n_2/A_{eff} , but these methods have so far been withheld from the Recommendations pending completion of the round robin evaluation of the methods.

As shown in Table II, the new organization of fiber measurement standards in the IEC is by fiber attributes. Continuous liaison between ITU-T and IEC is used to maintain harmonization between the test methods of the two bodies, including the choice of Reference Test Methods.

Current work in IEC SC86A WG1 includes the development of a technical report describing the measurement of a fiber's nonlinear coefficient, the revision of IEC 60793-1-41 (multimode fiber bandwidth measurement) to include a launching condition needed for fibers used in high bit-rate applications, and the conversion of the polarization mode dispersion technical report to a standard test (IEC 60793-1-48).

Both the ITU-T and IEC have recently restructured their fiber standards documents as well. These new specification structures make it easier to incorporate new fiber design variations that evolve when the performance of each fiber type is optimized for a variety of applications. Examples of this are new non-zero dispersion-shifted fibers for multichannel transmission, and an extended wavelength range low water peak fiber.

Procedures for obtaining standards documents from these organizations can be found on their respective websites, www.itu.int and www.iec.ch.

Table II Organization of Fiber Measurement Standards in IEC 60793-1

Attribute	IEC Document Number	Measurement method(s) included
Fiber geometry	60793-1-20	Refracted near-field Transverse interference Grey-scale, near-field Mechanical diameter
Coating geometry	60793-1-21	Coating geometry Mechanical
Length	60793-1-22	Delay measuring Fibre elongation Backscattering
Fiber proof test	60793-1-30	Constant stress Constant longitudinal strain Constant bending strain
Tensile strength	60793-1-31	Short length Long length
Strippability	60793-1-32	Mechanical
Stress corrosion susceptibility	60793-1-33	Dynamic fatigue, axial tension Dynamic fatigue, 2-point bending Static fatigue, axial tension Static fatigue, 2-point bending Static fatigue, uniform bending
Fiber curl	60793-1-34	(Under consideration)
Attenuation	60793-1-40	Cut-back Insertion loss Backscattering Spectral attenuation modelling
Bandwidth	60793-1-41	Impulse response Frequency response
Chromatic Dispersion	60793-1-42	Phase-shift Spectral group delay, time domain Interferometric
Numerical aperture	60793-1-43	Far-field light distribution
Cut-off Wavelength	60793-1-44	Fibre & Cable cut-off
Mode field diameter	60793-1-45	Direct far-field scanning Variable aperture in the far field OTDR Near-field scan
Monitoring	60793-1-46	Transmitted power Backscattering Optical continuity
Macrobending sensitivity	60793-1-47	Power monitoring Cut-back
Polarization Mode Dispersion	60793-1-48	Conversion of Technical Report is Under Consideration
Damp heat exposure	60793-1-50	Damp heat exposure
Dry heat	60793-1-51	Dry heat
Change of temperature	60793-1-52	Change of temperature
Water immersion	60793-1-53	Water immersion
Nuclear Radiation	60793-1-54	Nuclear Radiation

Measurement Issues in PMD Compensators

Dipak Chowdhury
Corning Incorporated
Corning, NY 14831, Phone: (607) 974-3593, Fax: (607) 974-3405 e-mail: dipak@corning.com

With increasing bit-rate, polarization mode dispersion (PMD) is becoming a major system impairment [1-8]. PDM is defined as the statistical ensemble average of differential group delay (DGD) between the two principal states of polarization (PSP) [9-11]. The fact that PMD is a statistical parameter of the system, depending sensitively on environmental condition and deployment [11-13], mitigation of PMD induced impairment is not trivial. With increasing need of higher bit-rate (40 Gb/s and higher) and longer reach (1000-3200 Km) PMD is becoming an even larger issue than it was perceived to be a few years ago. Consequently a lot of effort is being given to mitigate PMD induced impairment in recent years [14-20]. Instead of addressing various methods of mitigating PMD induced impairments, in this paper we discuss some of the critical issues related to the real-time measurement of PMD and performance of PMD compensators (PMDC).

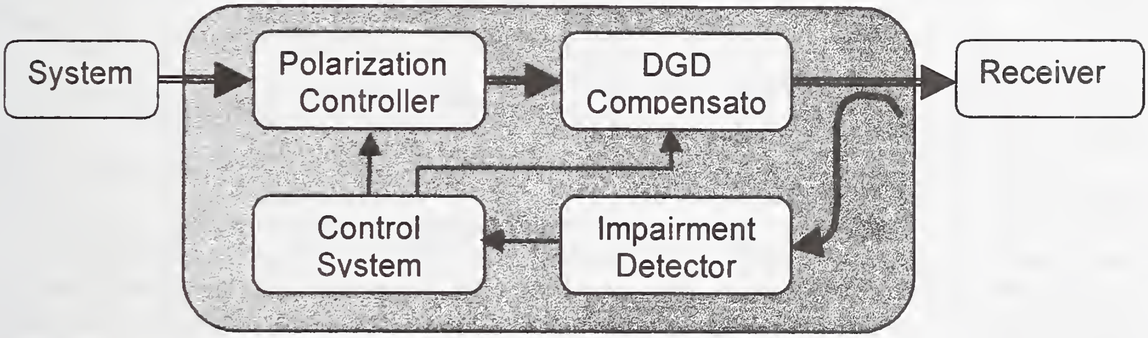

Figure 1: Basic block diagram of a PMDC. The thick lines are optical fiber. Thin lines are electronic signal path. The content inside the gray box is the PMDC.

The basic block diagram of a PMDC is shown in Fig. 1. Various implementations of each of the blocks within the PMDC are proposed and are still being worked on. However, for our discussion we will concentrate on issues related to two aspects of PMDC related measurements: (1) measurement of the *impairment detector* and; (2) measurement of the performance of the PMDC as a whole.

Two basic class of *impairment detectors* (ID) are proposed: (1) optical and; (2) electronic. Optical IDs depend on some type of dense spectral measurement of the states of polarization (SOP) over the signal spectrum. Whereas, the electronic measurement of PMD relies on a few spectral samples at specific frequencies over the signal spectra capturing the change in electrical spectrum induced by DGD. In addition, the ID requirements for mitigating the 1st and higher order PMD are significantly different. In the presentation we will discuss and compare various aspects of these two ID methods.

Two types of performance evaluation of PMDC are possible: (1) In the laboratory environment with controlled hardware emulating actual system induced DGD impairment, and; (2) In the field where a PMD impaired link is used to measure the performance of a PMDC [21]. Key issue for a laboratory environment performance test is the design of the emulator, which mimics the system induced PMD impairment. In this case the induced DGD is easily available by various types of measurement that are commercially available. Also, in the laboratory environment, it is easy to induce controlled but random fluctuations in DGD at any desired speed to test the response time of a given PMDC. Whereas the experimental setup for a field evaluation of the DGD has to be such that the impact of a given PMDC can be evaluated before and after the introduction of a PMDC. Also, in the field environment controlled variation in DGD with given speed is not trivial. Above all, availability of PMD impaired link for a given bit-rate might be difficult. In the presentation we will discuss these issues in detail with examples.

[1] C. D. Pool and J. Nagel, “Polarization effect in lightwave systems,” *in Optical Fiber Telecommunications IIIA*, I. P. Kaminow and T. L. Koch eds. (Academic Press, New York, 1997).

[2] P. R. Morkel, V. Syngal, D. J. Butler, and R. Newman, “PMD-induced BER penalties in optically amplified IM/DD lightwave systems,” *Electron. Lett.* **30**, 806-807 (1994).

[3] P. Ciprut et al. “Second-order polarization mode dispersion: impact on analog and digital transmissions,” *IEEE J. of Lightwave Technol.* **16**, 757-771 (1998).

[4] H. Bullow, “System outage probability due to first- and second-order PMD,” *IEEE Photonocs Tecnol. Lett.* **10**, 696-698 (1998).

[5] M. Karlsson, “Polarization mode dispersion-induced pulse broadening in optical fibers,” *Opt. Lett.* **23**, 688-690 (1998).

[6] C. D. Poole and C. R. Giles, “Polarization-dependent pulse compression and broadening due to polarization dispersion in dispersion-shifted fiber,” *Opt. Lett.* **13**, 155-157 (1988).

[7] C. Vassallo, “PMD pulse deformation,” *Electron. Lett.* **31**, 1597-1598 (1995).

[8] F. Bruyere, “Impact of first- and second-order PMD in optical digital transmission systems,” *Opt. Fiber Technol.* **2**, 269-280 (1996).

[9] N. Gisin, R. Passy, and J. P. Von der Weid, “Definition and measurement of polarization mode dispersion: interferometric versus fixed analyzer methods,” *IEEE Photon. Technol. Lett.* **6**, 730-732 (1994).

[10] C. D. Poole and R. E. Wagner, “Phenomenological approach to polarization dispersion in long single-mode fibers,” *Electron. Lett.* **22**, 1029-1030 (1986).

[11] G. J. Foschini and C. D. Poole, ``Statistical theory of polarization dispersion in single mode fibers," IEEE J. of Lightwave Technol. **9**, 1439--1456 (1991).

[12] C. D. Poole, “Measurement of polarization-mode dispersion in single-mode fibers with random mode coupling,” *Optics Lett.* **14**, 523-524 (1989).

[13] F. Curti, B. Daino, G. De Marchis, and D. Matera, ``Statistical treatment of the evolution of principal states of polarization in single-mode fibers," *IEEE J. of Lightwave Technol.* **8**, 1162--1165 (1990).

[14] D. Mahgerefteh and C. R. menyuk, “Effect of first-order PMD compensation on the statistics of pulse broadaning in a fiber with randomly varying birefringence,” *IEEE Photonocs Tecnol. Lett.* **11**, 340-342 (1999).

[15] R. Noe et. al., “Polarization mode dispersion compensation at 10, 20, and 40 Gb/s with various optical equalizers,” *IEEE J. of Lightwave Technol.* **17**, 1602-1616 (1999).

[16] H Rosenfeldt et. al. “First order PMD-compensation in a 10 Gbit/s NRZ field experiment using polarimetric feedback-signal,” ECOC’99.

[17] S. Hinz et. al. “Distributed fiberoptic PMD compensation of a 60 ps differential group delay at 40 Gbit/s,” ECOC’99.

[18] A. Meccozzi et. al., “A simple compensator for high order polarization mode dispersion effect,” **WL2-1** OFC’2000.

[19] H. Bülow, “PMD mitigation techniques and their effectiveness in installed fiber,” **TH1-1** OFC’2000.

[20] T. Takahashi et. al. “Automatic compensation technique for timewise fluctuating polarization mode dispersion in in-line amplifier systems,” *Electronics Letter* **30,** 38-349 (1994).

[21] D. A. Watley et. al. “Field evaluation of an optical PMD compensator using an installed 10 Gbit/s system,” **ThB6-2** OFC’2000.

A Poincare Sphere Method for Measuring Polarization-Mode Dispersion Using Four-Wave Mixing (FWM) in Single-Model Optical Fiber

Shuxian Song
Lightwave System, CIENA Corporation, ssong@ciena.com

Kenneth Demarest, Christopher Allen
ITTC, Department of Electrical Engineering and Computer Science, University of Kansas

Abstract: A nonlinear Poincare sphere method for measuring polarization-mode dispersion (PMD) using the four-wave mixing (FWM) effect in single-mode optical fibers is presented. This method is based on the FWM-power transfer function on the polarization states of the input signals. Average PMD can be obtained by using this method with measurements in just a narrow optical bandwidth.

Key words: Polarization Mode Dispersion, PMD measurement, Poincare-Sphere Method, Four-wave mixing (FWM)

I. Introduction

Polarization-mode dispersion (PMD) is one of the major limiting factors of ultrahigh-bit-rate optical fiber communication systems. Currently, PMD is a big concern when upgrading legacy networks of installed fiber to 10 Gb/s (OC-192) rates and higher. For example, at 10 Gb/s (OC-192), the limit on PMD is about 10 ps [1]. Knowledge of the PMD in the fiber plant is becoming very critical for system designs, evaluations and installations.

Measuring PMD for installed fiber still is not an easy task. The time-domain methods are degraded by polarization state fluctuations, caused by polarization mode coupling in the fiber [2]. On the other hand, the frequency-domain method is limited by the motion-less condition. Any motion of the measurement apparatus, especially at the ends the fibers, can totally destroy the measured results [2, 3]. Maintaining a motionless condition is often difficult, especially with field measurements.

Recently, a novel nonlinear method was presented for measuring PMD using four-wave mixing (FWM) [4]. It alleviated the strict requirement for a motion-less condition. This paper presents a new technique for measuring PMD that is based on the same nonlinear effect (four-wave mixing, FWM) as in [4], but uses the Poincare sphere method to calculate PMD. In this method, two signals at different frequencies are launched into the fiber under tested. The output signals are then input to a dispersion-shifted fiber (DSF) to produce FWM. The FWM power in the DSF is related to the arc length on the Poincare sphere and is measured to determine the PMD value of the fiber under test. Theoretically, this method can produce a PMD value from each measurement point on FWM power, thus it greatly reduce the signal wavelength scanning range in the optical spectrum, though multiple measurements may be still needed to reduce the influence of FWM power fluctuation.

II. The theory of the method

FWM is a nonlinear process induced by Kerr effect in optical fiber. If three signals at frequencies f_i , f_j and f_k co-propagate through a single-mode fiber, the new frequency generated through FWM would be $f_l = f_i + f_j - f_k$. For the partially degenerate case, $f_i = f_j$, the newly generated frequency is $f_l = 2f_i - f_k$. The generated FWM power depends not only on the signal frequency separations, input signal power and fiber loss and nonlinear characteristics [5, 6, 7], but also on the input signal polarization states [4, 8]. The FWM power transfer function on the state of polarization (SOP) of the input pump signals can be written as [4]

$$F(SOP_1, SOP_2) = \frac{1}{2}[1 + \bar{s}_1(\omega_1) \cdot \bar{s}_2(\omega_2)]$$
$$= \frac{1}{2}[1 + s_1^{(1)} s_1^{(2)} + s_2^{(1)} s_2^{(2)} + s_3^{(1)} s_3^{(2)}] \quad (1)$$

Where $\bar{s}_1(\omega_1) = [s_1^{(1)} \quad s_2^{(1)} \quad s_3^{(1)}]^T$ and $\bar{s}_2(\omega_2) = [s_1^{(2)} \quad s_2^{(2)} \quad s_3^{(2)}]^T$ are the normalized vectors representing the two polarization states of the two input signals at frequencies ω_1 and ω_2, repectively. (1) is valid when the PMD in the fiber (measurement fiber) is small. This transfer function has been verified by both simulation and experiments in [4].

On the surface of Poincare sphere, we can write (1) as

$$F\ (s) = \frac{1}{2}[1 + \cos(\ \phi\ )]$$
$$= \frac{1}{2}[1 + \cos(\ s\ )] \quad (2)$$

where ϕ is the angle between the two polarization vectors and s is the arc length between the two end points of the two polarization vectors on the Poincare sphere. From (2), we can write s as a function of F, that is

$$s = \cos^{-1}(2F - 1) \quad (3)$$

By definition, the first-order PMD is calculated by [9]

$$PMD = \left| \frac{ds}{d\omega} \right| \quad (4)$$

where ω is the signal angular frequency. Substituting (3) into (4), we get

$$PMD = \frac{1}{\sqrt{F(1-F)}} \left| \frac{dF}{d\omega} \right| \quad (5)$$

If we use wavelength instead of frequency, (5) becomes

$$PMD = \frac{\lambda^2}{2\pi c \sqrt{F(1-F)}} \left| \frac{dF}{d\lambda} \right| \quad (6)$$

where λ is the wavelength and c is the speed of light.

The FWM transfer function, F, is obtained by measuring the FWM efficiency as a function of the signal wavelength separation. In real measurements, F needs to be calibrated with the zero-PMD case to reduce the effects of chromatic dispersion in measurement fiber. The derivative in (6) should also be replaced by a difference equation and we get

$$PMD = \frac{\lambda^2}{2\pi c \sqrt{F(1-F)}} \left| \frac{\Delta F}{\Delta \lambda} \right| \quad (7)$$

where ΔF is the change in FWM efficiency inside the small wavelength window $\Delta\lambda$. To reduce the influence of FWM power fluctuation, multiple measurements are needed either at one wavelength or at multiple wavelengths.

III. Experimental results

An experimental setup for measuring PMD using FWM is shown in Fig. 1. Here, a PMD emulator was used to generate a known amount of PMD in the system and served as the fiber under test. A 17.5-km dispersion shifted fiber (DSF) with a zero-dispersion wavelength of 1551 nm was used as the measurement fiber to produce FWM. The FWM power was measured by an optical spectrum analyzer. In our measurements, the wavelength of one input signal was fixed at 1554.0 nm, and the other signal wavelength was varied, where the range of variation chosen depended on the expected PMD values. During measurements, the PMD emulator was first set to zero PMD and the FWM efficiency was measured and recorded, where the FWM efficiency is defined as the FWM power normalized by its maximum value which occurs when the polarization states of two input signals are aligned. This data was used for calibrating the FWM efficiencies for the non-zero PMD cases. Fig. 2(a) and (b) show the measured FWM efficiency vs. the signal wavelength separation for two PMD values, 10 ps and 20 ps, after calibration. The PMD-induced periodic variations on FWM power is clearly observed when signal wavelength is swept. The minimum measurable FWM level was limited by ASE noise.

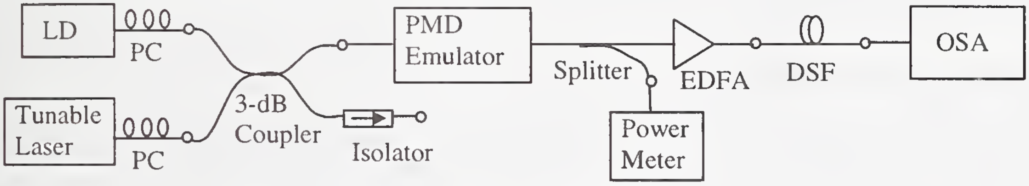

Fig. 1 Experimental setup for measuring PMD using FWM.
LD--Laser diode; PC--Polarization controller; EDFA--Erbium-doped fiber amplifier; DSF--Dispersion-shifted fiber; OSA--Optical spectrum analyzer

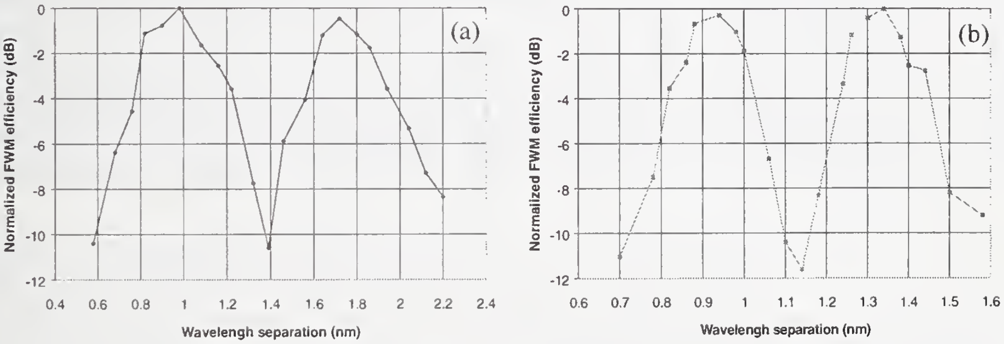

Fig. 2 Normalized FWM efficiency for PMD =10 ps and PMD = 20 ps after calibrated with zero-PMD case. (a) PMD = 10 ps, (b) PMD = 20 ps.

Fig. 3 shows measured average PMD for different given PMD. The measured mean PMD values were obtained by averaging the measurements in different wavelength ranges, represented by the periods of variations of FWM efficiency on wavelength, as show in Fig. 2. Four cases in Fig. 3 correspond to 0.5, 1, 1.5 and 2 periods. The measured results for all four cases follow well with the given values, but are mostly a little bit lower than the true PMD. This is due to measurement errors around the notch areas of the measured FWM efficiency curve. Theoretically, the notches of the FWM efficiency curve should have approached zero, but in experiments these points are non-zero due to the amplified spontaneous emission in the erbium-doped fiber amplifier (EDFA).

To estimate the optical bandwidth needed for this method, Table 1 gives the calculated width in nanometer for each period of the FWM power variations with different PMD values. It agrees well with measured FWM data in Fig. 2. For high PMD (> 10 ps), the period is quite narrow. Thus the nonlinear Poincare sphere method can measure PMD without scanning measurement signals in a wide optical bandwidth.

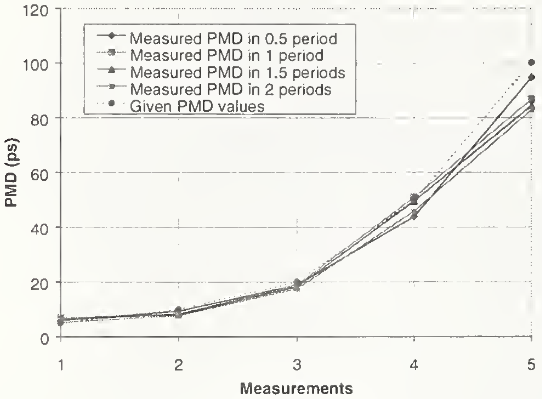

Fig. 3 Measured mean PMD and the given PMD.

Table 1 The wavelength width of one period of FWM power variations for different PMD values

PMD (ps)	5	10	20	50	100
Wavelength width (nm) per FWM period	1.6	0.8	0.4	0.16	0.08

IV. Conclusion and discussion

In summary, we have presented a new Poincare sphere method for measuring PMD by using FWM generation in single-mode optical fiber. It is based on the FWM power transfer function vs. the polarization states of the pump signals. Compared to the traditional Poincare sphere method, this method does not require measurement of the Stokes vectors and is less insensitive to mechanical vibration of measurement apparatus. Compared to the nonlinear fixed polarization analyzer method, this method does not need to scan a wide optical bandwidth and thus has fewer requirements on the measurement fiber.

Similar to the nonlinear method in [4], this technique may also be used as an in situ PMD measurement or monitoring method on dense wavelength-division multiplexed (DWM), traffic-carrying fibers. If the polarization states of the transmitted signals are fixed, the FWM products in the measurement fiber generated by wavelength channels may provide an estimate of the PMD. This can be done either span-by-span or over several spans.

References:

[1] Kapron, F., A. Dori, J. Peters, H. Knehr, "Polarization-mode dispersion: should you be concerned," *Proceedings of NFOEC'96*, Vol. 3, pp. 757-768, Sept. 1996.

[2] Namihira, Y., Maeda, J., "Comparison of various polarization mode dispersion measurement methods in optical fibers," *Electronics Letters*, Vol. 28, No. 25, pp. 2265-2266, Dec. 1992.

[3] Galtarossa, A., G. Gianello, C. G. Someda, M. Schiano, "In-field comparison among polarization-mode-dispersion measurement techniques," *IEEE J. of Lightwave Technology*, Vol. 14, No. 1, pp. 42-48, Jan. 1996.

[4] Song, S., C. Allen, K. Demarest, R. Hui, "A novel nonlinear method for measuring polarization mode dispersion," *IEEE J. of Lightwave Technology*, Vol. 17, No. 12, pp. 2530-2533, Dec. 1999.

[5] Hill, K. O., D. C. Johnson, B. S. Kawasaki, and R. I. MacDonald, " CW three-wave mixing in single-mode fibers," *J. Appl. Phys.*, 49(10), pp. 5098-5106, Oct. 1978.

[6] Shibata, N., R. P. Braun, and R. G. Warrts, "Phase-mismatch dependence of efficiency of wave generation through four-wave mixing in a single-mode fiber," *IEEE J. of Quantum Electronics,* Vol. QE-23, No. 7, pp. 1205-1211, July 1987.

[7] Song, S., C. Allen, K. Demarest, R. Hui, "Intensity effect on four-wave in single-mode fiber," *IEEE J. of Lightwave Technology*, Vol. 17, No. 11, pp. 2285-2290, Nov. 1999.

[8] Inoue, K., "Polarization effect on four-wave mixing efficiency in a single-mode fiber," *IEEE J. of Quantum Electronics*, Vol. 28, No. 4, pp. 883-895, April 1992.

[9] Poole, D. C., and D. L. Favin, “Polarization-mode dispersion measurement based on transmission spectra through a polarizer,” J. Lightwave Technol., vol. 12, pp. 917-929, June 1994.

Modulation Phase Shift measurement of PMD: towards an engineered solution

A J Barlow, J Henstock, C Mackechnie
PerkinElmer Optoelectronics, Wokingham, U.K.

Abstract: *This paper reports the development of the Modulation Phase Shift method for measuring PMD and DGD in fibers and components. In particular we examine practical issues for the implementation of the method.*

Introduction: Polarisation Mode Dispersion (PMD) remains important for optical communications, despite the impending deployment of PMD compensation methods. These methods depend on a full understanding of the PMD phenomenon in fibers and components. In particular, the compensation of first order as well as second order PMD require a detailed verification of that behaviour within DWDM channels or in components and devices that have very narrow transmission bands.

Some but not all, of the traditional PMD measurement techniques developed for fibers will operate over narrow wavelength bands and/or give full PSP information [1], [2], [3]. Included in these is the long-established modulation phase shift (MPS) method [4], which is a direct time domain measurement of differential group delay (DGD). It effectively uses so little optical bandwidth [5] that it may be considered as a “spot” measurement of DGD. By inference the DGD can be determined without any form of polarisation differentiation with respect to wavelength [6]. Therefore, second order PMD vectors can be obtained from the data with only one stage of differentiation.

The MPS method has received increasing attention recently, particularly for the study of DGD in high PMD fibers, and for second order PMD effects [7]. It has also been used in the study of PMD in fiber Bragg gratings [8], where the narrow band nature of the technique is particularly advantageous in exploring regions of high ripple.

Background: Implementation of MPS is generally straightforward, but does pose some difficult and/or expensive engineering issues. In particular, the method requires repeatable polarisation states to be generated before entering the test fiber/device or to be sensed leaving the test fiber/device. The most obvious method is to use polarisation controllers and look for minimum and maximum delays over all possible polarisation states, but this involves a lengthy “search and measure” algorithm for each DGD point. Other methods using polarisation modulation [9] and demodulation scheme after polarisation searching to remove thermal drift effects have been proposed [10].

A simpler four-state launch set up was proposed by Williams [11]. This allows the full DGD and PSP [6] information to be obtained from four input states and four corresponding delay/phase measurements. This is additionally attractive since polarisation dependent loss (PDL) can be detected from power readings at the same polarisation states. Finally, if two of the chosen states are mutually orthogonal, it becomes possible to measure chromatic delay (and dispersion) without error when there is very large PMD and hence second order PMD [6].

In this paper, we examine the Williams four-state method in some detail. This technique has the attraction of simple implementation and excellent compatibility with current dispersion measurement hardware. Two aspects were examined: a) the robustness of the analysis in the presence of measurement noise, b) the detailed design of a practical hardware solution.

A) Data analysis: In the final equation used to calculate DGD, both Williams' equation 9 [11] and Jopson's formulation [6] involve the squares of the phase delays measured for the four input polarisation states. Therefore, any noise in the phase due to instrumentation will undergo a non-linear transformation and "rectification" (i.e. loss of sign of noise). The noise would no longer be averaged to zero and so would show up as a bias. This bias is a direct result of the noise level.

Figure 1: Simulation Result showing the effect of phase noise in the MPS method.

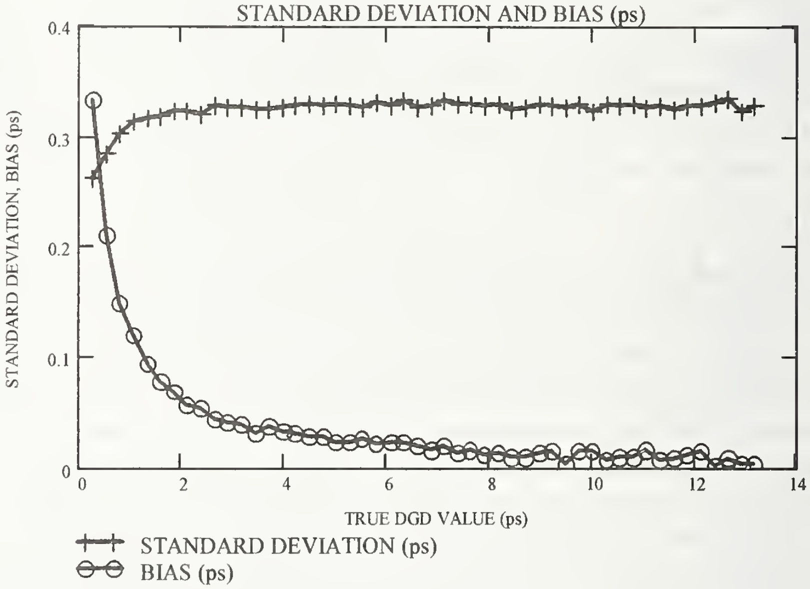

To test this hypothesis, random bipolar phase noise was added to nominal phase values and these were applied to Williams' formula to calculate DGD. The calculation was repeated for different DGD levels and over 10000 simulation runs. The result is shown in figure 1 is for an equivalent delay noise level of 0.15 ps- a value typical of some MPS measurement systems.

Clearly we can see three features:

1) The standard deviation (sigma) of the results is approximately twice the 0.15 ps noise level of one individual delay reading. This is logical as there are four delay readings, so overall noise increases as $\sqrt{4}=2$ times.
2) There is indeed a bias that is always positive, which increases as DGD decreases to ~0.3 ps at 0.5 ps true DGD level. This bias is indeed indicative of the bipolar noise being "rectified" by the action of the DGD calculation equation.
3) The bias only exceeds the noise level at very low DGD values.

Therefore, while the bias is clearly non-negligible, it is generally only significant for DGDs below 1 ps, where it becomes comparable to the measurement noise. Furthermore, because the bias may be fitted easily to an equation and depends only upon the system noise level, it is therefore possible to correct the bias.

B) Design: We have implemented the MPS method using an adapted chromatic dispersion test set [12], employing a tuneable laser source. A simple mechanical switch/polarizer assembly, which provides the four switched polarisation states, was designed. This system was capable of being highly automated and allows rapid and routine measurements of DGD and PMD in fibers and components, along with dispersion and delay. The rapid switching eliminated thermal drift effects.

Figure 2 shows the results obtained on a telecommunications fiber selected for its high PMD.

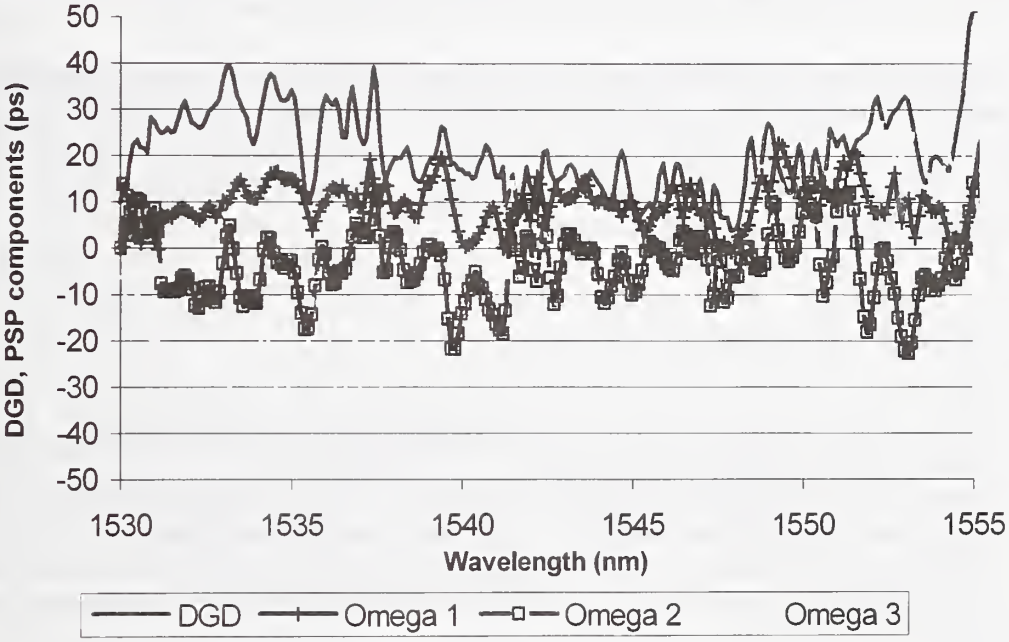

Figure 2: DGD and Principal States measured in a high PMD fiber spool. PMD~20ps

Also shown are the PSP components of the fiber over this wavelength range. This fiber was a standard telecommunications single mode fiber wound on a standard shipping spool. This fiber has a PMD in the region of 20ps, yet is only 4.2 km long.

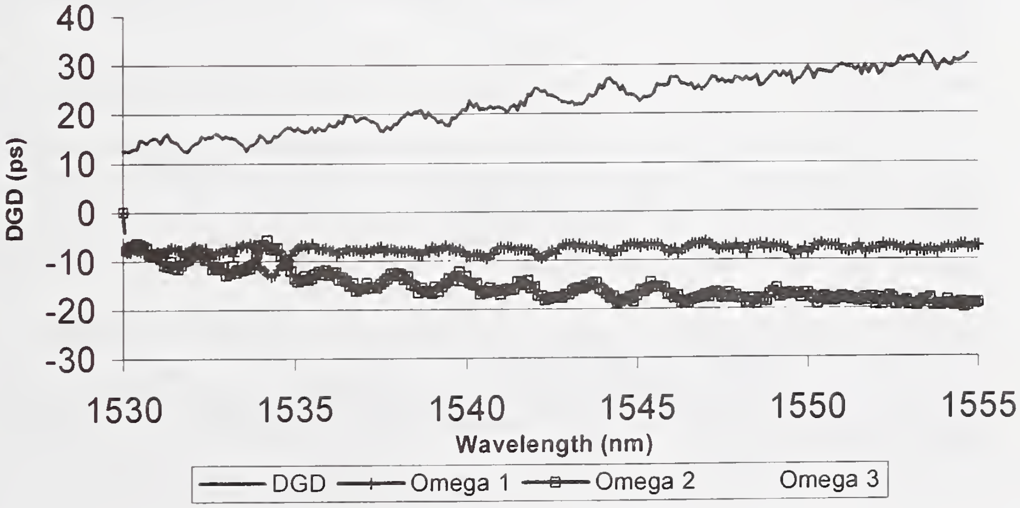

Figure 3: DGD and Principal States measured in a Hi-Bi fiber artefact. DGD~15 ps

Figure 3 shows a PMD measurement in a simple length of Hi-Bi fiber, showing a steady DGD variation with wavelength. This is indicative of low mode-coupling behaviour. Slight drift in the DGD/Principal axis positions was attributed to the effects of the fiber lead birefringence and to thermal drift in the fiber leads. The latter can be eliminated by altering the polarisation-switching pattern and will be presented later.

Conclusions: We have examined two issues related to correct engineering of the Modulation Phase Shift method, each related to the four-state excitation technique. We have shown that while in general instrumentation noise can give rise to a bias, that this bias is easily corrected and is generally much lower than the DGD repeatability level. Similarly, we have shown that it is possible to implement the four-state scheme with elimination of thermal drifts using simple and inexpensive hardware.

The modulation phase shift method is therefore an extremely potent method for DGD investigations in fibers and components, allowing ultra-narrow band DGD measurements, for PSP and PMD2 information to be derived, while simultaneously allowing full compatibility with existing methods/hardware for chromatic delay/dispersion and PDL measurement.

Acknowledgements: The authors thank P Williams and R Jopson for helpful discussions over the course of this work.

References:

[1] TIA FOTP-196 "Guideline for Polarization- Mode Dispersion Measurement in Single-Mode Fiber Optic Components and Devices" 1999.
[2] HEFFNER, B.L., "Automated Measurement of Polarization Mode Dispersion Using Jones Matrix Eigenanalysis", IEEE Photonics Technol. Lett., 1992, **4**(9), pp1066 - 1069.
[3] JOPSON, R. M., NELSON, L. E., AND KOGELNIK, H., " Measurement of Second-order Polarization Mode Dispersion vectors in Optical Fibers", IEEE Photon. Technol. Lett., 11,1999, pp. 1153-1155.
[4] SANO, K. KUDOU, T. and OZEKI, T., "Simultaneous measurement of Group Delay Time Dispersion and Polarization Mode Dispersion", Proceedings of 22nd ECOC, 1996. Paper TuP.09; also MONERIE M, "Polarisation Mode Dispersion measurements in long Single Mode Fibers" El. Lett. 16, 1980, pp. 907-908.
[5] WILLIAMS, P.A, BARLOW, A.J., MACKECHNIE, C., AND SCHLAGER, J.B.; "Narrowband measurements of polarization-mode dispersion using the modulation phase shift technique", NIST SOFM, 98, Sept 98.
[6] JOPSON, R. M., NELSON, L.E., KOGELNIK, H. and GORDON, J.P.; "Vector Measurement of Polarization-Mode Dispersion using the Polarization-Dependent Signal Delay Method", LEOS99, post-deadline paper, Nov 99.
[7] DAL FORNO, A., PARADISI, A., PASSY, R., and VON DER WEID, J.; "Experimental and Theoretical Modeling of Polarization-Mode Dispersion in Single-Mode Fibers", IEEE Jnl. Photonics Technol. Lett., 12, 2000, pp 296- 298.
[8] BERCHELOT L., GOURHANT, J, RIANT, I, SANSONETTI, P, "Vectorial Model of Bragg Gratings", El. Lett, 36, 2000, pp 744-745.
[9] US patent 4,750,833.
[10] TIA FOTP-197 "Differential group delay measurement of single-mode components and devices by the differential phase shift method" ,2000
[11] WILLIAMS, P. "Modulation Phase Shift Measurement of PMD using only four launched polarisation states: a new algorithm", El. Lett, 35, 199, pp. 1578-1579.
[12] PERKINELMER CD400.

Interpretation of PMD Measurements in Components: A Case Study

Normand Cyr
EXFO Electro-Optical Engineering, Inc., 465 Godin Ave, Vanier, Québec, Canada, G1M 3G7.

Abstract: Peculiar PMD behavior that may arise in optical components are highlighted through a case study, the arrayed-waveguide-grating. The emphasis is put on interpretations of PMD measurements that can be misleading. Descriptions are given and appropriate interpretations proposed.

1. Introduction

The usual, and simple interpretation of polarization mode dispersion (PMD) in strongly-coupled, single-mode fibers is based on the following premise: in principle, the probability density function (pdf) of the PMD-induced pulse spreading, including higher-order PMD, is deducible from a single parameter, the root-mean-square differential group delay (rms DGD). From this pdf, one can predict the pdf of BER fluctuations at a given bitrate. Also, it is assumed that the polarization dispersion vector varies little within the bandwidth of a telecom signal, so that only the local DGD value, or the smallest orders of PMD are considered. This holds in principle, at least.

In contrast, optical components may show, owing to their very nature and variety, hard to predict combinations of PMD, PDL, multipath interference (MPI), and filter effects in the case of narrow band components. We illustrate some peculiar PMD behavior that may arise through a particular case study, the arrayed-waveguide-grating (AWG) filter. The aim is to discuss the relevance and significance of PMD measurements for this particular case, which raises such questions as: does the measurement yields the correct result, does the familiar relation between the measured DGD and the expected pulse spreading still hold, how should the results be delivered or interpreted if not, and have the relevant parameters been measured here in the first place?

2. Simulation of the Device Under Test

The AWG is modeled as a multipath interferometer. The incident "beam" is split into multiple paths of different lengths, and the output field is the sum of the output fields of all paths. With this simple model, we can easily take into account the birefringence of the waveguides, small reflections at interfaces on both sides of the waveguides, and off-centering of the power weighting function (uneven splitting of the power between waveguides). The main features are that:

- Two sets of waveguides are interlaced, with slightly shifted peak-transmission wavelengths.
- Any two consecutive waveguides of the same set have the same path-length difference.
- Each waveguide is represented by a (2x2) Jones matrix. The Jones matrix of the device is the sum of all these. It is used to compute the DGD, DAS, principal states of polarization (PSPs), PDL, and transmission, all as a function of optical frequency. The differential attenuation slope (DAS) /1/ is the difference of the ω-derivatives of the PSPs attenuation coefficients.
- The birefringence is assumed to originate from the waveguide geometry. Accordingly, the birefringence axes of all waveguides are assumed to be in the same direction.
- We take into account small reflections that may occur at interfaces on both sides of the device, creating what might be termed "false PMD". To analyze this effect, the output field of each waveguide is the sum of the fields from the first pass and from one double reflection.

3. Results and interpretation

The AWG simulated in this study was assumed to be characterized by the following key parameters, representative of realistic devices. The parameters common to all results are the mean index n_0=1.5, the birefringence $\Delta n/n_0 = 5.17\text{x}10^{-5}$, the DGD of the mid-waveguide $\delta\tau_0$=16.8 fs, the average length L=6.5 cm, and the FSR=2.512 THz . Also, the number of waveguides is 87 per set, the power weighting function (hereafter named the window) is gaussian with a standard deviation of 30 (in number of guides), and the filter bandwidth is FWHM ~ 78 GHz (0.626 nm). Parameters that are varied are the reflection coefficient, R, equal on both sides and independent of SOP, and the window offsetting parameter, a, expressed in terms of the number of guides.

3.1 No Reflection, Centered Window

The results with R = 0 and a = 0 are shown if Figure 1. The DGD have a constant value of 16.8 fs (Fig. 1c). The polarization dependent shift of the transmission is ±5 GHz. The combination of birefringence and filter effect generates a large PDL with steep variations outside the flat portion of the filter (Fig. 1b). The usual relation between DGD and PMD-induced pulse spreading (maximum of DGD/2) holds in this case, as expected. No surprise up to this point.

However, even in this "ideal" case, attention should be paid to the PMD-filter combination. It gives a very large (up to 4 ps within FWHM), steeply varying DAS (Fig. 1d), which may contribute to pulse spreading /1,2/. This happens when PMD and significant PDL coexist, so that the two PSPs are no longer orthogonal, resulting in interference between them instead of a simple addition of power /2/. In this simulation, it is assumed for simplicity that waveguides are uniform, that they all have the same birefringence axes, and that no PDL exists other that the one created by the birefringence-filter interaction. The PSPs then remain strictly orthogonal, so that the DAS, even large, has no significant effect on pulse spreading. However, a less perfect uniformity or some additional PDL would result in some overlap of the PSPs. The consequence can be a PMD-induced spreading significantly larger than inferred from the DGD value. In such an eventuality, the most relevant parameters to be measured should be DAS and PSP overlap.

3.2 Double Reflection and "False PMD"

We now turn to a more striking effect. With R = -30 dB, the DGD oscillates, from 0 to a maximum value of 1 ps (Fig 2a), with a period $FSR_{dr} = 1/\tau_{dr}$ (53 periods within FWHM), where τ_{dr} is the round-trip time through the waveguide section ("dr" stands for double reflection). The maximum is approximately given by $DGD_{max} = \delta\tau_0 + R|\sin\phi|\tau_{dr}$, where ϕ is the retardance of the mid-waveguide at peak-transmission wavelength (1550 nm). Parameters have been set such that $\sin\phi$=1. The pulse spreading in such case is simply due to a double reflection. Apart from a negligible residual, it remains the same regardless of the PMD, be it DGD = 0 (with Δn=0), or DGD = 16.8 fs (if $\sin\phi$=0), or a DGD that oscillates up to 1 ps, with a mean value of 338 fs. The double reflection can be "imaged" in a large, fast oscillating DGD, but the pulse spreading is not caused by PMD, and should not be interpreted as being. In that sense, the reflection-induced DGD can be viewed as "false PMD". We also point out that in any case, it is not the mean value of such a rapidly oscillating DGD that is the primary determinant of the pulse spreading. Rather, the assumption that the dispersion vector varies little within the bandwidth of the signal fails completely here, for a bitrate of, say, 10 Gb/s. Higher orders of PMD are dominant. In short, the mean-DGD is not relevant in this case. Moreover, in a DGD measurement using a polarimetric

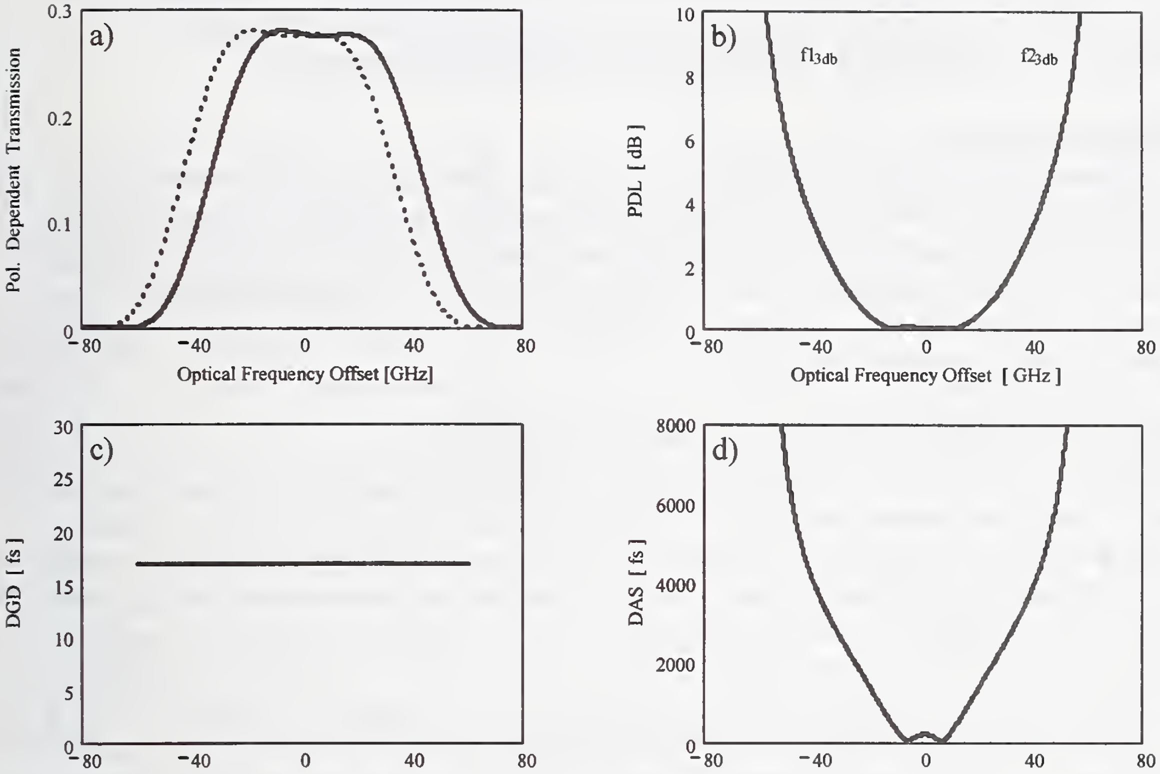

Figure 1: PMD-PDL behavior of the AWG, no reflection **(R = 0)**, centered window **(a = 0)**. **a)** Filter transmission: input-SOP aligned with fast(—) or slow(---) birefringence axis ($\Delta n/n_0$ = $5.17\text{x}10^{-5}$, PDW=10GHz). **b)** PDL due to filter-birefringence combination: mean PDL = 0.81dB within ~80GHz filter bandwidth (FWHM, unpolarized input). **c)** Constant DGD=16.8fs. **d)** Differential Attenuation Slope (DAS) up to 4 ps within the 3dB bandwidth.

DGD with Double Reflection, or Off-Center Window

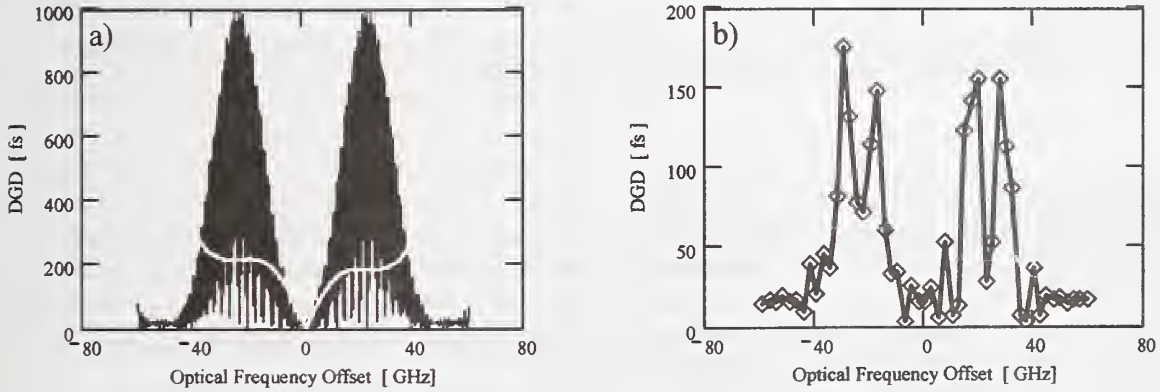

Figure 2: DGD behavior. **a)** True DGD: with a = 0, **R= -30 dB (black)**, and R = 0, **a = 2 (white).** Note: L=6.5cm ⇒ FSR_{dr} =1.46GHz. **b)** With R= -30 dB and a = 0, DGD that would be obtained through polarimetric measurement using a tunable laser, with 0.02 nm steps, (Stokes parameters analysis; JME or Generalized Poincaré Sphere Analysis /3/ (GPSA)).

method, it is likely that the wavelength step will be too large. With a small step such as 0.02 nm, a DGD curve would be obtained, but not showing fast oscillations (under-sampling), and giving underestimated values (see Fig 2.b). A solution to this is discussed in section 3.4.

3.3 Off-Center Window

Another unfamiliar PMD behavior is illustrated in Fig 2.a (white curve). It occurs with an off-centering of the window, here as small as a = 2. Such steep variations, right in the middle of the filter bandwidth, demand careful investigation, because high-order PMD is likely to be a major, if not dominant contributor to PMD-induced spreading. This is but one example of what may occur in narrow band components, as a result of the interplay between PMD and phase variations occurring within the bandwidth of a filter.

3.4 PMD Measurements with a Large Resolution Bandwidth

Considering that small reflections with large delays are likely to occur in a number of optical components, it seems reasonable that, when PMD measurement are made, one should routinely proceed with the following steps. First, detect double reflections with large delays (e.g. with an OLCR). If a non negligible reflection exists, at least it will not be interpreted as PMD, and the real problem will be identified, i.e. double reflection, not PMD. Then, use a technique capable of measuring the intrinsic PMD, independent of reflection (as the 16.8 fs of the above case study). This can be done through standard polarimetric methods, by measuring the output-SOP as a function of optical frequency, but with a resolution bandwidth larger than FSR_{dr} . Then, the fast reflection-induced oscillations of the output-SOP are simply filtered out. In practical situations, FSR_{dr} should be smaller than the bandwidth of the DUT, and in the case of wideband DUTs, the round-trip delay will be very much larger than any reasonable intrinsic DGD. If, say, 0 to 100 fs are to be measured in wideband DUTs, a resolution bandwidth of even as much as 1 THz should be small enough. Moreover, such a large resolution bandwidth can significantly suppress measurement noise, an advantage that is lost if a narrowband, tunable laser is used.

As an example of implementation, a complete device characterization can be performed with a wideband source, measuring the output-SOP as a function of frequency with a polarimetric interferometer (used as Fourier-transform spectrum analyzer). Before proceeding to PMD measurement, the same interferometer can be used to detect reflections, measure round-trip delays, and select a scanning range with a maximum delay smaller than the round-trip delays (equivalent to a resolution bandwidth larger than FSR_{dr} in the frequency domain).

References:

/1/ N.Gisin, B.Huttner, N.Cyr, "Influence of polarization dependent loss on birefringent optical fiber networks," Technical Digest of the 25th Optical Fiber Conference (OFC'2000), Baltimore, Maryland, March 2000, session TuG1-1, p.86 .

/2/ N.Gisin, B.Huttner, "Combined effects of polarization mode dispersion and polarization dependent losses in optical fibers," Optics Communications, **142**, 1 October 1997, p.119.

/3/ To be published: A generalization of the Poincaré Sphere Analysis that includes DUTs with large PDL.

An Intercomparison of Polarisation Mode Dispersion Measurements and Calibration Artefacts

D J Ives, National Physical Laboratory UK,
UK FOToN Group[1].

Abstract: *This paper reports the results of an intercomparison of Polarisation Mode Dispersion (PMD) measurements on a set of six artefacts circulated within the UK FOToN group. The purpose of the intercomparison was to provide:- a snapshot of current PMD measurement capability, a comparison of possible PMD calibration artefacts and a chance to highlight possible future PMD measurement problems.*

Introduction: Polarisation Mode Dispersion (PMD) is an important parameter in the specification of optical fibre and optical fibre components for use in the new high bit rate systems. The measurement of PMD has become routine, however the statistical nature of the parameter has denied the area of a stable calibration artefact. This intercomparison was set up to provide a snapshot of current PMD measurements and a comparison of possible PMD measurement calibration artefacts.

Definitions: For the purposes of this intercomparison polarisation mode dispersion (PMD) is defined as the RMS differential group delay (DGD). PMD, $\Delta\tau$, is given by:

$$\Delta\tau = \sqrt{\sum_{i=1}^{N} \frac{\delta\tau_i^{\,2}}{N}},$$

where $\delta\tau$ is the DGD and the sum is over all wavelengths and/or temperatures.

Artefacts: Six artefacts were chosen for the intercomparison to give a range of PMD values. These were divided into two groups, those with weak polarisation mode coupling and those with strong polarisation mode coupling. The weak mode coupled artefacts were:

1) A temperature stabilised single quartz waveplate. This provided a PMD of ~0.3 ps.
2) A ~6 m HiBi patch cord providing a PMD of ~12.5 ps.
3) A WDM device constructed from a WDM filter and a length of HiBi fibre to provide a device with approximately 1 nm of spectral bandwidth and a PMD of ~1.5 ps.

The strong mode coupled artefacts were:

4) A 13 km length of dispersion shifted fibre on a shipping reel. This provided a PMD of ~0.3 ps and a real fibre against which to assess the other artefacts.
5) A temperature stabilised 32 quartz waveplate stack. The plates being stacked randomly to give strong polarisation mode coupling. The device has a proven stability and a PMD of ~0.5 ps.
6) A high PMD emulator based around a number of HiBi fibre segments joined at random angles. This provided a PMD of ~8 ps.

Measurements: Each participant was given basic information about each artefact including the type of polarisation mode coupling regime and the approximate PMD value to allow the correct setting of the

---

[1] FOToN, Fibre Optic Technology Network is a pan European network aimed at promoting the exchange of best measurement practice and facilitating commercial exploitation within the areas of optical fibre, optical fibre component and optical fibre instrumentation technology.

measuring instruments. The participants were asked to measure the PMD of each artefact and provide basic information about the test method, wavelength range, temperature, accuracy and traceability.

Methods: The following PMD measurement methods were employed which cover both time and frequency domain techniques[1].

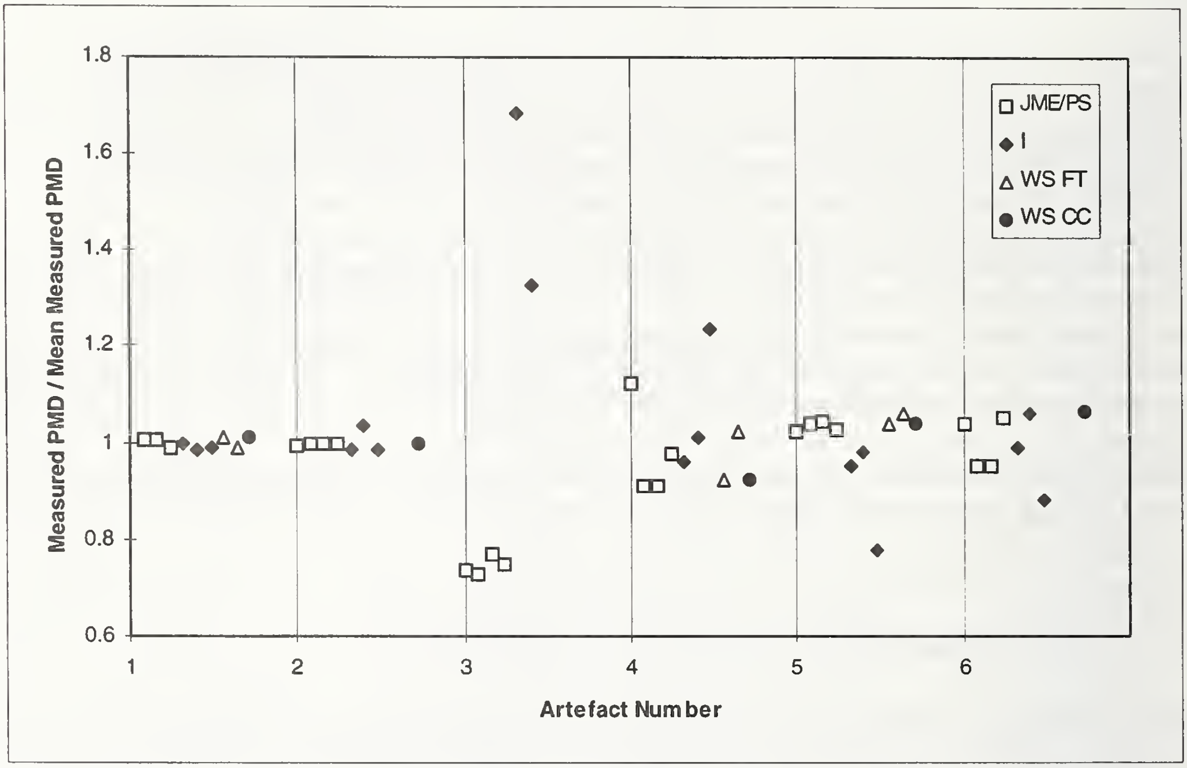

Figure 1 The normalised measured PMD of each artefact in the 1550nm window.

JME/PS) Jones Matrix Eigenanalysis or Poincaré sphere analysis of polarimeter based measurement methods[2,3,4]. A tunable narrow band source and a polarimeter is used to measure the output polarisation state as a function of optical frequency for a number of different input polarisation states. The change of the output polarisation state with optical frequency is used to calculate the PMD by either Jones Matrix Eigenanalysis or Stokes vector rotation of arc on the Poincaré sphere analysis.

I) Interferometric methods[5] using the limited coherence length of a broadband optical source to probe the PMD. For no polarisation mode coupled artefacts the interferogram is a number of peaks the separation of which gives the PMD. For high polarisation mode coupled artefacts the FWHM of the interferogram gives the PMD.

WS FT) Wavelength scan with fourier analysis[6]. This method is based on the transmission of a polarised broadband optical source through the artefact. The output is passed through a fixed analyser to an optical spectrum analyser or equivalent wavelength scanning device. The fourier transform of the scan is equivalent to an interferometric measurement and can be analysed similarly.

WS CC) Wavelength scan with cycle counting analysis[1]. The fixed analyser wavelength scan trace is analysed by counting the extrema to calculate the PMD. A factor of k=0.82 was used where there was known to be strong polarisation mode coupling.

Results: The results shown in Figure 1 represent the PMD measurements in the 1550 nm window (except wavelength scan fourier transform (WS FT) technique which are for the dual 1310 and 1550 nm windows). The measurements were all performed between 18°C and 25°C. The measured PMD for each artefact was normalised by dividing by the mean measured PMD for that artefact in order to highlight the relative variations between the different artefacts.

Artefact	Approx PMD	Inter-laboratory Repeatability (1σ)	Typical Laboratory Repeatability (1σ)	Expected Statistical Variation[7] (1σ)
1) Quartz Waveplate	0.3ps	1%	1%	0%
2) ~6m HiBi patch cord	12.5 ps	1.5%	0.2%	0%
3) WDM Filter + HiBi Fibre	1.5 ps	41% (2.5%)	4%	0%
4) 13km DS fibre on shipping reel	0.3 ps	11%	6%	18%
5) 32 quartz waveplate stack	0.5 ps	8.5%	2%	14%
6) High PMD emulator	8 ps	7%	1%	4%

The table above shows the repeatability of PMD measurements for each artefact. The interlaboratory repeatability is the standard deviation of the all the available measurements from all the laboratories except for the WDM device (3) where the figure in brackets corresponds to the standard deviation of the JME/PS measurements alone. The typical laboratory repeatability is the RMS average of each laboratory's repeatability and gives an indication of the repeatability of individual participants. The expected statistical variation in the final column is the variation expected due to the statistical nature of PMD in mode coupled fibre for a single PMD measurement with a wavelength range of 100nm. It does not strictly apply to the fixed mode coupled artefacts (5) and (6) but is an indication of the variation expected for real fibre with a similar PMD. The variation would be observed for artefacts (5) and (6) if each participant measured a different 100nm wavelength range.

Conclusions: The following conclusions for each artefact have been drawn from this intercomparison:

1) Non mode coupled devices with a broad spectral transmission can be routinely measured by all the techniques with an interlaboratory repeatability of 1%.
2) The high value of PMD with the ~6m HiBi patch cord and the high PMD emulator were outside the PMD measurement range of some of the instruments.
3) The WDM device gives significant measurement problems due to the narrow spectral transmission bandwidth. The JME/PS techniques were able to perform the measurement with a repeatability of 2.5%. The restricted spectral bandwidth lead the Inteferometric and wavelength scan techniques to have a minimum measurable PMD which is much greater than the actual PMD. WDM devices with a lower PMD will probably need a new measurement technique.
4) The real fibre shows the expected statistical variation. All the laboratories were able to measure the PMD to within the expected statistical accuracy.
5) The 32 quartz waveplate stack shows considerable variation for the interferometric method. This is probably due to different launch and receive polarisation states and different wavelength ranges. The JME/PS method shows better interlaboratory repeatability where there are similar wavelength ranges.
6) The high PMD emulator shows interlaboratory repeatability larger than the statistical expectation of real fibre for a 100nm wavelength scan. This may be as the statistically independent wavelength ranges are closer together for high PMD. This leads to a smaller wavelength difference giving a larger PMD variation. Also some of the participants used smaller wavelength ranges, as the higher PMD requires a smaller wavelength step and this will lead to a larger expected statistical variation.

These results are in broad agreement with previous PMD measurement intercomparisons[8,9] but also highlight the future problem of measuring PMD within restricted WDM bandwidths.

Acknowledgements: I would like to acknowledge Perkin Elmer for providing the single quartz waveplate, Nortel Networks for the WDM filter and Fibercore for the high PMD emulator. NPL provided the 32 quartz waveplate stack artefact.

I would like to acknowledge the participants from the UK FOToN group:

R Martin	Anritsu Ltd
L Gleeson	BT Labs
M Harrop	Corning Cables Systems
T Hart	Fibercore
R Brunt	Lambda Photometric Ltd
D Watley	Nortel Networks
A Barlow	Perkin Elmer
C Wallace	Pirelli Cables
A S Siddiqui	University of Essex

References:

[1] NAMIHIRA Y., MAEDA J. "Polarisation Mode Dispersion Measurements in Optical Fibres.", *SOFM Boulder 92*, 1992, **NIST Special Publication 839**, pp145 - 150.

[2] HEFFNER B.L., "Automated Measurement of Polarization Mode Dispersion Using Jones Matrix Eigenanalysis.", *IEEE Photonics Tech. Lett.*, 1992, **4**(9), pp1066 - 1069.

[3] POOLE C.D., BERGANO N.S., WAGNER R.E., SCHULTE H.J., "Polarisation Dispersion and Principle States in a 147km Undersea Lightwave Cable.", *J. of Light. Tech.*, 1988, **6**, pp1185 - 1190.

[4] NAMIHIRA Y., KAWAZAWA T., WAKABAYASHI H., "Polarisation Mode Dispersion Measurements in 1520km EDFA System.", *Elect. Lett.*, 1992, **28**(9), pp881 - 883.

[5] GISIN N., VON DER WEID J-P., PELLAUX J-P., "Polarisation Mode Dispersion of Short and Long Single-Mode Fibers.", *J of Light. Tech.*, 1991, **9**, pp821 - 827.

[6] BARLOW A.J., "Polarisation Mode Dispersion Measurement using Fourier Analysis: Investigation of Mode Coupling Behaviour in Fibers.", *SOFM Boulder 94*, 1994, **NIST Special Publication 864**, pp167 - 170.

[7] GISIN N., GISIN B., VON DER WEID J.P., PASSY R., "How accurately can one measure a statistical quantity like Polarization Mode Dispersion.", *SOFM Boulder 96*, 1996, **NIST Special Publication 905**, pp131 - 134.

[8] WILLIAMS P.A., "TIA round robin for the measurement of PMD", *SOFM Boulder 96*, 1996, **NIST Special Publication 905**, pp155 - 158.

[9] GISIN N., et al, "Definition of polarization mode dispersion and first results of the COST 241 round-robin measurements", *Pure Appl. Opt.*, 1995, **4**, pp511 - 522.

High Speed Soliton Transmission on Fiber Links with High PMD

Peter A. Andrekson
Department of Microelectronics, Photonics Laboratory
Chalmers University of Technology
Gothenburg, Sweden

Polarization-mode dispersion (PMD) is considered an increasingly important obstacle for realizing high capacity lightwave transmission systems. Several solutions to this problem have been proposed, and the most obvious one is to simply boost the aggregate fiber capacity by inserting more and more Wavelength-Division-Multiplexed (WDM) channels, as has been done commercially with great success over the past years. There are, however, clear cost advantages in increasing the per channel data rate rather than increasing the number of wavelength channels. Thus, 10 Gb/s line rates are now commercial and 40 Gb/s line rates are currently seriously being considered, while 160 Gb/s line rates are still at a very early research stage. When considering upgrading old fiber lines to 10 Gb/s, PMD is likely to be one of the key limiting factors, as PMD values for older fibers typically may be in the range of 0.5 – 1 ps/√km. If we consider, somewhat arbitrarily, that the Differential Group Delay (DGD) of the fiber link must be smaller than 10% of the bit-slot duration for an acceptably small outage probability, the maximum PMD limited propagation distance would, in the above example at 10 Gb/s, be in the range 100 – 400 km.

Much effort and progress has resulted in new, very low PMD fibers with PMD values around 0.1 ps/√km and 10 Gb/s data could thus be transmitted over oceanic distances (≈ 10 Mm). However, as line rates soon are expected to reach 40 Gb/s, the best available fiber would then reach only about 600 km (while at 160 Gb/s, the maximum distance would be as short as 40 km). It should be pointed out that in the above examples, with the allowable DGD being 10% of the bit-slot, relies on using the NRZ format [1]. Other formats, such as the RZ or the phase-shaped binary transmission format [2] may be more resilient to PMD, albeit perhaps at the expense of other drawbacks, e.g. spectral efficiency.

As the line-rates go up and the PMD is not expected to be significantly reduced in the near-term, other techniques to combat the impact of PMD have been proposed and evaluated. These technique all essentially rely on PMD compensating sub-systems that adaptively track and compensate the PMD induced changes dynamically, either using optical solutions or electrical solutions after detection [3].

In this presentation, we will focus on the features of soliton pulse propagation in fiber links corrupted by PMD. Solitons are nonlinear pulses that have been proven to be robust in presence of various perturbations. Their resilience to PMD was first observed in a polarization-maintaining fiber several years ago [4]. It was, however, not until recently this feature was first observed in a real transmission experiment using conventional fiber [5].

Much of our soliton and PMD related research was conducted on installed optical Dispersions-Shifted Fiber (DSF). The fiber was installed in the central part of Sweden in 1991 and had a link average PMD value of about 0.3 ps/√km. A maximum of 400 km of fiber was available during most of 1998. Our experiments were conducted as part of the European Union ACTS program in a projects named MIDAS. Fig 1 shows schematically the field site venue and experimental setup for propagating single-wavelength 40 Gb/s solitons.

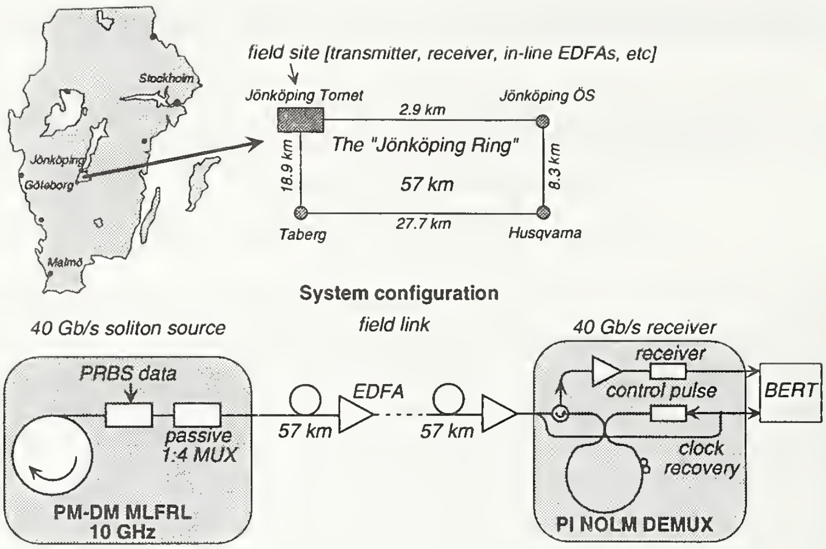

Fig. 1 *Soliton field transmission venue and experimental setup.*

A Mode-Locked Fiber Ring Laser (MLFRL) was used as a wavelength tunable, chirp-free pulse source providing width adjustable pulses at 10 GHz. After data encoding, passive fiber multiplexing yielded a 40 Gb/s stream of data in which intentional timing alteration among the pulses (i.e. a slight deviation from the nominal 25 ps) was introduced to easily recover a 10 GHz clock at the receiver side. All active optics, including optical amplifiers located every 57 km, were conveniently located in one of the hubs. On the receiver side, a Polarization-Insensitive Nonlinear Optical Loop Mirror (PI-NOLM) served to demultiplex the data to 10 Gb/s.

As the accumulated DGD over the available 400 km was as large as 6 ps (24% of the bit-slot), the PMD was expected to be the key limiting factor in this experiments. This was also confirmed through numerical simulations. Nevertheless, as we used solitons and their PMD robustness, we were able to achieve error-free performance over the entire link as indicated in Fig. 2, which illustrates the bit-error rate (BER) vs. received optical power both before and after transmission over the link for all four time-multiplexed channels. The pulses were 10 ps wide and the link average Group-Velocity Dispersion (GVD) was 0.2 ps/(km nm), while the average link loss was 0.33 dB/km.

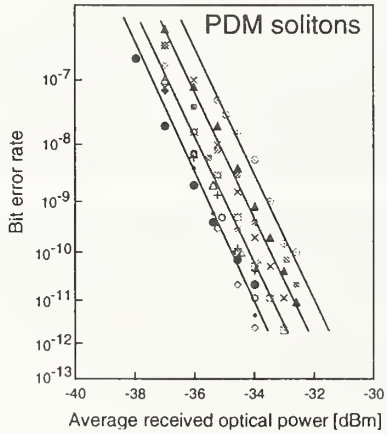

Fig. 2 *BER vs received power before and after transmission for all four channels of the 40 Gb/s soliton data over 400 km of installed fiber. The word length was* 2^{15}*-1.*

We studied both parallel polarized and polarization-division multiplexed (PDM) soliton transmission [6]. Fig. 2 represents the results with PDM solitons, which resulted in a transmission penalty of about 0.5 dB for each channel. The penalty was larger for the parallel polarized solitons (about 1-3 dB). This was contrary to simulated results, which clearly showed that for the high amount of PMD in this case, PDM solitons suffer much more as there is no mechanism to stabilize the relative temporal position of the orthogonal pulses. The reason for the experimental observation, on the other hand, was found to be caused by less interference (not included in the numerical model) in the case of PDM pulses arising from non-ideal pulse extinction in the formation of the high bit-rate data in the multiplexer.

We also carried out single-wavelength PDM soliton transmission at 80 Gb/s by simply reducing the pulse width to about 5 ps, adding one section to the multiplexer and modifying the demultiplexer for 80 Gb/s operation. The GVD was approximately 0.1 ps/km·nm. Error-free operation was achieved for all eight TDM channels over 172 km (3 spans) [7]. This represents the first (and still only) optical transmission field experiment at single wavelength bit-rates beyond 40 Gb/s. Fig. 3 shows the sensitivity (@ BER = 10^{-9}, 2^{15}-1) of the eight TDM channels at 0 km and at 172 km as well as a typical demultiplexed eye diagram at the receiver. The penalty was in the range 0.6 – 1.6 dB.

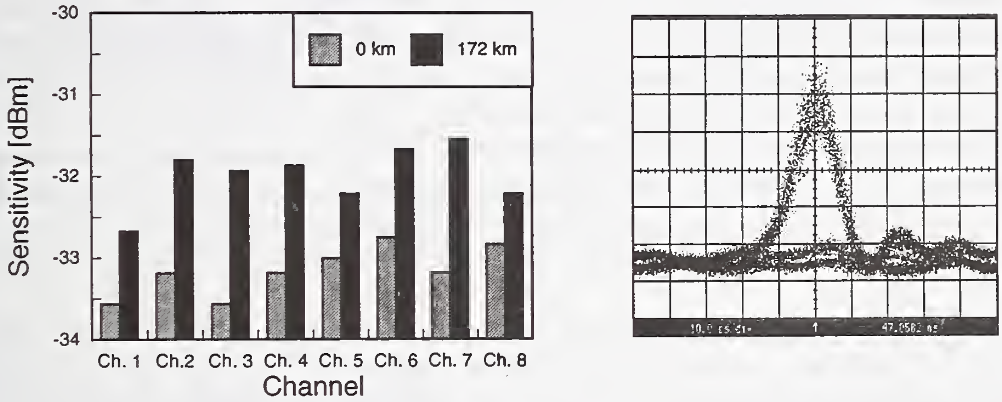

Fig. 3 Sensitivity before and after transmission over 172 km installed fiber with 80 Gb/s PDM solitons and corresponding demultiplexed eye diagram.

As it was clear from the transmission experiments, that PMD was the most important limiting factor, we conducted extensive measurements of PMD both in the laboratory and in the field link. Of particular interest/concern is the temporal evolution of the PMD. We conducted continuous long-term DGD measurements (36 days) simultaneously in two independent 114 km long spans of the installed link [8]. The wavelength range was 1505 – 1565 nm (0.1 nm step size) which was sufficient to yield a constant average DGD over time (corresponding to 0.26 ps/√km). Fig. 4 shows an example of such a DGD measurement. As the fibers were located within the same cable there was a strong correlation between the fibers in terms of DGD change over time (~ 10% /day) as well as of the change of the angle of the principal axis (~ 20° /day). The DGD probability distribution was found to be approximately Maxwellian.

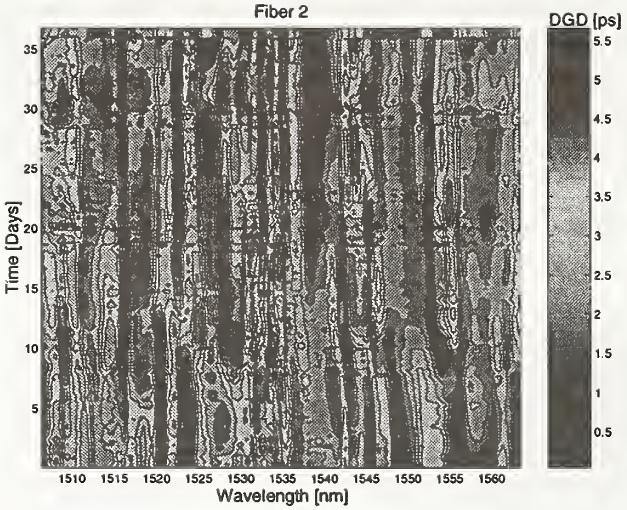

Fig. 4 Measured DGD of 114 km installed fiber over 36 days in the wavelength range 1505 – 1565 nm

We, furthermore, studied the local accumulation of the DGD along the fibers with a novel P-OTDR technique [9]. By studying the back-scattered signal originating at a certain distance versus the wavelength of the input pulse, one obtains a "fixed-analyzer" spectrum (see left side in Fig. 5) from which one can calculate the accumulated average DGD by counting the number of extrema. The right hand side of Fig. 5 shows an example of the evolution of the local DGD in a 57 km long leg of the installed link. (The total DGD was identical to that measured with conventional techniques). This technique is very promising to localize poor, i.e. high PMD, sections in fiber optic transmission links.

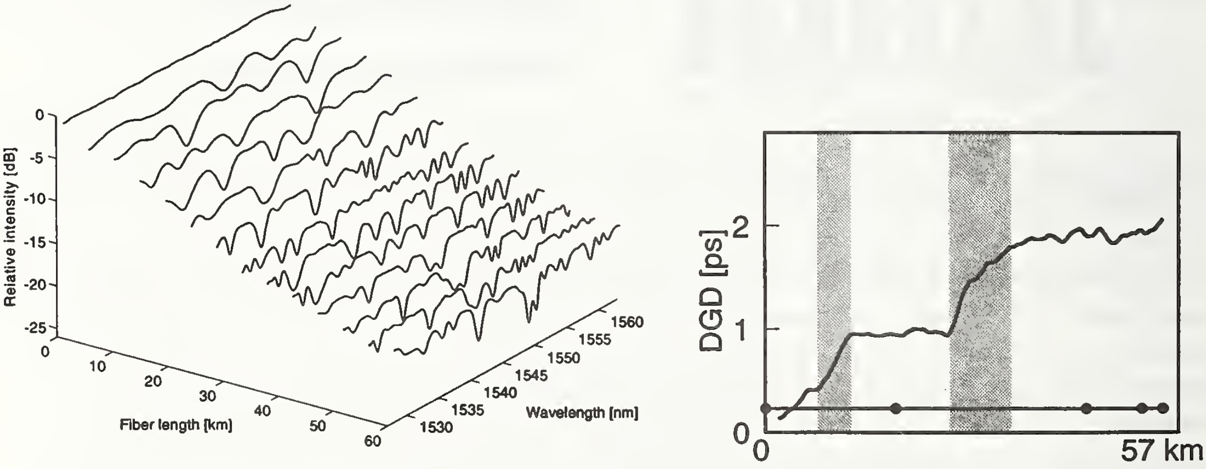

Fig. 5 Left: P-OTDR traces in the wavelength-distance space. Right: Corresponding accumulation of DGD along the fiber section. The shaded areas correspond to portions of the fiber where the DGD is rapidly increasing, i.e. the local PMD is large.

In order to substantiate more rigorously the soliton PMD robustness that we observed in the field fiber link [5], and where this was evidenced in a few given cases, we recently conducted similar tests in a more controlled laboratory environment [10]. Fig. 6 illustrates the setup and the pulse behavior when linear pulses are being propagated through a fiber link corrupted by PMD. First the actual DGD was measured at the wavelength of interest. Then the pulse width at the link output was measured about ten times with different, random input state of polarizations, before the whole procedure was repeated over many hours such that the actual DGD was allowed to drift due to environmental changes. The input pulse width was originating from a MLFRL providing essentially chirp-free 12.5 ps wide pulses. The link was made up of a 150 km of DSF and the link average DGD was 5 ps.

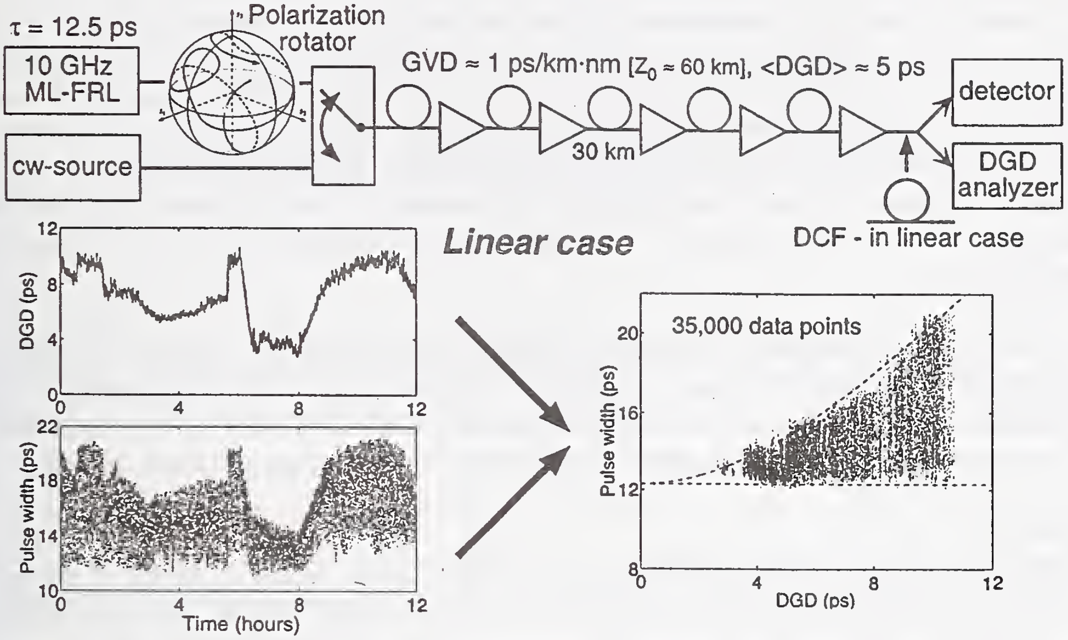

Fig. 6 *Experimental setup (top) and behavior of linear pulses to study pulse-width variations caused by PMD in a 150 km long DSF link. The dashed lines are guides to the eye.*

In Fig. 6, where results with linear pulses are depicted, a short piece of Dispersion-Compensating Fiber (DCF) was used to compensate for the link GVD. By combining the DGD-trace and the pulse-width trace as on the right hand side in Fig. 6, the results are intuitively making sense: the larger the DGD the larger is both the average pulse width and the pulse width variation. When using solitons, on the other hand, the situation differs substantially as illustrated in Fig. 7.

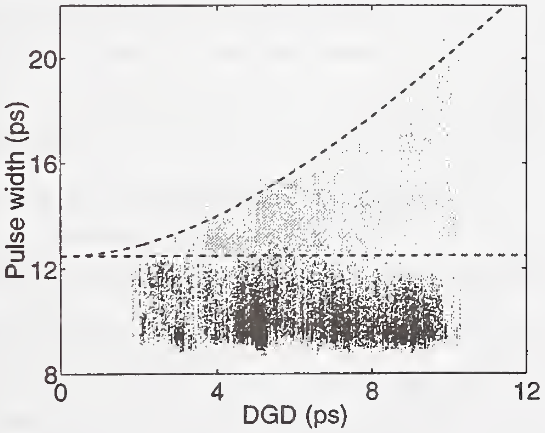

Fig. 7 *Output pulse width vs link DGD for linear pulses (grey dots – from Fig. 6) and for solitons (black dots)*

With the solitons, we increased the power (N-value ≈ 1.2) and omitted the DCF. This resulted in an average output pulse width slightly shorter (10.5 ps) than at the input, but more importantly, also in a reduction of the pulse width variation, particularly at high DGD values. Thus, it is clearly expected that the outage probability can be substantially reduced by the use of solitons. The observed behavior was also confirmed through numerical simulations, which indicated a reduction of rms-pulse width variation of about 50% relative to that with linear pulses. We have very recently also conducted similar experiments with Dispersion-Managed (DM) solitons [11]. We used a 500 km long link with dispersion maps consisting of alternating sections of about 27 km standard SMF (GVD = 16 ps/(km nm)) and 4 km of DCF (GVD = -104 ps/(km nm)). Link average GVDs of 0.1 and 1.0 ps/(km nm) were studied. EDFAs were placed at every second map ($L_{amp} \approx 62$ km). We studied the PMD robustness for different pulse widths ranging from 11 ps to 22 ps and found in all cases significant PMD robustness similar to the constant GVD case described in Figures 6-7.

In conclusion, it now is clearly evidenced that solitons have, from a systems viewpoint, a very interesting feature in its robustness to PMD. It applies to conventional solitons as well as to DM solitons. This feature may be very useful to combine with other techniques to compensate for the effects of PMD to enhance system performance further. We believe part of the success of our 40 Gb/s and 80 Gb/s soliton field transmission experiments relies on this feature.

Acknowledgements

The author wishes to acknowledge the contributions from, P.O. Hedekvist, B.E. Olsson, B. Bakhshi, J. Hansryd, E. Kolltveit, J. Brentel, A. Boyle, M. Karlsson, H. Sunnerud, X. Zhang, J. Li, and C. Xie. This work was financially supported by the ACTS project MIDAS, the following Swedish councils; SSF, NUTEK TFR, and Chalmers Center for High-Speed Technology. Telia is acknowledged for supplying the installed fiber lines, the ORC of Southampton University for supplying the DS-PM fiber in the ring laser, and Ericsson for supplying DFB-EA chips.

References

1. H. Bülow, "Polarization mode dispersion (PMD) sensitivity of a 10 Gb/s transmission system," Proc. ECOC 96, TuD3.6, Oslo, 1999
2. S. Lanne et al., "Extension of polarization-mode dispersion limit using optical mitigation and phase-shaped binary transmission," Proc OFC 2000, ThH3, Baltimore, 2000
3. see e.g. H. Bülow, "PMD mitigation tecnhiques and their effectiveness in installed fiber," Proc OFC 2000, ThH1, Baltimore, 2000
4. M.N. Islam et al., "Soliton trapping in birefringent optical fibers', Opt. Lett., v. 14, pp. 1011-1013, 1989
5. B. Bakhshi et al., "Experimental observation of soliton robustness to polarization dispersion pulse broadening," Electron. Lett., v. 35, pp. 65-66, 1999
6. E. Kolltveit et al., "Single-wavelength 40 Gb/s soliton field transmission experiment over 400 km installed fibre," Electron. Lett., v. 35, pp. 75-76, 1999
7. J. Hansryd et al., "80 Gbit/s single wavelength soliton transmission over 172 km of installed fibre," Electron. Lett., v. 35, pp. 313-315, 1999
8. M. Karlsson et al., "Long-term measurement of PMD and polarization drift in installed fibers," accepted for publication in J. Lightwave Technol., 2000
9. H. Sunnerud et al., "Technique for characterization of polarization mode dispersion accumulation along optical fibers," Electron. Lett., vol.34, pp. 397-398, 1998
10. H. Sunnerud et al., "Experimental quantification of soliton robustness to polarization-mode dispersion," to be presented at ECOC2000, Munich, Germany, September 2000
11. H. Sunnerud etal., "Experimental quantification of soliton robustness to polarization-mode dispersion in dispersion-managed systems," submitted to IEEE Photonics Technol., Lett., 2000

Characterization of high-order PMD

A. Eyal, Y. Li and A. Yariv

Dept. of Applied Physics, California Institute of Technology, M.S. 128-95,
Pasadena, CA, 91125 USA,

Polarization Mode Dispersion (PMD) is currently one of the primary obstacles to ultrahigh speed optical communication systems. Traditionally, the effects of PMD were described in terms of three descriptors: a pair of Principal Polarization States (PSPs) and the Differential Group Delay between them (DGD) [1]. At low communication speeds the values of these descriptors at mid-channel are sufficient to fully describe the effects of PMD over the transmitted signal. As the communication speed increases these descriptors can no longer be assumed constant within the modulation bandwidth. Commonly termed as high order PMD, this phenomenon necessitates the development of analytical tools for its description. Several approaches appear in the literature for the description of high order PMD. The most common approach is based on the PMD vector (PMDV), $\vec{\Omega}$, which in the absence of polarization dependent loss (PDL) is a real, three dimensional vector whose magnitude is equal to the DGD and its orientation is parallel to the Poincare sphere representation of the fast PSP. According to this approach the descriptors of high-order PMD are the derivatives of the PMDV with respect to frequency [2]. Another approach is based on a Taylor-expansion of the Jones matrix of the medium. This approach was used to describe PMD-induced pulse broadening and compression near the zero-dispersion frequency [3]. According to a third approach the second-order effects of PMD are studied by constructing a Jones matrix with principal states and DGD that depends linearly on the frequency [4]. Recently, we introduced a new approach for describing high-order PMD which is based on an exponential expansion of the Jones matrix of the medium [5]. While this variety of descriptions is helpful in giving insight to different aspects of the phenomenon it may lead to confusions. In this paper we define a set of easy-to-measure descriptors that fully characterize high-order PMD. Our goal is to provide a consistent system of terms which can be adopted by the optical community for characterization and measurement of high order PMD. The method we use is a generalization of Poole and Wagner 'phenomenological approach' [1]. It is based on a recursive procedure in which the descriptors of the $n+1$ order are defined by using the descriptors of lower orders and the $n+1$ frequency derivative of the Jones matrix of the medium. The first-order descriptors are the well known PSPs and the DGD between them and the second order descriptors corresponds in a simple manner to the frequency derivative of the PMDV, $\vec{\Omega}'$. In each recursion stage, e.g. the $k+1$ stage, we first analytically cancel the effects of the k'th -order PMD by mentally introducing a compensation system after the transmission medium. The compensation system is defined in terms of the k'th -order descriptors. The $k+1$ descriptors are then defined by identifying two PSPs which satisfy the condition that when the frequency is changed they show no variation up to the k'th order in frequency. The third descriptor of this order is the difference between the propagation parameters of these PSPs.

Let the field at the input of a linear transmission medium be described by: $\vec{E}_{in} = Ae^{i\omega t}\hat{\varepsilon}_{in}$ where $\hat{\varepsilon}_{in}$ is a unit Jones vector representing the input state of polarization (SOP), ω is the optical frequency and A is the complex amplitude of the field. Using Jones' formulation, the output field is given by: $\vec{E}_{out} = \mathbf{T}(\omega)\vec{E}_{in}$ where $\mathbf{T}(\omega)$ is a frequency-dependent 2x2 complex matrix. It is convenient to choose a frame of reference in which $\mathbf{T}(\omega_0) = \mathbf{I}$ where ω_0 is the frequency at mid-range and $\mathbf{I}$ is the identity matrix. In this frame of reference the variations of the output field as function of frequency near ω_0 are described by:

$$\vec{E}'_{out}\Big|_{\omega_0} = \mathbf{T}'\Big|_{\omega_0}\vec{E}_{in} = \mathbf{T}'\vec{E}_{out}\Big|_{\omega_0} \tag{1}$$

The first-order PSPs are derived from the requirement that the SOP at the output of the medium will be independent of frequency to first order in $\Omega \equiv (\omega - \omega_0)$. Namely, it is required that the first order variation (with frequency) of the output field will be parallel to the output field. This is described by the following eigen-value equation:

$$\mathbf{T}'\vec{E}_{out} = \alpha_1\vec{E}_{out} \tag{2}$$

Where α_1 is scalar. The first order PSPs, $\hat{\varepsilon}_{1\pm}$, and their corresponding propagation parameters, $\alpha_{1\pm}$, are then respectively the eigen vectors and eigen values of $\mathrm{N}_1 \equiv \mathbf{T}'\big|_{\omega_0}$. Usually, we are interested in the difference between the propagation parameters, $\Delta\alpha_1 \equiv \alpha_{1+} - \alpha_{1-}$, the imaginary part of which is the DGD and the real part corresponds to the differential loss/gain dispersion of the medium. It is possible to cancel the first order PMD by breaking the output-signal into two components which are aligned with the PSPs, propagate them in media with propagation parameters which are equal and opposite to $\alpha_{1\pm}$ and then recombine the components. Analytically, such a compensation system is described by:

$$\mathbf{C}_1(\Omega) = \mathbf{P}_1\mathbf{Q}_1(\Omega)^{-1}\mathbf{P}_1^{-1} = \exp(-\Omega\mathbf{N}_1) \tag{3}$$

where $\mathbf{P}_1$ and $\mathbf{Q}_1$ are 2x2 matrices defined by:

$$\mathbf{P}_1 \equiv \begin{bmatrix}\hat{\varepsilon}_{1+} & \hat{\varepsilon}_{1-}\end{bmatrix}, \quad \mathbf{Q}_1 \equiv \begin{bmatrix} e^{\Omega\,\alpha_{1+}} & 0 \\ 0 & e^{\Omega\,\alpha_{1-}} \end{bmatrix} \tag{4}$$

The compensated medium is described by $\mathbf{T}_1^c(\omega) = \mathbf{C}_1(\omega - \omega_0)\mathbf{T}(\omega)$. It can be easily verified that $d\mathbf{T}_1^c(\omega)/d\omega\big|_{\omega_0} = \mathbf{O}$ ($\mathbf{O}$ is the zero matrix). In such a medium any polarization state is a *first-order* PSP, however there are, in general, only two polarization states that are stationary to *second-order* in frequency, i.e their corresponding Jones vectors satisfy: $\vec{E}''_{out}\big|_{\omega_0} = \alpha_2\vec{E}_{out}$. Like the first order PSPs these second-order PSPs satisfy an eigen-value equation:

$$\frac{d^2\mathbf{T}_1^c}{d\omega^2}\vec{E}_{out} = \alpha_2\vec{E}_{out} \tag{5}$$

The descriptors of second order PMD are thus the eigen vectors of $\mathbf{N}_2 \equiv d^2\mathbf{T}_1^c(\omega)/d\omega^2\big|_{\omega_0}$ and the difference between the eigen values, $\Delta\alpha_2 \equiv \alpha_{2+} - \alpha_{2-}$. Again we can eliminate the second-order effects by transmitting the output of $\mathbf{T}_1^c(\omega)$ through a compensating medium whose Jones matrix is given by:

$$\mathbf{C}_2(\Omega) = \mathbf{P}_2\mathbf{Q}_2(\Omega)^{-1}\mathbf{P}_2^{-1} = \exp\left(-\tfrac{1}{2}\Omega^2\mathbf{N}_2\right) \tag{6}$$

where:

$$\mathbf{P}_2 \equiv \left[\hat{\varepsilon}_{2+} \quad \hat{\varepsilon}_{2-}\right] \;, \quad \mathbf{Q}_2 \equiv \begin{bmatrix} e^{\frac{1}{2}\Omega^2\alpha_{2+}} & 0 \\ 0 & e^{\frac{1}{2}\Omega^2\alpha_{2-}} \end{bmatrix} \tag{7}$$

It has been shown in [6] that the Poincare sphere representations of the second-order PSPs are parallel to the derivative of the PMDV, $\vec{\Omega}'$, and $\mathrm{Im}\{\Delta\alpha_2\}$ is equal to $\left|\vec{\Omega}'\right|$. In general, this correspondence does not extend to higher orders.

The second-order compensated medium is described by $\mathbf{T}_2^c(\omega) = \mathbf{C}_2(\omega-\omega_0)\mathbf{T}_1^c(\omega)$ and satisfies $d^{(n)}\mathbf{T}_2^c(\omega)/d\omega^{(n)}\big|_{\omega_0} = \mathbf{O}$ for $n = 1,2$. The recursive procedure of descriptors-definition can be summarized as follows: The k'th -order PSPs and their corresponding dispersion parameters are respectively the eigen-vectors and eigen-values of the characteristic matrices, $\mathbf{N}_k \equiv d^{(k)}\mathbf{T}_{k-1}^c(\omega)/d\omega^{(k)}\big|_{\omega_0}$, where $\mathbf{T}_k^c(\omega)$, the k'th - order compensated medium, is defined by:

$$\begin{aligned} &\mathbf{T}_0^c(\omega) \equiv \mathbf{T}(\omega) \\ &\mathbf{T}_k^c(\omega) \equiv \exp\left[-\frac{1}{k!}(\omega-\omega_0)^k \left.\frac{d^k\mathbf{T}_{k-1}^c}{d\omega^k}\right|_{\omega_0}\right]\mathbf{T}_{k-1}^c(\omega) \qquad k = 1,2\ldots \end{aligned} \tag{8}$$

Using this definitions it is straight forward to show that the compensated media satisfy:

$$\begin{aligned} &\mathbf{T}_k^c(\omega_0) = \mathbf{I} && \text{for all } k\text{'s} \\ &\left.\frac{d^{(j)}\mathbf{T}_k^c}{d\omega^{(j)}}\right|_{\omega_0} = \mathbf{O} && \text{for } 1 \leq \mathrm{j} \leq k \end{aligned} \tag{9}$$

Thus,

$$\mathbf{T}_k^c(\omega_0+\Omega) = \mathbf{T}_0^{-1}e^{-\Omega\mathbf{N}_1}e^{-\frac{1}{2}\Omega^2\mathbf{N}_2}\ldots e^{-\frac{1}{k!}\Omega^k\mathbf{N}_k}\mathbf{T}(\omega_0+\Omega) = \mathbf{I} + \mathrm{O}\left(\Omega^{k+1}\right), \tag{10}$$

which leads to exponential expansion of $\mathbf{T}$:

$$\mathbf{T}(\omega_0+\Omega) = \mathbf{T}_0 e^{\Omega\mathbf{N}_1}e^{\frac{1}{2}\Omega^2\mathbf{N}_2}e^{\frac{1}{6}\Omega^3\mathbf{N}_3}\ldots \tag{11}$$

A method for measurement of the characteristics matrices $\mathbf{N}_k$ is described in [7]. It is based on the fact that $\mathbf{N}_k$ can be expressed in terms of the derivatives of $\mathbf{T}(\omega)$ at ω_0 [3]. Thus the measurement of $\mathbf{N}_k$ or equivalently the high order PSPs and the corresponding difference in propagation parameters is equivalent to measuring the derivatives of the Jones matrix.

It is important to notice that this method of characterization is not unique. One can obtain infinitely many sets of descriptors in a similar manner. Each set of descriptors corresponds to a different compensation protocol. For example, placing the compensating systems before the medium instead of after it leads to a different set of descriptors. The non-uniqueness of the descriptors is a result of the fact that the transmission matrix of the medium and its derivatives are non-commuting operators. This is a fundamental characteristic of PMD that can not be avoided. The most simple example of this characteristic appears already in the case of first-order PMD: in general, a polarization dispersive medium posses different input PSPs and output PSPs (in this paper we avoided this issue by defining $\mathbf{T}(\omega_0)=\mathbf{I}$). Given that no unique set of descriptors exist one is free to choose the set that is most suitable for the application. The set that we chose is favorable since it leads to an insightful description of high order PMD in the time-domain [3]. The set is especially useful in quantifying the distortion of pulses due to second-order PMD.

In summary, a generalization of Pooles and Wagner 'Phenomenological approach' was used to define high-order PSPs and the corresponding propagation parameters. The measurement of these descriptors is a straight forward procedure which is equivalent to the measurement of a Jones matrix and its derivatives. It can be performed using standard, commercially available polarization analysis equipment. There is a simple correspondence between the proposed descriptors of the first two orders of PMD and the widely used PMDV and its frequency derivative. This correspondence does not extend to higher orders. The defined system of descriptors can be used to fully characterize the high order effects of PMD.

Reference:

1. C. D. Poole and R. E. Wagner. Phenomenological approach to polarization dispersion in long single-mode fibers. *Electronics Letters*, vol. 22 (no. 19): pp. 1029-1030, 1986.
2. P. Ciprut, B. Gisin, N. Gisin, R. Passy, J. P. Von der Weid, F. Prieto, and C. W. Zimmer. Second order polarization mode dispersion: Impact on analog and digital transmissions. *Journal of Lightwave Technology,* vol. 16 (no. 5), pp. 757-771, 1998.
3. C. D. Poole and C. R. Giles, Polarization dependent pulse compression and broadening due to polarization dispersion in dispersion shifted fibers, *Opt. Lett.* vol. 13, no. 2, pp. 155-157, 1988.
4. C. Francia, F. Bruyere, D. Penninckx and M. Chbat. PMD second order effects on pulse propagation in single mode optical fibers. *IEEE Photonics Technology Letters,* vol. 10 (no. 12), pp. 1739-1741, 1998.
5. A. Eyal, W.K. Marshall, M. Tur and A. Yariv, Representation of Second Order Polarization Mode Dispersion, *Elec.Lett*. vol. 35 no. 19, pp. 1658-1659 1999
6. A. Eyal, Y. Li, W.K. Marshall, M. Tur and A. Yariv. Statistical determination of the length dependence of high-order PMD. Accepted for publication in *Optics Letters*, July 2000.
7. Y. Li, A. Eyal, P-O Hedekvist and A. Yariv. Measurement of high order polarization mode dispersion. Accepted for publication in *IEEE Photonics Technology Letters*, July 2000.

Measurements of Enhanced BER fluctuations due to Combined PMD and PDL Effects in Optical Systems

N. Gisin and M. Wegmuller
Group of Applied Physics, University of Geneva, 1211 Geneva 4, Switzerland

A. Bessa dos Santos, J. P. von der Weid
Centre for Telecommunications Studies
Pontificia Universidade Católica do Rio de Janeiro, 22453-900, Rio de Janeiro, Brazil

Abstract

Polarisation effects that can't be explained neither by PMD nor by PDL alone have been predicted. Moreover, theoretical models and simulations suggest that these combined PMD+PDL effects may significantly increase the fluctuations that come along with polarisation effects. We present measurements of BER fluctuations in a concatenation of PMD and PDL elements. The result confirms that combined PMD+PDL effects may introduce fluctuations larger than those estimated by simple rms rules.

The fact that single mode fibres actually support two propagating modes, the polarisation modes, is nowadays well known [1-3]. Polarisation effects have been classified in two categories, the Polarisation Mode Dispersion (PMD) and the Polarisation Dependent Losses (PDL). The first one causes differential group delays, while the second one causes differential attenuation. Both could limit the transmission bandwidth, like any dispersion or attenuation phenomena. PMD has been widely studied. But with future networks incorporating many components like amplifiers, add-drops, multiplexers, etc, with non-zero PDL, the study of the latter is timely [4, 5].

The interplay between PMD and PDL is subtle, much more than usually thought. Linear attenuation and chromatic dispersion can well be described independently, but this is not the case of their polarisation-relatives! Indeed, as is well known, PMD results not only from birefringence, but also from polarisation mode coupling [6]. The latter strongly depends on the relative orientation between the Polarisation State at the output of one fiber section and the birefringence axis of the next one. But components with PDL do change the polarisation states, hence modify the polarisation coupling. Actually, the phenomenon is made more complex by the following fact: PDL does not merely rotate the polarisation states, it transforms them in a more complicated way [7]. Consequently, there is a need to study, understand, measure and master combined PMD + PDL effects. According to previous studies [8-12], these combined effects are not important in today's communication systems but could significantly affect future optical networks. In [8] a model of PMD + PDL that extends the well-accepted principal polarisation state model of PMD was developed. In [9, 10], this model has been tested in some special situations (admittedly, the values used for these tests do not correspond to values expected in telecom systems, but the purpose of these experiments was simply to test the theoretical model). In [11], numerical simulations based on this model predicted significant BER penalties due to combined PMD + PDL effects. In this letter we present BER measurement results on fibre artefacts with realistic values comparing experimental situations with PMD only, PDL only, and with both PMD and PDL.

The experimental set-up is shown in Fig. 1. The PMD devices were pieces of HiBi fibre with 22 ps PM delay each, both immersed in a thermal bath in order to maintain their birefringence stable. The PDL device was a thin (100 µm) glass plate inserted with a variable angle in a collimated beam. The variable attenuator adjusts the optical power transmitted through the test and reference paths to be the same for each measurement. The optical switches S1 and S2 commute the measuring system between the test and reference optical paths. The third switch commutes the signal between the power meter and the BER receiver. APC connectors were used to avoid interferometric noise. For each test path measurement a new reference point was measured. A PRBS sequence of $2^{23} - 1$ bits at 2.488 Gb/s was used and the BER values were determined after counting 200 errors. The various Polarisation Controllers (PC) allow to randomly varying the polarisation mode couplings. For each configuration of the test path the statistics of the BER while the PCs are randomly varied is recorded and the standard deviation σ computed. In order to make sure that we measure polarisation effects and not effects due to power fluctuations, for each configuration of the PCs we continuously recorded the power immediately before the BER-meter and adjusted the source power to maintain this power at a given fixed level. The level was chosen to obtain BER values close to $3x10^{-9}$ at the reference path.

In order to evaluate the effects of the PMD and PDL combination we first measured the BER statistics for pure PMD and pure PDL cases and then introduced all components in the link to measure the statistics due to the combination. Figure 2 presents the BER statistics for the isolated PMD and PDL (1 dB) cases and for the combined PMD and PDL, together with the reference path measurements. The reference statistics is sharply peaked, with its width $\sigma_{REF} = 0.07$ determined essentially by the number of counted errors. The same behaviour ($\sigma_{PDL} = 0.08$) was observed for the isolated PDL case, meaning that no distortion is induced by PDL in the absence of PMD. Pure PMD indeed introduces a distortion which is polarisation dependent, as it is clear by the wider distribution of the BER values ($\sigma_{PMD} = 0.27$). This distortion is given by the variable delay due to the combination of two HiBi fibres with their axes randomly oriented, plus the random input state of polarisation.

Figure 2 (c) displays the BER statistics for the combined PML and PDL case. A significantly wider distribution is now observed: $\sigma_{PMD+PDL} = 0.50$. Note that it is also much larger than the RMS value: $\sigma^2_{PMD+PDL} > \sigma^2_{PMD} + \sigma^2_{PDL}$ which is approximately 0.28. This confirms that PDL distributed along a birefringent fibre link can produce abnormal effects on the BER! The effects are abnormal in the sense that they are larger than expected from simple addition or RMS rules. Note that the abnormal effect may result in larger as well as in smaller BER values [8]. Hence, the mean value of the BER is not affected, but the fluctuations are significantly increased, in good agreement with our numerical simulation [11].

Moreover, the magnitude of the effects is already relevant even for PMD values as low as the usually admitted 10% of the bit slot.

In conclusion, we tested the model predictions in a simple combination of PMD and PDL devices with values close to common Telecom optical components. The observation of important effects indicate that the safety margins of future systems may have to be adjusted to take into account the combined PMD + PDL effects that will affect future networks incorporating large numbers of components, each with a small PDL.

Acknowledgements

This work was partially supported by the Swiss OFES within the European COST 265 project, and by CPqD Foundation (contract CTO/P&D/067/98), Brazilian National Research Council (CNPq) and FAPERJ.

References

1. C. D. Poole, R. W. Tkach, A. R. Chraplyvy e D. A. Fishman, "Fading in lightwave systems due to polarization-mode dispersion", *IEEE Photon. Technol. Lett.*, vol 3, 1, pp 68-70, 1991.
2. E. Iannone, F. Matera, A. Galtarosa, G. Gianello and M. Schiano, "Effect of Polarization Mode Dispersion on the performance of IM-DD Communication Systems" *IEEE Photonics Technol. Lett.*, vol. 5, 10, pp 1247-1249, 1993.
3. P. Ciprut, B. Gisin, N. Gisin, R.Passy, J.P. von der Weid, F. Prieto and C. Zimmer, "Second order polarization mode dispersion: impact on analog and digital transmission", J. Lightwave Tech. 16, pp.757-771, 1998.
4. A. Eyal and M. Tur, "Measurement of polarization mode dispersion in systems having polarization dependent loss or gain", IEEE Photon. Techno. Letts. 9, pp.1256-1258, 1997.
5. A. Elamari, N. Gisin, B. Perny, H. Zbinden and C. Zimmer, "Statistical prediction and experimental verification of concatenations of fiber optic components with polarization dependent loss" , J. Lightwave Tech. 16, pp.332-339, 1998.
6. C.D. Poole and R.E. Wagner, "Phenomenological approach to polarisation dispersion in long single-mode fibres", Electron. Letts. 22, pp.1029-1030, 1986.
7. N. Gisin, "Statistics of PDL", Opt. Comm. 114, pp.399-405, 1995.
8. N. Gisin and B. Huttner, "Combined effects of polarisation mode dispersion and polarisation dependent losses in optical fibers", Opt. Comm. 142, pp.119-125, 1997.
9. B. Huttner and N. Gisin, "Anomalous pulse spreading in birefringent optical fibers with polarisation-dependent losses", Opt. Letts. 22, pp.504-506, 1997.
10. B. Huttner, C. De Barros, B. Gisin and N. Gisin, "Polarisation-induced pulse spreading in birefringent optical fibres with zero differential group delay", Opt. Letts. 24, pp.370-372, 1999.
11. B. Huttner, C. Geiser and N. Gisin, "Polarization-induced distortions in optical fibre networks with polarization mode dispersion and polarization dependent losses", J. Quantum Electron., in press, 2000.
12. L. Chen, J. Cameron, X. Bao, "Statistics of PMD in presence of PDL in single mode fibers", Optics Commun. 169, 69-73, 1999.

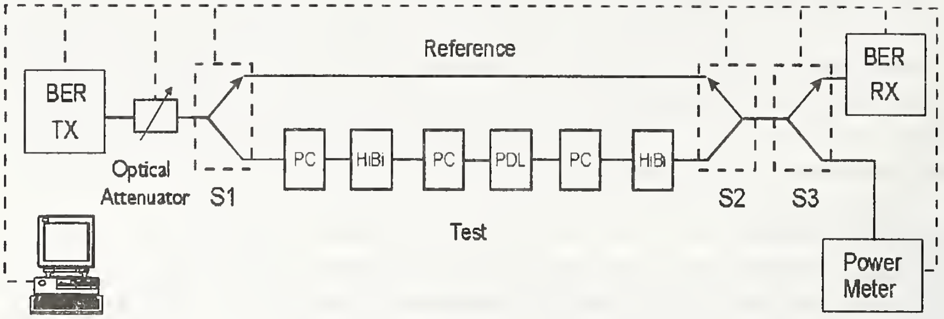

Figure 1

Experimental set-up for BER measurements.

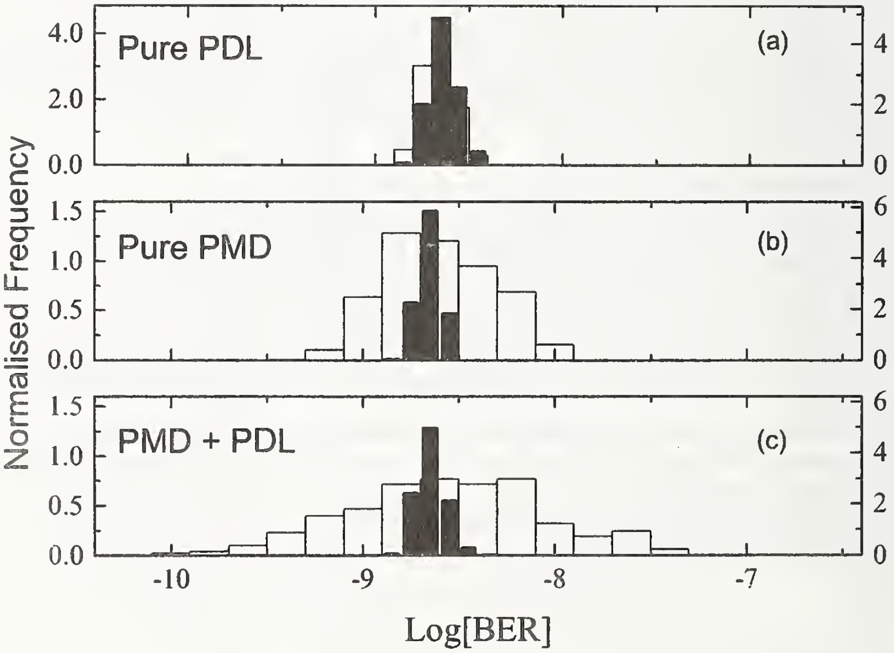

Figure 2

BER statistics for the pure PDL (a), pure PMD (b) and for the combined PMD+PDL (c) cases. Black bar graphs correspond to reference measurements.

Reflectometric characterization of distributed birefringence in installed single-mode fibers

Massimo Artiglia (1), Marco Schiano (1), Tiziana Tambosso (1)

Andrea Galtarossa (2), Luca Palmieri (2), Anna Pizzinat (2),

(1) CSELT, Via G. Reiss Romoli 274, 10148 Torino, Italy (massimo.artiglia@cselt.it)

(2) DEI, Università di Padova, Via G. Gradenigo 6/A, 35131 Padova, Italy

Abstract

We describe local birefringence measurements performed with a polarization sensitive OTDR on installed single-mode fibers. Results indicate that G.652 fibers are, on average, less birefringent than G.653 fibers.

Introduction

Nowadays research activities on PMD are mainly focused on two mayor topics. The first one is the analysis of PMD impairment on system performance [1] and includes the design of PMD compensators and emulators [2, 3]. The second topic is the local characterization of the fiber random birefringence and is aimed to a deeper understanding of the relationship between fiber birefringence and PMD behavior.

Distributed fiber birefringence has been studied and described by means of several theoretical models, but only recently it has become the subject of experimental characterizations, based on a polarization-sensitive OTDR technique (POTDR) [4].

Using this technique, the local beat length (i. e. the inverse of the birefringence vector modulus) of long single-mode fibers has been measured for the first time. The measurement of local beat-length is very important especially for fibre and optical cable manufacturers, since it may improve the control of fibre production or the control of cabling process in order to limit the effect of PMD. This aspect has become essential for new fiber installations due to the stringent requirements of next generation high-speed transmission systems.

Results of laboratory tests performed on fibers wound on drums were reported in ref. [4]. In this paper, we present the results of the first beat length measurements performed on installed optical fibers.

Measurement principle

The general feature of a POTDR equipment is a polarization analysis of the backscattered light from the fibre under test. When an optical pulse is launched into an optical fiber, its state of polarization (SOP) evolves randomly as a function of the pulse position inside the fiber. Consequently, also the backscattered field SOP varies at random. Thus, if a fixed polarizer is placed in front of the POTDR photodiode, the SOP random evolution produces fluctuations in the detected power. The basic idea, described in ref. [5], is that the fiber local beat length can be calculated from the *level crossing rate* (LCR) of the backscattered power passing through a polarizer, exploiting a further refinement of the statistical theory already developed for the "fixed-polarizer" PMD measurement technique.

In ref. [5] it is shown that the signal $T(z)$, representing the normalized backscattered power passing through a polarizer, can be expressed as:

$$T(z)=\frac{1}{2}[1+\hat{s}_B(z)\cdot\hat{p}]=\frac{1}{2}\{1+[R(z)M\hat{p}]\cdot[MR(z)\hat{s}_o]\} \qquad (1)$$

where $R(z)$ is the Müller matrix of the fiber, $M=diag(1,1,-1)$, and $\hat{s}_B(z)$, $\hat{s}_0$ and $\hat{p}$ are the Stokes unit-vectors representing the SOP of the backscattered field, the input SOP, and the fixed polarizer, respectively. The following step is to assume $\hat{p}=\hat{s}_0$ (i.e. the input SOP and the polarizer SOP are the same), so that eq. (1) simplifies to:

$$T(z)=\frac{1}{2}\{1+\hat{s}_f(z)\cdot[M\hat{s}_f(z)]\} \qquad (2)$$

where $\hat{s}_f(z) = R(z)\hat{s}_0$ is the Stokes unit-vector of the forward propagating field SOP. Since the statistical properties of $\hat{s}_f(z)$ are well known, we can calculate the statistical properties of $T(z)$. In Particular, the spatial frequency of the backscattered power fluctuations is related to the beat length L_B of the fiber by the following expression [5]:

$$L_B = \frac{4\sqrt{\upsilon}}{n(\upsilon)} \qquad (3)$$

where υ represents a generic level between 0 and 1, and $n(\upsilon)$ is the mean number of times $T(z)$ crosses the level υ per unit fiber length.

The condition $\hat{p} = \hat{s}_0$ can be simply attained by placing a linear (bi-directional) polarizer just before the fiber input. In spite of its simplicity, this solution suffers from a mayor drawback: the measured backscattered power fluctuations are originated not only by SOP variations, but also by fiber local loss and fading noise due to the pulse coherence. Since it is impossible to separate or compensate for these noise contributions, a more sophisticated experimental set-up is needed. As shown in fig. 1, an effective solution is to measure the complete SOP of the backscattered field, but this requires some further theoretical considerations. Actually, we have to take into account the optical splitter connected to the fiber under test (it can be a circulator as well as a directional coupler) which separates the forward path from the backward one. Referring to fig. 1, we can define two useful Müller matrices. R_{12} is the Müller matrix representing the optical path from the input of the splitter (point 1 in fig. 1) to the point where forward and backward path separate (point 2). R_{23} is the Müller matrix of the path from point 2 to the input of the polarization analyzer (point 3). The SOP measured by the analyzer can be expressed as follows: $\hat{s}_{Bm}(z) = R_{23}R_B(z)R_{12}\hat{s}_{in}$, where $R_B(z)$ is the matrix representing the round-trip propagation in the fiber [5], and $\hat{s}_{in}$ is the SOP at the input of the splitter (point 1). It can be noted that there is no control on the launched SOP, since, as we will show, the knowledge of $\hat{s}_{in}$ is not necessary. It is well known that the backscattered signal keeps memory of the initial SOP, and as a matter of facts $\langle R_B(z)\rangle = (M/3)$, where $\langle\cdot\rangle$ represents the ensemble average. If we assume that $R_B(z)$ is ergodic (as can be easily numerically verified), then the ergodic average is equal to the ensemble one, and we can write:

$$\langle \hat{s}_{Bm}(z)\rangle_\Delta = \frac{1}{\Delta}\int_\Delta \hat{s}_{Bm}(z)dz = \langle R_{23}R_B(z)R_{12}\hat{s}_{in}\rangle_\Delta = R_{23}\langle R_B(z)\rangle_\Delta R_{12}\hat{s}_{in} = \frac{1}{3}R_{23}MR_{12}\hat{s}_{in}$$

where $\langle\cdot\rangle_\Delta$ represents the ergodic average. Now it is easy to show that the signal $T(z)$ can be calculated from $\hat{s}_{Bm}$ only (i.e. from the SOP measured by the polarization analyzer only). It should be noted that $R_{12}\hat{s}_{in}$ is the SOP of the field at the fiber input (i.e. point 2): $R_{12}\hat{s}_{in} = \hat{s}_0$. Moreover $R_B(z) = MR^T(z)MR(z)$, and recalling that $R_{23}R_{23}^T$ is the identity matrix (as for any Müller matrix), it results:

$$3\langle \hat{s}_{Bm}(z)\rangle_\Delta \cdot \hat{s}_{Bm}(z) = (R_{23}MR_{12}\hat{s}_{in})\cdot(R_{23}R_BR_{12}\hat{s}_{in}) = (R_{23}M\hat{s}_0)^T R_{23}(MR^TMR)\hat{s}_0 = \hat{s}_f(z)\cdot[M\hat{s}_f(z)]$$

Now we can state that the signal $T(z)$ can be calculated as follows (the z dependence is omitted):

$$T(z) = \frac{1}{2}(1 + 3\langle \hat{s}_{Bm}(z)\rangle_\Delta \cdot \hat{s}_{Bm}(z)) = \frac{1}{2}[1 + \hat{s}_f \cdot (M\hat{s}_f)] \qquad (4)$$

Finally, the complete procedure for local beat length measurement is:

1. to measure the SOP of the backscattered field $\hat{s}_{Bm}(z)$;
2. to calculate $T(z)$ accordingly to eq. (4);
3. to perform the LCR analysis of $T(z)$ according to eq. (3).

Experimental set-up

The POTDR experimental set-up is shown in fig. 1. A high-resolution (64,000 sampling points) commercial OTDR was used to process and record the evolution of the backscattered power. Since the OTDR source optical bandwidth is too wide for POTDR measurements, the optical pulses were reformed by using a directly modulated external cavity laser followed by an erbium-doped fiber amplifier (EDFA). An acousto-optic modulator, placed after the EDFA, is necesary to block the spontaneous emission of the EDFA when the OTDR pulse is off. The backscattered field coming from the fiber under test through an optical circulator, is sent to an adjustable polarization analyzer and then to the OTDR detector. The polarization analyzer is composed by a rotating $\lambda/4$ waveplate followed by a fixed analyzer. To perform the backscattered field polarization analysis, 6 POTDR traces are acquired corresponding to 6 different positions of the rotating waveplate. Than the polarization ellipse is calculated for each point of the fiber, using a least square approximation algorithm. The interpolation error, averaged over the entire fiber length, is of the order of 2%.

This set-up lets to launch into the fiber under test pulses with a peak power sufficiently high to allow measurements on fibers more than 30 km long. The operating wavelength was 1532 nm. The pulse width was set to 5 ns, in order to achieve a spatial resolution of about 0.5 m that is consistent with the sampling step (0.6 m for the 40 km distance range). Based on our experience, this is highest resolution compatible with reliable measurements of the beat length (down to a few meters) that can be found in some high PMD telecommunication fibers.

Measurement results

Measurements were performed on a 23.6 km long cable, installed about 5 years ago between the ISCTI laboratory (Istituto Superiore delle Comunicazioni e delle Tecnologie dell'Informazione) located in Rome, and a shelter located in Pomezia. The optical link is composed of 10 cable sections spliced together. The first 9 sections are about 2.15 km long, the last one is 4 km long. The cable contains 80 single-mode fibers of three different types: 30 ITU-T G.652 standard step-index fibres, 30 ITU-T G.653 dispersion shifted fibres, and 20 ITU-T G.655 nonzero dispersion fibres. Out of these, seven G.652, seven G.653 and four G.655 fibers were characterized in terms of beat length.

We have applied the LCR analysis separately on each section of the link, because the sections show non uniform characteristics. For example, the upper graph of fig. 2 shows the evolution of the normalized power measured on a G.652 fiber (random fluctuations are evident). The lower graph shows the corresponding evolution of the beat length.

More results regarding G.652 fibers are shown in fig. 3. Each line refers to one fiber, and represents the evolution of the beat length averaged over the length of each section. Similar results are shown in fig. 4, referring to G.653 fibers, and in fig. 5, referring to G.655 fibers.

It can be seen that G.652 fibers are characterized by beat length values ranging between 10 and 110 meters. On the contrary, the beat length of G.653 (with the exception of section 4) and G.655 fibers assumes values between 10 and 30 meters. Hence, these two kinds of fiber are more birefringent. This could have been foreseen since G.653 and G.655 fibers have a more complicated index profile, which may induce a higher intrinsic birefringence.

Furthermore, G.652 fibers have lower intrinsic birefringence and consequently they should be more sensitive to extrinsic random perturbation. This may be the reason why they show larger fluctuations in the beat length values, compared with the other two kinds of fiber.

As far as the anomalous behavior of fibers in section 4 is concerned, it is unlikely to ascribe it to some sort of external perturbation. In fact it is hard to believe that a perturbation can at the same time increase the birefringence of G.652 fibers, decrease that of G.653 fibers and leave unaffected the G.655 ones. Most likely, section 4 of the cable behaves in a different way simply because its fibers may come from different production batches; however, at the time being we do not have any information supporting this hypothesis.

We have also measured the DGD of the fibers under test. On average, the PMD coefficient of G.652 and G.653 fibers is 0.032 and 0.231 ps/km$^{1/2}$, respectively. Such a result agrees with the larger birefringence of G.653 fibers. On the contrary, even if G.655 fibers have almost the same birefringence as G.653 fibers, their average PMD coefficient is as low as 0.061 ps/km$^{1/2}$. This result may be explained assuming that G.655 fibers have shorter correlation lengths with respect to G.653 fibers.

Acknowledgements

Authors are indebted to ISCTI for permission to use the Roma-Pomezia link and to S. Cascelli, M. Guglielmucci and L. Lattanzi for technical help during measurements.

A. Galtarossa, L. Palmieri and A. Pizzinat also thank IST/ATLAS project and MURST 40% project (prot. 9909198913) for supporting their activity.

References

[1] W. Weiershausen, R. Leppla, F. Küppers and H. Schöll, 25th ECOC (invited paper), Nice, (1999).

[2] F. Heissman, 24th ECOC (tutorial paper), Madrid, Spain (1998).

[3] C. R. Menyuk, 25th OFC (tutorial paper), Baltimore, Maryland (2000).

[4] A. Galtarossa, L. Palmieri, M. Schiano and T. Tambosso, Opt. Lett., vol. 26, 384 (2000).

[5] F. Corsi, A. Galtarossa, L. Palmieri, Journal of Lightwave Technology, Vol. 17, 1999.

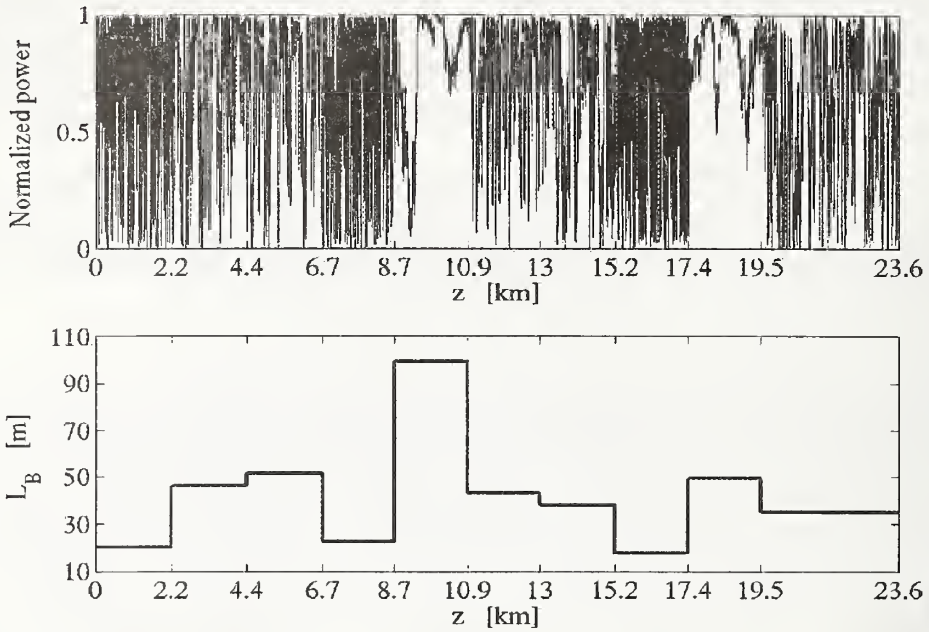

Figure 2: Evolution of the normalized power (upper window) and the corresponding beat length profile (lower window) of a G.652 fiber link.

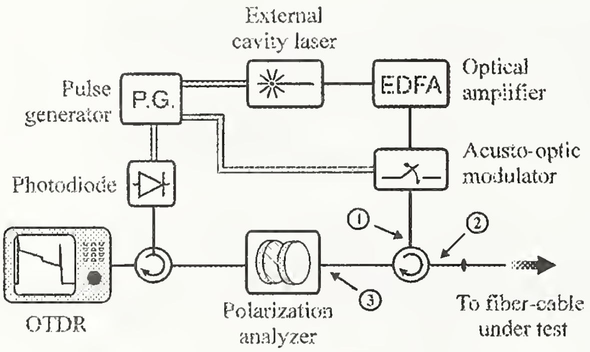

Figure 1: Scheme of the experimental set-up.

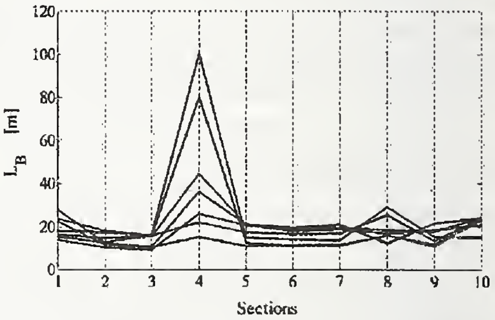

Figure 4: Beat length evolution along seven installed G.653 fibers.

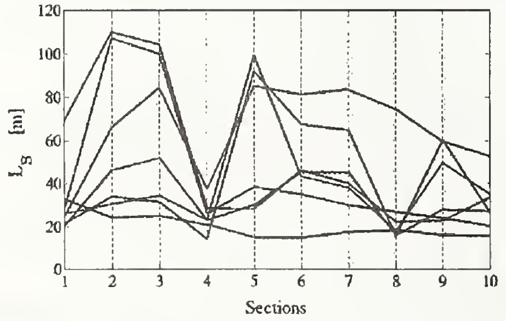

Figure 3: Beat length evolution along seven installed G.652 fibers.

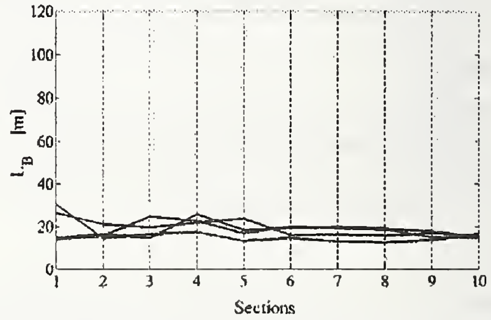

Figure 5: Beat length evolution along four installed G.655 fibers.

Accurate Spectral Characterization of Polarization Dependent Loss

R. M. Craig
National Institute of Standards and Technology, 325 Broadway, Boulder, CO 80303

Abstract – Building on previous work, a rapid, automated, non-mechanical measurement system for spectral characterization of polarization-dependent loss is presented. A deterministic fixed-states method in conjunction with real-time calibrated spectral information is used to infer wavelength-dependent Mueller matrix elements from power ratios at specific polarization states. Voltage-modulated liquid-crystal variable retarders set the input polarization states. A narrow, voltage-tuned filter generates a wavelength sweep from a broadband source. The sweep is calibrated in real-time by hydrogen cyanide reference lines. Actively balanced photodetection is employed to achieve low noise signals. I present polarization-dependent loss measurements from 0.0003 to 0.30 dB at 1550 nm to verify performance and also present results from artifact calibration standards of an all-fiber design.

Introduction

Until the advent of dense wavelength-division multiplexing (DWDM) systems, polarization dependent loss (PDL) was usually characterized only at a specific wavelength [1]. More recently, however, the wavelength dependence of PDL (WPDL) has assumed greater importance. A modification of a previously reported, deterministic fixed-states technique [2] has been implemented that allows the simultaneous characterization of wavelength dependence. The goal is to establish a capability for rapid measurement of WPDL to a resolution finer than 0.005 dB without sacrificing accuracy. This approach uses a non-mechanical technique employing ratio detection and simultaneous spectral calibration that is faster than most tunable-laser systems and more accurate than optical spectrum analyzers [3]. In addition, new results from an all-fiber WPDL artifact reference are presented. This artifact is intended to become a NIST Standard Reference Material (SRM) with a nominal PDL of 0.1 dB for the calibration of commercial instrumentation.

Concept

This method is a further variation of a matrix technique developed by Favin et al. [4], and relies solely on power ratio measurements over a wavelength range using specific polarization states. As in reference [2], four well defined polarization states are necessary to determine the first-row Mueller matrix elements of a component. The global polarization dependence of transmittance can be determined from these (wavelength dependent) matrix elements.

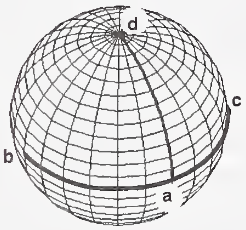

Figure 1A: Initial Poincaré trajectories of the liquid-crystal variable retarder (LCVR) pair.

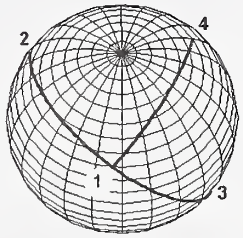

Figure 1B: LCVR trajectories following birefringent displacement

Because the measurement depends only on the relative coordinates of the four states, the only requirements on the set are that they maintain relative angular separations of 90° about the origin of the polarization (Poincaré) sphere, cf. Fig 1.

The four polarization states are produced by

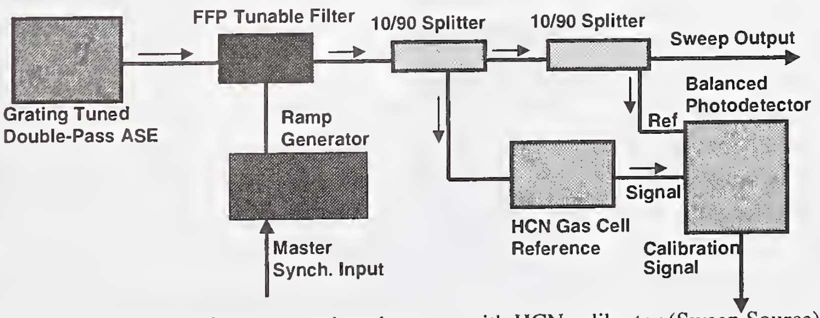

Figure 2: Diagram of swept wavelength source with HCN calibrator (Sweep Source)

two liquid-crystal variable-retarder (LCVR) units in series that hold the state during a wavelength sweep of a low-coherence polarized beam. The beam is generated by a double-pass amplified-spontaneous-emission (ASE) source followed by a fiber-Fabry-Perot tunable-filter (FFP-TF) driven by a ramp generator. The voltage ramp drives the filter across a selectable portion of the ASE spectrum in a repetitive sweep. This swept output passes through splitters and a NIST hydrogen cyanide (HCN) optical wavelength reference cell (SRM 2519), as shown in Fig. 2, which produces intensity modulated output. The HCN absorption spectrum is measured by an amplified differential photodetector capable of 50 dB common-mode-rejection through active gain balancing. The absorption peaks are fit by a least squares quadratic to known peak wavelengths following each scan, providing real-time spectral calibration of each sample point. An example of the absorption signature and the subsequent peak fit are shown in Fig. 3.

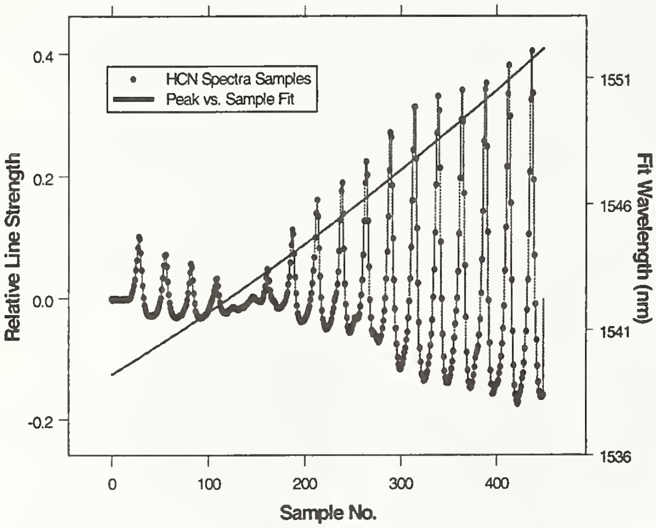

Figure 3: Typical P-branch HCN absorption signature from 1539 to 1551 nm with a quadratic calibration fit .

Following the LCVR units, the light is transmitted by a single mode fiber with arbitrary but relatively stable birefringence through a splitter to both the device-under-test (DUT) and to a second actively balanced photodetector. This detector is operated in a logarithmic ratio mode and senses the four output power ratios ($I_1(\lambda)\ldots I_4(\lambda)$). Input power ratios ($I_a(\lambda)\ldots I_d(\lambda)$) are measured in the same way with the DUT removed to establish a baseline system response. Following wavelength registration to account for drift, the four first-row Mueller matrix elements ($m_{11}(\lambda)\ldots m_{14}(\lambda)$) are calculated from these power ratios as in reference [2]. Information about the global transmittance extrema are contained in the first row matrix elements. The transmittance extrema, $T_{\min}(\lambda)$ and $T_{\max}(\lambda)$ are

$$T_{\max}(\lambda)=m_{11}(\lambda)+\sqrt{m_{12}(\lambda)^2+m_{13}(\lambda)^2+m_{14}(\lambda)^2} \quad ,$$

$$T_{\min}(\lambda)=m_{11}(\lambda)-\sqrt{m_{12}(\lambda)^2+m_{13}(\lambda)^2+m_{14}(\lambda)^2}$$

so $WPDL \equiv PDL(\lambda)=10\log\left[T_{\max}(\lambda)/T_{\min}(\lambda)\right]$ which applies over the entire polarization-state space and wavelength range.

Implementation

Figure 4 shows a schematic of the measurement system. The system consists of five major sections: ASE sweep source, cf. Fig. 2, LCVR polarization state generator, measurement and calibration section, clock, and control computer. The polarization-modulated light is connected to the DUT through a spectrally flattened 80/20 splitter and the power ratio is sampled through single-mode fiber and fiber connectors. Prior to any measurement, the empty

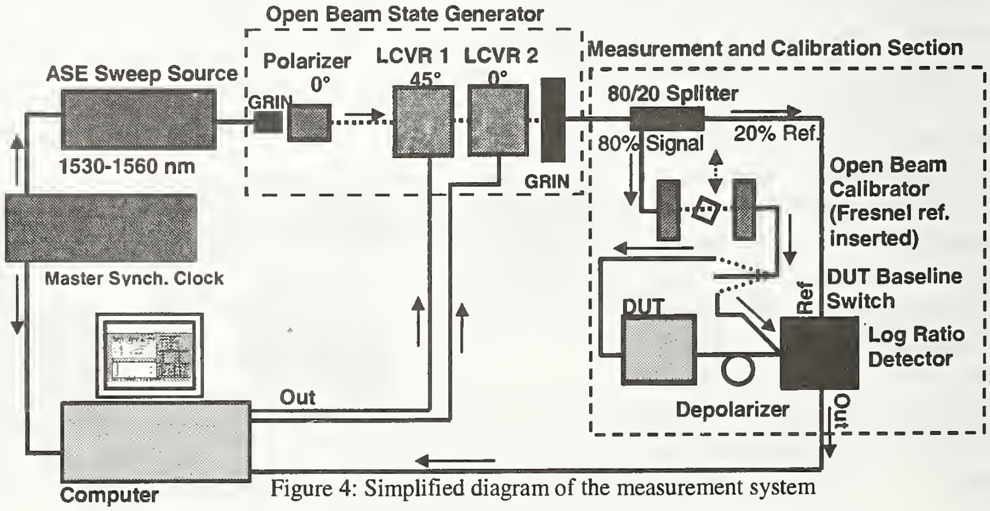

Figure 4: Simplified diagram of the measurement system

calibration cavity is switched directly to the detector for an initial baseline after which the Fresnel reference block is inserted at the appropriate angle to generate a calibration signal. Anti-reflection coated aspherical lenses are used to collimate the open beam and a polished BK7 glass cube acts as the Fresnel reference. The calibration signal is compared to the calculated value to give a calibration multiplier for all subsequent measurements during that session. Following calibration, the Fresnel reference is removed and another baseline is run for the DUT. The DUT is then inserted and switched in. The DUT output is depolarized with 40 m of high NA (0.37) multimode fiber to reduce the impact of PDL in the detector. Finally, the DUT WPDL signal is sampled at 450 points for each 12 nm wavelength scan. A scan period of 285 ms is required for each polarization state, after which the state is changed to the next in the series. An entire WPDL scan over the range of 1539 – 1551 nm takes less than 5 seconds including data processing time, which is currently the limiting factor.

Uncertainties

The design of this measurement system is both simpler and more sophisticated than that described in ref. [2] so that most uncertainties are now reduced by taking ratios. Items 1 and 2 below outline the two major systematic uncertainties in polarization and power that, together, comprise over 90% of the total systematic contributions. Discussion of minor effects will be deferred to a forthcoming publication. Values listed correspond to 1σ deviations in either signal power or polarization at 1545 nm.

1. *Polarization state accuracy.* Polarization state accuracy depends on both the measuring polarimeter and the LCVR bias calibration. I find that linear states exhibit an uncertainty of 0.69 % while the circular states have a 2.0 % uncertainty.
2. *System internal PDL variation.* The system retardance elements contribute their own PDL (0.02 dB) to that of the DUT. Given a maximum observed drift of the internal PDL over 5 minute intervals, this yields an uncertainty of 0.025 %.
3. *Propagated measurement system uncertainty.* Using the uncertainties above inherent to the measurement system, an error propagation model, based on the defining equations, calculates 0.0035 dB at 0.1 dB of PDL.
4. *PDL measurement repeatability.* Ten undisturbed measurements of a 0.12 dB BK7 WPDL were made following the initial baseline measurement. The random 1σ uncertainty averaged over all wavelengths yields 0.0012 dB as the effective single-sweep system noise and incorporates all effects that average down such as optical interference and detector noise. This component does not incorporate residual systematic wavelength dependence.
5. *Combined standard uncertainty.* Items 3 and 4 above are assumed uncorrelated, so the root-square-sum (RSS) at the 0.1 dB level is (0.0012 dB + 0.0035 dB) RSS = 0.0037 dB.
6. *Connector uncertainty.* As in reference [2], a significant source of uncertainty, which is not inherent to the LCVR system, is variations in measured PDL of DUT artifacts with connectorized pigtails following disconnection and reconnection. This could be explained by connector alignment (core offset) errors. For those artifacts, we add an additional 0.0029 dB uncertainty.

Stress and thermal drifts in pigtail birefringence must be minimized over the course of a measurement. The measurement method is sensitive to small errors in the matrix elements,

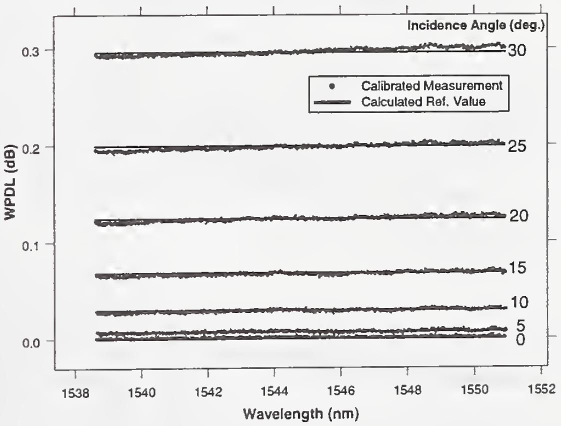

Figure 5: Open-beam BK7 artifact data calibrated at 30° incidence. Centerline is the calculated WPDL value. Residual wavelength slope falls within 2σ uncertainty.

such as those due to rotated, and therefore uncompensated, PDL between the baseline and DUT measurement. For this reason, one should calibrate the system prior to a measurement series.

Results

The primary artifact chosen to test the performance of the system provides a calculable PDL of moderate accuracy. The artifact consists of an open beam launcher/collimator followed by a 2.54 cm, polished BK7 glass cube. BK7 is convenient to use and has a well-known index of refraction. The cube is mounted on a rotation stage with 5' resolution. The beam pickup asphere is translated to compensate for beam displacement following rotation. Calculated (Fresnel) and measured WPDL values as a function of input angle are presented in Fig. 5 and are in good agreement. The residual system PDL was measured at 0° (normal incidence) as a 0.0014 ± 0.0006 dB offset over all wavelengths. A residual slope indicates a systematic uncertainty.

All-Fiber PDL Artifact Results

As mentioned in [5], a series of all-fiber PDL artifacts based on fusion-spliced sections of single-mode, polarizing, and multimode fiber was constructed. These artifacts form the basis of a new calibration transfer standard SRM at 0.1 dB. The artifact section is a few millimeters of polarizing fiber (18 dB/m extinction) that provides relatively stable PDL over the range of 0 - 40 °C. Some recent WPDL measurement results are presented in Fig. 6 using three SRM prototypes. A nearly constant positive slope is typical of polarizing fiber and is evident, with structure, in the data. This measurement system will be used to characterize WPDL in SRM artifacts.

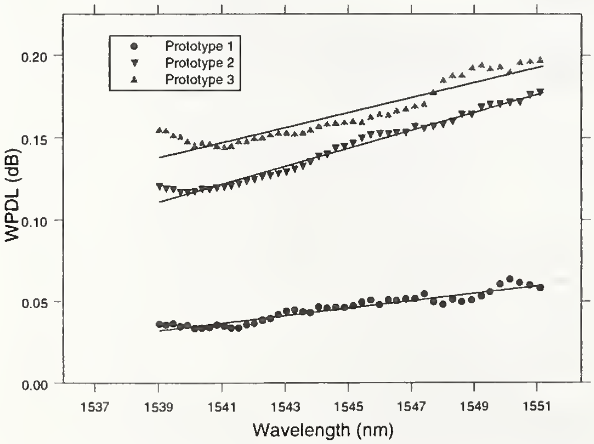

Figure 6: Wavelength dependent PDL for three SRM prototypes. A least-square fit line indicates trend.

Conclusions

An accurate, rapid, non-mechanical technique of characterizing the wavelength dependence of polarization-dependent loss for both single-mode and bulk-optic devices has been developed that offers advantages over more traditional methods. The technique demonstrates a single measurement uncertainty of 0.0037 dB and 0.0014 ± 0.0006 dB offset from PDL values calculated for an open-beam artifact. Additional measurement sweeps can be quickly averaged to improve random uncertainty by $1/\sqrt{N}$. Overall accuracy is dependent on calibration to a primary artifact.

Three WPDL artifact standard candidates have been tested and show the expected positive slope. Measurement resolution is sufficient to discern the wavelength dependent structure.

References

[1] M. Gadonna and A. Mabrouki "Polarization Sensitivity Measurements Methods for Passive Optical Components," *Conference on European Fibre Optic Communications and Networks, EFOC&N '93,* The Hague, Netherlands, Technical Digest, pp. 65-67.

[2] R. M. Craig, S. L. Gilbert and P. D. Hale, "High Resolution, Nonmechanical Approach to Polarization Dependent Transmission Measurements," *IEEE J. Lightwave Technol.*, vol. 16, pp. 1285-1294, July 1998.

[3] D. Derickson, ed., *Fiber Optic Test and Measurement.* Prentice Hall PTR, 1998, chap 9.5.

[4] D. L. Favin, B. M. Nyman, and G. Wolter, "System and Method for Measuring Polarization Dependent Loss," *U. S. Patent 5371597*, Dec. 6 1994; B. M. Nyman, D. L. Favin, and G. Wolter, "Automated System for Measuring Polarization Dependent Loss," *OFC '94*, San Jose, California, U.S.A., Technical Digest, pp. 230-231.

[5] R. M. Craig, S. L. Gilbert and P. D. Hale, "Accurate Polarization Dependent Loss Measurement and Calibration Standard Development," *SOFM '98*, Boulder, Colorado, Technical Digest, pp. 5-8 (1998).

Heterodyne system at 850 nm for measuring photoreceiver frequency response

Paul D. Hale[a] and C. M. Wang
National Institute of Standards and Technology
325 Broadway
Boulder, Colorado 80303

Abstract

We describe an 850 nm heterodyne system for measuring frequency response, that uses commercially available tunable external-cavity diode lasers. The system's frequency resolution and reproducibility are characterized. The advantage of a frequency response transfer standard consisting of a photodiode combined with an rf power-sensor is reviewed. The expanded uncertainty (k=2) for calibration of an 850 nm transfer standard between 5 MHz and 25 GHz is found to be about 1.1 % (0.05 dB).

Introduction

Because of the high demand for test equipment for short-wavelength applications, such as Gigabit Ethernet and Fibre Channel, NIST has constructed a heterodyne frequency response measurement system operating at 850 nm. Components, such as reference receivers for eye-pattern testing require frequency response characterized with uncertainties of 0.3 dB or less[1]. Customers of standards laboratories often prefer that transfer standard receivers be calibrated with uncertainties that are a factor of 3 to 4 smaller. The use of the heterodyne method for photoreceiver frequency response measurement is certainly not new[2, 3, 4, 5, 6, 7]; however, description of work applicable to the short-wavelength telecommunications window has been limited, and reported with an associated uncertainty larger than 0.3 dB[2, 8]. In this work we report the calibration of a combined photodiode/rf power-sensor transfer standard and its expanded uncertainty of 0.05 dB. We estimate the expanded uncertainty for calibration of a stand-alone photodiode to be about 0.1 dB.

Heterodyne principle

The underlying concepts of precision heterodyne photoreceiver frequency response measurements have been described in detail previously[6, 9]. The heterodyne beat note at frequency f is generated by combining beams from two "single-frequency" lasers in a free-space beamsplitter and mixing them on a photodiode. The photodiode is connected to an external bias network and dc blocking capacitor. We assume the laser beams have the same polarization and spatial mode after passing through the beamsplitter. A dc return path must be provided for the photodiode, either through a bias T or through a matching resistor or attenuator. The photocurrent i_p generated by the photodiode due to the incident optical power is given by

$$i_p(f,t) = (P_{O1} + P_{O2})R(0) + 2\sqrt{P_{O1}P_{O2}}R(f)\cos(2\pi f t)\,, \tag{1}$$

where $R(f)$ is the responsivity of the detector (in A/W) at frequency f and P_{Ok} is the power from the kth laser. The first term on the right side is the dc photocurrent i_{dc} that flows through the bias supply, and the second term is the rf photocurrent i_{rf} that flows through the rf load (the rf power-sensor) through a dc blocking capacitor. The mean squared photocurrents generated by the photodiode are

$$\begin{aligned} \left\langle i_{dc}^2 \right\rangle &= (P_{O1} + P_{O2})^2 R^2(0) \\ \left\langle i_{rf}^2 \right\rangle &= 2P_{O1}P_{O2}R^2(f)\,. \end{aligned} \tag{2}$$

If P_{O1} is nearly equal to P_{O2}, then $2(P_{O1}P_{O2})$ is, to first order, equal to $0.5(P_{O1}+P_{O2})^2$. The normalized frequency response $\Re^2(f)$, which is defined as $R^2(f)/R^2(0)$, can then be found by taking the ratio of the rf electrical power P_{rf} to half the dc electrical power delivered to a load Z_L,

---

[a] Supported in part by the Office of Naval Research and the Space and Naval Warfare Systems Center.

$$\Re^2(f) \equiv \frac{R^2(f)}{R^2(0)} \simeq \frac{2P_{rf}}{\langle i_{dc}^2 \rangle Z_L}. \tag{3}$$

P_{rf} is a function of frequency and includes corrections for the sensor's calibration factor and electrical mismatch, and is the power that would be delivered to an ideal load Z_L=50 Ω[10]. The normalized frequency response is expressed in decibels as 20log[$\Re(f)$].

The ratio on the right side of eq (3) is insensitive to variations in optical power and simplifies the measurement apparatus because only the total photocurrent in the photodiode need be monitored, instead of the power coupled to the detector from each laser. $\Re^2(f)$ is an unbiased metric for comparing measurements made with different systems. A common practice when comparing measurements of frequency response is to add an offset to each curve to make the responses equal at some frequency or over some range of frequencies. This practice can be misleading since it assumes that both systems impart negligible error at that frequency.

Combined photodiode/rf power-sensor transfer standard

Uncertainty in the measurement of a photodiode's frequency response using eq (3) includes the calibration uncertainty of the power-sensor used to measure P_{rf}. Combined with other user uncertainties, this may give an unacceptable uncertainty for the intended application. The uncertainty can be reduced by calibrating the frequency response of the photodiode combined with the rf power-sensor and bias T or attenuator used for dc return. This method totally eliminates uncertainties due to power-sensor calibration and impedance mismatch. The combined frequency response $\mathbb{R}^2(f)$ includes the power-sensor's calibration factor and impedance mismatch, and is given by

$$\mathbb{R}^2(f) = \frac{\Re^2(f)}{C} = \frac{2P_m}{\langle i_{dc}^2 \rangle R_L}. \tag{4}$$

In eq (4), P_m is the indication of the power meter after zeroing and calibration against the 50 MHz reference signal (from the power meter) using a calibration factor of 100 %. C is a frequency-dependent factor that

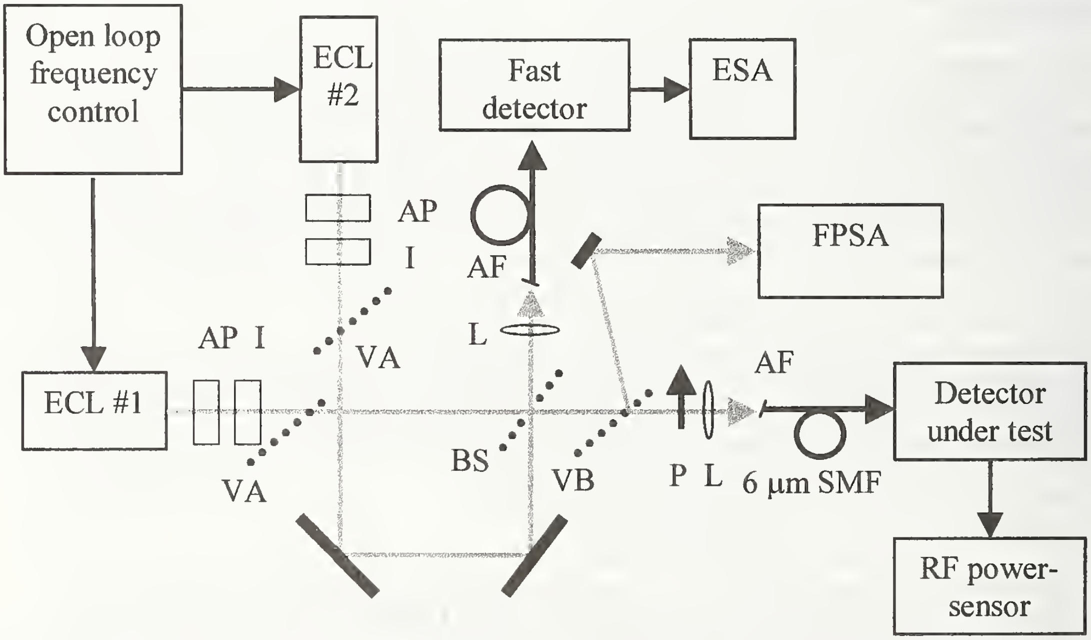

Figure 1. Simplified schematic diagram of 850 nm heterodyne system. Frequency control and data acquisition is performed by a personal computer. Labeled components are external cavity laser (ECL), anamorphic prism pair (AP), isolator (I), beamsplitter (BS), variable attenuator (VA), variable beamsplitter (VB), polarizer (P), lens (L), angled fiber end (AF), Fabry-Perot spectrum analyzer (FPSA), single-mode fiber (SMF), and electrical spectrum analyzer (ESA).

includes power-sensor calibration and mismatch correction factors but does not need to be known. The relative optical modulation depth of an arbitrary source can be found using a transfer standard with calibrated $\mathbb{R}^2(f)$. Uncertainty can be reduced further, at the expense of functionality[9], by normalizing $\mathbb{R}^2(f)$ to $\mathbb{R}^2(50\,\text{MHz})$. This normalization eliminates uncertainty due to the power meter's 50 MHz reference source.

850 nm heterodyne measurement system

A simplified schematic diagram of the heterodyne system is shown in figure 1. The system uses two single-mode semiconductor lasers that are grating-tuned near 850 nm. The lasers are adjusted so that nearly equal power from each laser is delivered to the device under test (DUT) as measured by the bias-current monitor. The combined laser beams pass through a polarizer so that the signal from each laser is in the same polarization state when it reaches the DUT, ensuring nearly 100% modulation depth. The frequency of each laser can be tuned by tilting the grating with a piezoelectric transducer to give beat frequencies between a few megahertz and several hundred gigahertz. The voltage applied to the transducer is controlled by a computer and digital-to-analog converter. The beat frequency is measured with an electrical spectrum analyzer since the frequency jitter is too large to properly trigger an rf counter. As the frequency is scanned, data are acquired automatically by the computer.

Resolution

To characterize the frequency resolution of the measurement system, we measured electrical "interference fringes." The electrical output of a photoreceiver was split in a three-resistor power divider. One arm of the divider was connected to a long coaxial line terminated by a 45 Ω resistor. The other arm of the divider went to an rf power-sensor. The frequency of one of the lasers was swept and the rf power and dc photocurrent were recorded for four different scans. The variance of the measured signal can be expressed in a Taylor-series expansion as

$$\sigma_{Total}^{2} \approx \sigma_{N}^{2} + \sigma_{J}^{2}\left(g'(f)\right)^{2}, \tag{5}$$

where σ_{Total}^2 is the total measured signal variance, σ_N^2 is the additive noise variance, σ_J^2 is the frequency jitter variance, and $g'(f)$ is the derivative of the ideal response curve. To estimate the quantities in eq (5), we first selected an appropriate set of frequencies f_i where $i = 1, 2, \ldots n$. A cubic B-spline was fit to the 4 combined scans. The result is shown in figure 2. For each scan, the frequency response at f_i and the first-order derivative $g'(f_i)$ are estimated using the B-spline. The sample variance s_i^2 at f_i is then calculated from the response of each of the 4 scans. The jitter is the square root of the slope b of the simple linear fit: $s_i^2 = a + b(g'(f_i))^2$. The highest resolution achievable is about 0.48 MHz, and is limited by the scan rate, laser frequency jitter, and time constants of the data acquisition equipment.

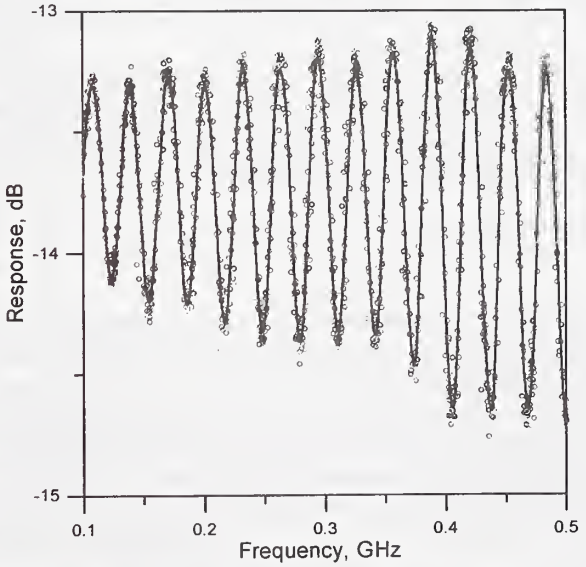

Figure 2. Results of four separate high-resolution scans (°) and B-spline fit to data (solid line) to estimate frequency jitter.

Environmental effects (reproducibility)

The combined response of a 50 GHz bandwidth rf power-sensor, adapter, and matched photodiode with 12 GHz nominal bandwidth was measured three times over a span of seven months. Each measurement consisted of three or four scans that were then kernel smoothed[7, 9] to estimate the response in 50 MHz increments from 50 MHz to 25 GHz. At the beginning of each scan, the power-sensor was connected to the power meter's reference signal and calibrated using a calibration factor of 100 %. The dc photocurrent due to each laser was matched at about 50 μA., giving about –42 dB(re:1 mW) rf power at low frequencies. The typical response and reproducibility with and without normalization is shown in figure 3. The uncertainty after normalization is similar to that observed on the 1319 nm heterodyne system, about 0.12 % (0.005 dB) below 20 GHz. Uncertainty in the un-normalized measurements is typically 0.3 % (0.018 dB).

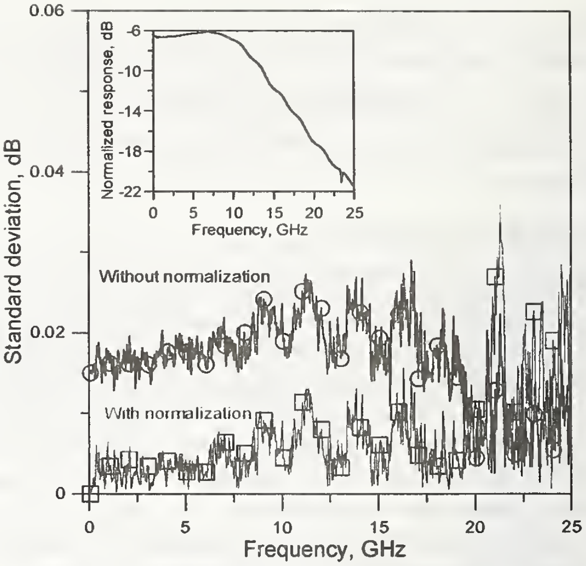

Figure 3. Standard deviation of the three measurements with and without normalization to the 50 MHz value. Inset shows nominal normalized response of photodiode combined with power-sensor.

Uncertainty analysis

The measurement uncertainty of the normalized response of a combined photodiode/rf power-sensor transfer standard in the 850 nm heterodyne measurement system is similar to that previously described for the NIST 1319 nm heterodyne system[9]. The dominant terms are due to the power meter's range-scaling uncertainty (0.5 %) and reproducibility (0.12 %). The combined uncertainty (root sum of squares) is then 0.52 % and the expanded uncertainty, with coverage factor k=2, is 1.1 % (0.05 dB). Uncertainty for measurement of the photodiode response alone would include the un-normalized reproducibility and the power-sensor's calibration uncertainty (about 1 % , 1σ, below 20 GHz), giving a combined uncertainty of about 1.1 % and expanded uncertainty of 2.3 % (0.1 dB). Also, mismatch uncertainty or mismatch correction uncertainty would need to be included. Although using a combined photodiode/rf power-sensor transfer standard may not be suitable for all applications, the uncertainty in its calibration is more than a factor of 2 smaller than that for a photodiode alone.

---

[1] *Optical interfaces for equipments and systems relating to the synchronous digital hierarchy*, CCITT (now ITU-TS) recommendation G.957, Geneva, 1990.

[2] L. Piccari and P. Spano, "New method for measuring ultrawide frequency response of optical detectors," *Electron. Lett.* **18**, 116-118 (1982).

[3] S. Kawanishi, A. Takada, M. Saruwatari, "Wide-band frequency-response measurement of optical receivers using optical heterodyne detection," *J. Lightwave Technol.* **7**, 92-98 (1989).

[4] T. S. Tan, R. J. Jungerman, S. S. Elliot, "Optical receiver and modulator frequency response measurement with a Nd:YAG ring laser heterodyne technique," *IEEE Trans. Microwave Theory Tech.* **37**, 1217-1222 (1989).

[5] R. T. Hawkins, M. D. Jones, S. H. Pepper, and J. H. Goll, "Comparison of fast photodetector response measurements by optical heterodyne and pulse response techniques," *J. Lightwave Technol.* **9**, 1289-1294 (1991).

[6] D. A. Humphreys, "Measurement of high-speed photodiodes using DFB heterodyne system with microwave reflectometer,“ SPIE Proceedings Vol. 1680, *High-speed electronics and optoelectronics conference,* 138-152 (1992).

[7] P. D. Hale, C. M. Wang, R. Park, and W. Y. Lau, "A transfer standard for measuring photoreceiver frequency response," *J. Lightwave Technol.*, **14** 2457-2466, 1996.

[8] New Focus Inc., *1999/00 Catalog, Vol.10*, p. 86.

[9] P. D. Hale and C. M. Wang, "Calibration service of optoelectronic frequency response at 1319 nm for combined photodiode/rf power-sensor transfer standards," Natl. Inst. Stand. Technol. Spec. Publ. 250-51, Dec. 1999.

[10] *Fundamentals of rf and microwave power measurements*, Hewlett-Packard Application Note 64-1A, 1997.

Time-domain measurement of the frequency response of high-speed photoreceivers to 50 GHz*

Tracy S. Clement, Paul D. Hale, Kevin C. Coakley, and C. M. Wang
National Institute of Standards and Technology
325 Broadway, Boulder, CO 80303
clementt@boulder.nist.gov

Abstract

We determine the frequency response of high-speed photoreceivers from time-domain measurements collected with a 50 GHz sampling oscilloscope. In order to obtain accurate results, it is important to correct the signals for time-base distortion in the oscilloscope, electrical mismatch, oscilloscope jitter, laser pulse width, oscilloscope frequency response, and nonlinear response of the detector. Results are compared to the response obtained from a calibrated heterodyne system, and they differ by less than ±0.1 dB up to 25 GHz, and by less than ±1.0 dB at 50 GHz.

Introduction

Accurate measurement of the response of high-speed photoreceivers is necessary for applications in high-speed optoelectronic systems such as Gigabit Ethernet and Fibre Channel. We have developed a method for measuring the response of high-speed photoreceivers at frequencies up to 50 GHz by use of a sampling oscilloscope. Historically, both impulse and CW excitation have been widely used to characterize high-speed photoreceivers. Because of the extreme differences in peak powers used in these two families of measurement methods, it has been suggested that the measurement method should depend on the intended application of the photoreceiver[1]. Heterodyne methods have been shown to be extremely accurate[2], but can be very slow and give only the magnitude of the response. Time-domain measurements can be performed very quickly and can give both the magnitude and phase of the response. Work has been done previously by Hawkins et al. to compare heterodyne measurements and oscilloscope-based impulse-response measurements[3]. In our work we correct the impulse response measurements for the effects of oscilloscope frequency response, jitter, and laser pulse width previously considered by the Hawkins group, and we extend their work by correcting for time-base distortion, electrical mismatch, and measurement nonlinearity.

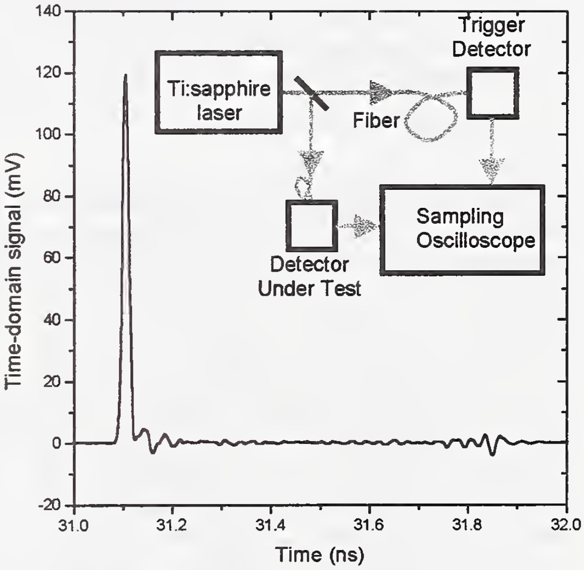

Figure 1. Time-domain photodiode signal. (Inset: schematic of time-domain measurement system.)

Experimental configuration

The inset of figure 1 shows a schematic of the time-domain measurement system. A mode-locked, Ti:sapphire laser provides pulses with a full-width at half-maximum (FWHM) less than 100 fs at 800 nm, with a repetition rate of approximately 80 MHz. The laser beam is split to provide an optical pulse to the detector under test in one arm and a trigger signal for the oscilloscope in the other arm. Reflective neutral-density filters provide attenuation in each arm. The sample arm contains 15 cm of single-mode fiber, which is connected to the detector under test. Dispersion in the optical fiber broadens the optical pulse to $\tau_p \approx 180$ fs FWHM. The optical pulse is convolved with the photoreceiver response in the time domain. We correct for the measured pulse width in the frequency domain (assuming a Gaussian pulse shape),

$$F(\omega) = \frac{F_{observed}(\omega)}{\exp\left\{-\frac{\omega^2 \tau_p^2}{8\ln(2)}\right\}}. \qquad (1)$$

---

* Publication of the U.S. Government. Not subject to copyright in the United States.

We make every effort to ensure that the optical pulse is as short as possible, which results in a very small correction for the convolution with the finite width pulse (3.5×10^{-3} dB at 50 GHz).

The measurements reported here are performed with a commercially available photodiode having a 25 GHz nominal electrical bandwidth. The photodiode is packaged with an internal 50 Ω matching resistor and has an external responsivity of about 0.2 A/W. The photodiode is connected to a 50 GHz sampling oscilloscope, where the response to the ultrashort optical pulses is sampled over a 10 ns time interval, just under the repetition period of the laser. Figure 1 shows a portion of a typical time-domain signal. The pulse duration is 15.7 ps FWHM. An electrical reflection is clearly visible at 750 ps after the peak of the pulse.

In order to improve the signal-to-noise ratio, 100 waveforms are acquired from the oscilloscope in just over two minutes. If the waveforms are averaged internally by the oscilloscope, drift acts to broaden the pulse, and the response in the frequency-domain is reduced by 1.4 dB at 50 GHz. To compensate for the drift, we align the individual waveforms before averaging (using an algorithm based on cross-correlation of all possible pairs of waveforms[4]). Although it is marginally slower to acquire individual waveforms from the oscilloscope, the time-domain technique still has the advantage of increased speed of data acquisition over that of a traditional heterodyne method. For example, it takes less than fifteen minutes to obtain 100 data sets at each of six different laser powers with the time-domain method, while the heterodyne method takes several hours.

Time-base distortion and jitter correction

Time-base distortion (TBD) is a deterministic deviation in the sample times of the oscilloscope from ideal, evenly spaced sample times. An estimate of the TBD during the same time window as in the photodiode measurements is determined by acquiring multiple sine waves with the oscilloscope and analyzing the data with an efficient least-squares algorithm[5]. The time axis of the averaged waveform is adjusted by the TBD estimate, and the resulting signal is interpolated onto an evenly spaced time grid using a regression spline model[6]. The signal is then transformed to the frequency domain using a fast-Fourier transform. In figure 2, the black curve shows this frequency-domain response of the photodiode up to 50 GHz. The ripple on the signal comes from multiple reflections between the photodiode and the oscilloscope, and must be corrected to determine the frequency response.

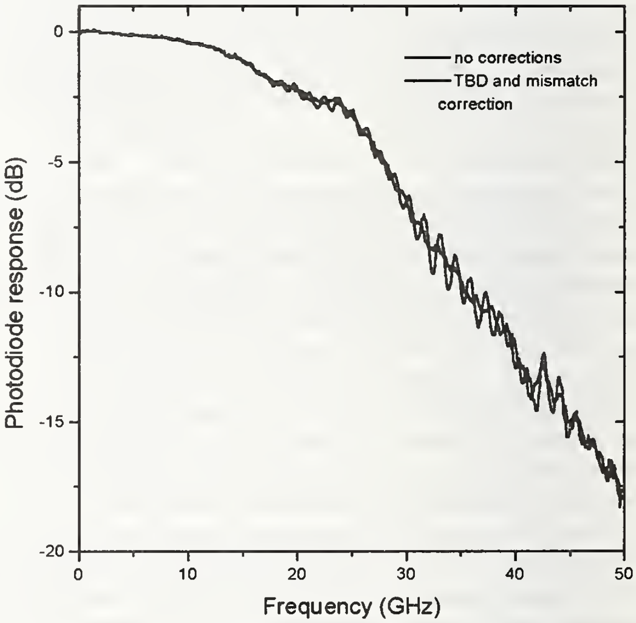

Figure 2. Photodiode frequency response with and without TBD and mismatch corrections

The effect of jitter on an averaged signal is that of a lowpass filter[7]. The variance of the measured signal can be expressed in a Taylor-series expansion as

$$\sigma_{Total}^{2} \approx \sigma_{N}^{2} + \sigma_{J}^{2}\left(\frac{dV}{dt}\right)^{2}, \tag{2}$$

where σ_{Total}^2 is the total measured signal variance, σ_N^2 is the additive noise variance, σ_J^2 is the jitter variance, and dV/dt is the derivative of the ideal time-domain waveform. Typically $\sigma_J \approx 1.1$-1.2 ps for our work. $F(\omega)$ is then multiplied by $\exp(\sigma_J^2\omega^2/2)$ to deconvolve the jitter effects.

Mismatch and oscilloscope response correction

Electrical mismatch between the photoreceiver and the oscilloscope causes multiple reflections and dispersion of the time-domain signal as seen in figure 1. Reflection coefficients for both the photoreceiver and the oscilloscope are measured from 100 MHz to 50 GHz with a vector network analyzer. The measured signal in the frequency-domain, $F(\omega)$, can be corrected for mismatch to give the actual signal, $F(\omega)_{pd}$, generated by the photodiode,

$$F(\omega)_{\mathrm{pd}} = F(\omega)\times(1-\Gamma_s\Gamma_{\mathrm{pd}}), \tag{3}$$

where Γ_s is the electrical reflection coefficient of the oscilloscope, and Γ_{pd} is the electrical reflection coefficient of the photodiode.

We choose not to window the data in the time-domain[3] to remove the reflections because the initial impulse response and its reflections overlap. Thus, windowing would remove an unknown portion of the pulse and introduce an unknown amount of error in the frequency response. Inserting a delay line between the photodiode and the oscilloscope could reduce the overlap of the signal with the reflection, but the effects of the delay line would also need to be measured and accounted for. In addition, windowing the data can introduce incorrect information at low frequencies.

The gray curve in figure 2 shows the frequency-domain response of the photodiode after mismatch and TBD correction. The magnitude of the ripples is greatly reduced by the mismatch correction, although there is still some small effect remaining, especially above 30 GHz. The importance of the TBD correction is especially apparent when combined with the mismatch correction. Without TBD correction, the ripples due to electrical mismatch are only partially reduced because the spacing of the electrical reflections is distorted by the TBD.

The frequency-domain photodiode response must be corrected for the response of the 50 GHz oscilloscope. The magnitude response of the oscilloscope is measured by direct comparison to a calibrated power meter, and the phase response of the sampling oscilloscope is determined with a "nose-to-nose" measurement[8].

Laser power dependence

Although the average power incident on the photodiode is relatively low, the peak power during the femtosecond laser pulse can reach tens of kilowatts, producing very high instantaneous carrier densities and peak currents. At very high currents, space-charge effects and carrier-recombination nonlinearities may significantly degrade the photoreceiver performance[1,9]. In addition, nonlinearity in the vertical response of the oscilloscope may cause changes in the photodiode response.

We take data at many different input powers ranging from 5 to 100 μW. Figure 3 graphs the frequency response of the photodiode at some representative input powers. (We actually take data at more powers on the lower end, but they become hard to distinguish in such a graph.) The response decreases as a function of increasing power. For the lowest powers, this decrease can be approximated as a linear function of increasing power and increasing frequency. At higher powers (above ~30 μW), significant nonlinear effects are also evident.

In order to correct for the power-dependent effects, we observe the response as a function of power at many frequencies. Assuming that the effect is linear at low powers, we obtain a correction factor in dB/(μW*GHz), and use this to effectively extrapolate the data back to zero average power. After this correction, the responses for all of the relatively low-power inputs (below ~30 μW average power) agree within the noise of the measurement.

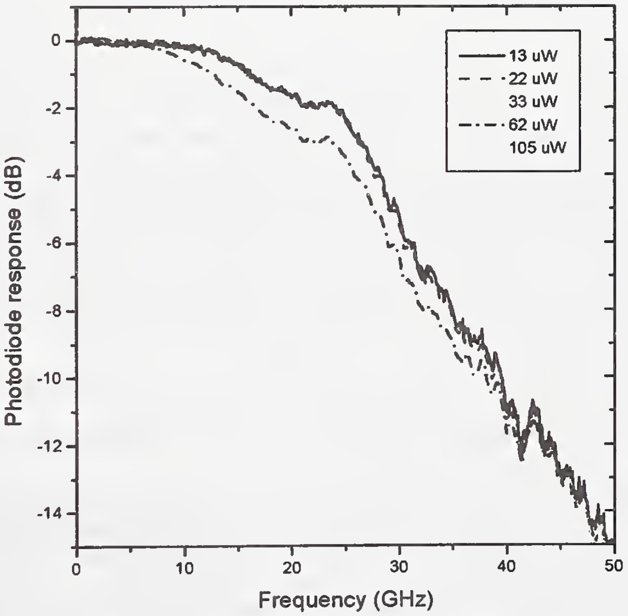

Figure 3. Frequency response for various input powers

Comparison to heterodyne experiment

We have measured the frequency response of the same photodiode with a heterodyne technique[10]. Figure 4 shows the difference between a time-domain measurement with all of the above corrections applied and the measured heterodyne data. The disagreement is less than 0.1 dB from 100 MHz to 25 GHz. At higher frequencies (inset) the difference increases to an average value of ~0.6 dB at 50 GHz, with excursions of about ±0.5 dB, probably due to mismatch that is not corrected in the time-domain measurement. We have also used the time-domain technique described here to obtain the frequency response of several other photoreceivers, and comparisons with heterodyne measurements show similar agreement. Although we have not focused on it in this paper, the time-domain technique determines the phase as well as the magnitude of the frequency response of a photoreceiver, while the heterodyne method can determine only the magnitude.

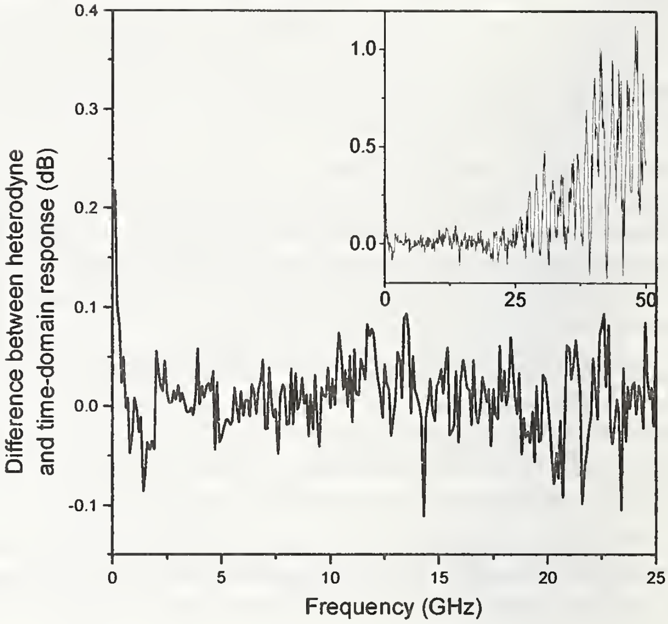

Figure 4. Difference between heterodyne and time-domain response.

Acknowledgements: Part of this work was supported by the Office of Naval Research and the Space and Naval Warfare Systems Center. We thank Don Larson for early contributions to this work.

References:

[1] J. E. Bowers and C. A. Burrus, "Ultrawide-band long-wavelength p-i-n photodetectors," *J. Lightwave Technol.*, 5 1339-1350 (1987).

[2] A. D. Gifford, D. A. Humphreys, and P. D. Hale, "Comparison of photodiode frequency response measurements to 40 GHz between NPL and NIST," *Electron. Lett.*, 31 397-398 (1995).

[3] R. T. Hawkins, M. D. Jones, S. H. Pepper, and J. H. Goll, "Comparison of fast photodetector response measurements by optical heterodyne and pulse response techniques," *J. Lightwave Technol.* **9**, 1289-1294 (1991).

[4] K. J. Coakley and P. D. Hale, "Alignment of noisy signals," submitted to *IEEE Trans. Instrum. Meas.*

[5] C. M. Wang, P. D. Hale, and K. J. Coakley, "Least-squares estimation of time-base distortion of sampling oscilloscopes," *IEEE Trans. Instrum. Meas.*, 48, 1324-1332 (1999).

[6] Y. Rolan, J. Schoukens, and G. Vandersteen, "Signal reconstruction for nonequidistant finite length sample sets: a KIS approach," *IEEE Trans. Instrum. Meas.*, 47, 1046-1052 (1998).

[7] W. L. Gans, "The measurement and deconvolution of time jitter in equivalent-time waveform samplers," *IEEE Instrum. Meas.*, vol. 32, pp 126-133, 1983.

[8] P. D. Hale, T. S. Clement, K. J. Coakley, C. M .Wang, D. C. DeGroot, and A. P. Verdoni, "Estimating the magnitude and phase response of a 50 GHz sampling oscilloscope using the 'nose-to-nose' method," *55th ARFTG Conference Digest*, (June 2000).

[9] K. J. Williams and R. D. Esman, "Photodiode DC and microwave nonlinearity at high currents due to carrier recombination nonlinearities," *IEEE Photon. Tech. Lett.*, 10, 1015-1017 (1998).

[10] P. D. Hale and C. M. Wang, "Heterodyne system at 850 nm for measuring photoreceiver frequency response," submitted to *Symposium on optical fiber measurement*. See also P. D. Hale and C. M. Wang, "Calibration service of optoelectronic frequency response at 1319 nm for combined photodiode/rf power-sensor transfer standards," Natl. Inst. Stand. Technol. Spec. Publ. 250-51, Dec. 1999.

Optical amplifier measurement issues: doped fiber, semiconductor and Raman

Jack Dupre
Agilent Technologies
Santa Rosa, CA

1 Introduction

Optical amplification is critical to the continued explosive growth of optical fiber telecommunications. Increased transmission capacity through higher channel density and wider optical bandwidth per fiber has placed stringent performance requirements on optical amplifiers used in booster, in-line, and preamplifier applications. Additional requirements are imposed by all-optical networking where channels are dynamically added and dropped. While the preponderance of optical amplifiers today is of the erbium-doped fiber (EDFA) type, Raman and semiconductor (SOA) amplifiers are also commonly used. Each amplifier type has unique measurement issues.

This paper addresses some of the key measurement issues for each type of optical amplifier.

2. Erbium-doped fiber amplifiers for dense WDM applications

Gain and noise figure characterization for amplifiers with multichannel stimulus is complex because the parameters are dependent on the power level in *all* of the input channels. To simplify the test apparatus, *signal- spontaneous noise figure* [1], which is derived from amplified spontaneous emission (ASE) measurements on an optical spectrum analyzer, is commonly used. To measure ASE in the presence of the spontaneous emission from the laser sources, methods using direct interpolation and time-domain extinction (TDE) are used. [2,3]. A typical configuration for TDE is shown in Figure 1. To precisely characterize gain and noise figure for a particular multichannel plan, the multichannel test source must duplicate the multichannel plan in wavelength and power level. This is problematic for testing amplifiers that are used with a number of channel plans as the source is very complex and must be

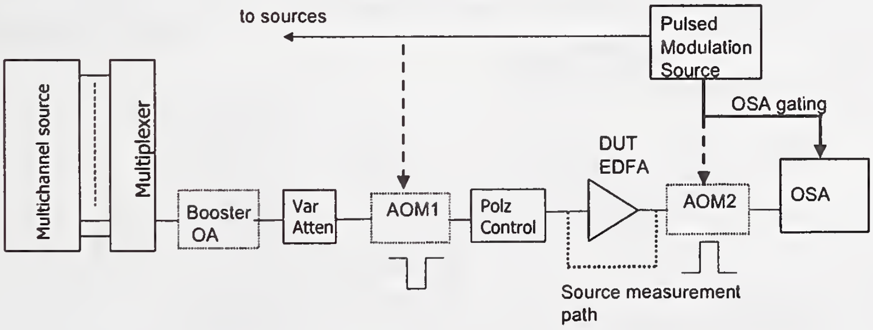

Fig. 1 Typical setup for measuring gain and noise figure using time-domain extinction (TDE).

reconfigured for alternative channel plans. However, using the largely homogeneous saturation characteristics of the EDFA, a *reduced set* of laser sources may be used with a minor compromise in measurement accuracy [4]. A limitation on the reduction in the number of lasers is imposed by spectral hole burning (SHB). As shown in Fig. 2, SHB is a wavelength-localized depression in gain that is signal power dependent. It is important that in regions where SHB is significant, at least one test laser must be placed within a spectral hole width. Careful measurements of SHB [5] show that hole depth is deepest and width the narrowest in the 1535-nm region and is small above 1550 nm. Simulations suggest that 16 to 32 equally spaced lasers are required to eliminate errors due to SHB [6]. Judicious wavelength placement (closer spacing in the 1535-nm region) could further reduce this number. For L-band designs, it has been reported that the localized gain depression caused by SHB is not a factor [7].

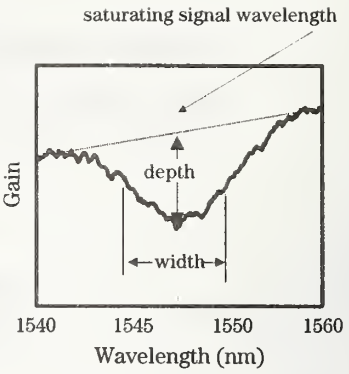

Fig. 2 Spectral hole burning is a localized signal-dependent depression in gain.

A further refinement of the reduced source approach is to combine a small-signal probe with the saturating multichannel source. The probe may be either a tunable laser or broadband noise. The broadband noise probe method, often called noise gain profile (NGP), is generally preferred because of its measurement speed. It uses a noise source such as an edge-emitting LED to simultaneously probe the entire EDFA band. It is often implemented with modulated saturating laser sources and in conjunction with time domain extinction. Fig. 4 shows a typical implementation of NGP. Compared to the direct TDE approach of Fig. 1, NGP can have the following advantages:

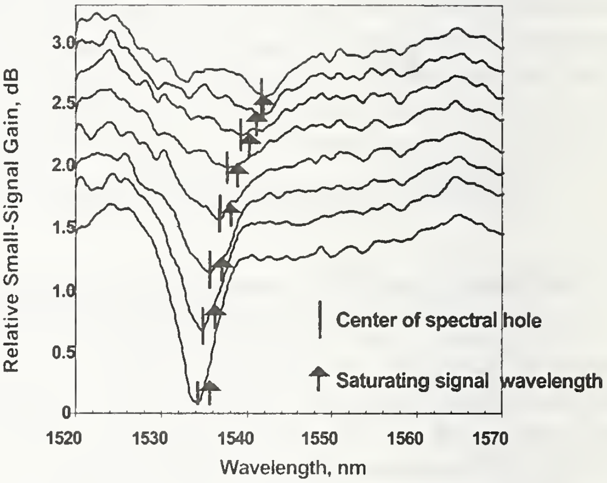

Fig. 3. SHB measurements on a 1480-nm single pump silica-fiber based EDFA.

- Resolution of the gain and noise figure data is limited only by the optical spectrum analyzer's display resolution--not by the number of lasers in the multichannel source.
- By keeping the total input power constant, the gain and noise figure are largely immune to power level variation of the individual lasers.
- Measurement speed is independent of the number of lasers so can be faster for large channel count.

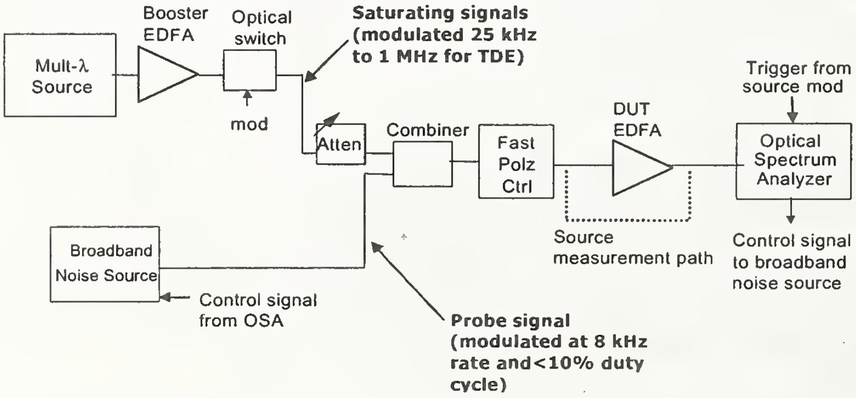

Fig. 4. Typical setup for measuring gain and noise figure using noise gain profile (NGP).

While TDE and NGP are inherently different measurement methods, it is important to that they measure the same gain and noise figure parameters. To confirm this, measurements made with three methods were compared and results for gain and noise figure are shown in Fig. 5. In addition to results for TDE and NGP, measurements were also made using the interpolation with source subtraction (ISS) method. For TDE and ISS, data is only available at the wavelengths of the multichannel source while, for NGP the data is continuous from 1528 to 1563 nm. The measurements for all three methods agree to within ±0.125 dB.

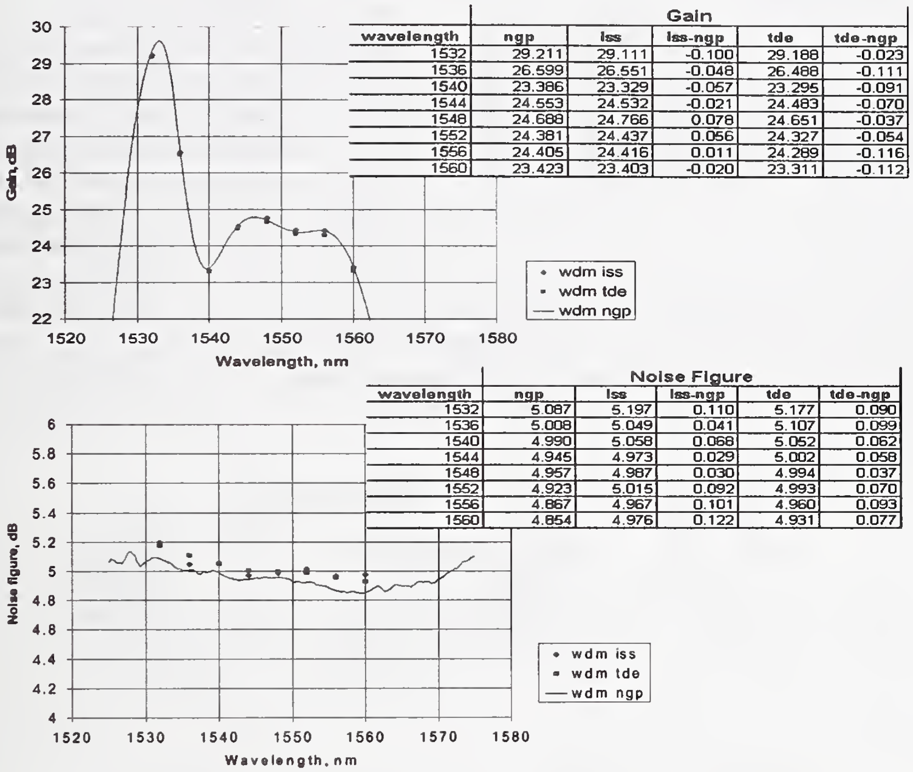

	Gain				
wavelength	ngp	iss	iss-ngp	tde	tde-ngp
1532	29.211	29.111	-0.100	29.188	-0.023
1536	26.599	26.551	-0.048	26.488	-0.111
1540	23.386	23.329	-0.057	23.295	-0.091
1544	24.553	24.532	-0.021	24.483	-0.070
1548	24.688	24.766	0.078	24.651	-0.037
1552	24.381	24.437	0.056	24.327	-0.054
1556	24.405	24.416	0.011	24.289	-0.116
1560	23.423	23.403	-0.020	23.311	-0.112

	Noise Figure				
wavelength	ngp	iss	iss-ngp	tde	tde-ngp
1532	5.087	5.197	0.110	5.177	0.090
1536	5.008	5.049	0.041	5.107	0.099
1540	4.990	5.058	0.068	5.052	0.062
1544	4.945	4.973	0.029	5.002	0.058
1548	4.957	4.987	0.030	4.994	0.037
1552	4.923	5.015	0.092	4.993	0.070
1556	4.867	4.967	0.101	4.960	0.093
1560	4.854	4.976	0.122	4.931	0.077

Fig. 5 . Gain and noise figure comparisons for multichannel ISS, TDE and NGP methods.

A further simplification in the measurement method for variable and complex source environments it to use a *single* tunable laser and characterize the SHB effect vs. wavelength [8]. While additional correlation studies are necessary to qualify the accuracy of the modeling of SHB, early results are promising as shown in Fig. 6. Single laser gain measurements correlate with multichannel measurements to within 0.3 dB.

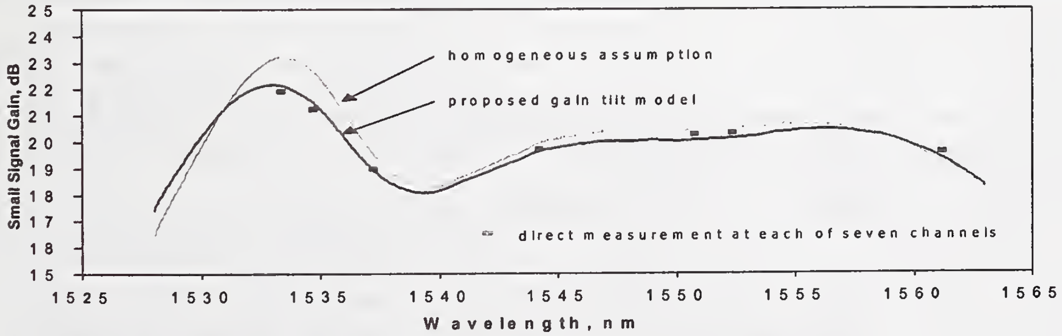

Fig. 6. Predicted multichannel gain from SHB modeling and a homogeneous model are compared to direct measurements with a multichannel source.

Another important issue in testing EDFAs is the effect of polarization. The test setups in Fig. 1 and Fig. 2 both incorporate polarization controllers to either:

(1) Scramble the state of polarization (SOP) in order to measure amplifier parameters for the *average* SOP , or

(2) Vary the SOP and make measurements to collect the polarization dependency of the amplifier parameters.

When testing with a multichannel source, the *polarization hole burning* (PHB) phenomenon is of particular concern. To understand the effect of PHB, consider two signals in the same wavelength vicinity – a large signal and a small signal. The large signal sets the inversion level. An additional laser provides a small signal probe. Because of PHB, the gain in the polarization state of the large signal is depressed. This gain depression also will impact the small signal if it is in the same polarization state. However, if the small signal is in the polarization state orthogonal to the large signal, it does not experience the gain depression. The difference between the gain in the polarization state aligned with the large signal and that for the orthogonal state is usually referred to as polarization-dependent gain (PDG). With a multichannel source, it is usually desirable to measure gain with randomly aligned source polarization. This can be accomplished in three ways as shown in Fig. 7. The first method is to individually scramble each source. The second is to slowly scramble the combined sources followed by a birefringent element to decorrelate the SOP of adjacent channels. The third method is to utilize a fast polarization scrambler after the combiner. In this context, slow and fast scrambling are with respect to the erbium-ion relaxation time.

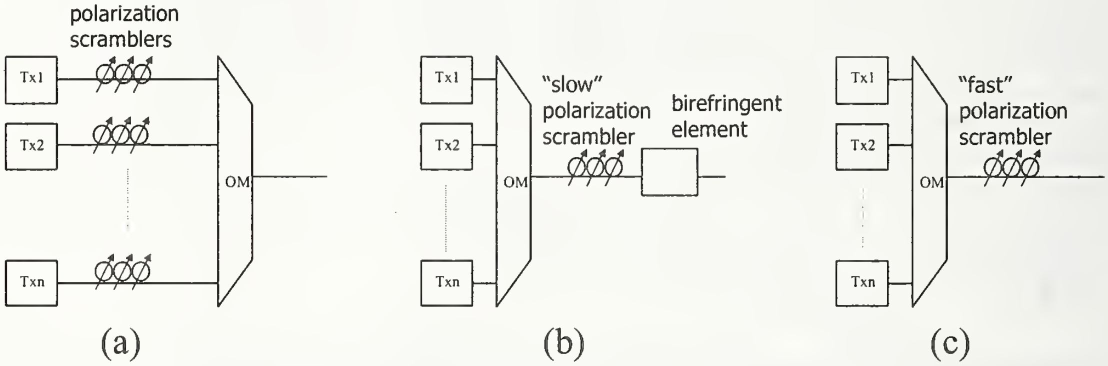

Fig. 7. When using a multichannel source, errors due to PHB are eliminated by (a) scrambling the polarization of each channel, (b) scrambling the combined source and using a birefringent element, or (3) using a fast polarization scrambler.

3. Raman amplifiers

Raman amplification is increasingly being considered to extend the wavelength range for a transmission system or to extend the distance between repeaters. The active element that is pumped to achieve gain may be the actual link transmission fiber itself or, like a conventional EDFA, the active fiber may be packaged with the pump laser. In the case of Raman-pumped transmission fiber, significant performance advantages can be realized over EDFA-only systems [9]. In addition, WDM pumping can provide a 100-nm operating band with very flat gain characteristics [10]. Test issues result primarily from a unique noise generation mechanism and much faster time dynamics when compared to the EDFA.

The important noise mechanisms in a Raman amplifier are amplified spontaneous emission (ASE) and double Rayleigh scatter noise. As with an EDFA, ASE can be measured with an optical spectrum analyzer and the signal-spontaneous noise figure, $F_{sig\text{-}spon}$, calculated. TDE, as discussed above for the EDFA, cannot be used because of the significantly faster gain relaxation time for Raman gain. Interpolation must be used. Another significant issue is that double Rayleigh scattering cannot be observed as an increase in ASE because it results in heterodyne noise in an optical receiver. The total noise figure -- which includes the double Rayleigh backscatter noise component-- must be measured with an electrical spectrum analyzer method.

The electrical spectrum analyzer test method (Fig. 8) for measuring F_{total} was once commonly used for EDFA measurements but was abandoned because of the difficulty to obtain repeatable and accurate results and because, for the EDFA, $F_{sig\text{-}spon}$ measured with an optical spectrum analyzer was sufficient. One of the major sources of measurement uncertainty was the calibration of the optical receiver. By using a RIN standard [11], this major source of uncertainty can be greatly reduced. Calibration of an optical receiver with a RIN standard is shown in Fig. 9. Consisting of an ASE source and a stable bandpass filter, the optical power is measured on a well-calibrated optical power meter. The intensity noise spectral density is then known precisely and used as the calibration standard for the optical receiver.

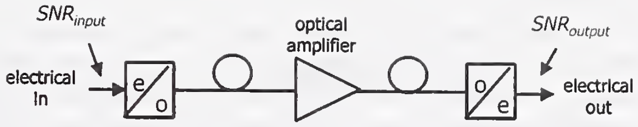

$$F_{total} = \frac{SNR_{input}}{SNR_{output}}$$

Fig. 8. Total noise figure is defined in terms of the electrical signal-to-noise ratios at the input and output of ideal e/o and o/e converters. F_{total} includes the effect of double-Rayleigh backscatter.

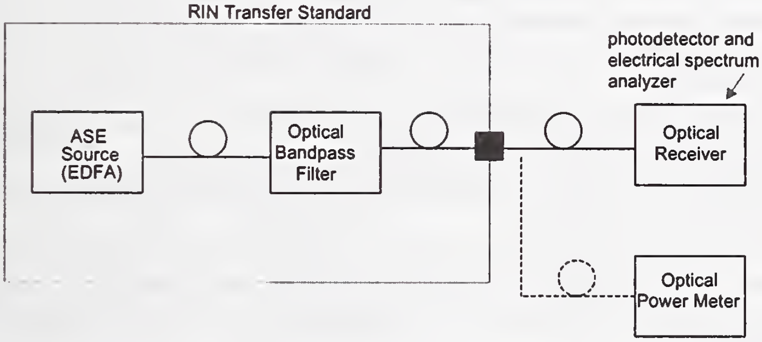

Fig. 9. The accuracy of an electrical-method noise figure measuring setup in improved by calibrating the intensity noise frequency response with a RIN standard.

Through NIST, a Measurement Assurance Program (MAP) or Calibration Service is available for the spectral density of relative intensity noise [12].

4. Semiconductor optical amplifiers

While the EDFA has become the prevalent amplifier type and Raman is emerging to provide better performance, the semiconductor optical amplifier (SOA) continues to progress as a potentially more compact and lower cost alternative. While not usually considered as a commercially viable option for 1550-nm transmission systems because of the refinement of the EDFA, 32 channel × 10 Gbit/s over 160 km using SOAs has been reported [13].

The SOA also has applications in optical switching and as a non-linear device in applications such as wavelength conversion. The SOA may also be applied in the 1310-nm window where doped-fiber amplifiers have not proven to be viable.

Test methods for gain and noise figure of the SOA can leverage greatly from the EDFA experience. Signal-spontaneous noise figure using the optical spectrum analyzer interpolation method may be used. Like the Raman amplifier, time-domain extinction cannot be used because of the short carrier lifetime. Additional test issues relate to properties that are unique to the SOA. These include polarization dependence, gain ripple, and gain clamping laser artifacts. In an EDFA polarization dependencies are so small that they may be ignored in many applications. This is not true with the SOW in that it is inherently polarization dependent and excellent design is required to minimize this effect. Gain ripple with sub-nanometer period is also inherent due to reflections between the gain medium facets. Active gain clamping with a control laser is commonly employed to achieve automatic gain control. The gain clamping laser leakage needs to be measured.

5. Acknowledgements

The author wishes to acknowledge Douglas Baney of Agilent Technologies Laboratories and Jim Stimple of Agilent Technologies, Lightwave Division for their many contributions to this paper.

6. References

[1] IEC Publication 61290-3, Basic specification for optical fibre amplifiers test methods – Part 3: Test methods for noise figure parameters.

[2] J. Aspell, J.E. Federici, B.M. Nyman, D.L. Wilson, and D.S. Shenk, "Accurate noise figure measurements of erbium-doped fiber amplifiers in saturation conditions" *Optical Fiber Communications*, Vol. 5, 1992 OSA Technical Digest Series (Optical Society of America, Washington, DC, 1992), paper ThA4.

[3] D. Baney, J. Dupre, "Pulsed source technique for optical amplifier noise measurement," *European Conference on Communications*, paper WeP2.11, Berlin, 1993.

[4] D. Baney, J. Stimple, "WDM EDFA gain characterization with a reduced set of saturating channels," IEEE, *Photon. Technol. Lett.* 8(12), pp. 1615-1617.

[5] E. R Rudkevich, D.M. Baney, J. Stimple, D. Derickson, and G. Wang, "Nonresonant spectral -hole burning in erbium-doped fiber amplifiers," *IEEE Photon. Technol. Lett.*, vol. 11, no. 5, 542 (1999).

[6] P. Wysocki, "Measurement of Wide-Bandwidth Gain-Flat Amplifiers," *Symposium on Optical Fiber Measurements*, pp. 9-14 (1998).

[7] F. A. Flood, "Inhomogeneous Gain Saturation Behavior in L-Band EDFAs," *IEEE, Photon. Technol. Lett.* 12(8), August, 2000.

[8] J. Stimple and J. Dupre, "A method to predict multichannel gain from single laser measurements," *Optical Amplifiers and Their Application*, Tech. Dig. 2000.

[9] C. Fludger, A. Maroney, and N. Jolley, "An analysis of the improvements in OSNR from distributed Raman amplifiers using modern transmission fibres" *Optical Fiber Communications*, 2000, paper FF2-2, OSA Technical Digest Series, Optical Society of America, Washington, DC, 2000.

[10] Y. Emori and S. Namiki, "100 nm bandwidth flat gain Raman amplifiers pumped and gain equalized by 12-wavelength-channel WDM high power laser diodes," *Optical Fiber Communications*, 1999 OSA Technical Digest Series, Optical Society of America, Washington, DC, 1999, paper PD-19.

[11] D. M. Baney and R.L. Jungerman, "Optical noise standard for the electrical method of optical amplifier noise figure measurement, *Optical Amplifiers and Their Application*, paper MB3, OAA'97, Optical Society of America, Washington, DC, 1997.

[12] G.E. Obarski and J. D. Splett, "Measurement Assurance Program for the Spectral Density of Relative Intensity Noise of Optical Fiber Sources Near 1550 nm," NIST Special Publication Series, SP-250.

[13] L.H. Spiekman, A.H. Gnauck, J.M. Wiesenfeld, and L.D. Garrett, "DWDM transmission of thirty-two 10Gbit/s channels through 160km link using semiconductor optical amplifiers," *Electron. Lett.*, 2000, 36, pp. 1046-1047.

COMPARISON OF ERBIUM AMPLIFIER CHARACTERISATION USING AN ITU GRID WITH VARYING CHANNEL SEPARATIONS

M.E. Bray, R.T. Elliott and K.P. Jones

Nortel Networks, Brixham Road, Paignton, Devon, UK, TQ4 7BE (MBray@nortelnetworks.com)

Abstract: 100GHz spacing ITU grid source measurements of gain and noise figure of EDFAs are presented. Channel numbers can be halved or quartered giving deltas to the 100GHz measurements of <~0.15dB and <~0.3dB respectively.

Introduction

Recently wavelength division multiplexed erbium doped fibre amplifier (EDFA) designs have progressed from "red band" (~1540-1560nm) to "full band" (~1530-1560nm) and eventually "extended band" (~1570-1600nm). As this happened problems have become apparent with existing methods of EDFA measurement such as the noise-gain profile technique[1]. These methods suffer because they concentrate the power saturating the amplifier into one or a very small number of channels. Spectral hole burning, and the dependence of the amplifier's saturation on the wavelength of the saturating signal, lead to the results obtained to these techniques being unrepresentative of EDFA system performance[2].

For accurate measurements the test source used must accurately represent the multi-channel loading used within the system for which the amplifier is designed. Here we present gain and noise figure results for an amplifier tested with lasers separated by 100GHz at the wavelengths defined by the ITU[3]. Fully populating an ITU grid is expensive. Results have also been obtained using sources with separations of 200, 400 and 800 GHz. These are compared here to the 100 GHz benchmark to investigate cost reduction by the use of sub-populated grids. To the authors' knowledge previous work has only modelled sub-populated grids[4].

It should be noted, that the gains and noise figures are only calculated at the source wavelengths in this technique, so some of the separations may be prohibited by their reduced spectral resolution

Test

The method used is the time domain extinction technique. In this method, the sources are on-off modulated before the device under test at a sufficient frequency that the amplifier saturation does not significantly alter during the off phase. Measurements on the optical spectrum analyser are gated so that they occur when the sources are on (measuring signals and ASE noise) and also when they are off (measuring ASE noise only). Back to back signal measurements are also made to characterise the input to the amplifier.

A schematic of the test equipment is shown in Fig. 1. The ITU sources are coupled together and fed into a boost EDFA. This increases the input power to the device under test. The ITU sources are also monitored on a wavemeter. The boosted signals are modulated by an acousto-optic modulator, which operates with a 50% duty cycle. After passing through a variable optical attenuator which controls the input power to the device under test, the polarisation of the signals is randomised by a polarisation scrambler. The signals then pass through the device under test (or bypass it for back to back measurements), and then through an attenuator to condition the power into the optical spectrum analyser. Another acousto-optic modulator with a 25% duty cycle then gates the signals before measurement on an optical spectrum analyser. By varying the phase of the second modulator with respect to the first the optical spectrum analyser can measure signal or ASE traces. The timing diagram for the acousto-optic modulators is shown in Fig. 2.

Figure 1 Schematic of test equipment

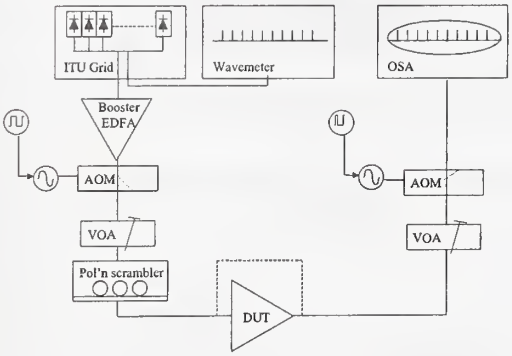

Figure 2 Timing diagram of acousto-optic modulators

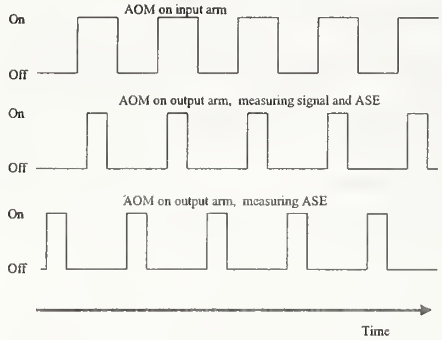

Results

Input power, output power and ASE spectra were collected from a flattened full band amplifier operating at its nominal gain condition. An example set of measured spectra is shown in Fig. 3. The input spectrum in this graph has been offset by -10dBm to clarify the results. The data was then manipulated to obtain gain and noise figure spectra. This process was repeated for several source grid wavelength plans with separations of 100, 200, 400 and 800 GHz.

Figure 3 Measured input,output and ASE spectra

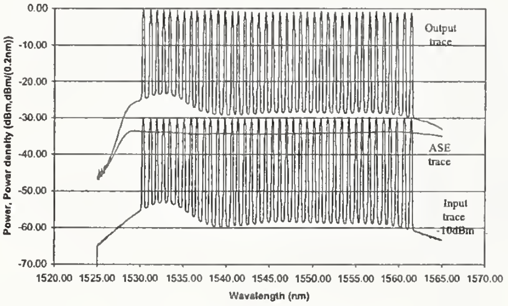

Figure 4 Gain spectra measured using varying channel separations

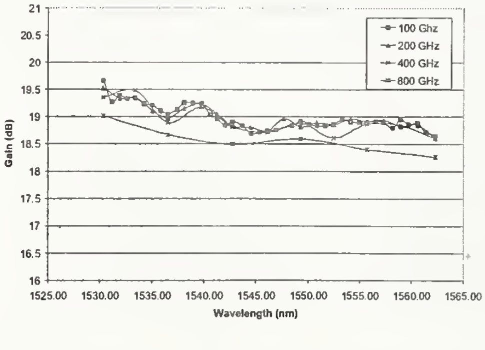

Figure 5 Noise figure spectra measured using varying channel separations

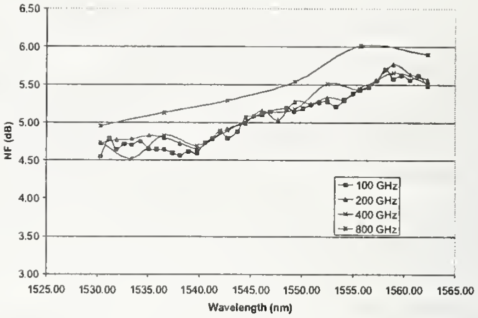

Figures 4 and 5 show the gain and noise figure results calculated from the measurements. The graphs for all the channel separations show very similar spectral profiles. The 200 and 400 GHz measurements are close in absolute value to the 100 GHz benchmark, however the 800 GHz measurements, while retaining the same profile, displays an offset to the other measurements in both gain and noise figure. This may be explained by spectral hole burning. The greater intensity in each of the channels leads to deeper holes being burnt around each channel, reducing the gain and increasing the noise figure.

Close inspection of the figures shows that the 100 GHz and 200 GHz measurements are in very good agreement for both noise figure and gain. The difference in gain and noise figure measurements are less than 0.1dB and 0.15dB respectively. While the "average" values for the 400 GHz gain and noise figures follow the 100 GHz values well, the individual values oscillate about the 100 GHz trace. The differences of gain and noise figure measurements between the 100 and 400 GHz traces are both up to 0.3 dB. This is larger than the error predicted by previously published modelling [4].

Conclusion

The expansion of the erbium amplifier spectrum used in wavelength division multiplexed optical systems has placed additional requirements on test methods. Single channel sources are no longer sufficient to set amplifiers in the correct saturation condition. In addition they lead to errors due to spectral hole burning.

Ideally a source with the same channels and powers as the system for which the amplifier is designed should be used. However the capital requirement of such a source for full band amplifiers and beyond is severe.

It is shown here that a source with 40 100GHz spacing channels can be very accurately represented by a source with half the channels at twice the spacing. This represents a source cost saving of up to 50%. If a slightly lower accuracy of the measurements can be accepted, then the spacing can be increased by another factor of 2 to 400 GHz, reducing the number of sources by a factor of 2 again. Increasing the spacing to 800GHz reduces the accuracy unacceptably.

It should be noted however that reducing the number of sources reduces the spectral resolution of both gain and noise figure, and this should be considered while designing a test system.

References

1 The noise gain profile technique explained in "The 1996 Lightwave Transmission Seminar & Exhibition", W. Benger, and J. Vobis, Hewlett-Packard, pp64-65, 1996

2 C. Hentschel and J. Dupre, "EDFA measurements for WDM applications", "The 1998 Lightwave Symposium", Hewlett-Packard, pp63-80, 1998

3 ITU Draft G.mcs "Optical interfaces for multichannel systems optical amplifiers", Question 16/15, Appendix IV

4 P. Wysocki, "Measurement of wide-bandwidth gain-flat amplifiers", Symposium on optical fiber measurements, 1998, pp9-14

Gamma and Proton Radiation Effects in Erbium-Doped Fiber Amplifiers: Active and Passive Measurements

Todd S. Rose, Deana Gunn[‡] and George C. Valley

Photonics Technology Department, Electronics and Photonics Laboratory
The Aerospace Corporation
2350 East El Segundo Blvd., El Segundo, CA 90245

ABSTRACT

Commercially available Er-doped fibers were irradiated with 5.6- and 28-MeV protons and ^{60}Co gamma rays, up to levels of 50 krad. Transmission spectra under passive conditions (no pump or signal) were measured at several radiation levels for the six types of the fiber tested. Comparison between the damage caused by the gammas and protons were made for two fiber types. Samples from three of the fiber types were configured as optical amplifiers using a 980-nm pump and a 1550-nm signal. *In situ* measurements of the gain, noise figure and ASE were made as a function of pump power at several levels of radiation. A computer code, based on a conventional fiber amplifier model, was written to simulate performance using input data provided by the fiber vendor and anchored to measurements made prior to radiation. Comparison between the simulations and experimental data show that the radiation-induced loss determined from the amplifier measurements can be a factor of two to three smaller than that determined from the passive transmission spectra.

1. INTRODUCTION

Because of the potential use of erbium-doped fiber amplifiers in space for optical intersatellite links and other applications, the effects of radiation on these components has attracted interest by many groups over the past several years [1-5]. Although high-energy protons are the primary threat to components within a typical spacecraft enclosure, most radiation tests to date have been conducted with ^{60}Co gamma emission sources since they are more accessible and less expensive to operate than high-energy particle accelerators. For this reason, only a limited number of tests involving erbium fibers and protons are discussed in the literature [4,6]. Equivalent doses of gammas and protons are expected to cause the same amount of damage in a glassy system. It is important to note, however, that only the dose at the core is relevant to a fiber's performance, a point that seems to be neglected in the literature. In all but the most extreme radiation conditions, color center formation in the outer claddings of fibers is not only significantly less than in the core, but inconsequential as well. Furthermore, traditional passive radiation tests, or transmission measurements, are not adequate in predicting the performance of a fiber as an amplifier. In the absence of optically induced annealing and other unknown processes, the measured gain and noise figure (NF) of the amplifier should relate to the measured passive loss. However, any quantitative relation between the passive loss and noise figure derived from experiment must meticulously consider the effects of other "components" such as filters, polarizers, splices and the method in which the NFs were determined.

2. EXPERIMENTAL SET-UP AND RESULTS

Radiation-induced transmission losses were measured for six commercially available fibers from Lucent Technologies. Of the six fiber types, four are primarily used as amplifiers (HE980, HP980, MP980, and LP980), while two are used as super-luminescent sources (HG980 and R37003). In all transmission measurements, 3-m Er-fiber samples were fusion spliced to 3-m SMF-28 fiber leads at each end. Each Er section was concentrically spooled into a flat annular geometry with a diameter on the order of 7.5 to 10 cm and mounted to a sheet of cardboard, which was placed inside the ^{60}Co chamber. (This mounting geometry ensured that the Er fibers were irradiated uniformly, which is particularly important for comparing the gamma and low-energy proton results discussed below.) The undoped fiber leads were connected to a broadband white light source and to an optical spectrum analyzer (OSA). The gamma tests were conducted over a 10-hour period at a rate of 1.4 rad/sec. *In situ*

[‡] Present address: Hughes Space and Communications, El Segundo, CA

transmission spectra for the fibers were acquired at 10-krad intervals up to a total dose of 50 krad. A representative example is shown for HP980 in Fig. 1. The induced loss spectra for all the fibers at 50 krad are displayed in Fig. 2, which were obtained by normalizing the 50-krad transmission spectra to the pre-irradiation levels.

Proton tests for HE980 and HP980 fibers were conducted at the Lawrence Berkeley 88-in. cyclotron facility. The samples received up to 50 krad (at the fiber core) of 5.6- and 28-MeV protons. The fluences required to deliver 50-krad doses to the fiber cores at 5.6- and 28-MeV were 4.3 x 10^{10}/cm^2 and 1.9 x 10^{11}/cm^2, respectively. On average, the fiber samples received the entire proton dose over 1 hr (i.e. 14 rad/sec). A comparison of the 5.6- and 28-MeV protons and ^{60}Co gamma results, displayed in Fig. 3, show that for each fiber type, equivalent radiation doses cause comparable amounts of damage in the fibers. While there is little variation in the HE980 data (which is consistent with other work [4]), there is some spread in the HP980 data, which could arise from the doping variations known to occur in this fiber.

The effects of gamma radiation on the gain and noise figure of 10-meter samples of MP980, HE980 and HP980 fibers were investigated using the ^{60}Co chamber and irradiated up to 50 krad at a dose rate of ~3 rad/sec. The fibers were forward-pumped at 980 nm with input powers ranging between 5 and 50 mW. The input –40 dBm signal at 1550 nm was obtained from a tunable laser source with a 150-kHz linewidth and a side-mode suppression ratio > 45 dB. For the HP980 and MP980 fibers, an isolator was used at the output facet to eliminate the amplified spontaneous emission (ASE) backscatter, which caused lasing at the higher pump powers. The gain vs. pump power and the noise figure vs. pump power are shown at 10-krad intervals, up to 50 krad, in Fig. 4 for the three fibers. The solid lines through the data points are the theoretical fits to the amplifier performance, which will be discussed in the following section.

3. MODELING

A computer code was written that solves the conventional EDFA equations [7,8] allowing for arbitrary modifications, such as the addition of a saturable distributed loss, which are necessary for simulating radiation effects. (Although a commercial program, OASIX, [7] is available to model certain fibers, it cannot be modified to evaluate radiation effects, since the source code is unavailable.) Our model consists of standard equations for the pump at 980 nm, the co-propagating signal in the 1500-1600 nm band, and the forward and backward amplified spontaneous emission, all of which are coupled through the ground and excited state erbium number density. Input parameters to the code include the overlap integrals for the gain and absorption spectra [8] and the saturation parameter [7], which are provided by the fiber vendor (Lucent Technologies).

Modeling the gain and noise figure of an LNA requires knowledge of three optical loss parameters: the loss at the pump and signal wavelengths entering the LNA fiber and the loss from the LNA fiber to the OSA at the signal wavelength. These three parameters, which range from 0 to a few dB, were determined for each LNA fiber prior to radiation damage and are held fixed for all ensuing calculations. The only variables used to fit all the subsequent radiation data are the radiation-induced losses at the pump and signal wavelengths. Our fitting results for the MP980, HE980, and HP980 fibers in Fig. 4 show that we are able to model the effects of radiation quite well using our prescribed approach. Interestingly, we observe that while the gain continues to degrade with radiation, that NFs are unaffected at high pump powers. We further note that the radiation-induced losses at the pump and signal wavelengths obtained by fitting the amplifier results are factors of 2-3 lower than those obtained from passive transmission measurements. Thus, operation of the amplifier reduces the effect of the radiation, either by optical annealing or bleaching.

4. CONCLUSION

We have discussed our current investigation into the radiation sensitivity of erbium-doped fibers used as low noise amplifier fibers for space applications. Our comparative tests show that it is valid to use gamma radiation to simulate the energetic protons found in the space environment. We have measured the passive transmission through these fibers, as well as the gain and NFs of the fibers in active amplifier configurations. We attribute the degradation in performance primarily to radiation-induced absorption of the 980-nm pump light. If high enough pump levels are used in the amplifiers (achieving inversion saturation levels), this problem may be alleviated. Furthermore, having the amplifier in a pumped operating state will allow continuous photo-annealing and recovery to occur, decreasing the amount of degradation. Design parameters such as fiber composition and fiber length are extremely critical to the performance of these components in a radiation environment. Further work is necessary to model the degradation and recovery mechanisms.

5. ACKNOWLEDGEMENTS

The authors would like to thank W.A. Kolasinski of the Aerospace Corporation for his invaluable assistance with the proton measurements. This work was funded by Aerospace IR&D.

REFERENCES

[1] G. M. Williams, M. A. Putnam, C. G. Askins, M. E. Gingerich, and E. J. Friebele, "Radiation effects in erbium-doped optical fibers," *Electron. Lett.*, vol. 28, 10 Sept. 1992, p. 1816-1818.

[2] W. C. Goltsos, "Radiation-induced loss studies in Er-doped fiber amplifier systems," *SPIE*, vol.2699, May 1996, p. 304-309.

[3] G. M. Williams and E. J. Friebele, "Space radiation effects on erbium-doped fiber devices: sources, amplifiers, and passive measurements," *IEEE Trans. on Nuc. Sci.*, vol. 45, no. 3, June 1998, p. 1531-1536.

[4] G. M. Williams, M. A. Putnam, and E. J. Friebele, "Space radiation effects on erbium doped fibers," SPIE vol. 2811, May 1996, p. 30-37.

[5] E. W. Taylor, S. J. McKinney, A. D. Sanchez, A. H. Paxton, D. M. Craig, J. E. Winter, R. Ewart, K. Miller, T. O'Connor, R. Kaliski, "Gamma-ray induced effects in erbium-doped fiber optic amplifiers," SPIE conference on Photonics for Space Environments VI, July 1998, p. 16-23.

[6] R.H. Boucher, W.F. Woodward, T.S. Lomheim, R.M. Shima, D.J. Asman, K.M. Lillan, J. LeGrand, and G.J. Goellner, "Proton-induced degradation in interferometric fiber optic gyroscopes," Opt. Eng, vol 35, no. 4, pp. 955-976, 1996.

[7] P.C. Becker, N.A. Olsson and J.R. Simpson, Erbium-doped Fiber Amplifiers: Fundamentals and Technology, Academic Press, Boston, 1999.

[8] C.R. Giles and E. Desurvire, "Modeling erbium-doped fiber ampifiers", J.Ligthwave Tech., vol. 9, no. 2, pp. 271-283, 1991.

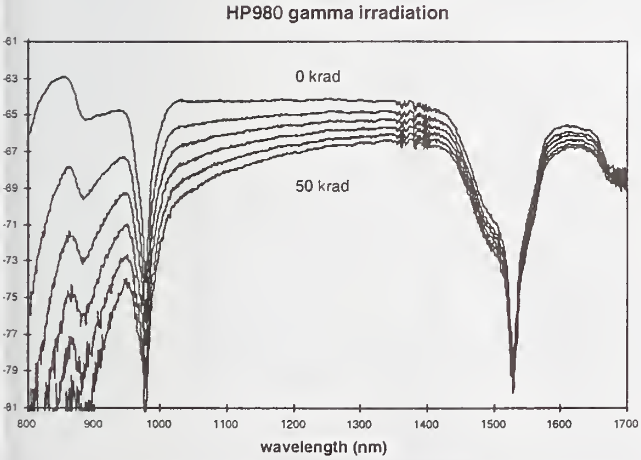

Fig. 1 Transmission spectra of gamma-irradiated HP980 at 10-krad intervals

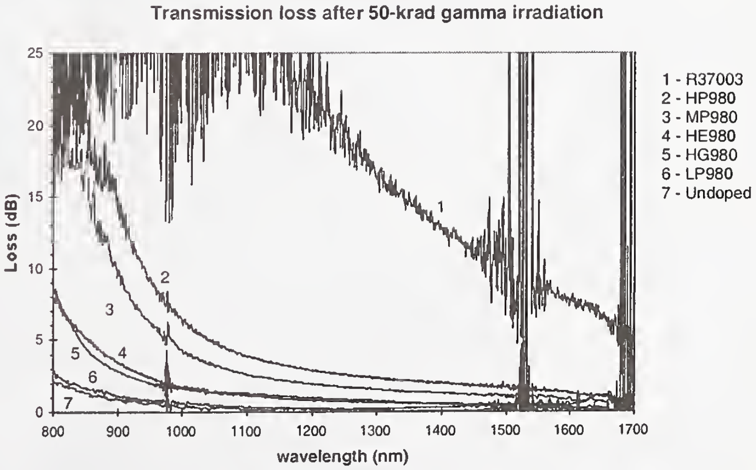

Fig. 2 Transmission loss spectra for 3-m Er-doped fibers after 50-krad gamma exposure. Spectrum displayed for R37003 shows loss after only 10 krad.

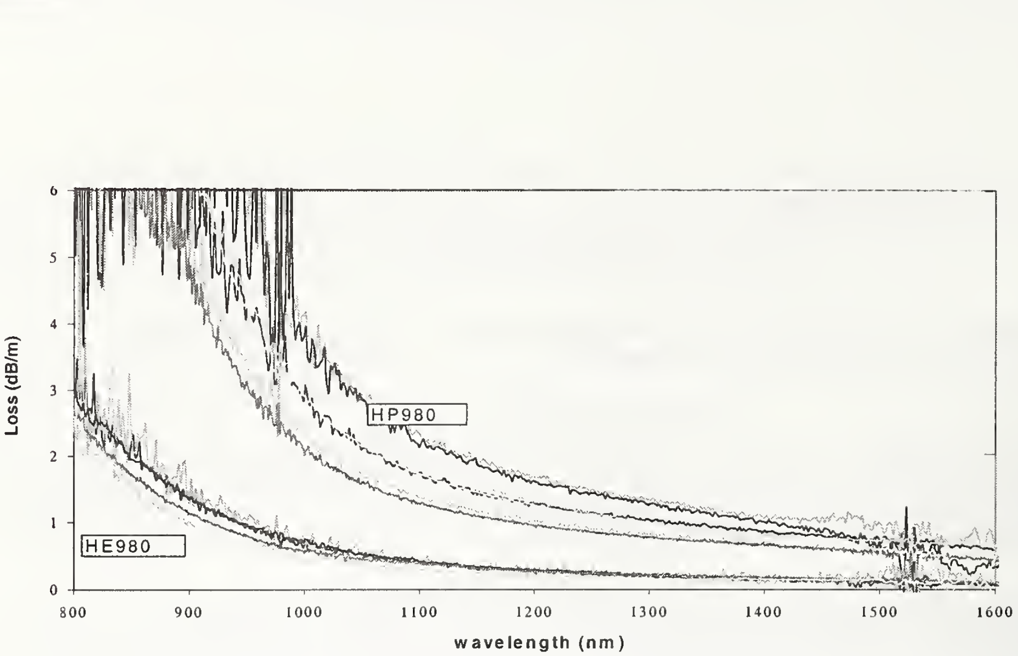

Fig. 3 Transmission loss spectra for 3-m HP980 and HE980 fibers after 50 krad exposure to ^{60}Co gammas and 5.6 and 28 MeV protons. The spread in the HP980 data is attributed to variations in the dopant concentrations.

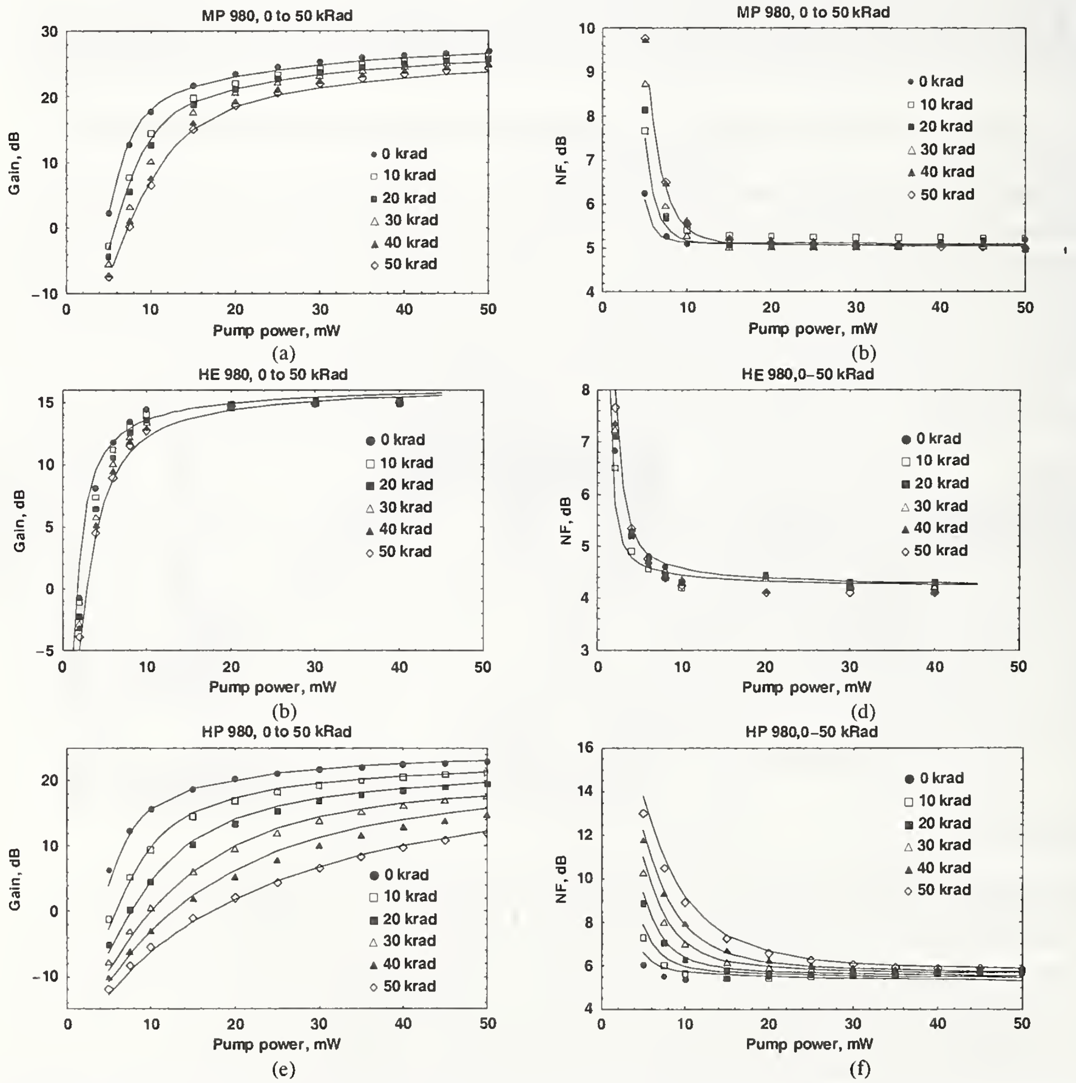

(a) (b)

(b) (d)

(e) (f)

Fig.4 Gain and Noise Figure as a function of pump power for 5 levels of radiation damage. The solid lines represent calculations while the symbols represent the measurements. (a) and (b) MP980. (c) and (d) HE980. (e) and (f) HP980.

ISSUES IN RAMAN GAIN MEASUREMENTS

R.H. Stolen
Virginia Tech., Dept. of Electrical and Computer Engineering
Blacksburg, VA 24060, stolen@vt.edu

I. INTRODUCTION

Applications of fiber Raman amplifiers as well as undesirable Raman interactions in dense WDM transmission systems have increased the importance of accurate measurements of Raman gain. Fortunately this need for increased accuracy comes at a time of increased precision and ease of fiber measurements. Now details of Raman gain measurements that had previously been lost in the measurement uncertainties are becoming significant.

Here these issues of Raman measurements are divided up into: the basic fused silica Raman spectrum, the effects of Germanium doping, the effective area, frequency dependence of Raman gain, polarization dependence, and the influence of four-wave mixing. In all of these areas there is need for both improved understanding and better measurements.

II. BASIC FUSED SILICA SPECTRUM

Raman gain measurements in both silica-core and Ge-doped fibers look very much like the fused silica Raman gain spectrum shown in Fig.1. This gain spectrum is a composite of measurements by several different authors of spontaneous Raman scattering in bulk silica samples and silica-core fibers.[1] The two curves are for scattering of light polarized parallel and perpendicular to the polarization of the exciting light. The spontaneous spectrum differs from the gain spectrum by the Bose-Einstein population factor, n+1, where $n=1/[\exp(h\nu c/k_BT)-1]$; h is Planck's constant, ν is the phonon frequency in cm^{-1}, k_B is the Boltzmann constant, T is the temperature in degrees Kelvin, and c is the vacuum velocity of light.

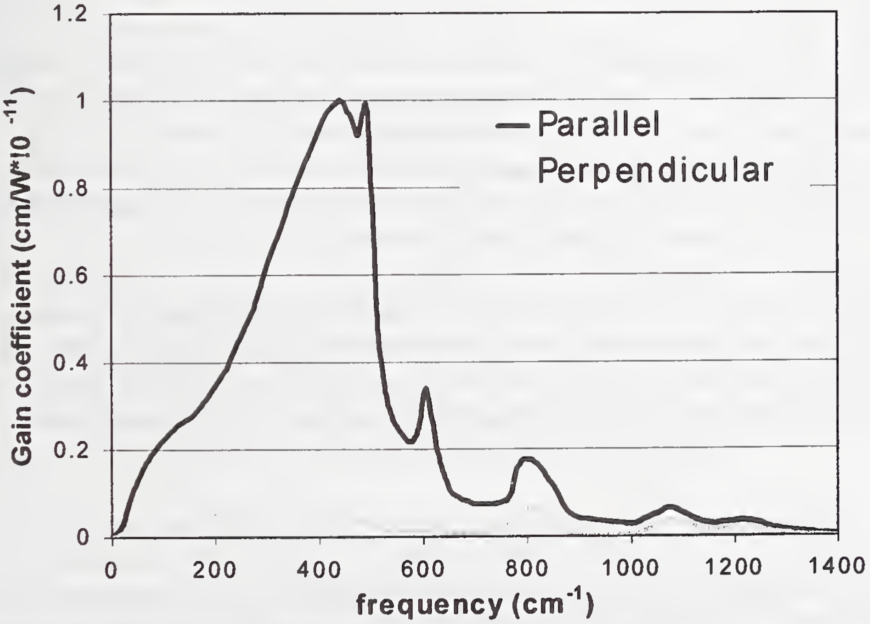

Fig. 1. Parallel and perpendicular Raman gain spectrum of fused silica as compiled from various sources.[1]

The absolute value of the peak gain usually comes from one of two sources. In the first, a gain coefficient of 1.86 x 10^{-11} cm/W was obtained for a pump at 526 nm in a fiber short enough to maintain linear polarization; the results agreed with bulk measurements in fused silica.[2] Including the wavelength dependence of the gain coefficient leads to a convenient gain coefficient of approximately 1.0 x 10^{-11} cm/W for a pump wavelength of 1.0 microns. A gain of 2.46 x 10^{-11} cm/W was obtained from spontaneous scattering from a 488 nm source in bulk silica samples.[3] This translates to a gain of 1.2 x 10^{-11} cm/W at 1.0 microns. This difference between gain measurements is not yet resolved.

A discussion of the spectrum itself can be conveniently divided into three regimes:

A. 100-500 cm^{-1}: This is the regime of interest for fiber Raman amplifiers. Over this range of frequency shifts the gain is highly polarized. The perpendicular contribution to the gain is small and gain measurements agree fairly well with measurements of spontaneous scattering. As discussed later, the gain for randomly polarized light is half that for pump and signal light of the same polarization state.

B. 0-100 cm^{-1}: This low frequency regime is of concern for Raman interactions of channels in dense WDM systems. Here bulk Raman studies show that the gain is depolarized with the perpendicular gain about 1/3 of the parallel gain. Note that a measurement of perpendicular and parallel Raman gains in a silica-core polarization-maintaining fiber found a ratio of perpendicular to parallel gains of 45%. The discrepancy between bulk and fiber measurements is not understood.[4] This is a regime where more work is needed.

C. >500 cm^{-1}: For frequency shifts greater than 500 cm^{-1} the Raman gain is small and generally not of importance in silica-based optical fibers. There are two exceptions in which a strong sharp Raman line appears when certain dopants are incorporated into the glass. These lines are useful for producing large frequency shifts in fiber Raman lasers. Phosphorus doping leads to a line at 1330 cm^{-1} [5] and H_2 or D_2 in the glass produces lines with extremely large shifts of 4139 and 2975 cm^{-1}[6] Note that the weak Raman line at 1070 cm^{-1} in pure fused silica is the strongly infrared-active Si-O stretching vibration whose overtones produce the long wavelength transmission cutoff around 1.7 microns in silica fibers.

III. GERMANIUM DOPING

Germanium doping raises the Raman gain coefficient. The effect is small in standard fibers, which contain about 4 mole % GeO_2 but can raise the gain by about 50% in dispersion-shifted fibers. The gain is more than doubled in dispersion-compensating fibers. A careful series of measurements has been reported for spontaneous Raman scattering vs GeO_2 concentration in a Ge-doped MCVD preform.[7] The maximum increase is at a shift of 430 cm^{-1} where 20 mole % GeO_2 raises the gain by a factor of 2.6 over pure silica glass. For shifts less than 200 cm^{-1} the increase is approximately a factor of 2.

In a fiber the mode field penetrates into the cladding so the effective Raman gain coefficient will be some average over the doping profile, which will be less than the increase in gain from the maximum at the core center. The proper way to include the increase in Raman gain from Ge-doping is to include it in the calculation of the overlap integral. Similar issues arise in calculating the increase in nonlinear index from Ge-doping.[8]

IV. EFFECTIVE AREA

Most of the increase in Raman gain in highly Ge-doped single-mode fibers comes from a decrease in effective area. Usually the uncertainty in measurement of Aeff is greater than most of the details discussed here.

Note that the effective area for Raman gain is actually:

$$Aeff = 2\pi \frac{\int \Psi p^2 rdr \int \Psi s^2 rdr}{\int \Psi p^2 \; \Psi s^2 \; rdr}$$

where Ψp and Ψs are the mode fields of the pump and signal. So far it has made little difference whether Aeff is calculated using only Ψp or Ψs. In some fiber designs Aeff changes rapidly with wavelength and more care will be necessary.

V. WAVELENGTH DEPENDENCE

Raman gain is usually taken at the pump wavelength and the gain varies as $1/\lambda_p$. Actually the gain will fall off slightly faster with wavelength because the polarizibility of the ions in the glass decreases slightly with wavelength. This is the same decrease in polarizibility that causes the wavelength dependence of both the linear and nonlinear refractive indices. If we make some rather drastic assumptions we can argue that the gain coefficient should vary as: $(n^2 -1)^2/ n^2$. This is not a large effect. If we calculate n using standard Sellmeier coefficients [9], it amounts to only 2% between 1.0 and 1.5 microns. Including this factor, however, means that the gain measurement at 526 nm of Ref.2 translates to 0.96×10^{-11} cm/W at 1 micron. This may explain a some lower values of gain coefficient obtained at 1.5 microns.[10]

There are some other approximations made in the relation of the gain coefficient to the spontaneous Raman cross section. The small difference between pump and signal frequencies is neglected as well as the difference in refractive indices at pump and signal wavelengths.

VI. POLARIZATION DEPENDENCE

Most Raman gain measurements are made in non-PM fibers where polarization is scrambled. It is usually a good approximation to take the gain with scrambled polarizaions to be ½ that for linear polarization of pump and signal waves. This, however, neglects the perpendicular contribution to the gain. In the range 100-500 cm^{-1} the perpendicular contribution is small. In the range 0-100 cm^{-1} the perpendicular contribution needs to be included. As a first approximation the simplest procedure for randomly polarized light is to add the parallel and perpendicular gains and divide by two.

In low PMD fibers the measured gain may actually be closer to the polarized gain even though the state of polarization is not maintained.[11] This is because the gain is maximum as long as the states of polarization of the pump and signal waves are the same - even for elliptical polarizations. Eventually the gain will drop when the polarization states get out of step because of the wavelength difference between pump and signal. For example, this polarization length will be 2 km in a low PMD fiber with effective birefringence of 10^{-8} for a wavelength difference between pump and signal of 100 nm in the 1500 nm wavelength range. At 10 nm pump-signal separation the polarization length is 20 km, which is the nonlinear effective length for typical fibers in this wavelength range. This means that for Raman interaction between dense WDM channels the gain should often be the polarized gain.

There is still the additional factor of the perpendicular gain in the 0-100 cm^{-1} range. How this contributes when the polarization state varies is still not well understood. Treatment of the total parallel and perpendicular gains in this region should probably start with a general treatment using both the parallel and perpendicular Raman response functions.[12].

VII. FOUR-WAVE MIXING

An additional complication for Raman gain measurements with small frequency separation between pump and signal is four-wave mixing which can also amplify the signal. This problem can be overcome if the dispersion is high enough that the coherence length for four-wave mixing is short.

The best way to avoid problems with four-wave mixing as well as from uncertainties over the polarization length is to use a counterpropagating pump. This is the configuration for most Raman amplifiers to avoid introducing noise from pump fluctuations. The real problems are likely to arise with dense WDM channels

VIII. CONCLUSION

So far, the major problems with Raman gain measurements seem to be in accurate measurement of the effective area and an understanding of the effect of randomly varying polarization for small wavelength separation between pump and signal. Of the additional corrections to the properties of the gain coefficient, the next of importance is probably the modification to the $1/\lambda_p$ dependence.

REFERENCES

1. R.H. Stolen, C.Lee, and R.K. Jain, "Development of the stimulated Raman spectrum in single-mode fibers," J.Opt.Soc.Am., 652 (1984). The low frequency data includes subsequent measurements of scattering at small frequency shift and low temperature. The perpendicular spectrum was compiled from several published sources. Both curves are available as data files from the author.
2. R.H. Stolen and E.P. Ippen, "Raman gain in glass optical waveguides," Appl. Phys. Lett., 22, 276 (1973).
3. R.Hellwarth, J.Cherlow, and T-T. Yang, "Origin and frequency dependence of nonlinear optical susceptibilities of glasses," Phys.Rev. B 11, 964 (1975).
4. D.J.Dougherty, F.X.Kartner, H.A.Haus, E.P. Ippen, " Measurement of the Raman gain spectrum of optical fibers," Opt. Lett., 20, 31 (1995).
5. V.I.Karpov, E.M.Dianov, A.S.Kurkov, V.M.Paramonov, V.N.Protopopov, M.P.Bachynski, W.R.L.Clements, LD-pumped 1.48-μm laser based on Yb-doped double-clad fiber and phosphorosilicate-fiber Raman converter," OFC'99, San Diego, CA Feb.21-26, 1999: paper WM3.
6. A.R. Chraplyvy and J. Stone, "Single-pass mode-locked or Q-switched pump operation of D_2 gas-in-glass fiber Raman lasers operating at 1.56 μm wavelength," Opt. Lett., 10, 344 (1985).
7. S.T.Davey, D.L.Williams, B.J.Ainslie, W.J.M.Rothwell, B.Wakefield, "Optical gain spectrum of GeO_2-SiO_2 Raman fibre amplifiers," IEE Proceedings, 136, 301 (1989).
8. D.L.Philon, D.W.Peckham, I.Brener, "Measurement of the non-linear index of refraction N_2, for various fiber types," OFC'2000, Baltimore, MD March 7-10 (2000); paper ThL5.
9. G.P. Agrawal "Fiber-Optic Communication Systems," (John Wiley, New York, 1997) p.41.
10. V. L DaSilva and J.R.Simpson, "Comparison of Raman efficiencies in optical fiber," OFC'94, San Jose, CA, Feb.20-25 (1994): p.136.
11. R.H. Stolen, "Polarization effects in fiber Raman and Brillouin lasers," IEEE J.Quantum Electron., QE-15, 1157 (1979).
12. C-J.Chen, C.R.Menyuk, M.N.Islam, R.H.Stolen, "Numerical study of the Raman effect and its impact on soliton-dragging logic gates," Opt. Lett., 16, 1647 (1991).

Broadband Raman Gain Characterization in Various Optical Fibers

F. Koch[*], S.A.E. Lewis[*+], S.V. Chernikov[*+], and J. R . Taylor[*]

[*]Femtosecond Optics Group, Physics Department, Imperial College,
Prince Consort Road, London SW7 2BW, UK
[+]IP Fibre Optics Ltd, Hoppingwood Farm, Robin Hood Way, London SW20 0AB
Email: fkoch@ic.ac.uk

Raman scattering in optical fibers currently attracts considerable research interest. The use of stimulated Raman scattering as a gain mechanism gives certain advantages over Erbium doped Fiber Amplifiers (EDFA) in that gain can be provided anywhere within the wavelength range of transparency in optical fibers. The use as distributed amplifiers as a way of upgrading older systems and for soliton transmission is also advantageous compared to EDFAs. Additional Raman scattering is a source of noise in wavelength division multiplexing (WDM) systems where the Raman gain is a source of cross-talk between channels. For accurate modeling and estimation of these effects the Raman gain coefficient needs to be known accurately. The effect of Germanium doping has been investigated previously [1], however here we show the fine structural differences for different dopant levels and provide an estimation of the relation between maximum gain and dopant level.

The technique for the determination of the Raman gain coefficient is based on the measurement of the amplified spontaneous emission (ASE) [2] along the test fiber pumped by a narrow linewidth high-power fiber Raman laser. Figure 1 shows the experimental set up with a circulator used to multiplex and de-multiplex the pump and ASE signal from the fiber under test. The ASE power can be determined similar to the technique in reference [3], but in Equation 1 we distinguished between the loss at the pump wavelength (α_p) and the loss at the signal wavelength (used in the calculation for the Gain G). Also included is a thermal factor Φ [4]. ν_s is the signal frequency, Δf the frequency difference between pump and signal and h is Planks constant. For every pump power P the ASE power in the backwards direction can be calculated from Equation 1. In the experiment we measured the dependency of the ASE power with an optical spectrum analyser (OSA) as a function of the pump power. All measurements had to take the losses between point A (see Figure 1) inside the test fiber and the spectrum analyser into account. A least square fitting algorithm fitted the measured data to Equation 1 with the Raman gain coefficient $C_r=G_r/A_{eff}$ as variable. For higher pump powers Rayleigh scattering of the forward ASE into the backward direction also contributed to the measured signal and increased the error of the fitting. By limiting the pump power this error was minimized and no additional terms for the Rayleigh scattering were required to be added.

Figure 2 shows the normalized gain coefficient for three different fibers with different Germanium concentrations. The pure silica core fiber (PSCF) shows more fine structure and the secondary peak (at 490 cm^{-1}) is higher than the first (at 444 cm^{-1}). Also the peaks at longer wavelength shifts are narrower. The dispersion-shifted fiber (DSF) with a medium Germanium content (~5-6 %) still shows the second peak (at 480 cm^{-1}) but it is much lower now. In the high Germanium content dispersion compensating fiber (DCF) (16% to 18%)all the features in the gain spectrum are washed out as a result of the Germanium doping.

In Figure 3 the peak Raman gain coefficient for all measured fibers is shown as a function of Germanium content. A clear connection between the Raman gain coefficient and the Germanium indicates that the dispersion compensating fiber gives the highest Raman coefficient.

This figure only indicates the Raman gain coefficient C_r, however the maximum gain achievable and the performance of an amplifier depends on many more factors such as the losses, effective area of the fiber, Rayleigh scattering and noise figure of the amplifier [5]. For minimum cross talk in WDM systems other factors such as the dispersion have to be taken into account.

In conclusion we have measured the Raman gain coefficient for fibers with different Germanium dopant content and showed structural differences for the different dopant levels. A clear relationship between the Germanium content and the maximum Raman gain coefficient was shown.

$$P_{ASEBack}(P) := G\cdot\left(C_r\cdot P\cdot\int_0^L \frac{\exp(-\alpha_p\cdot\xi)}{G}\,d\xi\right)\cdot 2\cdot h\cdot\nu_s\cdot\Delta f\cdot\Phi$$

Equation 1

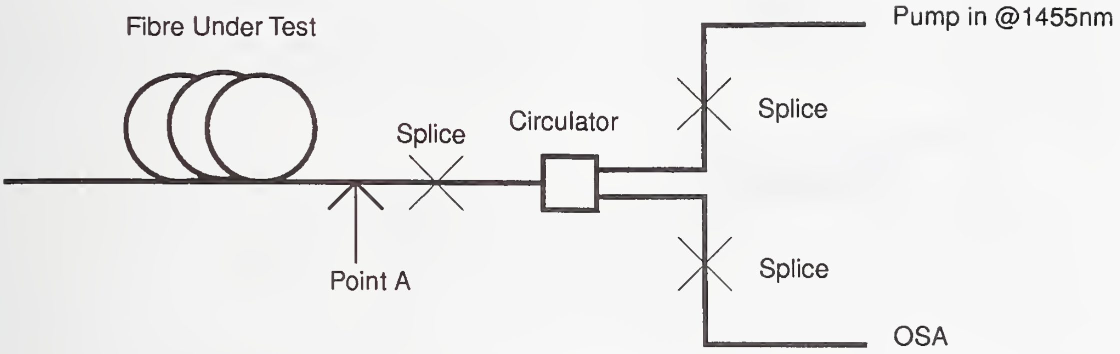

Figure 1 "Experimental Set-Up"

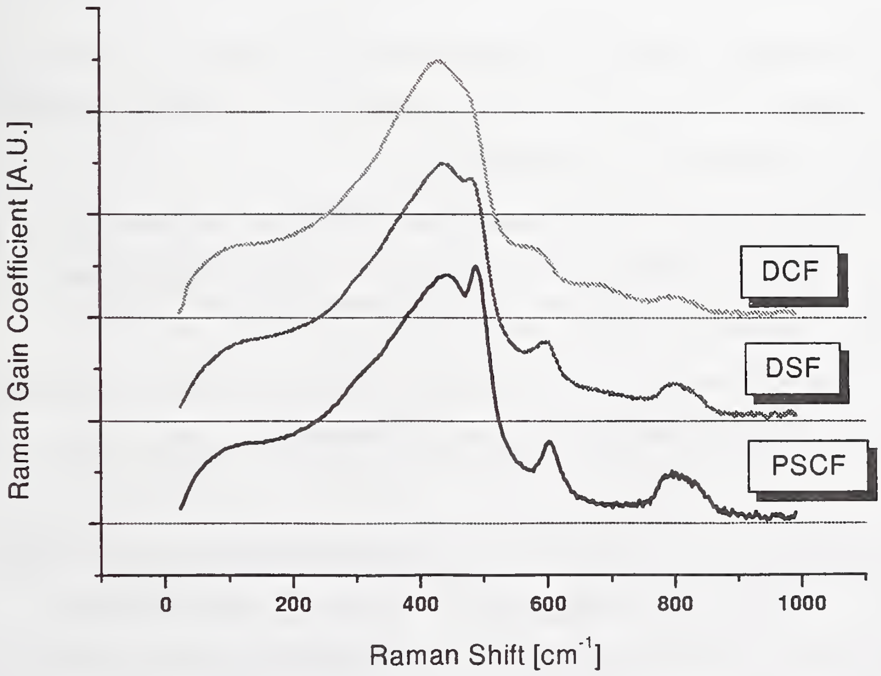

Figure 2 "Normalized Gain of Various Fibers"

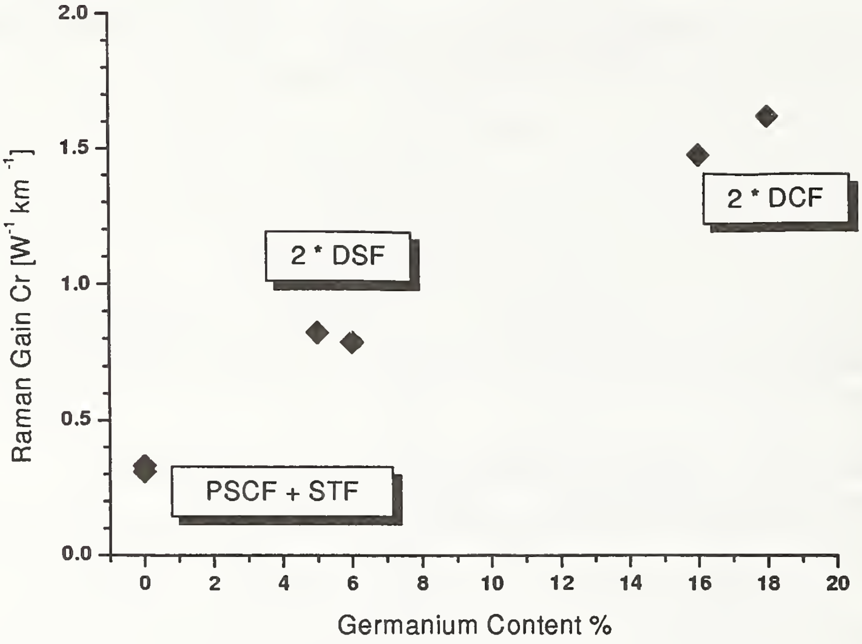

Figure 3 "Gain for Different Germanium Contents"

References:

(1) "Optical gain spectrum of GeO_2-SiO_2 Raman fibre amplifiers", S.T. Davey, D.L. Williams, B.J. Ainslie, W.J.M. Rothwell, B. Wakefield-B, IEE-Proceedings-J-(Optoelectronics), Vol.136, No.6; Dec. 1989; p.301-6

(2) "Technique For Measurement Of The Raman Gain Coefficient In Optical Fibers", D. Mahgerefteh, D.L. Butler, J. Goldhar, B. Rosenberg, G.L. Burdge, Optics Letters, 1996, Vol.21, No.24, pp.2026-2028

(3) "Theory And Implementation Of A Raman Active Fiber Delay-Line", E. Desurvire, M.J.F. Digonnet, H.J. Shaw, Journal Of Lightwave Technology, 1986, Vol.4, No.4, pp.426-443

(4) "Temperature-dependent gain and noise in fiber Raman amplifiers", S.A.E. Lewis, S.V. Chernikov, J. R . Taylor, Optics Letters, 1999, Vol.24, No.24, pp.1823-1825

(5) "An Analysis Of The Improvements In OSNR From Distributed Raman Amplifiers Using Modern Transmission Fibres", C. Fludger, A. Maroney, N. Jolley, R. Mears, OFC2000, Paper FF2

Raman spectra of line fibres measured over 30 THz

D. Hamoir, N. Torabi, A. Bergonzo, S. Borne and D. Bayart

Alcatel, Corporate Research Center, Route de Nozay, 91460 Marcoussis, France
E-mail : dominique.hamoir@alcatel.fr

Abstract: *The Raman efficiency of line fibres is measured over a total range of 30 THz. The effect of tuning the pump from 1400 to 1486 nm is shown. The information presented is essential for designing future wide band transmissions with distributed Raman amplification.*

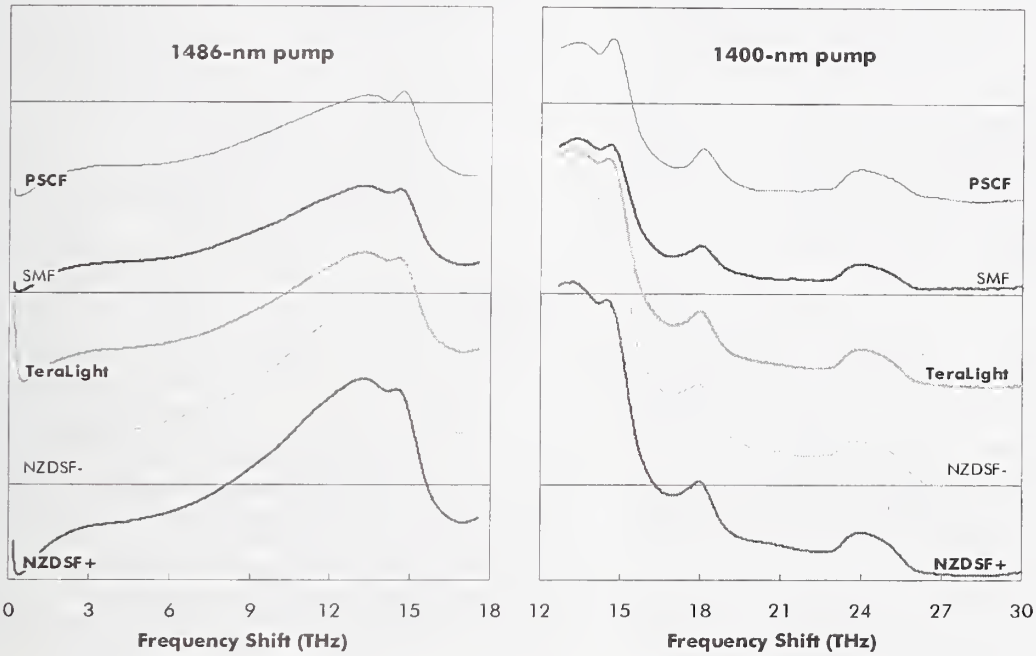

Figure 1 : Raman gain coefficient in W^{-1}.km^{-1}, with a scale of 0.4 W^{-1}.km^{-1}/div. For each fibre, the zero line is the division below the fibre name.

Introduction

The transmission capacity of optical fibres is limited by the signal-to-noise ratio required at reception and by non-linear effects. Distributed amplification is one of the solutions that allow to further push the performance of transmission systems. Stimulated Raman scattering (SRS) is a privileged way of obtaining a distributed amplification because it is intrinsic to every silica-based glass. This allows using standard line fibres as amplification media /1/.

Although it is beneficial for distributed amplification, SRS is a major limitation in very-dense, wide-band transmission systems /2,3/. This impairment is known as Raman tilt.

The Raman spectra of line fibres have been measured in the past /1-4/. However these measurements were often relatively limited in bandwidth. They frequently disregarded Raman-shifts exceeding 18 THz and those focusing on amplification considerations usually neglected small shifts. However the design of wide-band systems with distributed Raman amplification requires the prediction of pump-pump and signal-signal interactions with small frequency differences, as well as the interactions between the higher-frequency pumps and the lower-frequency signals. Hence it is fundamental to know the Raman gain coefficients of the line fibres for shifts ranging from virtually 0 THz up to 26 THz or more.

To answer this need we measured the Raman efficiency of standard line fibres from 120 GHz up to 30 THz.

We also got valuable information on the effects of changing the wavelength of the pump inside the 1.4-µm band when considering amplification in the 1.5-µm band.

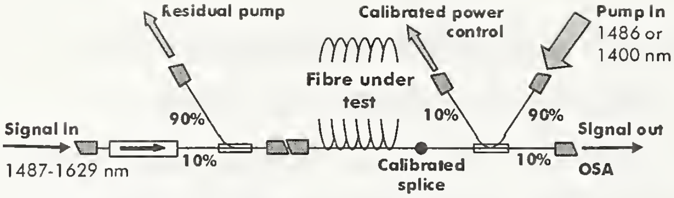

Figure 2 : Set-up for precise on/off gain measurement

Experiments

Indeed we pumped the fibres with wavelengths sitting on both sides of the pumping-band used for Raman amplification in the C+L band : 1486 nm for a first series of measurements and 1400 nm for a second. The signal was tuned from 1487 to 1629 nm, centred on the C+L band. The experimental set-up is shown in figure 2. We choose to inject 200 to 300 mW of pump into the fibre under test. This choice ensured minimal measurement errors along with low amplified spontaneous emission and amplified Rayleigh scattering. The pumping power was measured thanks to a calibrated coupler. The splice to the fibre was calibrated by cut-back. Hence the pumping power injected into each fibre was known with a good precision.

Since Raman gain is rather low, even very low for certain frequency shifts, an extreme accuracy is required in the gain measurement. We choose to perform "on/off" gain measurements to cancel out every inaccuracies on the (spectrally-dependent) attenuation of components, of connectors, of splices and of the fibre itself. For each fibre we acquired a reference spectrum at the "signal out" port, for which the pump was off, and a second spectrum in the exact same conditions, except that the pump was turned on and its power precisely controlled. The precision of the gain curve obtained after subtracting the two spectra was limited only by the power-repeatability of the signal laser and by the relative accuracy of the optical spectrum analyser (OSA).

The power of the tunable signal source was adjusted before measuring the spectra. A small-signal is required so that the "on"-spectrum is not affected by saturation or by stimulated Brillouin scattering in the high-gain regions. However the signal should be powerful enough to get a good precision vs integration-time compromise and to ensure that the contribution of amplified spontaneous emission to the "on"-spectrum is negligible. As a consequence we checked the gain as a function of the signal power and then choose a signal power in the upper part of the linear regime.

Results

The pump lasers were not polarised : the Raman efficiency measured (figure 1) is the exact mean value of the efficiencies obtained when the polarisation of the signal is maintained either parallel or orthogonal to that of a polarised pump.

The Raman efficiency of a given fibre is defined as $C_R = G_{on/off} \cdot (\ln(10)/10) / (P_{pump} \cdot L_{eff})$, where $g_{on/off}$ is the on/off gain measured with a pumping power P_{pump}, injected into the fibre of effective length L_{eff}.

In figure 1 the fibres are ranked by their peak gain-coefficient at 13.3-THz, when pumped at 1486 nm (figure 1, left). The non-zero-dispersion shifted fibres with positive and negative dispersion at 1.55 µm presented the highest peak coefficients (0.84 and 0.77 $W^{-1}.km^{-1}$). Then came the TeraLight (0.57 $W^{-1}.km^{-1}$). The lowest peak coefficients were obtained with a standard single-mode fibre (0.45 $W^{-1}.km^{-1}$) and with a pure silica core fibre (0.43 $W^{-1}.km^{-1}$). All these fibres are respectively referred to as NZDSF+, NZDSF-, TeraLight, SMF and PSCF.

Table 1 : Fibres under test

	Length (km)	Effective area @ 1558 nm (µm²)	Chromatic dispersion ($ps.nm^{-1}.km^{-1}$)	Dispersion slope ($ps.nm^{-2}.km^{-1}$)
NZDSF+	24.7	55	3.2	0.07
NZDSF-	23.1	55	-2.3	0.08
TeraLight	50.0	67	8.0	0.058
SMF	23.3	83	17.0	0.058
PSCF	18.4	78	18.0	0.055
	Measured		Nominal at 1.55 µm	

If the pump and signal modes were not altered, changing the wavelength of the pump should not modify the peak efficiency of a given fibre when expressed in $(photons/s)^{-1}.km^{-1}$. In such a case the peak efficiency expressed in $W^{-1}.km^{-1}$ should only scale with the pump wavelength because the energy per pump photon changes. In particular the Raman efficiency should be reduced by 6 % when pumping at 1400 nm instead of 1486 nm.

On the contrary we found much higher peak efficiencies with the 1400-nm pump (figure 1, right) than with the 1486-nm pump (figure 1, left). Indeed the peak efficiencies obtained with the 1400-nm pump were 1.25, 1.29, 1.01, 0.65 and 0.65 $W^{-1}.km^{-1}$ for respectively the NZDSF+, NZDSF-, TeraLight, SMF and PSCF. This strong improvement in efficiency can be explained as follows : with lower pump and signal wavelengths the pump and signal modes are more confined into the Ge-doped core, in addition to what the pump-to-signal mode overlap is improved.

Figure 3, next page, compares the Raman efficiencies of the fibres for small frequency shifts, corresponding to signal-signal and to pump-pump interactions in C+L band systems with distributed amplification. Our results are in good agreement with /2/. The gain spectra can be exploited for shifts beyond 300 to 500 GHz, the lower part of the spectra being affected by back-reflections of the pump into the signal path. As a general rule, fibres that offer higher peak gain coefficients unfortunately induce more tilt.

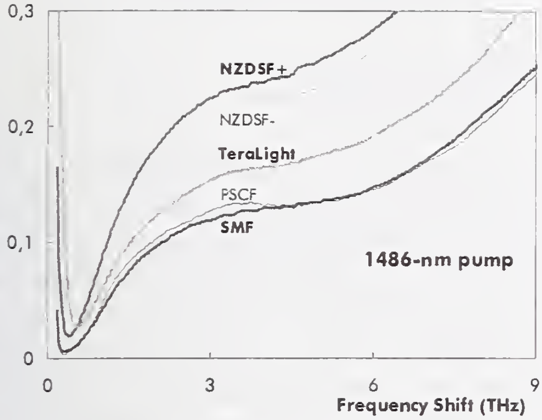

Figure 3 : Raman gain coefficient in $W^{-1}.km^{-1}$.

This is confirmed by figure 4 where each gain curve has been normalised with respect to its peak value. Figure 4, left shows that the normalised gain curves measured are somewhat similar in shape for frequency-shifts up to 18 THz, despite differences to be expected in their composition.

However some slight differences can be observed from one fibre to the other. For frequency shifts involved in Raman tilt, below 9 THz, the PSCF presents higher normalised gain coefficients than the other fibres. This is in agreement with reference /5/. Indeed, the spontaneous Raman spectra of vitreous SiO_2 and GeO_2 in reference /5/ permit to derive that the amplitude of the so-called boson-peak, at about 3 THz, is higher with SiO_2 than with GeO_2 when normalised with respect to the main, 13.3-THz peak.

Additional information can be derived from figures 1 and 4. The broad 13.3-THz peak is strongly affected by Ge doping (figure 1). This main peak extends up to beyond 20 THz. The sharp secondary peaks at about 14.5 THz and 18 THz seem to be specific to pure silica as their absolute amplitudes are much less affected by Ge doping (figure 1), which turns into very sharp peaks for the PSCF when normalised (figure 4). These deductions are confirmed by the data of reference /5/ on pure SiO_2 and GeO_2 glasses.

Conclusion

We have measured and compared the Raman efficiencies of standard line fibres for frequency shifts ranging from a few hundreds of GHz up to 30 THz, allowing to record even the 18-THz and 24-THz peaks of the Raman spectra. We observed that the 13.3-THz-peak gain-coefficient of NZDSF+ was twice as large as that of PSCF. We also showed that the peak efficiency was much higher for a 1400-nm pump than for a 1486-nm one, due to the important change in pump/signal/core overlap. We also saw that Raman tilt unfortunately increased with the peak gain coefficient. Finally the normalised gain curves were found to be rather similar from one fibre to the other.

These new data are essential for designing future transmission systems based on distributed Raman amplification.

In addition we would like to underline that the attenuation at the pump wavelength is also paramount when designing a system with Raman amplification. Aspects such as the attenuation at the signal wavelength, the resistance to other non-linear effects and PMD are as well of great importance. The best fibre for a given application is the best compromise.

Acknowledgement

The authors wish to thank P. Guénot, F. Leplingard and S. Bigo for fruitful discussions.

References

/1/ C. Fludger et al., paper FF2, OFC'00 (2000).
/2/ S. Bigo et al., paper WJ7, OFC'99 (1999).
/3/ G. Shaulov et al, paper TuA4, OFC'00 (2000).
/4/ V. L. da Silva et al., paper WK13, OFC'94 (1994).
/5/ F. L. Galeener, 8th International Conf. on Raman Spectroscopy, p. 529 (1982).

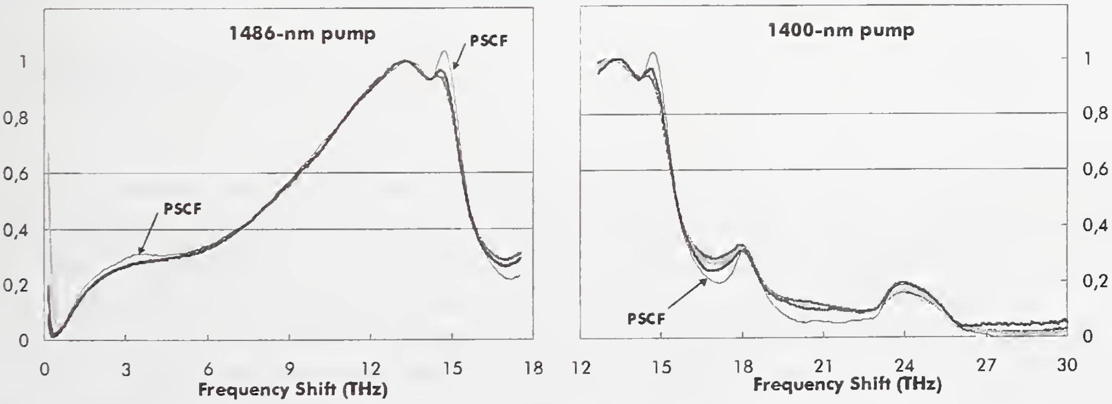

Figure 4 : Normalised Raman gain curves

Raman Gain Measurements in Optical Fibers

Stuart Gray
Corning Incorporated, SP-AR-01-1,Corning, NY, 14831

The use of distributed Raman amplification has recently been demonstrated to be a key technology in upgrading the capacity or extending the reach of optical fiber communication systems [1]. The design of systems including Raman amplification requires a detailed understanding of how the Raman gain varies between different commercially available fiber types and also the variation within the manufacturing tolerances of a particular fiber design. In this paper I will describe a simple technique for measuring the spectrum of the Raman gain coefficient in an optical fiber and discuss measurements made on fibers with different effective areas. I will also present data on the gain and noise figure characteristics of distributed Raman amplification in different fiber designs.

The technique for measuring Raman gain coefficients is illustrated in Figure 1. The output of a broadband LED source covering the spectral range from 1300-1700 nm is transmitted through the fiber under test and the light at the output is collected on an optical spectrum analyzer (OSA). The length of fiber measured is typically 5-20 km. The pump source is a cascaded Raman resonator with an output wavelength of 1486 nm pumped at 1100 nm by an Ytterbium double clad fiber laser. In all measurements the pump and signal are counter-propagated.
To calculate the Raman gain coefficient three spectra are recorded. First the spectrum of the un-amplified LED signal is taken. Second, the pump is turned on and the launched power is monitored through a calibrated tap coupler. The spectrum recorded at the output contains both the amplified signal and amplified spontaneous emission (ASE). Finally, the LED is turned off while leaving the pump on and a spectrum of the ASE is recorded and subtracted from the previous spectrum to obtain the spectrum of just the amplified signal. The pump power is then calibrated and the Raman gain coefficient calculated. This technique works because in the small signal (un-depleted pump) regime the amplified signal and ASE are independent of each other (see, for example, [2]). The Raman gain coefficient is then calculated using the following equation.

$$G = \exp\left(\frac{g_R P}{A\alpha}\left(1 - \exp(-\alpha L)\right)\right)$$

Here, G is the signal gain, α is the fiber attenuation at the pump wavelength, L is the fiber length, P is the pump power launched into the fiber, g_R is the Raman coefficient of the fiber material and A is the effective area. The quantity $g_R/\alpha A$ can be used to compare the Raman efficiency of different fibers and will be referred to below as the Raman figure of merit. The use of a broadband signal source for these measurements makes the procedure very fast compared to measuring the gain coefficient at discrete points using a tunable laser and also provides an essentially continuous spectrum.

The value of g_R/A measured using the above technique is shown in figure 2 as a function of frequency offset from the pump for two commercially available fiber types, standard single-mode fiber (SMF) and a non-zero dispersion shifted fiber (NZ-DSF). The Raman coefficient is plotted in units of W^{-1} km^{-1} for an unpolarized pump. The properties of these fibers are summarized in Table 1 where the attenuation and mode field diameter are given at the pump wavelength. The NZ-DSF has a Raman coefficient 20% higher than SMF. This difference results from the smaller effective area of NZ-DSF combined with a higher GeO_2 content than exists in SMF. The figure of merit for the NZ-DSF fiber is also correspondingly larger than in SMF and demonstrates the higher Raman pump efficiency of the NZ-DSF fiber.

The design of a product for the distributed Raman amplification market has to take into account variations in the Raman efficiency caused by the manufacturing distribution. This has been studied for NZ-DSF by measuring the Raman figure of merit of several fibers with varying mode field diameters. The properties of these fibers are summarized in table 2. The figure of merit of these fibers varied from 8.7 to 9.4, a difference of 8%. This directly leads to an 8% variation in the pump power required to achieve a fixed amount of gain in these fibers and has to be included in the design of an appropriate pump module.

The design of a system incorporating distributed Raman amplification has to include the noise properties of the distributed amplification process and its interaction with the lumped erbium doped fiber amplifiers (EDFAs). Therefore the noise figure of the distributed Raman amplifier has to be characterized in different fibers as a function of the distributed gain. The gain and noise figure of the distributed amplifier are defined by equating the gain and ASE to be equivalent to that generated by a discrete amplifier placed at the end of the transmission span. This amplifier is in general not physically realizable and often gives noise figures that are below zero.

The gain and equivalent noise figure (ENF) are measured using a setup similar to that shown in Figure 1 but with the LED replaced by a DFB laser and the test fiber replaced by typically 75-90 km of transmission fiber to represent a complete system span. A signal wavelength of 1590 nm was chosen for these measurements which corresponds to the peak of the Raman gain curve for the 1486 nm pump wavelength. The noise figure is calculated using ASE interpolation method on the OSA and includes corrections for the coupling loss of the circulator.

Measured values of gain and noise figure for SMF and NZ-DSF fibers are shown in Figure 3. In each case, a power of –10 dBm was used at the input. The behavior of the two fibers is very similar. Initially the ENF decreases almost linearly with increasing Raman gain to a minimum at gains of ~30 dB. Minimum equivalent noise figures of ~-4 dB were observed in both fibers. As the gain is increased further the measured ENF increases rapidly due to the effect of double Rayleigh scattering of the ASE. Identical behavior has been seen in both fibers for input powers in the range –40 to 0 dBm. Gains greater than 37 dB were not observed in SMF due to the limited pump power available. The impact of double Rayleigh scattering, a cause of multiple-path interference, is expected to be different for different fiber types because the capture coefficient of a fiber for scattered light varies as the inverse of effective area [3]. This is likely to place an upper limit on the amount of distributed Raman gain which can be used in a particular fiber type before double Rayleigh scattering noise degrades system performance.

In conclusion, I have described a technique for measuring the Raman gain spectrum of an optical fiber using a broadband signal source and have used this setup to measure the variation of Raman gain efficiency in fibers with different mode field diameters. The distribution of Raman properties requires a similar variation in the levels of pump power required to achieve a particular level of Raman gain. The noise figure as a function of distributed Raman gain has also been measured for two different fiber types. The behavior of both fibers is similar in the regime where double Rayleigh scattering is negligible. When double Rayleigh scattering becomes important the noise figure is expected to increase most rapidly in the fiber with the smaller effective area and higher capture coefficient.

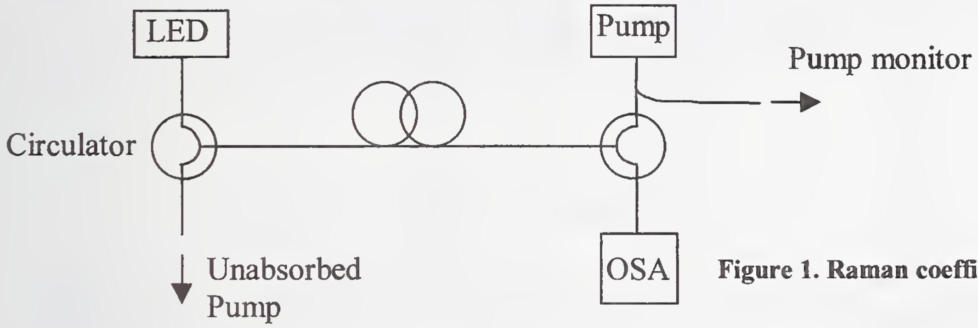

Figure 1. Raman coefficient measuring system

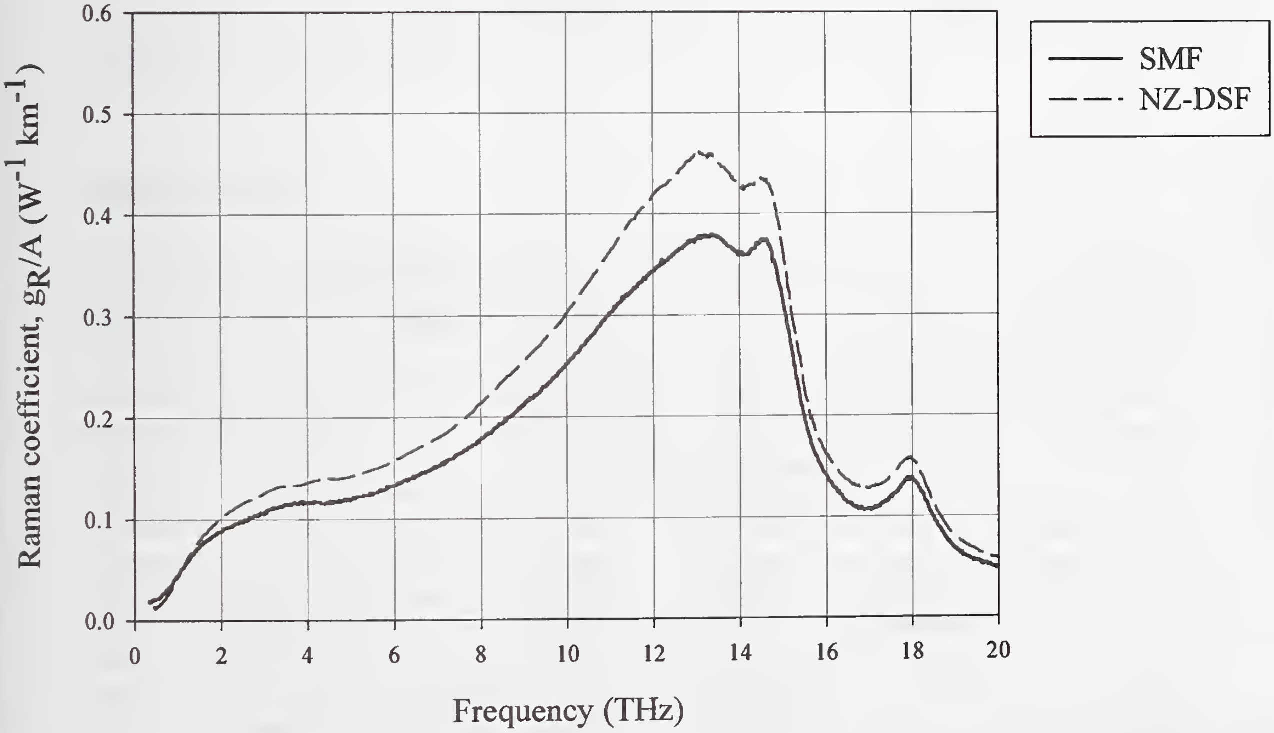

Figure 2 . Raman spectra of transmission fibers

Fiber Type	MFD @ 1480 nm (μm)	g_R/A (km^{-1} W^{-1})	α @ 1480 nm (km^{-1})	Figure Of Merit
SMF	9.78	0.380	0.05	7.6
NZDSF	8.85	0.457	0.05	9.1

Table 1. Parameters of fibers in figure 2

Fiber	MFD (1550 nm) (μm)	α (1550 nm) (dB/km)	Figure Of Merit (pump =1486 nm)
1	9.77	0.2	9.38
2	9.68	0.2	9.04
3	9.78	0.2	9.22
4	9.78	0.2	9.12
5	9.77	0.2	9.04
6	9.74	0.2	9.23
7	9.74	0.2	9.35
8	9.77	0.2	8.69

Table 2. Properties of several NZ-DS fibers

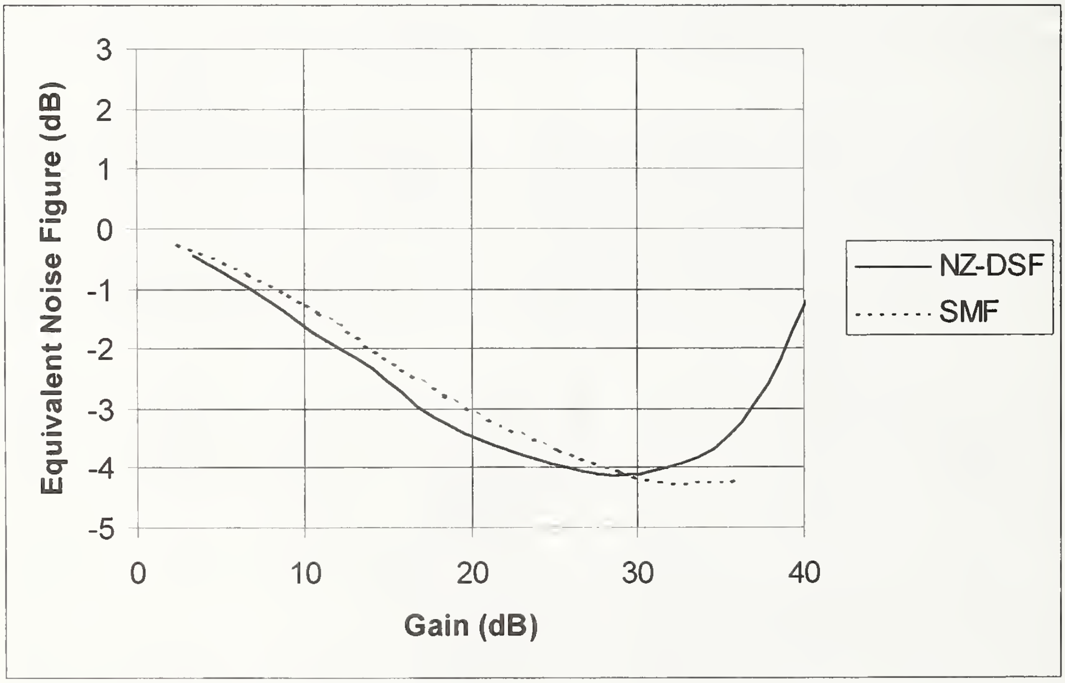

Figure 3. Gain v NF for SMF and NZ-DSF

---

1. P. B. Hansen, L Eskildsen, S.G. Grubb, A.J. Stentz, T.A. Strasser, J. Judkins, J.J. DeMarco, R. Pedrazzani and D.J. DiGiovanni, Photonics Technology Letters, vol. 9 pp 262-264 (1997).
2. S.R. Chinn, Electronics Letters, vol 33, pp 607-608 (1997).
3. E. Brinkmeyer, Electronics Letters, vol 16, pp 329-330 (1997).

Overview of coherent reflectometry techniques: characterization of components and small systems

M. Wegmüller, P. Oberson, J.P. von der Weid*, O. Guinnard, L. Guinnard,
C. Vinegoni, M. Legré, N. Gisin

Group of Applied Physics, University of Geneva, 20 Ecole-de-Médecine, CH-1211 Genève 4,
Switzerland, *mark.wegmuller@physics.unige.ch*
* Center for Telecommunications Studies, PUC-Rio, Rio de Janeiro, 22453-900 Brazil

Abstract

Coherent reflectometry techniques have important advantages over direct detection techniques: larger sensitivity, larger dynamic range, better resolution, and spurious light suppression. The measurement range is typically limited to <1 m for Optical Low Coherence Reflectometry, and to <~1 km for Coherent Optical Frequency Domain Reflectometry. Especially the second technique is therefore well suited for measurements of optical modules with extended components and for small systems.

Introduction

The advantages of coherent reflectometry techniques are well known. In fact, they are still the only techniques giving two point resolutions in the mm range. Of the two major coherent reflectometry techniques Optical Low Coherence Reflectometry (OLCR) and Coherent Optical Frequency Domain Reflectometry (OFDR), the first is well established and widely used for component characterization [1]. In typical OLCR implementations, the measurement range is however limited to below 1 m. None of the proposals to extend this value have been retained on a large basis so far, mainly for the sake of having robust and compact OLCR devices.

Although a sub-metric range is well adapted for the characterization of single, compact components, it is too small for larger, more complicated optical modules including several composites as couplers, WDMs, taps, modulators, etc. The path length in such devices can easily reach some tens of meters, and OFDR has to be employed. Although this technique is well known for several years, it has not seen broad commercial implementation so far. The main reason is that the constraints on the source are heavy, and a simple, non-expensive yet reliable source giving the desired performance was lacking. In this paper, a novel OFDR device based on a simple, mechanically tunable fiber laser [2] is presented. After giving the characteristics of this device, several applications relevant for small systems metrology are presented.

Principles of OFDR

To avoid all confusion, let us first stress that only the technique of coherent OFDR is considered here (there exists also a 'normal', non-coherent OFDR technique which is the frequency domain analogous of OTDR and measures the modulation transfer function [1]). The coherent OFDR technique (Fig.1) is based on the detection of a beat signal between the distributed reflections from the fiber under test (Rayleigh backscatter, connectors, etc.) and a fixed Fresnel reflection (local oscillator). Using a linear frequency sweep of the laser, one can straightforwardly map the measured beat frequencies on a distance scale, whereas the normed square power for a given beat frequency gives the reflectivity at the corresponding distance. For a good general overview of the OFDR principles and limits, the reader is referred to [3]. In the OFDR used for the measurements presented here, several important improvements have been implemented described in the following along with the specifications of the present device.

Range: The measurement range of OFDR is limited by the coherence length of the source and by its phase noise. The first one leads to signal fading, the second one reduces the dynamic range [3]. The fiber laser employed presently has a very large coherence length of about 3.3 km (FWHM bandwidth of 10 kHz) [1]. Fig.2 demonstrates the corresponding signal fading of about 5 dB/km, and the reduction in the dynamic range, limiting the useful range to about 2 km. Using more sophisticated (and complicated) sources or signal corrections, an order of magnitude larger ranges have been demonstrated [4]. However, the spatial resolution drops below the one achievable with OTDR, so the interest of such methods is questionable from an applications point of view. Fig.3 demonstrates that the 2 km range of our OFDR device is sufficiently large to assure a smooth transition between OFDR and OTDR applications.

Resolution: The maximum two-point resolution is given by the frequency excursion of the source. However, this value can be seriously deteriorated by nonlinearities in the frequency sweep. In our device, this is corrected for by using the signal from a reference interferometer from which the instantaneous frequency is calculated. For the fiber laser used, a maximum detuning of 0.3 nm is employed (41 GHz), giving a resolution of 5 mm as illustrated by Fig.4. The two point resolution also depends on the measurement range and on the number of points used. This is because the slope of the frequency excursion has to be reduced for a larger range so that no aliasing in the sampling is encountered (i.e. maximum beat frequency<Nyquist-frequency). The two point resolution and the measurement range become

$$\Delta l_{2p} \approx \frac{6.5}{N} L_{\max} \quad , \qquad L_{\max} \approx \frac{c}{6n} \frac{N}{\delta\nu} \ ,$$

respectively, where N is the number of sampling points (typically 8192), $\delta\nu$ the maximum frequency excursion, c the speed of light, and n the group index. Consequently, for a given range, the resolution is given by 0.08% of the distance range. For the maximum 5 mm resolution, the range is 6.6 m.

The importance of having a good resolution is clear from Fig.5. A line of 6 pigtails connected with FC-APCs was measured using different resolutions. This was achieved by changing the number of points N of the OFDR acquisition. Using 512 points (20 cm resolution, curve at top), the high quality connector at 8 m is covered by the Rayleigh light, and the fiber break after the last connector can not be discerned from the connector reflection (see inset). With 8192 points (12 mm resolution), the Rayleigh level drops by about 12 dB, and the small reflection from the high quality connector can be easily detected. Further, one clearly sees that the fiber break is after the last connector and not in front of it, an important feature for applications like fault detection in optical modules.

A consequence of having a high spatial resolution is that the Rayleigh backscattering (RBS) becomes very noisy due to the coherent speckle. Note that this is a physical limit (and not a technological one) affecting all high-resolution reflectometry methods. As less scatterers take part in the interference, the RBS becomes more peaked. This can somewhat be reduced by dithering the center frequency and averaging. In our device, the possible change in center frequency is however restricted by mechanical constraints of the fiber laser, and the smoothed RBS still varies somewhat. If one can average over sufficiently large distances, small losses can still be identified, as is demonstrated by Fig.6 which shows a measurement of a bad splice with 0.4 dB loss.

Polarization dependence, sensitivity, and dynamic range: As for all coherent techniques, the signal will depend on the polarization state of the reflected light. This can be advantageous to get information about the beatlength distribution (see below), but is typically an unwanted effect in standard applications. We therefore included a polarization diversity detection scheme in our OFDR device, reducing the polarization dependence of the reflected light to less than 0.5 dB. The sensitivity and dynamic range of the present device is -110 dB and 80 dB, illustrated in Fig.4. As was mentioned before, the dynamic range decreases with distance (see Fig.2) because of the source phase noise. Using time domain averaging, a sensitivity of -152dB with a dynamic range of 106 dB has been demonstrated in earlier work [5]. This technique however requires a very stable phase of the reflected signal, which is only achievable for short measurement distances.

Some measurement examples using OFDR

Due to its high sensitivity, dynamic range, resolution, and accuracy, OFDR is useful for a vast range of different applications in fiber metrology, like e.g. measurements of WDM components [6], distributed gain measurements in EDFAs [7,8], or local birefringence [9.10].

Measurement of distributed gain in EDFAs: The coherent detection scheme of OFDR leads to a strong rejection of background light from ASE or residual pump light. OFDR is therefore ideally suited for non-destructive, distributed gain measurements in EDFA. Fig.7 shows a measurement of the gain distribution in a 12 m long, 500ppm Er-doped fiber pumped by 1480 nm light. The set of curves was obtained by gradually increasing the pump power from no pump at all (lowest curve) to +15 dBm (top curve). Clearly, pump saturation led to gain clamping, with a maximum gain reached at 4.5 m. After that distance, the Er ions were no longer inverted due to a lack of pump power, and the signal is reabsorbed. Cut-back measurements were in very good agreement with the OFDR gain measurements, typically to within the OFDR precision of 0.5dB.

Note that it is difficult to exactly model the gain distribution, as the necessary model parameters are hard to measure with sufficient precision. This is demonstrated in Fig.7 by the solid and dashed lines, where two sets of model parameters obtained in different ways were used [8]. The dotted line on the other hand was obtained by varying the model parameters for good agreement with the measurement.

Measurement of distributed birefringence: The polarization dependence of the coherent detection used in the OFDR can be exploited to get information about the evolution of the polarization state along the fiber [9,10]. Due to the enhanced range of the OFDR at hand, we can get a much better statistics of the distributed fiber birefringence. Moreover, the polarization independent signal from the polarization diversity detection is used to subtract the (polarization independent) Rayleigh structure, thereby removing the frequencies that are not related with the fiber birefringence. Fig.8 shows the polarization dependent reflections from a 1km long low PMD fiber after removal of the Rayleigh noise and normalization to zero mean power. This curve is then Fourier transformed to get information about the rotation period of the polarization vector, i.e. the beatlength. The figure shows that there is not one specific, well-defined beatlength period, but a distribution of such values. While the structure of the peaks changes somewhat for different launch polarizations, the mean value of the distribution is fairly constant (variations of about 0.5m, i.e. 5%, were observed for the present example). An interesting feature is that the value of birefringence is found to vary along the fiber. From the normalized return signal, it can be seen that the polarization changes slower towards the end of the fiber. Indeed, by Fourier transforming only a section of the curve in Fig.8, mean values for the beatlength of 9.4m and 13.1m were found for fiber sections from 100-300 and 700-900m, respectively. Note that when we inverted the fiber, we found the beatlength to be decreasing, demonstrating that this feature is not an artefact of the measurement technique, but indeed reflects the polarization properties of the fiber. For comparison, we performed a similar measurement on a high PMD fiber (1.9 ps/√km). Using the same range of 2km as before, the polarization dependent signal was found to be often flat and 3dB lower than the polarization independent one. This happens if the polarization is rapidly varying on a distance scale smaller than the OFDR resolution, so that only an averaged value is obtained. Looking at these flat sections with an increased resolution indeed revealed fast polarization changes. The measurement was therefore done with a much higher OFDR resolution on a 100m section of the fiber. As Fig.9 shows, two distinctive peaks can be discerned as is expected from the theory in [9] for a fiber with well-defined birefringence. The (mean) beatlength accounts to 55 cm.

Conclusions

For the measurement of optical modules and small systems, the range of typical OLCR devices, very valuable for component characterization, is not sufficient. OTDRs on the other hand lack the advantages of a coherent detection scheme. With the progress of technology, coherent OFDR devices can now be realized that are capable of making the transition between the two techniques.

Such a novel OFDR device, based on a mechanically tuned fiber laser, was presented here. With its range (6 m to 1 km), resolution (0.08% of range), sensitivity (-110 dB), and dynamic range (80 dB), it is well adapted for a vast range of different applications in fiber metrology, like e.g. measurements of all kinds of components and their combinations (connectors, WDMs, couplers, taps, modulators, and to some degree even isolators or circulators), distributed gain measurements in EDFAs, or distributed local birefringence measurements.

Acknowledgements: *Support by the Swiss Department for Education and Research (OFES) in the framework of the European Project COST 265 is acknowledged.*

References

1 W.V. Sorin, "Optical Reflectometry for Component Characterization", in Fiber Optic Test and Measurement, 7Hewlett-Packard, Ed. D.Derickson, Prentice Hall, 1998

2 P.Oberson, B.Huttner, O.Guinnard, L.Guinnard, G.Ribordy, N.Gisin, "OFDR with a narrow linewidth fiber laser", appears in the June issue of *IEEE Photon. Technol. Lett.*, 2000

3 J.P.von der Weid, R.Passy, G.Mussy, N.Gisin, "On the characterization of optical fiber network components with OFDR", *J. Lightwave Technol.*, vol. 15, no. 7, 1997, p. 1131-1141

4 K. Tsuji, K.Shimizu, T.Horiguchi, Y.Koyamada, "Coherent OFDR using phase-decorrelated reflected and reference lightwaves", *J. Lightwave Technol.*, vol. 15, no. 7, 1997, p 1102-1109

5 G.Mussi, N.Gisin, R.Passy, J.P. von der Weid, "152.5dB sensitivity high dynamic range OFDR", *Electron. Lett.*, vol. 32, 1996, p. 926-927

6 J.P. von der Weid, R.Passy, A.O.Dal Forno, B.Huttner, N.Gisin, "Return loss measurements of WDM filters with tunable coherent OFDR", *IEEE Photon. Technol. Lett.*, vol. 9, no. 11, 1997, p. 1508-1510

7 M.Wegmuller, P.Oberson, O.Guinnard, B.Huttner, L.Guinnard, N.Gisin, "Non-destructive measurements of the distributed gain in Er doped fibers with improved accuracy using OFDR", *appears in Tech. Digest, CLEO/Europe 2000*

8 M.Wegmuller, P.Oberson, O.Guinnard, B.Huttner, L.Guinnard, C.Vinegoni, N.Gisin, *submitted to J. Lightwave Technol.*

9 B.Huttner, J.Reecht, N.Gisin, R.Passy, J.P. von der Weid, "Local birefringence measurements in single-mode fibers with coherent OFDR", *IEEE Photon. Technol. Lett.*, vol. 10, no. 10, 1998, p.1458-1460

10 M.Wegmuller, J.P. von der Weid, P.Oberson, N.Gisin, "High resolution fiber distributed measurements with coherent OFDR", *appears in Tech. Digest, ECOC 2000*

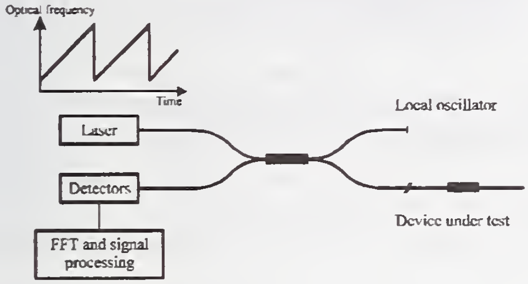

Fig.1: Set-up of the OFDR

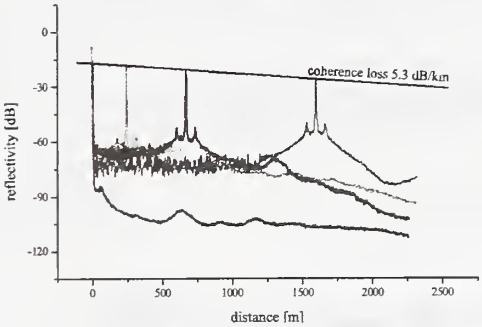

Fig.2: Fresnel reflections at different distances. The two pedestals are from acoustic perturbations

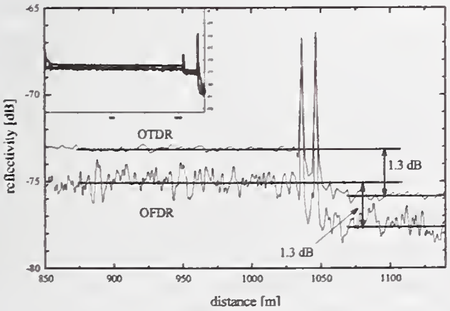

Fig.3: Measurements of a 10m jumper after a 1km SMF using OFDR and OTDR

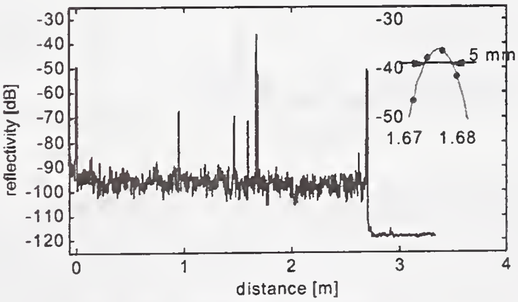

Fig.4: Short range measurement of a series of fibers with FC/PC and FC/APC connectors

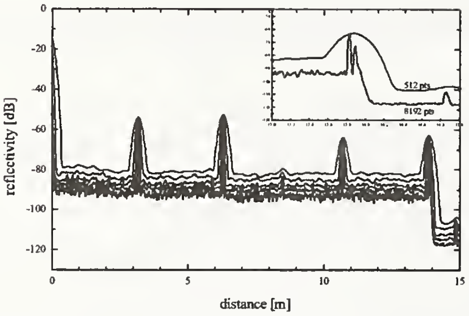

Fig.5: OFDR traces of a line of 6 jumpers using different two point resolution settings

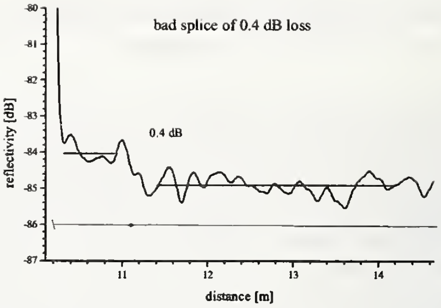

Fig.6: Measurement of a bad splice

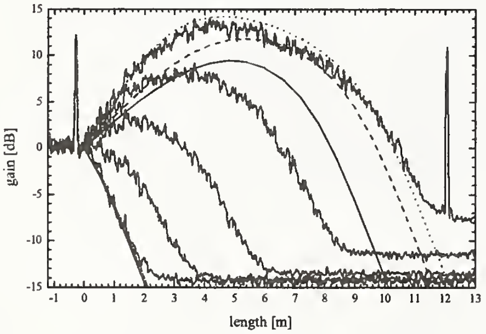

Fig.7: Distributed gain measurements in an 500 ppm Er-doped fiber for different pump powers.

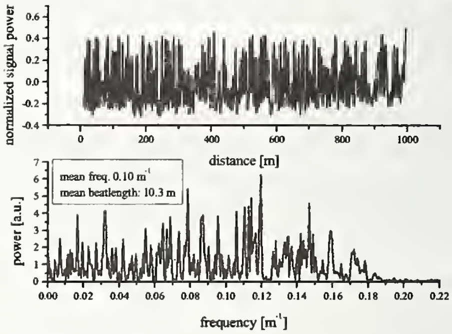

Fig.8: OFDR measurement of distributed birefringence of a low PMD standard fibre

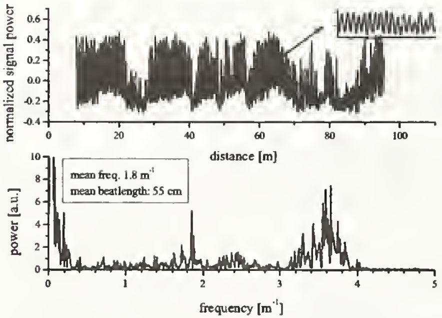

Fig.9: OFDR measurement of distributed birefringence of a large PMD fibre

Fiber Bragg Grating Metrology Round Robin: Telecom Group

A. H. Rose, C.-M. Wang, and S. D. Dyer
NIST, Boulder, CO 80303

Abstract

We briefly discuss the measurement of center wavelength, bandwidth, minimum transmittance, and relative group delay ripple from a fiber Bragg grating round robin among a group of telecom companies. We find that the state of fiber Bragg grating metrology in industry, needs improvement in most areas (transmittance, reflectance, wavelength, and relative group delay). Source amplified spontaneous emission can be a limiting effect in the minimum transmittance measurements, and wavelength accuracy and step size are critical for measurement of bandwidth and relative group delay ripple.

1. Introduction

In this paper we report on some of the results from a fiber Bragg grating (FBG) round robin conducted by NIST. FBGs are extremely important for telecommunication and sensor applications. In new wavelength-division multiplexed (WDM) optical-fiber communication systems, FBGs are used as wavelength filters and dispersion compensators. Also, FBGs make excellent strain sensors that can be networked to obtain distributed strain measurements of large structures, such as bridges and ships. In spite of the numerous and growing commercial applications of FBGs, there are no standard measurement procedures, and a variety of definitions are being used for important parameters.

Two parallel round robins were organized to assist industry in evaluating FBGs for telecommunication and sensor applications. The round robin participants in the two groups were, ADC, Agilent, Corning, Perkin Elmer, GNnet-test, NPL, and 3M in the telecom group, and Blue Road Research, CiDRA, EXFO, Micron Optics, NRL in the sensors group. Because no formal methods for analyzing the spectral or relative group delay (RGD) data existed only raw data, from the participants, were sent to NIST. In this paper we discuss only selected measurements from the telecom group on the center wavelength, bandwidth, and transmittance of a FBG at 1552.526 nm (corresponding to the International Telecommunication Union (ITU) channel 0) with a 50 GHz bandwidth. Also from the telecom group, we discuss the RGD measurements on a chirped FBG that was 16 nm wide.

2. Measurement Techniques

Measurement techniques varied among the participants. The telecom group used primarily a grating-tuned diode laser, power meter, and wavelength meter system for spectral measurements. The system used by NIST to make spectral measurements is shown in Fig. 1. A tunable fiber Fabry-Perot (FFP) filter was used to filter amplified spontaneous emission (ASE) from a grating-tuned diode laser. A wavelength meter provided the wavelength scale to an uncertainty of 0.2 pm. The detectors and lock-in amplifiers are linear to within 1% over the 60 dB measurement range. However, only relative reflectance and transmittance data are reported because losses in each of the participant's measurement systems are not known. Source power fluctuations are removed by monitoring the power at the second coupler port. The coupler splitting ratio has a weak wavelength dependence of about 0.01 dB/nm over the 1540 to 1560 nm range.

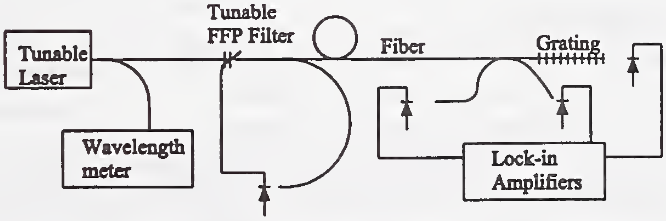

Figure 1 A schematic of NIST's spectral measurement system.

The effect of the tunable FFP filter on the laser can be seen in Figs. 2 and 3. Fig. 2 shows the unfiltered and filtered output of the tunable laser over the 1350 to 1650 nm band. These data were taken with a, 1 nm resolution, optical spectrum analyzer. The laser peak power at 1553 nm was about 308 μW and the integrated ASE across the measured spectra in Fig. 2 was about 1.7 μW. The ratio of these powers is about 23 dB and is a good measure of the dynamic range of the system without the tunable FFP filter. With the FFP filter the ASE is suppressed so that the transmitted laser power is about 174 μW and the integrated ASE power is about 76 pW, for a power ratio of about 64 dB.

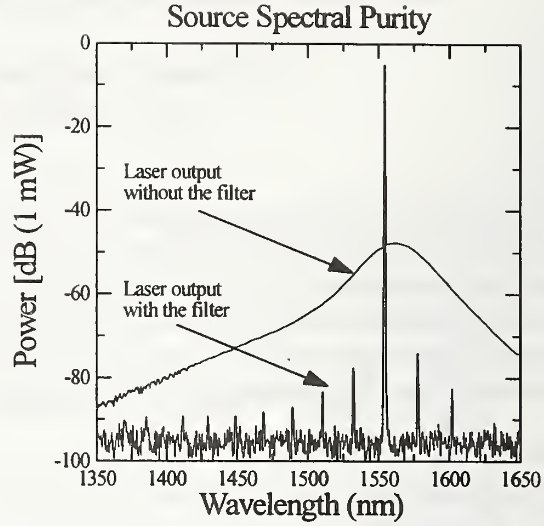

Figure 2 ASE from a tunable laser diode with and without a tunable FFP filter.

Fig. 3 shows the effect of the ASE on a measurement of a FBG's relative transmittance. Without the FFP filter the minimum relative transmittance is only about -25 dB. With the FFP filter the minimum relative transmittance is about -65 dB.

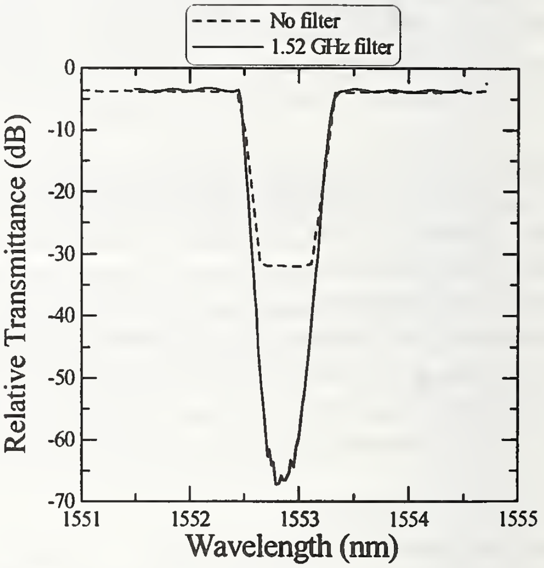

Figure 3 The effect of ASE on the measurement of transmittance in a FBG.

The RGD of the chirped FBG was determined by various rf-phase-shift techniques. A detailed description of the NIST system can be found in reference [1]. The repeatability (2σ) for NIST measurements on the RGD linear slope using the phase-shift system is about 0.25 ps/nm, which could be improved by reducing drift in the rf-modulator. NIST also employed a new low-coherence interferometer method to determine the RGD of the chirped grating. Details of this system are described in the literature [2, 3]. The low-coherence system has a RGD linear slope repeatability of about 0.02 ps/nm.

3. Analysis Methods

To determine the center wavelength and bandwidth of a grating from the reflectance data, NIST used the following methods. First, the maximum reflectance in the plateau region is determined. Then, wavelengths at reflectance values of -3 dB and -0.5 dB from the maximum plateau reflectance were found by interpolating between data. The center wavelength λ_c is defined as $(\lambda_+ - \lambda_-)/2$, and the bandwidth is defined as $c/(\lambda_+ - \lambda_-)$, where $\lambda_{+/-}$ are the wavelengths at data values -x dB (x = -0.5 or 3) on each side of the plateau region, and c is the speed of light. The minimum relative transmittance is determined from relative transmittance data by fitting a spline function to the data and locating the minimum. From the RGD data, the linear slope of the chirped grating is determined using a least squares fit from data within the -3 dB reflectance bandwidth. The residual RGD is found by subtracting the linear slope from the RGD reflectance data.

4. Round Robin Results

Both FBGs -3 dB center wavelength was monitored throughout the round robin to correct for any changes that might occur due to shipping damage or thermal shock. The ITU and chirped gratings did show measurable changes, 37 pm for the ITU, and 75 pm for the chirped, and were attributed to a mechanical shock that damaged other fibers in the grating box. Appropriate corrections were added to each participant's data. The gratings were place on a thermal-electric cooler and athermally packaged so temperature variations from lab to lab would not affect the FBG center wavelength.

The measurements of the minimum relative transmittance of the ITU grating, taken from the relative transmittance data showed the participants measuring about a 23 dB minimum; NIST measured a 27.5 dB minimum. As discussed earlier, for strong gratings, the minimum relative transmittance measurement is quite sensitive to the spectral purity of the laser light source. NIST's FFP filtered laser shows the lowest minimum transmittance, an indication that the participants probably had some amount of ASE in their measurement systems.

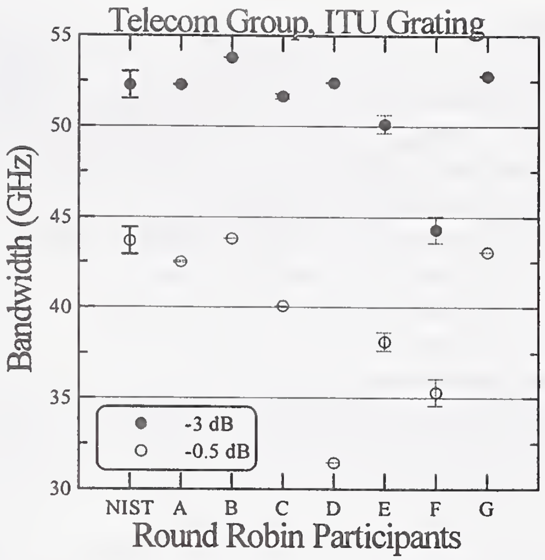

Figure 4 Bandwidth of the ITU grating using two band-edge criteria. Participant's error bars are only the fit uncertainty.

The ITU grating λ_c determined from the round robin reflectance data sets with a -3 dB criterion had a 27.5 pm range of values, with a standard deviation σ of 8 pm and a mean of 1552.521 nm. With a -0.5 dB criterion the λ_c values had a 42 pm range, with a σ of about 12 pm and a mean of about 1552.515 nm. Thus, no significant change in λ_c was found between the -0.5 and -3 dB criteria and the σ for each λ_c evaluation is adequate for WDM applications at present, but may need to be improved as system requirements increase.

Fig. 4 shows the results of the ITU grating bandwidth determined with the -3 dB and -0.5 dB band-edge criteria. The error bars for NIST uncertainty are 748 MHz while the participants error bars are just the fit uncertainty. For the -3 dB criterion, the mean bandwidth is 51.2 GHz with a range of 9.5 GHz and a σ of 3 GHz. In most cases the participants would pass this as a 50 GHz ITU grating using the -3 dB criterion [4].

For the -0.5 dB criterion the mean is about 39.7 GHz with a range of about 12 GHz and a σ of about 4 GHz. In some cases, where the bandwidth must fill the full channel spacing, the round robin participants would reject this grating as a 50 GHz ITU grating. The difference in the mean bandwidth, between the -0.5 and -3 dB criteria, is -11.5 GHz.

In some cases the participants data intervals were large enough to effect the determination of the bandwidth shown in Fig. 4. Participants C, E, and F all had coarse data sets. Participant D may not have normalized the reflectance to source power fluctuations. The -0.5 dB bandwidth is very sensitive to the shape of the ITU grating reflectance data.

The RGD linear slope of the chirped FBG was found by using a linear least squares fit to the RGD reflectance data, over the chirped grating's -3 dB bandwidth. From the round robin data the chirped FBG has a mean RGD linear slope of -6.81 ps/nm. Phase shift systems measure the RGD of all the fiber between the modulator and detector. Thus, to remove the system-fiber contribution to the FBG RGD linear slope the grating can be measured from both directions. The range on the mean of both directions of the RGD linear slope is 0.1 ps/nm with a σ of 0.04 ps/nm. If the system RGD is not removed, the range on the RGD linear slope is 1.1 ps/nm, a factor of ten worse.

Fig. 5 shows a portion of the residual RGD spectra taken with the NIST rf and low-coherence systems and with participant's A, B, E, and G systems. For most cases the ripple measurements agree, but wavelength accuracy, measurement uncertainty, and rf sideband averaging can lead to several ps differences [5]. The difference between the low-coherence system and rf phase shift systems is still being investigated, but no major differences have been observed [2]. The other round robin participant's RGD data could not be used to compare the ripple because of coarse wavelength steps. Fig. 5 illustrates the need for precision RGD ripple measurements, because over a 0.5 nm wavelength span the RGD changes rapidly from +5 to - 4 ps. Chirped gratings with larger RGD linear slopes will have larger RGD ripple amplitudes, increasing the need for more precision in RGD ripple measurements for WDM systems.

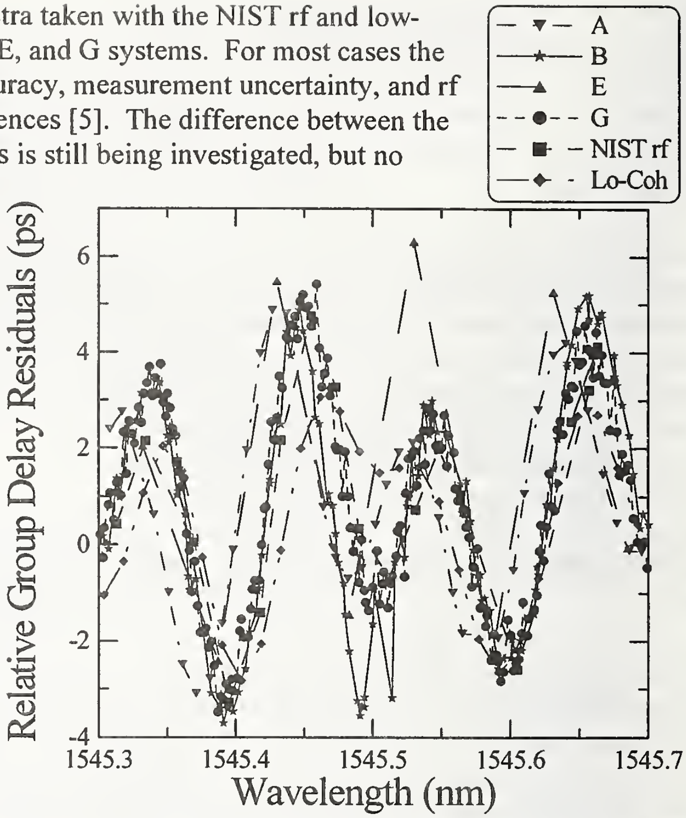

Figure 5 A portion of the RGD ripple from the chirped FBG as measured by various participants and NIST systems.

5. Conclusions

Metrology for WDM components, such as FBGs, must improve to meet the demands of current and future WDM networks. From this sampling of the round robin results we can draw the following conclusions. The source spectral purity is critical, ASE from diode sources must be substantially reduced. Wavelength accuracy <1 pm and <10 pm step sizes are necessary for bandwidth and RGD ripple measurements. Source spectral power fluctuation removal is necessary for bandwidth measurements. When using rf-phase-shift systems the best way to remove the system bias is by taking the mean of both directions on the grating. Stabilizing rf-phase-shift measurement systems and working at rf frequencies that do not average over >10 pm is necessary for RGD ripple measurements. Also, RGD resolution <1 ps will be required for most WDM components as data rates increase. RGD measurements with the low-coherence system compare well with phase-shift systems and may be preferred for rapid component evaluation.

6. References

[1] S. E. Mechels, J. B. Schlager, and D. L. Franzen, "Accurate Measurements of the Zero-Dispersion Wavelength in Optical Fibers," *J. Res. Natl. Inst. Stand. Technol.*, vol. 102, May-Jun. 1997, pp. 333-347.

[2] S. D. Dyer, K. B. Rochford, A. H. Rose, "Fast and accurate low-coherence interferometric measurements of fiber Bragg grating dispersion and reflectance," *Optics Express*, vol. 5, Nov. 1999, pp. 262-266.

[3] S. D. Dyer and K. B. Rochford, "Low-coherence interferometric measurements of fiber Bragg grating dispersion," *Electron. Lett.*, vol. 35, 1999, pp. 1485-1486.

[4] Generic Requirements for Fiber Optic Branching Components, GR-1209-CORE, Issue 2, Feb. 1998, Telcordia.

[5] R. M. Fortenberry, "Enhanced Wavelength Resolution Chromatic Dispersion Measurements using Fixed Sideband Technique," *Tech. Digest OFC 2000*, TuG8, Mar. 2000, pp. 107-109.

Measurements of dense group delay ripple using the phase shift method: Effect of modulation frequency

T. Niemi, M. Uusimaa, and H. Ludvigsen

Metrology Research Institute, Helsinki University of Technology, P. O. Box 3000,
FIN-02015 HUT, Finland.

Abstract

The group delay ripple of a dispersion compensating grating has been measured and analyzed using the phase shift method. The dependence of modulation frequency has been investigated.

Introduction

Characterization of group delay and amplitude properties of various fiber-optic components is important in designing advanced optical networks. The phase shift method is an established technique for performing high-accuracy measurements of these parameters [1,2]. The phase and amplitude measurements are conventionally made with a vector voltmeter or a network analyzer. These devices typically have a resolution in the phase measurement on the order of 0.1 degree, which is enough for resolving the changes in the group delay with sub-picosecond accuracy. The accuracy of the measurement method to resolve the amplitude of the dense ripple in the group delay, however, depends critically on the selected modulation frequency [3,4]. In this work, the effect of the modulation frequency on the measured amplitude of the group delay ripple of chirped fiber Bragg gratings is investigated. It is shown that the choice of the modulation frequency is essential for obtaining reliable results.

Group delay measurements

We have characterized a 20-cm long fiber Bragg grating with a bandwidth of 2 nm and a nominal dispersion of –660 ps/nm. The experimental setup based on the phase shift method is outlined in Fig 1a. The light source is a wavelength-tunable laser (Photonetics TUNICS-PRI) whose wavelength is measured with a wavemeter (HP 86120B). The output of the laser was sinusoidally intensity modulated at a frequency of ω_m with a Mach-Zehnder modulator. The polarization of the light entering the modulator is tuned using a polarization controller. After the modulator the light is amplified with a fiber amplifier and divided into two paths one of which is the reference path and the other includes the component under test. The two optical signals are detected and amplified before they are fed to a two-channel digital sampling oscilloscope (Tektronix TDS820). The stored time traces of the detected signals are transferred to a computer for analysis of their relative phase and amplitude. The computer controls the wavelength of the tunable laser, the data acquisition and the wavelength measurement.

The measured group delay for three modulation frequencies are given in Fig. 1b. Each curve is an average of five measurements. In the wavelength range between 1554.01-1550.03 nm, the traces have almost sinusoidal ripple. This ripple has a period of ca. 1.9 GHz and an amplitude of ca. 130 ps when the modulation frequency is 250 MHz. The fast variations of the group delay are smoothed out as the modulation frequency was increased.

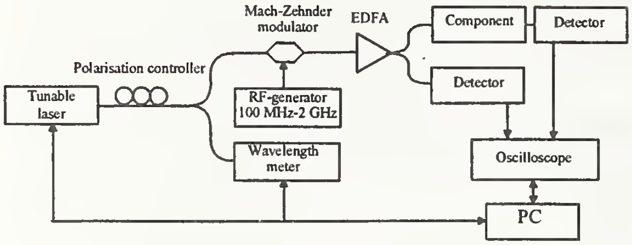

Figure 1a. The experimental setup based on the phase shift method.

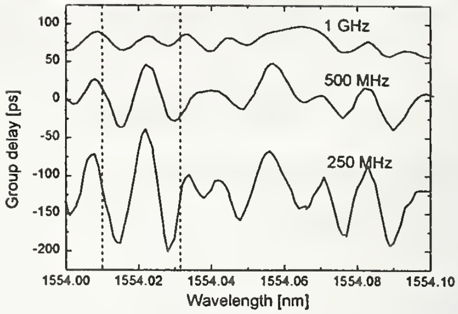

Figure 1b. Traces of the group delay ripple measured with three different modulation frequencies.

Analysis

The relation between the measured group delay $\tau_{GD}(\omega)$ of the component at the optical carrier frequency ω and the electrical phase shift $\theta(\omega)$ of the intensity modulated signal is given as

$$\tau_{GD}(\omega) = \frac{\theta(\omega)}{\omega_m}. \tag{1}$$

The group delay induced phase shift between the modulation sidebands in the component is usually approximated as a linear function of frequency in a narrow frequency range around the optical carrier. This approximation leads to accurate results when the variation of the group delay changes slowly with wavelength. However, in certain fiber optic components, such as chirped fiber Bragg gratings the group delay may fluctuate very rapidly.

By assuming that the variations in the group delay are sinusoidal (see Fig. 2a) we may write

$$\tau(\omega) = A_p \sin(\frac{\omega}{p}), \tag{2}$$

where A_p is the peak amplitude of the ripple and p indicates the period of the ripple. The phase shift of the optical sidebands can be obtained by integrating the group delay over the modulation bandwidth. The amplitude of the sinusoidal ripple as a function of the modulation frequency ω_m is then

$$A(\omega_m) = A_p \mathrm{sinc}(\frac{\omega_m}{p}). \tag{3}$$

Equation (3) shows that the measured amplitude is zero if the modulation frequency is a multiple of half the ripple period.

A comparison between the amplitude calculated from Eq. (3) and the measured data is given in Fig. 2b. The horizontal axis gives the modulation frequency normalized to the period of the measured ripple and the vertical axis presents the normalized amplitude of the ripple. The solid line plots Eq. (3) with p=1 and the squares are the measured ripple amplitudes. The overall agreement between the measured data and the model is good.

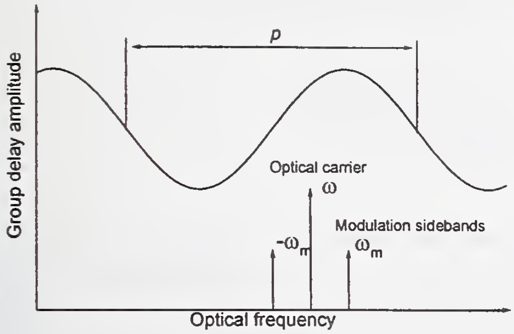

Figure 2a. Variation of the group delay and the optical signal.

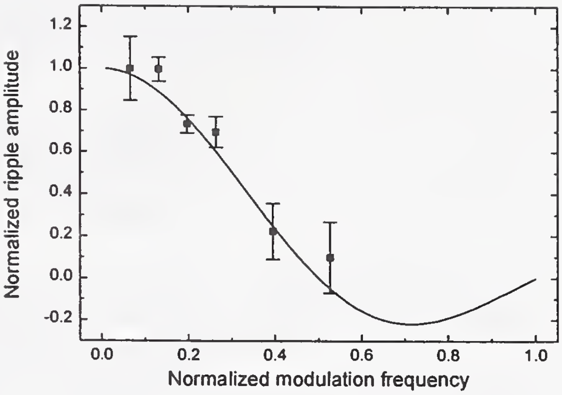

Figure 2b. Comparison between the model and the measured group delay amplitude.

The model predicts that the amplitude of the ripple should be inverted for normalized modulation frequency values in the range from 0.5 to 1. However, with the present setup it was not possible to verify this behavior.

Conclusion

In this paper, the effect of modulation frequency on the accuracy of the measured amplitude of the group delay ripple with the phase shift method was investigated. It was shown that the choice of the modulation frequency critically affects the measurement results. A model assuming sinusoidal variation of the ripple amplitude with optical frequency was used to describe the results. The model predicts that the amplitude of the ripples falls off as a sinc-function with modulation frequency. This was confirmed with measurements of the group delay ripple of a dispersion compensating grating. Accurate verification of the ripple is important since it has a degrading effect on the system performance if fiber Bragg gratings are used for dispersion compensation.

References

[1] M. L. Rocha and R. Kashyap, "Characterisation of fibre Bragg gratings: A study on accuracy and repeatability", in Digest of the *4th Optical Fibre Measurement Conference*, Teddington, United Kingdom, pp. 14-17, 1997.

[2] S. Ryu, Y. Horiuchi, and K. Mochizuki, "Novel chromatic dispersion measurement method over continuous gigahertz tuning range", *J. Lightwave Technol.*, Vol. 7, pp. 1177-1180, 1989.

[3] C. Clark, M. Farries, K. Visvanatha, and A. Tager, "Measuring chromatic dispersion of fiber gratings", *Lightwave*, pp. 70-77, February 1999.

[4] Y. Li, D. Way, N. Robinson, and S. Liu, "Impact of dispersion compensation gratings on OC-192 systems", in proceedings of *Conference on optical amplifiers and their applications*, Monterey, CA, paper TuB5, 1998.

A fast and accurate measurement of both transmission and reflection group delay in fiber Bragg gratings

Shellee D. Dyer and Kent B. Rochford
National Institute of Standards and Technology
Optoelectronics Division
325 Broadway, Boulder, CO 80303

We show that both the reflection and transmission group delay of fiber Bragg gratings can be accurately obtained from one low-coherence interferometric measurement. The spectral reflectance and transmittance of the grating can also be obtained from that same measurement. Both the reflection and transmission group delay can be obtained in less than 60 seconds. This technique can also be applied to the simultaneous measurement of the group delay of multiple fiber Bragg gratings in series.

1. Introduction

Low-coherence interferometry has several advantages over conventional techniques such as the modulation-phase shift method [1] for the characterization of fiber Bragg gratings (FBGs). A key advantage is the rapidity with which a measurement of group delay and reflectance can be obtained. The interferogram is obtained in less than a second, and processing the interferogram to obtain group delay or reflectance takes less than 60 seconds [2], compared with the conventional modulation-phase shift measurement, which can take several hours [1].

This measurement technique has low uncertainty (less than 1.5 ps) and, because of its speed, is immune to errors caused by thermal variations and instrument drift. Low-coherence interferometry is also immune to the ripple washout problems that can occur with the modulation-phase shift measurement [3].

2. Measurement Method

A diagram of the low-coherence interferometric system is shown in Fig. 1. A broadband Er superfluorescent fiber source (SFS) provides the input signal. This source is directed into a pair of fiber couplers. Fiber coupler 1 provides a comparison signal for the difference-over-sum (Δ/Σ) amplifier, as explained below. Fiber coupler 2 is part of a fiber-optic Michelson interferometer. The

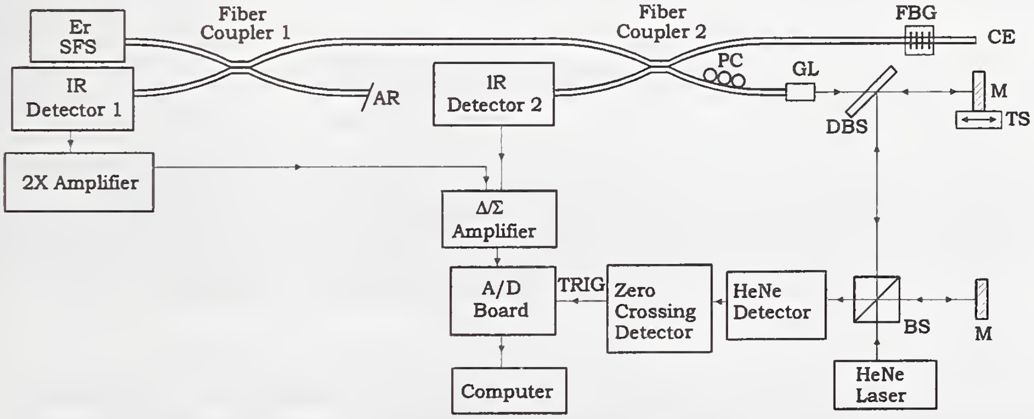

Figure 1. Diagram of low-coherence interferometric system for measurement of the transmission and reflection group delay of FBGs. AR: anti-reflection coating, PC: polarization controller, GL: grin lens, CE: cleaved endface, M: mirror, TS: translation stage, BS: beamsplitter, DBS: dichroic beamsplitter, Δ/Σ: difference over sum.

FBG under test is spliced onto the test arm of the interferometer. The far end of the grating's fiber pigtail is cleaved to produce a Fresnel reflection. This reflection facilitates the measurement of transmission group delay, as explained below.

The reference arm of the interferometer contains a variable-length air path so that the total optical path difference (OPD) of the interferometer can be varied. A frequency-stabilized HeNe laser interferometer monitors the position of the reference arm mirror, and a zero-crossing detector triggers sampling of the IR signal on positive-sloped zero crossings of the HeNe signal.

The light from the reference arm is recombined with the light from the test arm at fiber coupler 2, and the recombined light is directed onto the two IR detectors. The signals at the two IR detectors have similar source excess-noise characteristics, while the interference terms are 180° out of phase. Therefore, using a difference-over-sum amplifier will reduce excess noise from the SFS, which is the dominant noise source. This improves the interferogram's signal-to-noise ratio (SNR) by a factor of 3, and yields a corresponding improvement in the group delay SNR.

If the spacing between the FBG and the cleaved endface exceeds the width of the individual coherence functions, then the signal at the detector as a function of the OPD consists of two distinct signatures. One of these signatures represents the interference of light reflected from the FBG with the light reflected from the reference arm mirror. The other signature is created by the interference of light reflected from the test arm's cleaved endface with the light from the reference arm.

The shape and extent of the first signature is determined by the reflection characteristics of the FBG. Neglecting background dispersion, the complex degree of coherence $\gamma(\xi)$ of this interferogram is given by [4]

$$\gamma(\xi) = \int_{-\infty}^{\infty} G(\sigma) r(\sigma) \exp(j\phi_r(\sigma)) \exp(j2\pi\sigma\xi) d\sigma, \tag{1}$$

where ξ is the OPD, σ is the wavenumber, $G(\sigma)$ is the power spectral density of the Er SFS, and $r(\sigma)\exp(j\phi_r(\sigma))$ is the complex field reflection coefficient of the FBG. The reflection group delay (t_g) of this grating is calculated from the phase of the Fourier transform of the interferogram as follows:

$$t_g = \frac{1}{2\pi c} \frac{d}{d\sigma} \phi_r(\sigma). \tag{2}$$

Similarly, the second interferogram is related to the complex field transmission coefficient of the FBG as follows:

$$\gamma(\xi) = \int_{-\infty}^{\infty} G(\sigma) [t(\sigma) \exp(j\phi_t(\sigma))]^2 \exp(j2\pi\sigma\xi) d\sigma, \tag{3}$$

where $t(\sigma)\exp(j\phi_t(\sigma))$ is the complex field transmission coefficient of the FBG. The equations above are derived assuming that the only dispersion difference between the two arms arises from the dispersion of the FBG. In reality, there is a small background dispersion from the difference in the length of the test and reference arm fibers, but the slope of the background group delay is approximately 11 fs/nm, which is negligible compared with the dispersion of a typical FBG [5].

3. Data Processing

The reflection group delay was calculated from the FBG reflection interferogram. We truncated the interferogram at the points where the SNR was approximately unity. Next, we appended zeros to the interferogram array (zero padding) to obtain a total array length of 2^N. The choice of N determines the wavelength resolution of the group delay results. Larger values of N give better resolution, but if N is too large, computational errors such as roundoff error affect the accuracy of the results. For the results shown in this paper, we used N=18, giving a wavelength resolution of 14 pm.

To obtain the group delay, we took the Fourier transform of the truncated and padded interferogram. The magnitude of the Fourier transform is proportional to the magnitude of the field reflection coefficient of the FBG. The relative group delay of the FBG is determined by differentiating the phase of the Fourier transform.

The transmission group delay is calculated from the cleaved endface interferogram in a manner similar to the calculation of the reflection group delay. We truncate and zero pad the interferogram, take the Fourier transform, and then calculate group delay by differentiating the phase of the Fourier transform.

4. Experimental Results

We used our interferometric measurement system to determine the transmission and reflection group delay of a chirped FBG with a 5.4 nm bandwidth and a center wavelength of 1555.5 nm (grating A). We cleaved the end of the FBG fiber at a distance of approximately 2.7 cm from the grating. We then measured the interference pattern as a function of OPD and obtained two distinct signatures. From the second interferogram, we calculated the double-pass transmission group delay of this grating, which is shown in Fig. 2. Also shown in Fig. 2 is the relative power transmitted by the grating. The transmission group delay results are valid only in regions where the transmitted power is appreciable; in all other spectral regions there is insufficient signal for an accurate measurement. From Fig. 2, we see that the transmission group delay of this grating has features that extend beyond the 10dB reflection bandwidth of the grating.

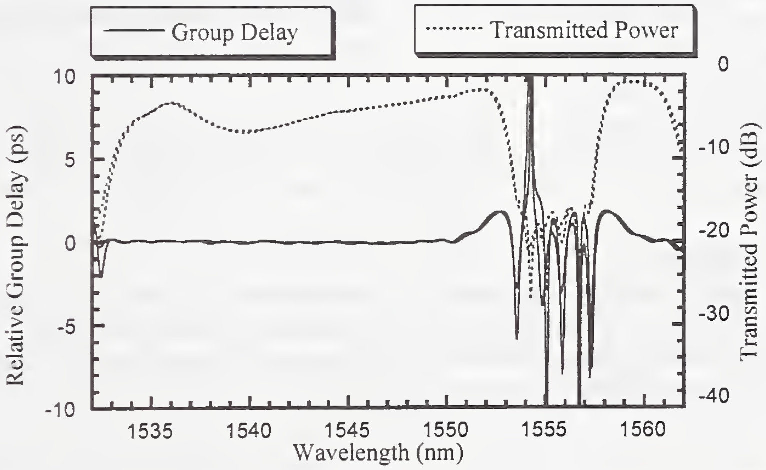

Figure 2. Double-pass transmission group delay and relative transmitted power of grating A. Results are shown from two repeated measurements.

We also used our interferometric system to measure the group delay of two gratings in series. We spliced a second grating approximately 6.5 cm after grating A. This second grating (grating B) had a center wavelength of 1548 nm and a 1.7 nm bandwidth. The endface of the test arm was immersed in index matching fluid; therefore, the interferometer output consisted of two separate interferograms, one for each of the two gratings. The shape of the interferogram from grating A's reflection is determined by the complex field reflection coefficient of that grating as given by Eq. 1. The light transmitted by grating A sees the effects of both gratings, and that interferogram is related to both gratings as follows:

$$\gamma(\xi) = \int_{-\infty}^{\infty} G(\sigma)[t_A(\sigma)\exp(j\phi_{tA}(\sigma))]^2 r_B(\sigma)\exp(j\phi_{rB}(\sigma))\exp(j2\pi\sigma\xi)d\sigma\,, \qquad (4)$$

where $t_A(\sigma)\exp(j\phi_{tA}(\sigma))$ is the complex field transmission coefficient of grating A, and $r_B(\sigma)\exp(j\phi_{rB}(\sigma))$ is the complex field reflection coefficient of grating B. We processed each interferogram separately by truncating each near the points where the SNR was equal to one. We then zero padded each interferogram to create arrays of length 2^{18} and calculated the Fourier transform of each padded interferogram. From the phase of the Fourier transform of grating A's interferogram, we obtained the reflection group delay of that grating, which is shown in Fig. 3. From the second interferogram, we obtained a group delay function, also shown in Fig. 3, which is the product of the reflection group delay of grating B with the double-pass transmission group delay of grating A. These results are relative group delay curves, and therefore each curve has its own arbitrary additive constant; the relative group delay difference between the gratings is not shown in this graph. Comparing this group delay product at wavelengths near 1548 nm with the transmission group delay of the grating A shown in Fig. 2, it is clear that the transmission group delay of grating A is very small at wavelengths near 1548 nm, and can be neglected compared with the reflection group delay of grating B.

We also measured the group delay difference arising from the fiber separation between the two gratings. To obtain this, we calculated the central fringe index of each individual interferogram [6]. Then we determined the group delay difference from the separation between the interferograms' central fringes. We calculated a total single-pass delay between the gratings of 315 ps, which is too large to show in Fig. 3.

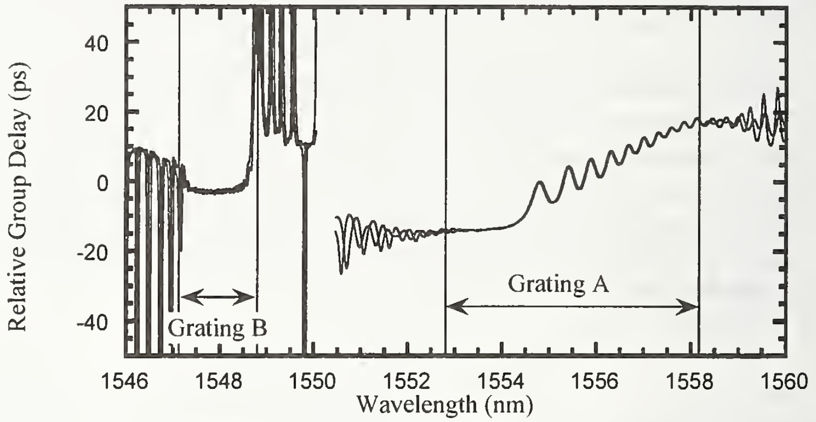

Figure 3. Plot of relative reflection group delay measured of two gratings in series. Results are shown from two repeated measurements. The relative group delay difference between the two gratings is not shown.

5. Conclusions

We have demonstrated the measurement of transmission group delay in FBGs, as well as the measurement of the group delay of multiple gratings in series using low-coherence interferometry. The key advantage of the low-coherence technique is speed, and it is possible to obtain the group delay measurements in less than 60 seconds.

References

[1] S.E. Mechels, J.B. Schlager, and D.L. Franzen, "Accurate measurements of the zero-dispersion wavelength in optical fibers," *J. Res. Natl. Inst. Stand. Technol.*, vol. 102, pp. 333-347, 1997.

[2] S.D. Dyer, K.B. Rochford, and A.H. Rose, "Fast and accurate low-coherence interferometric measurements of fiber Bragg grating dispersion and reflectance," *Optics Express*, vol. 5, pp. 262-266, 1999.

[3] R.M. Fortenberry, "Enhanced wavelength resolution chromatic dispersion measurements using fixed sideband technique," in *Optical Fiber Communications Conference*, OSA Technical Digest (Optical Society of America, Washington DC, 2000), TuG8, pp. 107-109.

[4] U. Wiedmann, P. Gallion, and G.-H. Duan, "A generalized approach to optical low-coherence reflectometry including spectral filtering effects," *Journal of Lightwave Technology*, vol. 16, pp. 1343-1347, 1998.

[5] S.D Dyer and K.B. Rochford, "Low-coherence interferometric measurements of fibre Bragg grating dispersion," *Electronics Letters*, vol. 35, pp. 1485-1486, 1999.

[6] B.L. Danielson and C.Y. Boisrobert, "Absolute optical ranging using low-coherence interferometry," *Applied Optics*, vol. 30, pp. 2975-2979, 1991.

Differential group delay measurements of chirped fiber Bragg gratings using photon counting

Hugues de Riedmatten, Mark Wegmüller, Hugo Zbinden, Nicolas Gisin

Group of Applied Physics
University of Geneva
Rue de l'école de médecine 20
1204 Geneva, Switzerland
E-mail: hugues.deriedmatten@physics.unige.ch

Abstract

We present a novel measurement method for the differential group delay of chirped fiber Bragg gratings, based on the time-of-flight of single photons. In contrast to existing techniques, the light source is a pulsed broadband LED. This simple and non-expensive source allows for measurements over a large spectral range with a high spectral resolution (8 pm) obtained from a tunable Fabry-Perot filter. The photons are detected by an InGaAs avalanche photodiode operated in photon counting mode, resulting in a precision for the differential group delay of 15 ps.

Introduction

Chirped fiber Bragg gratings are an attractive solution for chromatic dispersion compensation in all-fiber applications. They allow compensating for a large amount of differential group delay (DGD) in a very compact way. Further, by tailoring the dispersion slope, they can be ideally matched to the specific situation of deployment. Obviously, the DGD of the grating has to be exactly known for optimum compensation. Sufficiently accurate information can only be obtained from measurements of the DGD, and several methods have therefore been reported. They are either based on optical interferometry [1], or on direct phase-delay detection [2]. In both cases, a narrow band tunable laser was used to obtain a sufficiently good spectral resolution.

Here, we suggest to use a broadband source (pulsed LED) and a narrow band tunable filter instead. The advantage of using an LED is that one can cover a large spectral range. However, the intensity after the filter is very low and therefore impossible to detect with classical techniques. Consequently, one has to employ a photon counting detection. Intensive research and improvements in detector engineering have made this technique - well known in fields like astronomy or spectroscopy - also available at telecommunication wavelengths.

Measurement method

The measurement method is a time-of-flight technique giving the relative pulse delays experienced in the grating at different wavelengths. The setup is an adaptation of [3] and is shown in figure 1.

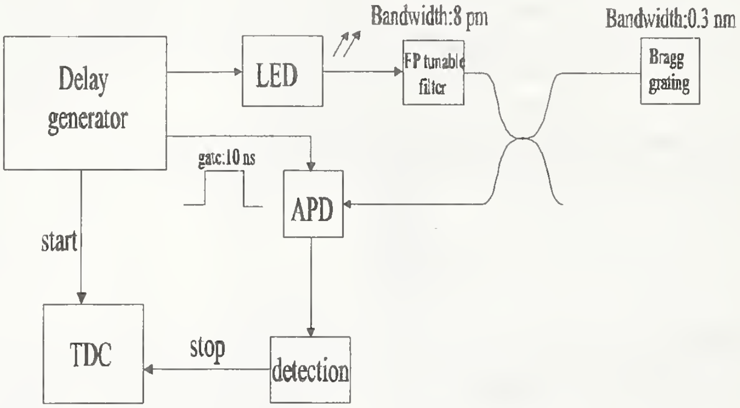

Figure 1 : Setup of the measurement technique

The light source is a standard LED for telecom applications, with a bandwidth of 60 nm (FWHM) centered around 1550 nm. Driven by a fast pulse generator, it produces pulses of 300 ps duration (FWHM) with peak power of 400 μW or 10^6 photons/pulse. The wavelength is selected with a tunable Fabry Perot filter with a bandwidth of 8 pm (FWHM). To increase the stability of the piezoelectrically tuned crystal, the filter is stabilized in temperature. After the filter, a pulse contains approximately 100 photons. The light is then injected onto the chirped Bragg grating through a 50/50 fiber coupler, so that the reflected photons can be detected at the second coupler output. The detector is an InGaAs avalanche photodiode (APD) used in the so-called Geiger mode. To reduce the noise, it is active only during a gate window triggered by the LED pulser. For a more detailed description of the detection scheme, the reader is referred to [4].

The time-of-flight is measured with a time to digital converter (TDC). The start is synchronized with the LED pulse, and the stop is given by the avalanche generated by the arrival of the reflected photon in the detector. The single measurements are stored in a histogram, and eventually a reflection peak with a FWHM of 500 ps emerges. The shape and width of this peak are due to a convolution of the LED pulse and of the time response of the detector. The integration time used is about 3 s for each wavelength, for a repetition rate of 10 kHz and a detection efficiency of 10 %. Note that this integration time can be drastically reduced by using a higher repetition rate and higher detection efficiency. The standard deviation of the peak position is about 15 ps.

Results for two chirped Bragg gratings

The method was tested with two chirped Bragg gratings (Photonics), with reflection bandwidths of 1.1 and 0.3 nm, respectively. Figures 2 and 3 show the measured group delays for the respective gratings, with the set of curves giving the results for measurements done from either

side of the gratings. Looking at the first grating, we see that the DGD is quite linear. The spectral resolution of 8 pm is not sufficient to resolve the gain ripple at present. As our signal power is far above the detection limit, this could however be improved upon by simply using a filter with a narrower bandwidth. As expected, the two DGD curves are symmetric.
This is not the case for the second grating, where a distinctive asymmetry can be observed. In fact, this grating is defective and also exhibits an uncommon reflectivity spectrum, obtained by monitoring the number of reflected photons as a function of wavelength. It is not yet fully understood if a defect in the index profile or blazing could lead to the observed asymmetry. Interestingly, similar asymmetries have been found with a different measurement technique for different gratings [5], indicating that this might be an important problem for production.

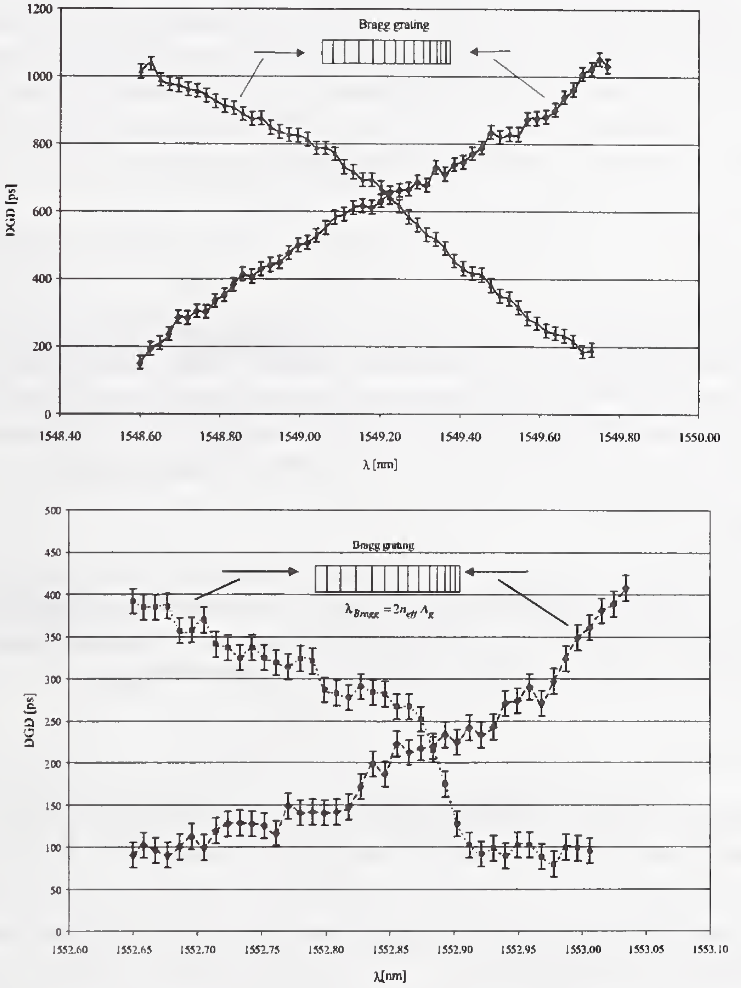

Figure 2: DGD measurements of two gratings with different reflective bandwidths.

The stability and precision of our photon counting DGD measurement set-up were tested by performing repeated measurements of time-of-flight with a fixed voltage applied to the FP filter, corresponding - in principle - to a fixed wavelength. The results are presented in figure 3. The variations in the time-of-flight are mainly due to electronic jitter. The standard deviation of these values of typically 10-20 ps gives a good estimation of the temporal precision of our method.

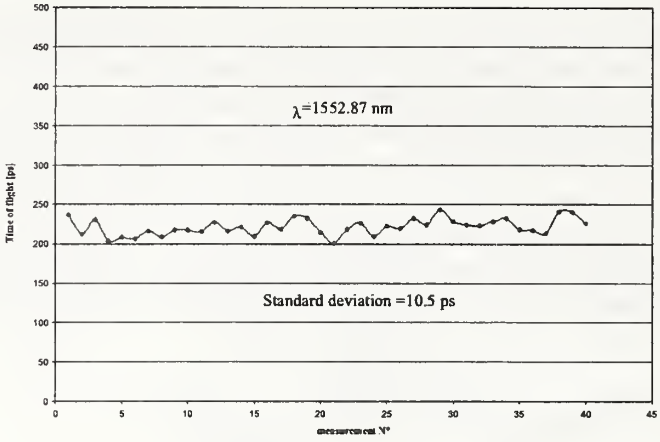

Figure 3 : Stability and precision of the measurement technique

Conclusions

A novel method for DGD measurements in chirped fiber Bragg gratings was presented. Its core elements are a pulsed LED followed by a high resolution tunable FP filter for the light source, and a photon counting detection. This allows for measurements over a spectral range as large as 60 nm with a DGD precision of 15 ps. The spectral resolution, essentially given by the employed filter bandwidth, was 8 pm, which could however be easily increased for ripple detection.

Acknowledgements

The authors would like to thank Jürgen Brendel for useful discussions and Christian Zimmer (Swisscom) for the gratings. Support by the Swiss Department for Education and Research (OFES) in the framework of the European Project COST 265 is acknowledged.

References

1 M.M Ohn, SY Huang, S.Sandgren, R.Measures, T.Alavie, *Measurements of fiber gratings using an interferometric and Fourier-Transform based technique, OFC'97,* Technical Digest, pp 154-155, 1997

2 R.Kashyap, M de Lacerda Rocha, *On the group delay characteristics of chirped fibre Bragg gratings*, Opt.Comm. **153** (1998) 19-22

3 J.Brendel, H. Zbinden, N.Gisin, *Single photon time of flight chromatic dispersion measurements*, OFMC 99, pp 75-78

4 G. Ribordy, J.D. Gauthier, H. Zbinden and N. Gisin, *Performance of InGaAs/InP avalanchephotodiodes as gated-mode photon counters*, Appl. Opt. **37**, 2272 (1998)

5 private communication COST 265 members

Measurement Issues for Dispersion Compensation

R. M. Jopson
Crawford Hill Laboratory
Bell Labs, Lucent Technologies

Abstract

The introduction of chromatic dispersion compensation to lightwave systems provides an opportunity to measure properties of the compensation. We describe the importance of some of these properties. We also discuss the interplay between the measurement of chromatic dispersion and the presence of polarization-mode dispersion.

Introduction

Most long-distance lightwave systems operating at bit rates of 10 Gb/s or higher require compensation of chromatic dispersion. Obviously, accurate measurement of chromatic dispersion is necessary for the successful implementation of compensation; however, other properties of the compensators are also of crucial importance. The relative importance of various characteristics depends on the design of the system in which the dispersion compensation is used. Optical nonlinearity can be of crucial importance in a compensator containing high optical powers but be negligible in compensators containing low optical powers. Polarization-mode dispersion (PMD) is a phenomenon that not only affects the measurement of chromatic dispersion but also invalidates a common definition of chromatic dispersion. We will describe the influence of PMD on chromatic dispersion and describe a method for measuring the PMD vector and chromatic dispersion simultaneously.

Dispersion Compensation

The chromatic dispersion of an object is obtained formally from a Taylor expansion of the propagation constant, $\beta(\omega)$, with respect to the angular frequency, ω:

$$\beta(\omega) = \beta_0 + \beta_1(\omega - \omega_0) + \tfrac{1}{2}\beta_2(\omega - \omega_0)^2 + \tfrac{1}{6}\beta_3(\omega - \omega_0)^3 + \dots\ .$$

The constants β_n are the n^{th}-order ω derivatives of $\beta(\omega)$ evaluated at ω_0. The first-order constant, β_1 is the reciprocal of the group velocity and is therefore a measure of pulse propagation delay when multiplied by the propagation distance. One convenient measure of chromatic dispersion, D, is the wavelength derivative of the propagation delay divided by the propagation distance. Using the speed of light, c, and the wavelength, λ, D can be expressed as

$$D = -\frac{2\pi c}{\lambda^2}\beta_2\ ,$$

and is often stated in units of ps/nm/km. Most long-haul lightwave systems operating at bit rates, B, of 10 Gb/s or higher use modulators to provide a signal optical bandwidth near the transform limit. For these systems, a 1 dB penalty is observed in a system of length L when the total chromatic dispersion, DL, is about $10^5/B^2$ $(\mathrm{Gb/s})^2$ ps/nm. Thus, for standard fiber, the dispersion limit is 60 km for 10 Gb/s and less than 4 km for 40 Gb/s. As transmission rates increase, these limits fuel a strong demand for dispersion compensation and a strong need for measurement of the properties of the dispersion compensation.

Many methods for dispersion compensation have been proposed and demonstrated. Four examples are dispersion compensating fiber, virtually-imaged phase-arrayed compensators, LP_{11} mode compensators, and chirped fiber gratings. For all of these methods, the chromatic dispersion is the primary parameter to measure. The importance of secondary parameters depends on the technology used for compensation. For instance, group delay ripple is a major concern for the chirped fiber gratings while the quality of a compensator employing the LP_{11} mode depends on reducing the multi-path interference to tolerable levels.

The relative importance of various parameters also depends on the design of the compensated system. When compensator nonlinearity is not an issue, important parameters are chromatic dispersion, optical loss and polarization-mode dispersion (PMD). For wavelength-division multiplexed systems, the spectra of these parameters are needed. However, the PMD spectrum usually evolves too rapidly to be useful so an understanding of PMD statistics is needed instead. The accuracy required for dispersion measurements depends on the application. In one study[1] of a 10 Gb/s, 8x80 km system operating with nonlinear transmission fiber, but linear dispersion compensation, Essiambre found that to limit the system penalty to 1 dB, the dispersion of the compensating fiber (and the transmission fiber) has to be known to within ±2.5%. In this study, it was assumed that the final dispersion compensation at the receiver could be optimized by trial and error or by dynamic dispersion compensation. If this freedom is removed, then the total system dispersion-length product must be known to within the $10^5/B^2$ $(\text{Gb/s})^2$ ps/nm limit mentioned above. For a 1000 km, 40 Gb/s system over standard fiber, this requires a dispersion measurement accuracy of ±0.2%.

Optical loss in the dispersion compensation will reduce the optical signal to noise ratio (OSNR) at the receiver and thereby impair performance. In most systems, an extra dB of loss in the dispersion compensation contributes much less than one dB reduction in the receiver OSNR. Therefore, an accuracy of several tenths of a dB in the loss measurement should suffice for predicting the effect of the compensation on the system OSNR. The spectrum of optical loss in the dispersion compensation also contributes to the overall gain shape of the system. A tenth of a dB accuracy in the loss spectrum would be needed for some system designs.

A common requirement for the mean PMD of a system is that it be less than one tenth of the bit period. On average, such a system having a Maxwellian PMD distribution can be expected to experience a penalty greater than 3 dB for no more than one second per year. The PMD specification for a system is an upper limit rather than a targeted value. Therefore, the PMD measurement need not be very accurate so long as the inaccuracy of the measurement is included when determining the acceptable values of mean system PMD. An important concern is the statistics of the PMD. The Maxwellian distribution results from the sum of many randomly coupled sources of birefringence. If the system PMD arises primarily from a small number of sources, the distribution will not be Maxwellian.

In addition to adding impairment to systems, PMD also adds uncertainty to the measurement of chromatic dispersion. Consider the apparatus shown in Figure 1. It is similar to equipment commonly used to measure chromatic dispersion except that polarization control and measurement components have been added. A network analyzer measures the phase delay of a 1 GHz amplitude modulation imposed on laser light that steps through a wavelength range. The chromatic dispersion is calculated from the slope of the measured delay versus wavelength curve.

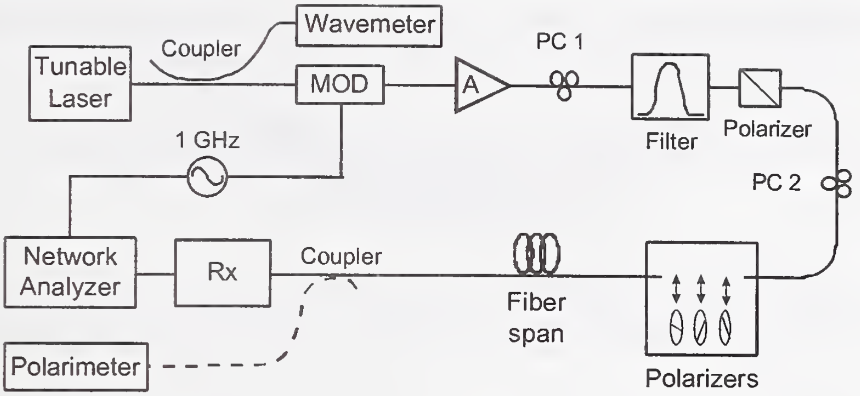

Figure 1. Apparatus used to measure chromatic dispersion and polarization-mode dispersion. MOD: modulator, A: optical amplifier, PC: polarization controller, Rx: receiver

However, in the presence of PMD, this delay depends on the dot product between the Stokes vectors representing the launch polarization, $\vec{s}$, and the PMD vector at the fiber input, $\vec{\tau}$. For pulsed input light, Mollenauer, et al. [2] showed that,

$$\tau_g = \tau_o + \frac{1}{2}\,\vec{\tau}\cdot\vec{s}\,.$$

The mean signal delay, τ_g, is the propagation-induced change in the first moment of the pulse envelope in the time domain [2-5], while τ_o is a polarization-independent delay. Similar relations can be derived for sinusoidal modulation[6,7]. They form the basis of the new PSD (polarization-dependent signal delay) method that measures PMD vectors and chromatic dispersion simultaneously [7,8].

Since PMD provides polarization dependent delay, it is not surprising that chromatic dispersion measurements can be affected by PMD. Figure 2 shows spectra of the delays that would be seen for special launch polarization conditions. The upper and lower solid curves would be observed if the launch polarizations were always aligned with the PMD vector, $\vec{\tau}$, and its negative, $-\vec{\tau}$ as the wavelength changed. A measured curve for light launched with fixed polarization, shown by the markers, wanders between these two envelope curves as predicted by the equation above. By launching four states of polarization, one can obtain τ_0, shown by the central solid curve, which is the relative delay that would be obtained in the absence of PMD. The chromatic dispersion can be determined from the slope of this curve, which is not influenced by PMD.

Summary

Signals propagating though dispersion compensation are subject to many of the same impairments that exist in other components in the transmission path. Therefore, the important measurement issues in dispersion compensators are similar to those in other parts of the system. However, polarization-mode dispersion is of special interest, not only because some compensation technologies tend to exhibit PMD, but also because PMD impairs the measurement of the most important property of compensators: chromatic dispersion.

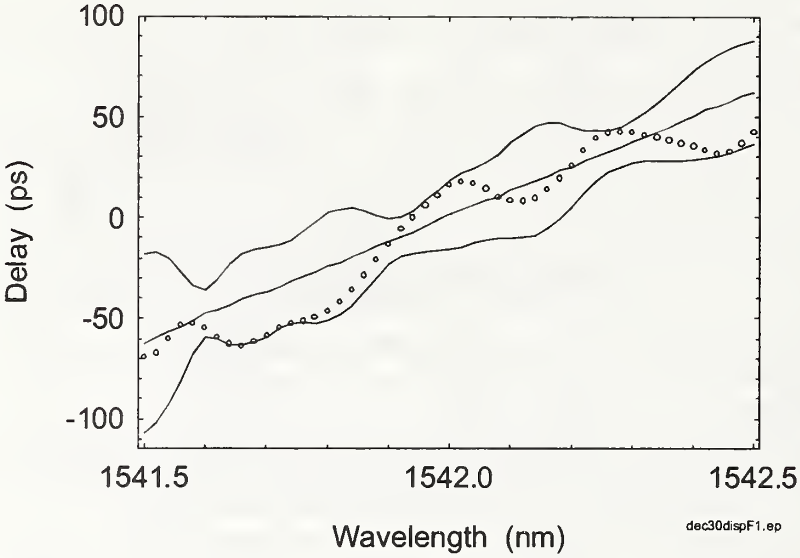

Figure 2. The effect of PMD on the fiber delay spectra. The central solid curve shows the relative delay that would be measured if the fiber had no PMD. The markers show measured delay for a fixed launch polarization. The outer solid curves show the delay that would be measured if the launch polarization was varied with wavelength so as to always launch along the slow principal state (upper curve) or the fast principal state (lower curve). A large, common-mode delay has been subtracted from all the curves.

References

[1] R-J. Essiambre, private communication.

[2] L. F. Mollenauer, and J. P. Gordon, "Birefringence-mediated timing jitter in soliton transmission," *Optics Lett.* **19**, 375-377 (1994).

[3] M. Karlsson, "Polarization mode dispersion-induced pulse broadening in optical fibers," *Optics Lett.* **23**, 688-690 (1998).

[4] W. Shieh, "Principal states of polarization for an optical pulse," *Photon. Technol. Lett.* **11**, 677-679 (1999).

[5] J. P. Gordon and H. Kogelnik, "PMD Fundamentals: Polarization mode dispersion in optical fibers," *Proceedings of the National Academy of Sciences,* **97**, 4541-4550 (2000).

[6] P. A. Williams, "Modulation phase-shift measurement of PMD using only four launched polarisation states: a new algorithm," *Electron. Lett.* **35**, 1578-1579 (1999).

[7] L. E. Nelson, R. M. Jopson, H. Kogelnik, and J. P. Gordon, "Measurement of polarization mode dispersion vectors using the polarization-dependent signal delay method", *Optics Express*, **6**, 158-167 (2000).

[8] R. M. Jopson, L. E. Nelson, H. Kogelnik, and J. P. Gordon, "Polarization-dependent signal delay method for measuring polarization mode dispersion vectors," LEOS'99 Postdeadline paper, PD1.1, San Francisco (1999).

Chromatic Dispersion Measurement using Phase-shift technique For Installed Long Haul Optical Submarine Cable

Toshio KAWAZAWA, Takuyuki YAMAGUCHI, Koji GOTO
757, Kawamuko-cyo, Tsuzuki-ku, Yokohama-shi, Kanagawa 224-0044, JAPAN
TEL:+81-45-476-7122, FAX:+81-45-476-7203
E-mail:kawazawa@kddscs.co.jp

Abstract

This is the first paper to report the behavior of chromatic dispersion (CD) for the installed long haul submarine cable system by Far-end CD measurement equipment. The system CD stability was within 5.6ps/nm and the system length was 0.7m elongation during one-day measurement.

1. Introduction

Fiber-optic communication systems require the use of dense wavelength division multiplexing (DWDM) and high power to meet the demands of data traffic growth. It is well known that in addition to linear penalties the transmission capacity of DWDM systems is limited by transmission fiber non-linearlities and chromatic dispersion (CD). In the recent long haul optical submarine cable system, the precise management of system CD is required to minimize the interaction between accumulated system CD and fiber nonlinearly. The submarine cable system consists of many fiber pieces and repeaters. The whole installed system CD could not be accurately characterized by individual piece of cable and repeater measurement cause of cumulative measurement error. Even if the CD is characterized by parts data, it is hard to accurately estimate due to replacement or insertion of cable or repeater. In addition, the system CD has a characteristic of environment dependency such as temperature, stress and tension in the installed condition. The evaluation of system CD has to be confirmed for such installation and cable repair in order to obtain the system performance by adjust the pre and post chromatic dispersion compensation.

In this paper, we have conducted high accurate CD measurement for long haul submarine cable system. The stability of system CD in installed 8,000km submarine cable system was evaluated and the variation of CD was stable within 5.6ps/nm that gives negligibly small impact for 10Gbit/s transmission performance.

2. Measurement configuration

2.1 CD Measurement Equipment

The CD measurement configuration is shown in figure2. The CD test equipment is using phase-shift technique by measurement of the relative group delay experienced by the various wavelengths. The optical reference channel as a suitable time delay generator was interposed between optical source and detector in order to compensate the fiber elongation [2]. The optical source was a wavelength tunable laser diode (WTL) with an external modulation (450MHz) as a signal channel. The signal channel was launched into the system under test. The spectral scan of the group delay is performed from 1547 to 1553nm with 0.12nm step. The wavelength meter is used to obtain the accurate wavelength of tunable laser light source. The optical source of reference channel (1550nm) is a laser diode (LD) and modulated by external modulator with same frequency as the channel signal, and the light launch to another fiber. At receiver side, the signal channel and reference channel phase shift is measured by the vector voltmeter as a delay detector. The time group delay was deduced from the corresponding phase shift ϕ through the relation $\tau=\phi/2\pi f$, f being the modulation frequency. The measured group delay was fitted by the quadratic expression, since the majority fiber of the installed submarine cable system was DSF. The chromatic dispersion $D(\lambda)=d\tau/d\lambda$ can be determined from the differentiated quadratic expression.

The system length L is calculated from the following formula $L=(c/n)\,\phi/2\pi f$, where L is a system length, c is light velocity in vacuum, n is refractive index of the fiber. The average refractive index is assumed 1.4738. The measured length is twice of real system length, because the end of the system under test was connected to another fiber pair in order to compare with the absolute phase value of reference channel phase and signal channel phase at same frequency generator. For far end CD measurement, the CD test equipment communicated on another fiber pair of the optical submarine cable system with reference channel of data modulation. The CD measurement time is about 15min for one time measurement.

2.2 System under test

The measured optical submarine cable system is designed for Trans-ocean pacific systems with

4subsystem, 16WDMx10Gbit/s (1545.5nm to 1554.5nm) and RZ pulse format. The output of repeater is +9.5dBm that is pumped with 980nm erbium-doped fiber amplifier, spaced by 45km. The cable spans are constructed using two types DSF (Dispersion Shift Fiber) and the -2ps/nm/km at 1550nm respectively. One is LCF (Large Core Fiber) to reduce optical power density at output of amplifier, and the other one is NZDSF (Non-zero Dispersion Shift Fiber) to reduce CD coefficient (Slope) at input of amplifier [1]. The nominal CD management block is nine DSF and one DCF span. The DCF (Chromatic Dispersion Compensation Fiber) cable is conventional single mode fiber (SMF) with 1.3um zero-dispersion wavelength (ZDW) to obtain a system ZDW of 1550nm. The maximum and average sea depth is approximately 6000m and 4800m, respectively.

3. Results

3.1 Stability of CD for installed submarine cable system

To confirm the installed optical submarine cable system stability, the continuously measurement was conducted for one day including measurement interruption. The number of spectral scan is 32points for each CD measurement. Figure 2 shows the group delay time and CD at beginning of the continuously measurement. The system consist of two different CD fiber type, but the quadratic equation well meet the measurement data, since the fitting error is less than 2.0E-11 during measurement period. Therefor the calculated CD slope is constant at measurement range.

The summary of the continuously measurement results and data are shown in table1 and figure3 respectively. The some lack of measurement data caused of measurement controller error. 0.7m (0.06m/day) cable elongation for system length was observed during measurement period. The trend of length variation was considered not only elongation but also shrink because the measurement period was shorter than the cycle of cable length variation. The average ZDW, CD slope and CD (@1550nm) were 1549.846nm, 0.08337ps/nm^2/km and 102.0ps/nm respectively. The variation of ZDW, CD slope and CD was 0.009nm, 0.00084ps/nm^2/km and 5.6ps/nm. The CD characteristics were not observation of increase and decrease tendency. From the point of system design, the CD fluctuation of 5.6ps/nm is satisfy the system requirement of the 10Gbit/s-transmission system. Because the robustness of submarine cable systems for CD is more than several ten ps/nm.

3.2 Accuracy of cumulative individual data

We compared to the cumulative individual CD data with CD measurement by using above test equipment during the system assembly test to confirm the system CD design. The individual data consists of the cable and repeater data that were measured at cable and repeater factory respectively. The difference of CD between the measurement data and the cumulative individual data is 1.2~6.4ps/nm for 1,128km length and 8 sample (4 fiber pairs). The results show that the cumulative individual data is good agreement with measurement results. Therefor, the cumulative individual CD data is reference to adjust the terminal CD equalization.

4. Conclusion

We have developed Far-end CD measurement equipment for the installed long-haul submarine cable system. The system CD stability was within 5.6ps/nm and the system length was 0.7m elongation during one-day measurement. We also confirmed that the individual data could calculate the system CD, but it is difficult to evaluate after the system repair including cable replacement, because there is no data of the cut cable CD. In such a case, the Far-end CD test equipment can evaluate the system CD for the installation and repair system.

5. Acknowledgement

The authors would like to thank Y.Horiuchi of KDD R&D Labs for his supports, and M.Imamura and E.Kimura of Advantest Co. for their co-operation.

6. References

[1] M.Suzuki, et al, OFC'98 San Jose, PD17, 1998.
[2] Y.Horiuchi, et al, Electronics Letters, 1993, vol.29, No.1 pp.4-5.

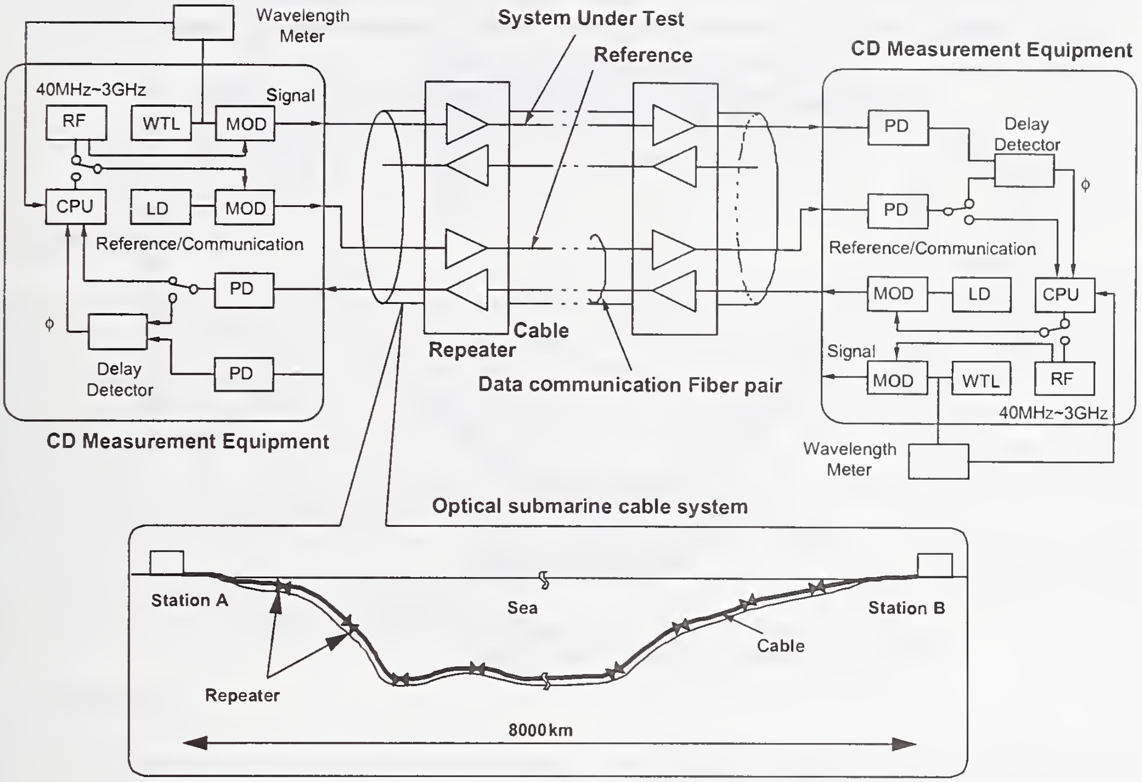

Fig.1 Chromatic dispersion Measurement for far end set up configuration

Table 1 Summary for Length and CD measurement of long haul optical submarine cable system

Statistic	Length [km]	ZDW [nm]	CD slope [ps/nm^2/km]	CD @1550nm [ps/nm]
Average	7963.1421	1549.846	0.08337	102.0
Maximum	7963.1424	1549.851	0.08377	104.8
Minimum	7963.1417	1549.842	0.08293	99.2
Dynamic Range	0.0007	0.009	0.00084	5.6
Standard deviation	0.0003	0.002	0.00021	1.4

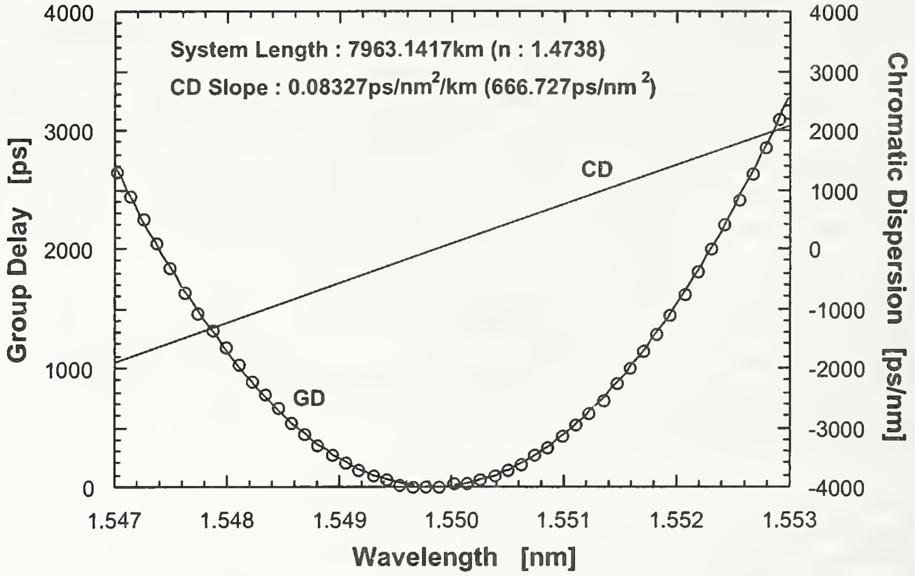

Fig.2 The results of Group delay time and Chromatic dispersion for long haul optical submarine cable system

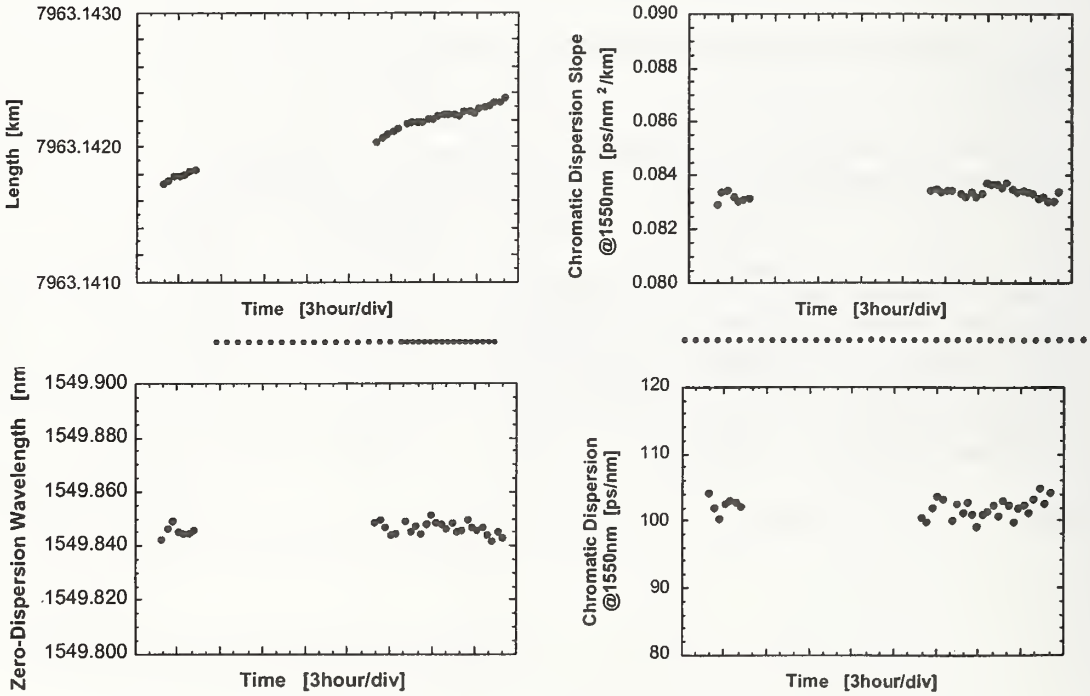

Fig.3 The continuously measurement results of system length and chromatic dispersion for long haul optical submarine cable system

A Novel Method for Measuring Chromatic Dispersion of Long Optical Fibers by Means of High Resolution Optical Ranging System Using a Frequency-Shifted Feedback Laser

Koichi Iiyama, Takahiro Maeda, and Saburo Takamiya
Department of Electrical and Electronic Engineering
Faculty of Engineering, Kanazawa University

1 Introduction

Recently, a new type of laser, a frequency-shifted feedback laser, has been actively studied [1-3]. The unique feature of the FSF laser is that an optical frequency shifter is incorporated in the laser cavity, which means that the optical beam in the laser cavity is frequency-shifted while recirculating in the laser cavity, and as a result, the optical frequency of the FSF laser is linearly chirped in time. The FSF laser is applicable to optical ranging system and optical frequency domain reflectometry (OFDR) by utilizing the characteristic feature of the frequency-chirped optical output. In the optical ranging system using a FSF laser, the spatial resolution of about 1 cm is achieved over 1 km measurement range.[4]

In this paper, we describe a novel measurement system of chromatic dispersion of long optical fibers by means of the optical ranging system using a FSF laser. The advantage of the proposed system is that no high-speed electronics and optics are necessary.

2 Principle

Figure 1 shows the system configuration for measuring the chromatic dispersion of optical fibers. The FSF laser consists of an erbium-doped optical fiber amplifier (EDFA), a tunable filter, an acoust-optic modulator (AOM) driven by 80 MHz, which was used as an optical frequency shifter, a polarization controller (PC), a polarizer and an output coupler. The light from the FSF laser is sent to the Michelson interferometer, in which an optical fiber under test (FUT) is connected in an arm of the interferometer, and the beat signal between the reflected light from the short arm (referred to as the reference light) and the reflected light at the far end of the fiber (referred to as the delayed light) is measured by the spectrum analyzer. Since the light from the FSF laser is frequency-chirped, the beat signal has a beat frequency proportional to the optical path difference between the reference and the delayed lights. If the optical fiber under test has chromatic dispersion, the beat frequency changes according to the wavelength of the FSF laser because the group velocity in the fiber depends on the wavelength. As a result, the chromatic dispersion can be estimated from the beat frequency change.

Now, we estimate the required spatial resolution in the proposed system. If the fiber length, the dispersion value, the wavelength separation, and the group velocity in the fiber are denoted by L (km), D (ps/nm/km), $\Delta\lambda$ (nm), and v_g (m/s), respectively, then the required spatial resolution δz is given by

$$\delta z = D \times L \times \Delta\lambda \times v_g \times 10^{-12} \quad \text{(m)} \tag{1}$$

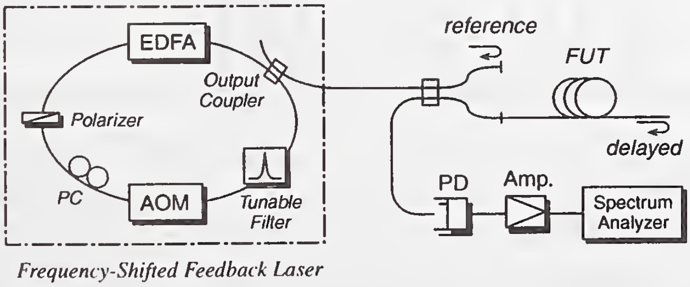

Figure 1: System configuration for measuring the chromatic dispersion.

where $v_g = c/n_g$, c is the light speed in vacuum, and n_g is the group refractive index of the fiber. The estimated spatial resolution for $D = 1$ ps/nm/km (a dispersion shifted fiber (DSF) is assumed), $c = 3 \times 10^8$ m/s, and $n_g = 1.46$ is tabulated in Table 1. It is found that the spatial resolution of about 1 cm is required for measuring the chromatic dispersion of long DSF's. Such a spatial resolution cannot be achieved in the conventional optical time domain reflectometry (OTDR) and OFDR. As can be seen in the next section, such a spatial resolution can be achieved in the optical ranging system using a FSF laser.

Table 1: Required spatial resolution in the proposed system.

L	$\Delta\lambda$	δz
100 km	1 nm	< 20.55 mm
	10 nm	< 20.55 cm
10 km	1 nm	< 2.055 mm
	10 nm	< 20.55 mm

3 Optical Ranging using a FSF laser

First, we investigated the performance of the optical ranging system using a FSF laser. Figure 2 shows the measured beat spectrum for (a) short optical fibers and (b) a long optical fiber. The frequency chirp range was about 20 GHz. It is found from Fig. 2(a) that the beat spectrum consist of two beat signals within the free spectral range (FSR) of the laser cavity, and the two beat signals approach each other with increasing the length of the optical fiber under test. The spatial resolution is about 1 cm. As is shown in Fig. 2(b), even if the optical fiber is long, we can obtain the beat spectrum similar to that for short optical fibers. The reason of such a beat spectrum is described as follows. The output of the FSF laser consists of a chirped frequency-comb, which means that many oscillating mode separated by the FSR of the FSF laser are simultaneously frequency-chirped. The number of the oscillating mode M is given by $\Delta F/\text{FSR}$, where ΔF is the chirp range, and M = 3,400 in our system. This is expressed as

$$\nu(t) = \frac{\nu_{FS}}{\tau_{RT}} t - \frac{q}{\tau_{RT}} \tag{2}$$

where $\nu(t)$ is the instantaneous optical frequency, ν_{FS} is the intracavity frequency shift caused by the AOM, $\tau_{RT} = 1/\text{FSR}$ is the round-trip time of the laser cavity, and q is an integer. As a result, the beat signal between the different oscillating modes can also been measured. The beat frequency f_B is expressed as

$$\begin{aligned} f_B &= \left[\frac{\nu_{FS}}{\tau_{RT}} t - \frac{q}{\tau_{RT}}\right] - \left[\frac{\nu_{FS}}{\tau_{RT}}(t - \tau_g) - \frac{q'}{\tau_{RT}}\right] \\ &= \frac{\nu_{FS}}{\tau_{RT}} \tau_g - \frac{m}{\tau_{RT}} \end{aligned} \tag{3}$$

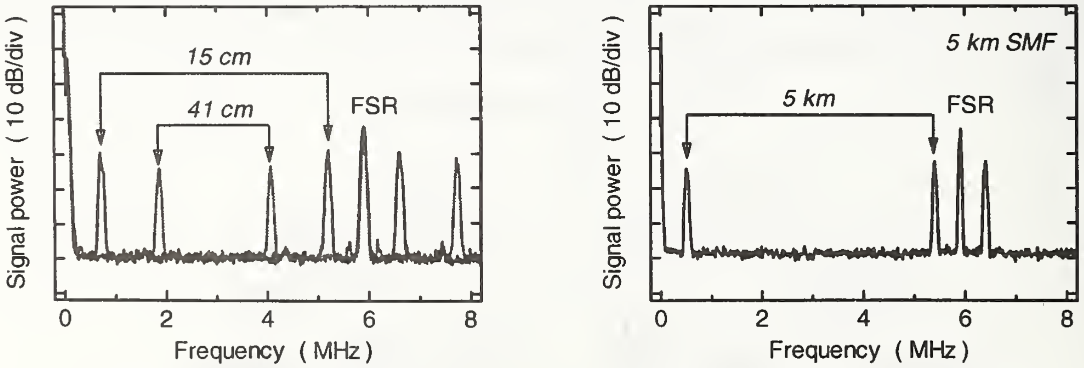

(a) For short optical fibers. (b) For a 5 km-long optical fiber.

Figure 2: Measured beat spectrum for short and long optical fibers.

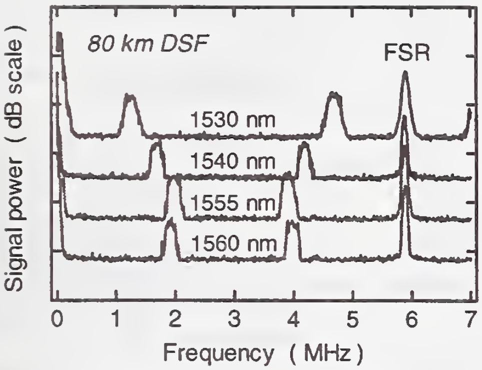

Figure 3: Measured beat spectrum for an 80 km-long DSF.

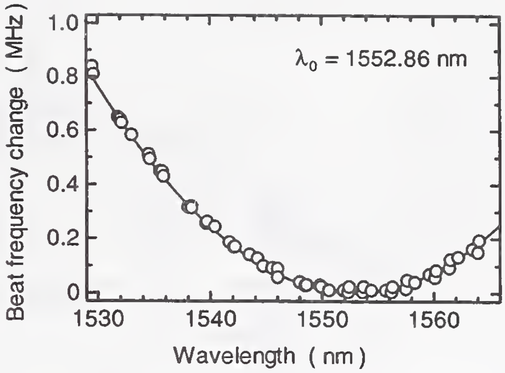

Figure 4: Measured beat frequency change for an 80 km-long DSF.

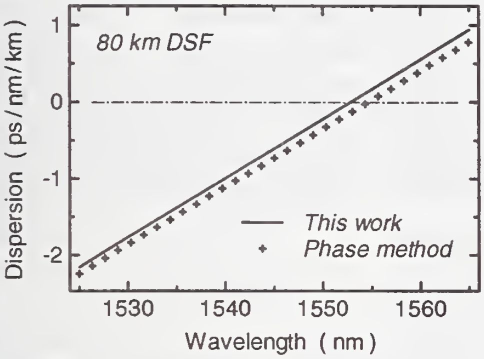

Figure 5: Estimated chromatic dispersion for an 80 km-long DSF.

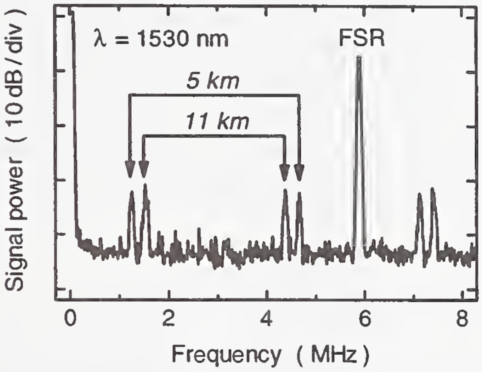

Figure 6: Beat spectrum for connected two SMF's.

where τ_g is the delay time between the reference and the delayed lights and $m = q - q'$ is a beat order. The beat order of the beat spectrum shown in Fig. 2(b) is $m \approx 2{,}000$. The spatial resolution is 1 cm, which is the same with that for short optical fibers.

4 Chromatic Dispersion Measurements

The chromatic dispersion of an 80 km-long DSF was estimated. Figure 3 shows the measured beat spectrum for different lasing wavelength of the FSF laser. The beat frequency depends on the wavelength. The beat frequency change against the lasing wavelength is shown in Fig. 4. The measured beat frequency change is well fitted with a parabolic function as shown in solid lines. The zero-dispersion wavelength λ_0 is the wavelength at which the beat frequency change is bottom (or peak) to be $\lambda_0 = 1552.86$ nm. From eq. (3), the change in the delay time $\delta\tau_g$ can be calculated from the beat frequency change δf_B to be

$$\delta\tau_g = \frac{\tau_{RT}}{\nu_{FS}}\delta f_B. \tag{4}$$

Therefore the chromatic dispersion can be estimated by differentiating the fitting curve shown in Fig. 3 with respect to the wavelength after converting δf_B to $\delta\tau_g$ by using eq. (4). Figure 5 shows the estimated chromatic dispersion against the wavelength. The solid line is the result by this work and the crosses are the result by the phase method. The chromatic dispersion can be well estimated by the proposed system.

Next, a 5 km-long single-mode fiber (SMF) and a 6 km-long SMF was connected by an FC/PC connector and were used as the optical fiber under test. In this experiment, the beat signals generated by the Fresnel

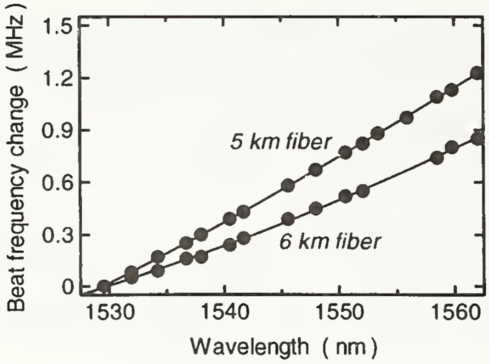

Figure 7: Measured beat frequency change for connected two SMF's.

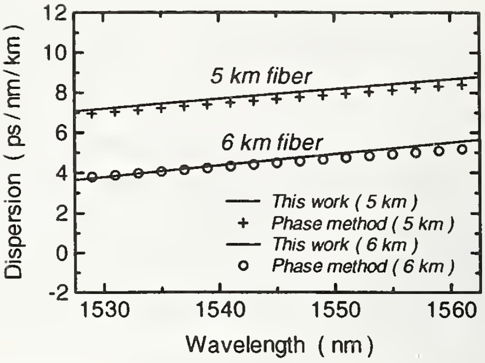

Figure 8: Estimated chromatic dispersion for 5 km-long and 6 km-long SMF's.

reflections at the connector and the far end of the fiber are simultaneously measured as shown in Fig. 6, and the chromatic dispersion of the individual fiber can be simultaneously estimated. The measured beat frequency change is shown in Fig. 7. The beat frequency change for the 6 km-long SMF is derived by subtracting the beat frequency change at the connector from that at the far end of the fiber. The estimated chromatic dispersion is shown in Fig. 8. The solid line is the result by this work and the crosses are the result by the phase method. The individual chromatic dispersion of the 5 km-long and the 6 km-long SMF's are simultaneously estimated.

5 Conclusion

We have proposed a novel method for measuring the chromatic dispersion of long optical fibers by means of optical ranging system using a FSF laser. The advantage of this system is that no high-speed electronics and optics is required. The chromatic dispersion for an 80 km-long DSF was estimated. And the individual chromatic dispersion of the connected two optical fibers could be simultaneously estimated. The proposed method is very useful technique for measuring the chromatic dispersion of the fibers as well as its length.

Acknowledgements

This work was carried out under the Cooperative Research Project Program of the Research Institute of Electrical and Communication (RIEC), Tohoku University, and the authors would like to thank to Prof. H. Ito, Dr. K. Nakamura and Mr. M. Yoshida of RIEC, Tohoku University, for their fruitful discussion. A part of this work was supported by the Telecommunications Advancement Foundation.

References

[1] K. Nakamura. *et. al.*: "Spectral characteristics of an all solid-state frequency-shifted feedback laser", *IEEE J. Quantum Electron.*, vol. 33, pp. 103 (1997).

[2] K. Nakamura, F. Kowalski, and H. Ito: "Chirped-frequency generation in a translated-grating-type frequency-shifted feedback laser", *Opt. Lett.*, vol. 22, pp.889 (1997).

[3] K. Kasahara, *et. al.*: "Dynamic properties of an all solid-state frequency-shifted feedback laser", *IEEE J. Quantum Electron.*, vol. 34, pp. 190 (1998).

[4] K. Nakamura, *et. al.*: "A new technique of optical ranging by a frequency-shifted feedback laser", *IEEE Photon. Technol. Lett.*, vol.=10, pp. 1772 (1998).

AUTHOR INDEX

☆U.S. GOVERNMENT PRINTING OFFICE:2000-460-746/36451

NIST Technical Publications

Periodical

Journal of Research of the National Institute of Standards and Technology—Reports NIST research and development in those disciplines of the physical and engineering sciences in which the Institute is active. These include physics, chemistry, engineering, mathematics, and computer sciences. Papers cover a broad range of subjects, with major emphasis on measurement methodology and the basic technology underlying standardization. Also included from time to time are survey articles on topics closely related to the Institute's technical and scientific programs. Issued six times a year.

Nonperiodicals

Monographs—Major contributions to the technical literature on various subjects related to the Institute's scientific and technical activities.

Handbooks—Recommended codes of engineering and industrial practice (including safety codes) developed in cooperation with interested industries, professional organizations, and regulatory bodies.

Special Publications—Include proceedings of conferences sponsored by NIST, NIST annual reports, and other special publications appropriate to this grouping such as wall charts, pocket cards, and bibliographies.

National Standard Reference Data Series—Provides quantitative data on the physical and chemical properties of materials, compiled from the world's literature and critically evaluated. Developed under a worldwide program coordinated by NIST under the authority of the National Standard Data Act (Public Law 90-396). NOTE: The Journal of Physical and Chemical Reference Data (JPCRD) is published bimonthly for NIST by the American Chemical Society (ACS) and the American Institute of Physics (AIP). Subscriptions, reprints, and supplements are available from ACS, 1155 Sixteenth St., NW, Washington, DC 20056.

Building Science Series—Disseminates technical information developed at the Institute on building materials, components, systems, and whole structures. The series presents research results, test methods, and performance criteria related to the structural and environmental functions and the durability and safety characteristics of building elements and systems.

Technical Notes—Studies or reports which are complete in themselves but restrictive in their treatment of a subject. Analogous to monographs but not so comprehensive in scope or definitive in treatment of the subject area. Often serve as a vehicle for final reports of work performed at NIST under the sponsorship of other government agencies.

Voluntary Product Standards—Developed under procedures published by the Department of Commerce in Part 10, Title 15, of the Code of Federal Regulations. The standards establish nationally recognized requirements for products, and provide all concerned interests with a basis for common understanding of the characteristics of the products. NIST administers this program in support of the efforts of private-sector standardizing organizations.

Order the **following** *NIST publications—FIPS and NISTIRs—from the National Technical Information Service, Springfield, VA 22161.*

Federal Information Processing Standards Publications (FIPS PUB)—Publications in this series collectively constitute the Federal Information Processing Standards Register. The Register serves as the official source of information in the Federal Government regarding standards issued by NIST pursuant to the Federal Property and Administrative Services Act of 1949 as amended, Public Law 89-306 (79 Stat. 1127), and as implemented by Executive Order 11717 (38 FR 12315, dated May 11, 1973) and Part 6 of Title 15 CFR (Code of Federal Regulations).

NIST Interagency Reports (NISTIR)—A special series of interim or final reports on work performed by NIST for outside sponsors (both government and nongovernment). In general, initial distribution is handled by the sponsor; public distribution is by the National Technical Information Service, Springfield, VA 22161, in paper copy or microfiche form.

U.S. Department of Commerce
National Institute of Standards
and Technology
325 Broadway
Boulder, Colorado 80303-3328

Official Business
Penalty for Private Use $300